

Doctoral Dissertation  
博士論文

**Neutron-capture element enrichment  
of early galaxies**

(初期銀河における中性子捕獲元素)

A Dissertation Submitted for the Degree of Doctor of Philosophy  
December 2022

令和4年12月博士（理学）申請  
Department of Physics, Graduate School of Science  
The University of Tokyo

東京大学大学院理学系研究科物理学専攻

Yuta Tarumi  
垂水 勇太



# Abstract

Elements heavier than iron are synthesized by neutron capture processes, which can be classified into  $s$  (slow) and  $r$  (rapid). For solar metallicity stars, the  $s$ -process elements are synthesized in asymptotic giant branch stars. The origin of  $r$ -process elements has not been identified for a long time, but observations of the electromagnetic counterparts of a neutron star merger event have provided evidence for synthesizing  $r$ -process elements. Neutron capture elements play an essential role in stellar archaeology because the timing of their synthesis is significantly different from that of magnesium and iron. The elemental abundances of stars can be measured for objects within the Milky Way's dark matter halo (200 kpc). The largest galaxy in this range is the Milky Way, with smaller dwarf galaxies and even smaller ultra-faint dwarf galaxies (UFDs).

This thesis aims to clarify the origin of neutron-capture elements and use these elements to probe the formation histories of galaxies. Chemical evolution studies for neutron-capture elements in the literature mainly focus on the Milky Way and classical dwarf galaxies. However, the chemical enrichment of UFDs needs to be studied as they are a valuable probe for the  $s$ -process enrichment: it can eliminate contributions from  $r$ -process events. In this thesis, I investigate the  $s$ -process enrichment of a UFD. I will show that it elucidates the need for a non-standard source of the  $s$ -process elements. To fully exploit the potential of UFDs as laboratories for cosmic nucleosynthesis, I need to study and further constrain the formation end evolution history of a UFD. I will show that the formation scenario of a UFD with an extended stellar profile can be successfully explained by an early merger. This is the first work that investigates the connection between the stellar density profile and the formation history.

While UFDs are useful to discretize contributions from rare events, Milky Way stars are suitable for studying statistical properties of nucleosynthesis sources, such as delay time distribution. For metal-poor stars in the Milky Way, a positive correlation is seen between  $r$ -process abundances and overall metallicity. It indicates that the  $r$ -process elements are produced with a significant time delay from progenitor star formation. The existence of a globular cluster with an internal  $r$ -process abundance spread can be explained by the inhomogeneity in the interstellar medium of a galaxy. It suggests that the number of star formation epochs in a globular cluster is one, in contrast to the standard formation scenario of globular clusters. Finally, I study the origin of an absorption feature in the spectrum of a neutron star merger. Helium is a possible candidate for the feature, which will be helpful as a probe for the physical condition of neutron star merger ejecta.

# Contents

<b>1</b>	<b>Neutron-capture elements in the Universe</b>	<b>4</b>
1.1	Cosmic elemental abundances . . . . .	4
1.1.1	Elements up to iron . . . . .	6
1.1.2	Iron-peak elements . . . . .	6
1.1.3	Neutron-capture processes . . . . .	7
1.2	Neutron-capture processes in the astrophysical environments . . . . .	7
1.2.1	<i>S</i> -process . . . . .	7
1.2.2	<i>R</i> -process . . . . .	12
<b>2</b>	<b>Introduction to the chemical evolution: what do we learn from spectroscopic observations?</b>	<b>16</b>
2.1	Chemical evolution of $\alpha$ elements in the Milky-Way and dwarf galaxies . . .	16
2.2	Barium . . . . .	18
2.3	Europium . . . . .	18
2.4	Strontium . . . . .	21
2.5	Ultrafaint dwarf galaxies . . . . .	21
2.6	Galaxies outside Local group . . . . .	22
2.7	Globular clusters . . . . .	22
2.8	Aim of this research . . . . .	23
<b>3</b>	<b><i>S</i>-process elements in ultrafaint dwarf galaxies</b>	<b>25</b>
3.1	Neutron-capture elements in ultrafaint dwarf galaxies . . . . .	25
3.2	Method . . . . .	26
3.2.1	Cosmological Simulations . . . . .	26
3.2.2	Chemical evolution . . . . .	27
3.2.3	Rotating massive stars and electron-capture supernovae . . . . .	29
3.3	Results . . . . .	30
3.3.1	Fiducial model . . . . .	30
3.3.2	Rotating massive star model . . . . .	32
3.3.3	Electron-capture supernova model . . . . .	33
3.4	Discussion . . . . .	33
3.4.1	<i>R</i> -process contribution . . . . .	33
3.4.2	Production of <i>s</i> -process elements in the fiducial model . . . . .	34
3.4.3	On additional sources – rotating massive stars . . . . .	35
3.4.4	On additional sources – electron-capture supernovae . . . . .	36
3.4.5	Initial mass function variation . . . . .	38
3.4.6	On ultra-faint dwarfs with internal Ba spreads . . . . .	39
3.4.7	Effects of tidal stripping . . . . .	41
3.5	Conclusions . . . . .	41
3.6	Additional analyses . . . . .	42
3.6.1	<i>R</i> -process . . . . .	42
3.6.2	Super-AGB . . . . .	42

<b>4</b>	<b>Formation of an extended ultrafaint dwarf galaxy via early mergers of building-blocks</b>	<b>44</b>
4.1	Stellar distribution profile in ultra-faint dwarf galaxies . . . . .	44
4.2	Simulations of early galaxies . . . . .	44
4.2.1	Galaxy formation model . . . . .	44
4.2.2	Final galaxy after the merger . . . . .	44
4.3	Properties of our merged galaxy . . . . .	46
4.3.1	Stellar distribution . . . . .	46
4.3.2	Outer halo stars . . . . .	48
4.3.3	Metallicity gradient . . . . .	48
4.4	Discussion . . . . .	48
4.4.1	Surface density profile . . . . .	48
4.4.2	Origin of the metallicity gradient . . . . .	51
4.4.3	Long-time evolution of an early merged galaxy . . . . .	52
4.4.4	Chemical enrichment . . . . .	52
4.4.5	Galactic building blocks . . . . .	53
4.4.6	On the fraction of galaxies with extended stellar profiles from early merger . . . . .	53
4.5	Summary and Conclusion . . . . .	54
<b>5</b>	<b><i>R</i>-process elements in the Milky-Way</b>	<b>55</b>
5.1	Enrichment of <i>r</i> -process elements in our galaxy . . . . .	55
5.2	Possible candidates for the <i>r</i> -process elements and their delay times . . . . .	56
5.2.1	The delayed scenario (neutron star merger model) . . . . .	56
5.2.2	No-delay scenario (rare supernova model) . . . . .	56
5.2.3	A "negative" delay scenario (collapsar model) . . . . .	57
5.3	<i>R</i> -process delay inferred from very metal-poor stars . . . . .	57
5.4	Conclusions and discussions . . . . .	63
5.5	Star formation history . . . . .	66
5.6	Analysis with Eu . . . . .	66
<b>6</b>	<b><i>R</i>-process abundance spread in a globular cluster</b>	<b>68</b>
6.1	Abundance anomalies and <i>r</i> -process abundance spread in a globular cluster .	68
6.2	Method . . . . .	69
6.2.1	Formation of globular clusters in cosmological simulation . . . . .	69
6.2.2	Element diffusion . . . . .	71
6.3	Results . . . . .	72
6.3.1	Eu abundance distribution . . . . .	72
6.3.2	Distribution of Eu abundance spread . . . . .	74
6.4	Discussion . . . . .	74
6.4.1	Sodium abundance . . . . .	75
6.4.2	Fraction of globular clusters with internal Eu spread . . . . .	77
6.4.3	Origin of <i>r</i> -process elements . . . . .	77
6.5	Conclusion . . . . .	78

<b>7</b>	<b>Non-local thermal equilibrium analysis for Helium and Strontium line signatures in kilonova</b>	<b>80</b>
7.1	Theoretical works on kilonova . . . . .	80
7.2	Basic picture . . . . .	81
7.2.1	He and Sr level structures . . . . .	81
7.2.2	Line optical depth . . . . .	83
7.2.3	Radioactive ionization . . . . .	85
7.3	Method . . . . .	85
7.3.1	Geometry . . . . .	86
7.3.2	Rate equations and Atomic data . . . . .	86
7.3.3	Radioactive ionization . . . . .	87
7.4	Spectrum calculation . . . . .	88
7.5	Result . . . . .	89
7.5.1	He model . . . . .	89
7.5.2	Sr model . . . . .	91
7.6	Effect of UV blanketing for He . . . . .	92
7.6.1	Comparison to SN Ibc on He lines . . . . .	92
7.7	Discussion . . . . .	94
7.7.1	He production in neutron star merger and spectral feature . . . . .	94
7.7.2	Non-local thermal equilibrium effect on Sr . . . . .	95
7.7.3	Comparison of He and Sr line features . . . . .	95
7.7.4	Model uncertainties and limitations . . . . .	96
7.8	Conclusion . . . . .	98
<b>8</b>	<b>Summary</b>	<b>99</b>
<b>9</b>	<b>Future prospects</b>	<b>100</b>
<b>A</b>	<b>Acronyms</b>	<b>103</b>



# 1 Neutron-capture elements in the Universe

## 1.1 Cosmic elemental abundances

[Alpher et al. \(1948\)](#) proposed that all the elements were synthesized during the Big Bang. They assumed that the cosmic baryons were initially composed of neutrons, and it captures another neutron while it keeps decaying into protons. The picture is questioned later: there are no stable isotopes at the mass numbers 5 and 8. Therefore, any two-body reactions cannot synthesize heavier nuclei: only the triple-alpha reaction can overcome the gap. The requirement for the density is high. Therefore, the possibility of the scenario above has been eliminated. Today, it is well accepted that the elements are synthesized inside stars and relevant explosive events, where high density allows the three-body reactions and further nucleosynthesis processes. The pioneering work is [Burbidge et al. \(1957\)](#): I will review the understanding of cosmic nucleosynthesis in this section.

Elements are a key to solving the cosmological history of matter circulation. This is because most elements are stable in the interstellar medium: they are not altered by any processes in the interstellar medium (ISM), except for very rare events of interaction with high-energy cosmic rays. In addition, as long as the energy is below meson production ( $\sim 140$  MeV), the number of nucleons is constant: only a transformation of a proton to a neutron and vice versa is allowed via  $\beta$  decays. Otherwise, all the processes are “reshuffling” of nucleons. Therefore, “cosmic nucleosynthesis” refers to the reshuffling of nucleons that were originally protons and neutrons. Elements are synthesized in high-energy and high-density environments such as stellar interiors. The high temperature enhances the possibility of tunneling, and high density allows the realization of the nucleosynthesis reactions that are still slow.

Figure 1 shows the solar abundances of elements. The abundances are obtained from [Asplund et al. \(2009\)](#). They mostly represent the solar photospheric abundances, except for a few rare elements, for which I use the abundances in meteorites (CI chondrites). A clear trend is an exponential decrease from the mass number 1 to 100, flat distribution from 100 to 210, and abrupt disappearance of heavier nuclei. [Burbidge et al. \(1957\)](#) has given a natural interpretation to this trend: the first exponential decrease represents the fact that the nucleosynthesis process becomes increasingly rare for massive nuclei. On the other hand, the flat trend after  $A \sim 100$  suggests that the frequency of the event is roughly constant. The abrupt drop of abundances with  $A > 210$  is the lack of isotopes with sufficiently long lifetimes: the only exceptions are  $^{232}\text{Th}$ ,  $^{235}\text{U}$ , and  $^{238}\text{U}$ .

The constant abundances for  $\sim 100 < A < 200$  is a consequence of neutron-capture processes. Considering the reaction path of neutron-capture and beta decay, at least two neutron-capture processes are required: *s*-process and *r*-process. The *s*-process is characterized by the slow capture of neutrons.  $\beta$  decay occurs when the nucleus becomes unstable. Therefore, nucleosynthesis proceeds along the path of the stable nuclei. On the other hand, the existence of neutron-rich nuclei cannot be explained by the addition of a small number of neutrons to the stable isotopes. It suggests that we need another process: the process should combine many neutrons at once, and then,  $\beta$  decays stop when the daughter nuclei are relatively stable to have a long lifetime. That is the *r*-process.

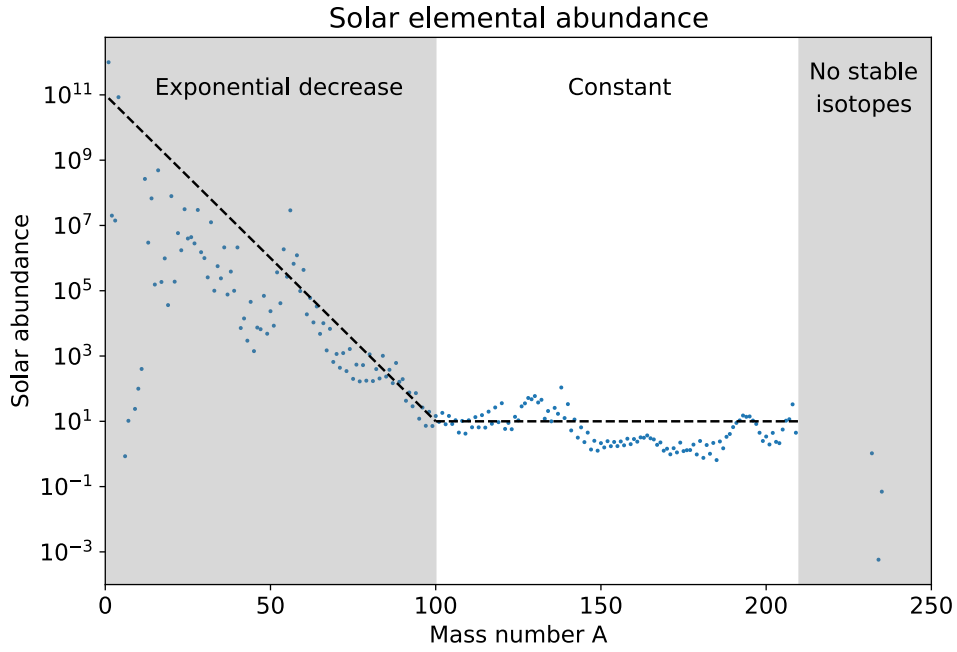


Figure 1: Abundance of elements in the Universe. Solar abundance is normalized so that Hydrogen abundance is  $10^{12}$ .

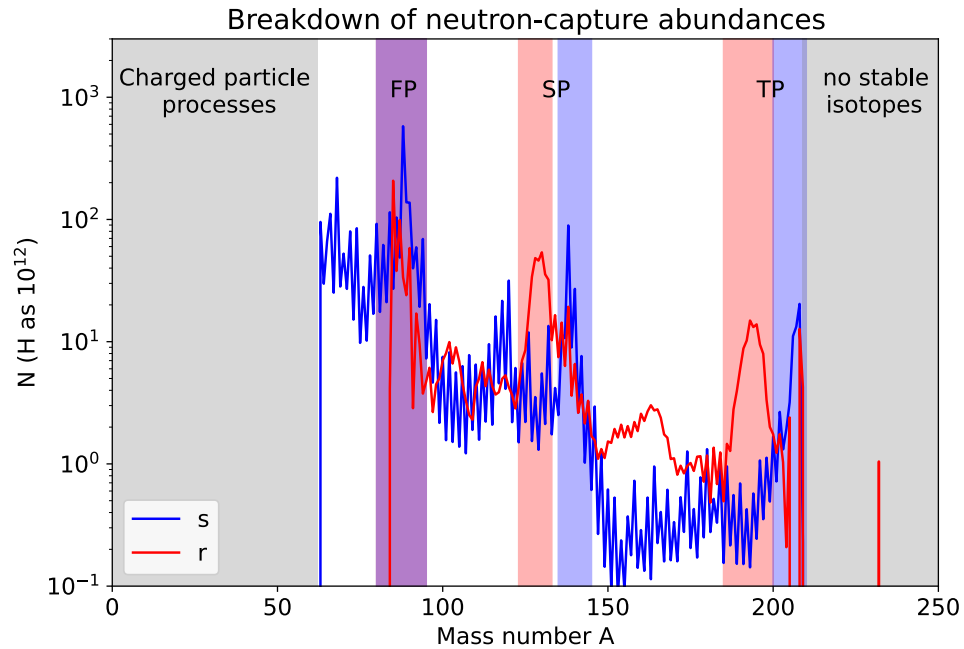
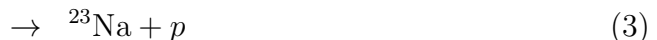


Figure 2: Decomposition of neutron-capture element abundances into *s*- and *r*-processes.

### 1.1.1 Elements up to iron

Charged particle processes are responsible for the synthesis of elements up to  $A \sim 100$ . These elements are mostly synthesized in stars. Since the central temperature of a star depends on the mass, the terminal point of the fusion reactions also depends on the mass. Stars more than  $\sim 0.08 M_{\odot}$  start burning Hydrogen in the core. During the main-sequence phase, a star burns effectively four protons into an  $\alpha$  particle via the pp chain or the CNO cycle. Once Hydrogen is exhausted in the core, the region of Hydrogen burning goes to a shell. The shell Hydrogen burning produces a huge luminosity. The envelope of the star bloats, and the surface temperature decreases while the luminosity increases. The Hydrogen shell-burning stars are the red giant branch stars.

If the star is sufficiently massive, Helium burning can be ignited in the core after the core contraction. This Helium burning is the triple  $\alpha$  reaction:  $3\alpha \rightarrow {}^{12}\text{C}$  and  ${}^{12}\text{C}$  is formed. Part of the  ${}^{12}\text{C}$  nucleus captures another  $\alpha$  particle to become  ${}^{16}\text{O}$ , and then become  ${}^{20}\text{Ne}$ . Therefore, the core composition after the Helium burning is a mixture of Carbon and Oxygen, called the “CO core”. Nuclear burning proceeds as Carbon burning:



Neon burning



Oxygen burning



and Silicon burning, which proceeds in a complex manner, and it ends at the nuclear statistical equilibrium, where elements around  ${}^{56}\text{Ni}$  compose the central material.  ${}^{56}\text{Ni}$  is the most abundant if the numbers of neutrons and protons are the same. The most stable nucleus is  ${}^{62}\text{Ni}$ . The region of the burning gets narrower as it proceeds to later stages: therefore, lighter elements are left outside, and the star looks like an “onion”. Lighter elements have more opportunities for formation, therefore, have higher abundances in general (see Figure 1).

### 1.1.2 Iron-peak elements

The thermonuclear explosion of a white dwarf (WD) is a factory of elements around the iron. A WD is formed as a remnant of stellar death of a low-to-intermediate mass ( $\lesssim 8 M_{\odot}$ ) star. Type-Ia supernovae are considered to be such explosions. There are two possible models for the progenitor: single-degenerate (SD) and double-degenerate (DD) models. In the SD model, the mass of a WD reaches its Chandrasekhar mass limit; then, the star undergoes

an explosion. On the other hand, the DD model considers the merger of two WDs causes thermonuclear detonation. Either way, the burning reaches a very high temperature, and the composition can be assumed to be a nuclear statistical equilibrium of similar numbers of neutrons and protons. This results in the synthesis of elements around the iron. The peak around the mass number  $A \simeq 60$  in Figure 1 shows the significant contribution from this process.

### 1.1.3 Neutron-capture processes

Elements heavier than the Fe group are synthesized via neutron-capture processes. The abrupt change of the abundance trend to a flat distribution after  $A \sim 100$  in Figure 1 is the consequence of neutron-capture processes. The abundance is not a decreasing function because neutrons do not feel the Coulomb barrier for nucleosynthesis. The critical parameter here is the neutron-capture cross section  $\sigma$ . In an environment with sufficient neutrons, the abundances of each element will follow  $\sigma^{-1}$ .

Figure 3 shows the lifetimes of each nucleus on the nuclear chart. *S*-process nucleosynthesis proceeds on the stable region on the chart because neutron captures are slower than the  $\beta$  decay. Once a resultant nucleus becomes unstable to decay, it quickly decays until the nucleus stabilizes. On the other hand, the *r*-process proceeds on the neutron-rich region: the path shifts to the bottom right of the chart. This is because of the quick neutron captures compared to the  $\beta$  decay. Nuclei do not care about moderate instability, and further neutron capture progresses. It continues until the decay lifetime becomes comparable to neutron captures of  $\sim$  ms.

The difference in the path on the chart gives a difference in the abundance pattern between these processes. Figure 2 shows the elemental abundance pattern for the *s* and *r* processes. In neutron-capture reactions, Many elements accumulate on the neutron magic numbers  $N = 50, 82$ , and  $126$  because their cross-sections are low. The accumulation appears as a “peak” on elemental abundances. The peak for  $N = 50, 82$ , and  $126$  is named the first, second, and third peaks. Nuclei synthesized in the *s*-process do not decay after the reactions. The *r*-process elements, on the other hand, decays after the neutron captures because they are unstable to  $\beta$  decays. The neutron number decreases in the decay process. Therefore, *r*-process peaks slightly shift to the lighter nuclei compared to the *s*-process peaks.

The following section explains the physical processes and astrophysical objects that contribute to the neutron-capture processes.

## 1.2 Neutron-capture processes in the astrophysical environments

### 1.2.1 *S*-process

The first analysis of the astrophysical *s*-process was phenomenological: the fundamental assumption is that a material is irradiated with a constant neutron flux. The evolution of the abundance for a nucleus  $A$  is given by:

$$\frac{dN(A)}{dt} = \lambda_n(A-1)N_s(A-1) - \lambda_n(A)N_s(A), \quad (9)$$

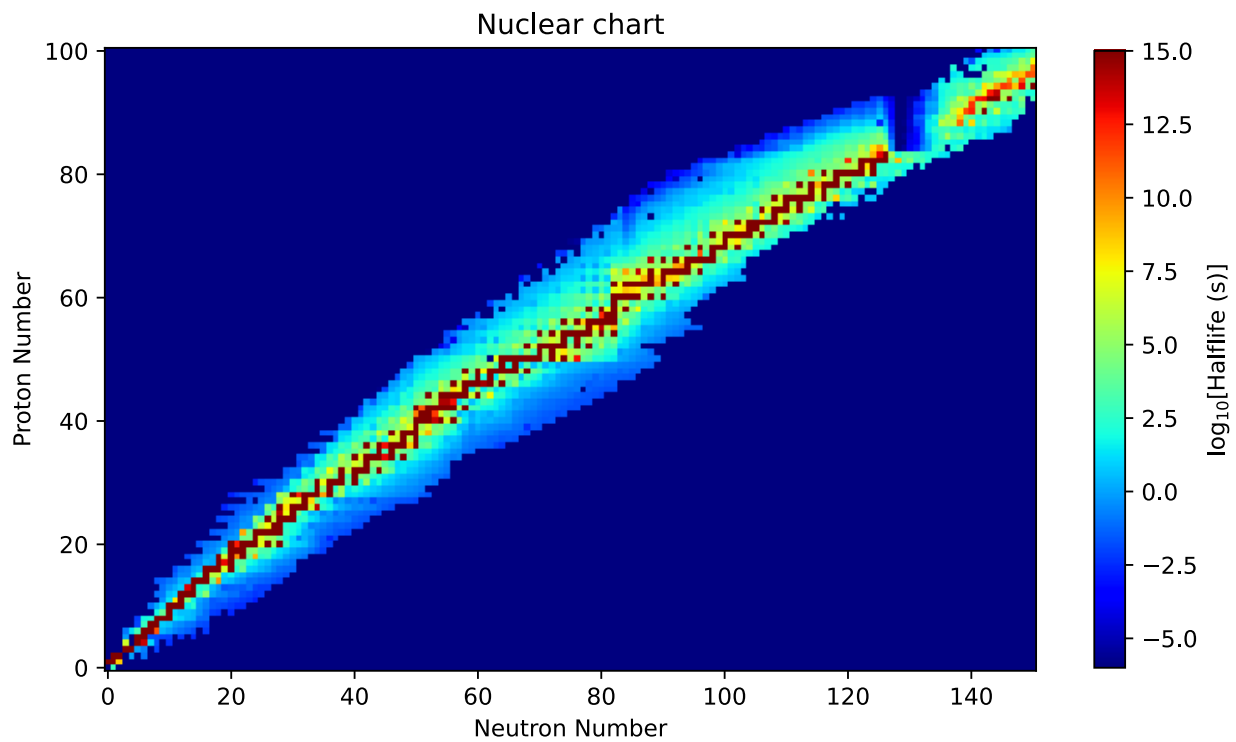


Figure 3: Nuclear chart

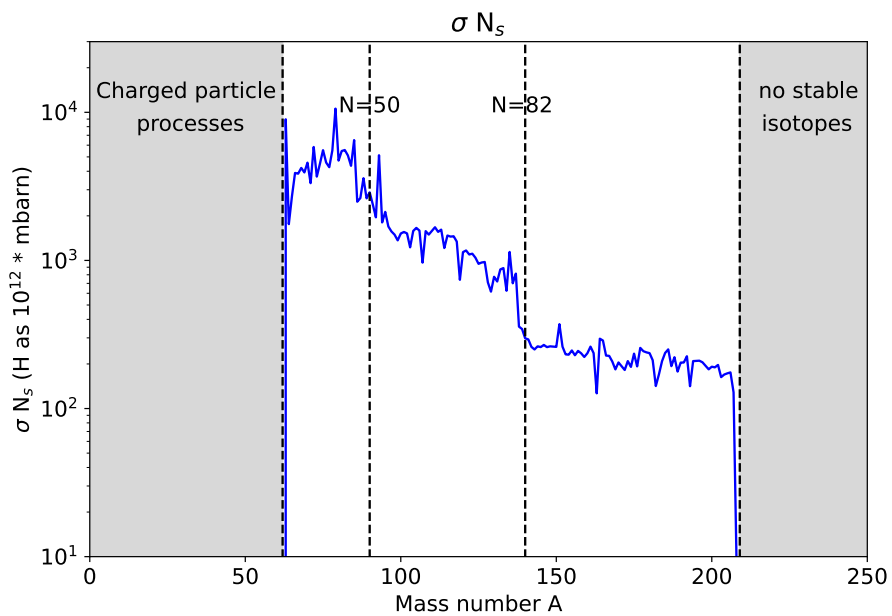


Figure 4: *s*-process abundances.

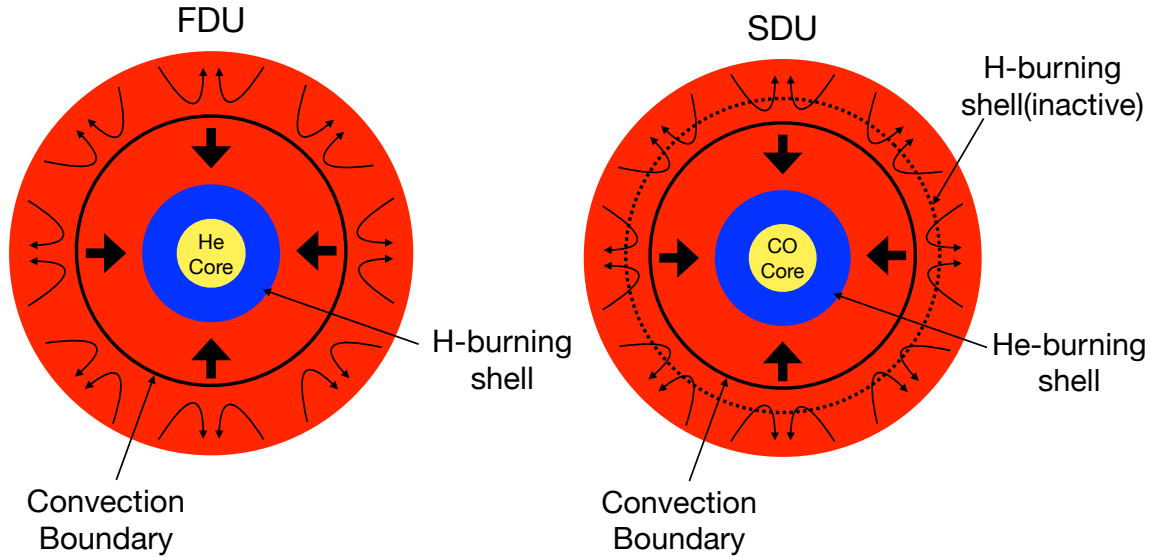


Figure 5: Schematic figure showing the stellar structure during the first dredge-up (FDU) and the second dredge-up (SDU).

where  $\lambda_n = \Phi\sigma$  is the neutron capture rate,  $\Phi = n_n v_T$  is the neutron flux. Here we have assumed that  $\beta$  decays do not play a role: all nuclei are considered to be instantly decaying or stable. This relation holds for all  $A$  on the  $s$ -process path. If the irradiation time is sufficiently long and the neutron flux  $\Phi$  is constant, the left-hand side goes to zero, and  $\sigma(A)N_s(A)$  is constant.

Figure 4 show the  $\sigma N$  values for the  $s$ -process contribution (Arlandini et al. 1999). Here,  $\sigma$  is the neutron-capture cross-section at 30 keV, and  $N$  is the abundance in the Universe, multiplied by the  $s$ -process contribution fraction. The cross-section is obtained from (Bao et al. 2000). The decline at the second neutron magic number  $N = 82$  is a consequence of multiple neutron irradiations: sometimes, the irradiation is insufficient to overcome the accumulation point at the magic number. To study the details of the  $s$ -process, we need nucleosynthesis studies together with the stellar evolution models.

**1.2.1.1 Stellar evolution of an asymptotic giant branch star** A star begins its life as a main-sequence star: it is composed of about 75 percent of Hydrogen, 25 percent of Helium, and a trace amount of heavy elements (“metals”). The star emits light using the energy produced in the Hydrogen nuclear fusion at the core. When the Hydrogen mass fraction becomes lower than  $\sim 10\%$ , it leaves the main sequence: the He core contracts while the H envelope expands. Stars with a low-temperature envelope are convective. Therefore material at the bottom of the convective envelope is dredged up to the surface (“first dredge-up”, FDU: see Figure 5). If the star’s initial mass is more than  $\sim 0.5 M_\odot$ , He is ignited in the core. The central He burning decreases the luminosity of the star. After the exhaustion of the core He, it becomes a giant again: He shell burning is ignited, while the CO core contracts. This is the asymptotic-giant branch (AGB) star.

During the early AGB (E-AGB) phase, the convective envelope progresses from the surface to the interior. If the star’s initial mass is  $\gtrsim 3.5 M_\odot$ , the convection digs the region where

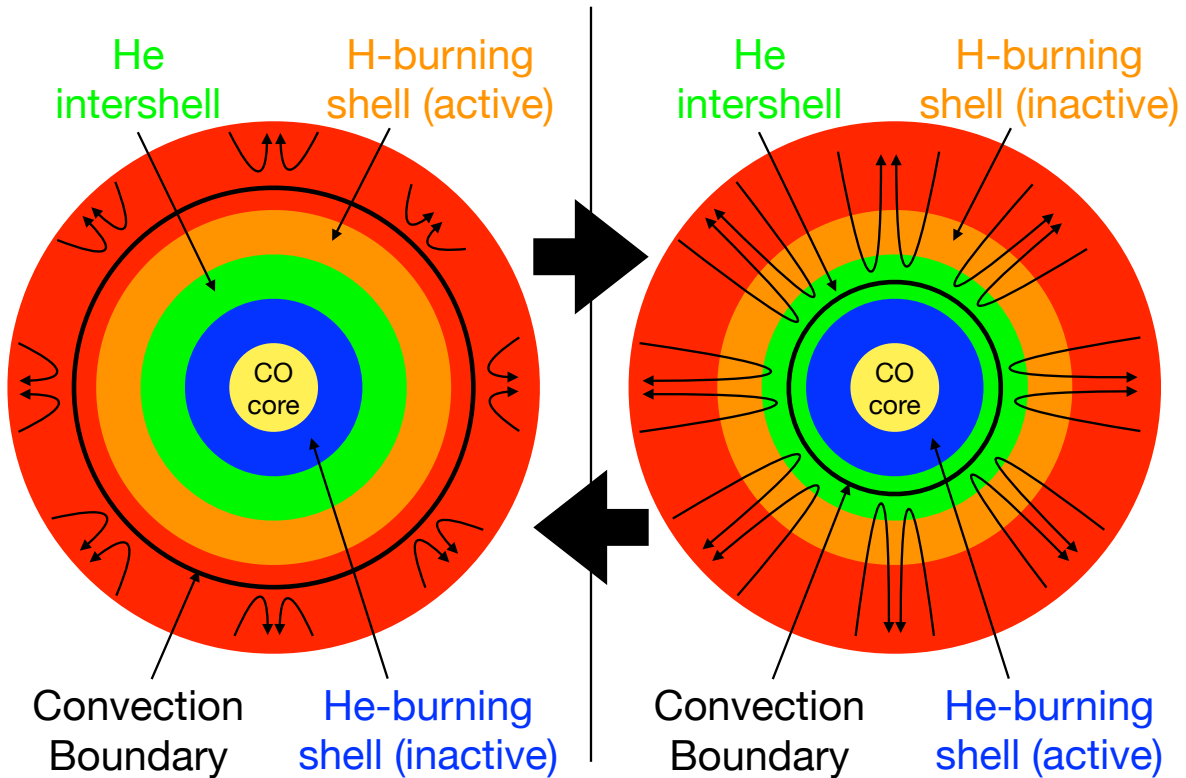


Figure 6: Schematic figure showing the stellar structure during the third dredge-up (TDU).

Hydrogen burning has affected the composition. Therefore, surface composition changes: this is the “second dredge-up” (SDU: see Figure 5). Note that less massive stars do not experience the SDU.

The E-AGB phase ends when Hydrogen shell burning is ignited. After this, the energy production is dominated by the shell Hydrogen burning for most of the time. Throughout this phase, the structure of the star is intermittently disrupted by thermal instability at the He shell. This phase is called the thermally-pulsing AGB (TP-AGB) phase. Between the Hydrogen and Helium shells, there is a radiative He layer: He intershell. The mass of the intershell grows as the H shell burns. The He sinks toward the center, and it results in the growth of He density at the inner region of the He shell, and the shell He burning rate increases. Once He shell burning begins, it produces energy strongly in a short period of time: it produces a thermal pulse. The pulse interrupts the intershell, and the region becomes convective. The convection dredges up the material produced in He burning: “third dredge-up” (TDU, see Figure 6). The star expands as the energy is produced, temperature decreases, and the burnings at Hydrogen and Helium shells stall. This cycle is repeated 10 – 100 times until the whole Hydrogen envelope is expelled by mass loss.

**1.2.1.2 *S*-process during AGB evolution** TDU is the phase for the *s*-process synthesis. However, forward modeling of the mixing process at the boundary of the convective envelope and radiative He intershell is difficult. A usual approach is to assume that some amount ( $\sim 10^{-4}$ ) of protons in the envelope is mixed into the He intershell. The mixed protons are captured by  $^{12}\text{C}$ :  $^{12}\text{C}(p, \gamma)^{13}\text{N}(\beta^+ \nu)^{13}\text{C}$  reactions produce  $^{13}\text{C}$ . Although  $^{13}\text{C}(p, \gamma)^{14}\text{N}$  is efficient,  $^{13}\text{C}$  remains in large amount if the proton is scarce: therefore, a small region that contains a lot of  $^{13}\text{C}$  remains: “ $^{13}\text{C}$  pocket”. The  $^{13}\text{C}(\alpha, n)^{16}\text{O}$  reaction is activated at  $\sim 80$  MK. The produced neutrons are then captured by heavy nuclei such as Fe, producing the *s*-process elements.

Historically,  $^{22}\text{Ne}(\alpha, n)^{25}\text{Mg}$  reactions are considered. Since their activation temperature is higher ( $\sim 300$  MK), relatively massive ( $\sim 5 M_{\odot}$ ) stars are considered. However, various problems have been found for this scenario: (i) neutron flux does not match the branching ratio in solar abundance stars, (ii) luminosity of the stars is overpredicted in stars undergoing  $^{22}\text{Ne}(\alpha, n)^{25}\text{Mg}$  reactions, to name a few. From these analyses, it is now well accepted that low-to-intermediate mass stars are the origins of the *s*-process elements in the Universe.

**1.2.1.3 Observational confirmation for the *s*-process in AGB stars** Observationally, Merrill (1952) has observed spectral features of TcI in the surface of a red giant star (“S-star”). Tc is also detected in a more evolved C-star (C/O ratio more than unity). Since the half-life of Tc of  $2 \times 10^5$  yr is shorter than the typical stellar evolution timescale, it is clear that Tc is synthesized in S and C stars. This is consistent with the TDU picture during TP-AGB stars: the pulse period is shorter than the lifetime of Tc. Therefore it remains on the surface of the star.

**1.2.1.4 *S*-process production in rotating massive stars** The stellar rotation has a crucial effect on the internal evolution of a star. In terms of chemical enrichment, they are proposed as the origin of “primary” Nitrogen, i.e., Nitrogen that originates from Hydrogen and Helium inside the star, not from Carbon, in a metal-poor environment (Chiappini et al. 2006). Stellar rotation facilitates the chemical diffusion between different layers inside a star. During core He burning, Carbon is synthesized due to the triple-alpha process. The Carbon diffuses to the radiative layer of He core. Also, the proton diffuses to the same layer from the stellar envelope. When the temperature of the layer becomes sufficiently high, protons are captured by the Carbon to produce Nitrogen (CNO cycle but with “primary” Carbon). Since no other processes are proposed to solve the primary Nitrogen problem, this is considered the solution.

For solar metallicity stars, *s*-process elements are dominantly produced by the AGB stars. However, Limongi and Chieffi (2018) and Prantzos et al. (2018) have pointed out that rotating massive stars contribute significantly to the *s*-process element production for low-metallicity stars. They have proposed that both  $^{13}\text{C}(\alpha, n)^{16}\text{O}$  and  $^{22}\text{Ne}(\alpha, n)^{25}\text{Mg}$  reactions contribute to the neutron production: the former reaction is for light neutron-capture (such as Nitrogen and Fluorine) while the latter is for the heaviest *s*-process elements. We have seen that Nitrogen production is enhanced during the core He burning phase. Since the layer with abundant Nitrogen is the “He” layer, there is a sufficient amount of  $\alpha$  particles. Therefore,  $\alpha$  particles are captured by Nitrogen to form  $^{22}\text{Ne}$  via  $^{14}\text{N}(\alpha, \gamma)^{18}\text{F}(\beta, \gamma)^{22}\text{Ne}$  reactions. Then, the  $^{22}\text{Ne}$  works as the neutron source for the *s*-process production.

Prantzos et al. (2018) study the contribution of rotating massive stars to the chemical evolution of the Milky Way using a one-zone model. They have calibrated the initial distribution of rotational velocities (“IDROV”) by requiring that (i) the primary behavior of  $^{14}\text{N}$  is explained and (ii) the  $s$ -process elements are not overproduced. As a result,  $\sim 20\%$  of stars at  $[\text{Fe}/\text{H}] = -3$  rotates at 300 km/s, which is about half of the break-up rotation velocity, while the fraction of fast rotators decrease significantly at  $[\text{Fe}/\text{H}] \geq -2$ . The remaining  $[\text{Fe}/\text{H}] = -3$  stars rotate at 150 km/s. At higher metallicity  $[\text{Fe}/\text{H}] > -2$ , the fraction of nonrotating stars increases, and at solar metallicity  $\sim 70\%$  of stars are nonrotating, while others are slow (150km/s) rotators.

## 1.2.2 $R$ -process

**1.2.2.1 Conditions for the  $r$ -process nucleosynthesis** In the  $r$ -process, the neutron capture reactions proceed far from the stable region of the nuclei chart. The condition for the “neutron capture faster than  $\beta$ -decay” can be written as:

$$N_n \langle \sigma v \rangle \gg \frac{1}{\tau_\beta}. \quad (10)$$

For typical neutron-rich nuclei (that are less neutron-rich than the neutron drip line),  $\tau_\beta \simeq 100$  ms. The astrophysical conditions for the  $r$ -process is typically  $10^9$  K. Therefore, the typical thermal velocity of a neutron is  $v/c \simeq 0.01$  or  $v \simeq 10^8$  cm s $^{-1}$ . The neutron-capture cross sections for neutron-rich nuclei at the energy of  $\sim 10^5$  eV is  $\sigma \simeq 10$  mb =  $10^{-26}$  cm $^2$ . Therefore, the requirement for the neutron density is  $N_n \gg 10^{19}$  [cm $^{-3}$ ]. Astrophysical sites for such an environment have been a crucial question for cosmic nucleosynthesis.

Such extremely high neutron density is obtained in an explosive event. Let us consider the following situation: initially, a very high-temperature and high-density material exists. Then, the material suddenly expands, and temperature and density decrease significantly. The neutron capture reactions occur during this expansion phase. After the density has dropped sufficiently, only  $\beta$ -decays occur, and the neutron-rich material becomes stable.

Due to the high density and temperature, reaction rates for capturing a nucleon and the photodisintegration rates are enormous. In such a condition, we can assume that the reactions are in a chemical equilibrium: nuclear statistical equilibrium (NSE). In this case, the Saha equilibrium for neutron capture holds:

$$\frac{N(A, Z)N_n}{N(A+1, Z)} = \frac{G(A, Z)}{G(A+1, Z)} \exp\left[-\frac{Q_n}{k_B T_n}\right] 2\left(\frac{2\pi m_n k_B T_n}{h}\right)^{3/2} \quad (11)$$

where  $Q_n$  is a binding energy of a neutron. The same reasoning is valid for a proton capture:

$$\frac{N(A, Z)N_p}{N(A+1, Z+1)} = \frac{G(A, Z)}{G(A+1, Z)} \exp\left[-\frac{Q_p}{k_B T_n}\right] 2\left(\frac{2\pi m_p k_B T_n}{h}\right)^{3/2}. \quad (12)$$

By repeating these relations, we obtain the abundances of any nuclei:

$$Y_i = Y_n^{N_i} Y_p^{Z_i} \frac{G_i(T) A_i^{3/2}}{2^{A_i}} \left(\frac{\rho}{m_u}\right)^{A_i-1} \left(\frac{2\pi\hbar^2}{m_u k T}\right)^{3(A_i-1)/2} \exp\left[\frac{B_i}{k T}\right] \quad (13)$$

where  $B_i$  is the nuclear binding energy. The equation shows that the abundance of all the nuclei can be described by  $\rho, Y_e = Y_n/(Y_n + Y_p)$ , and  $T$ .

If the ejecta interacts via weak interactions, we need to consider their effect explicitly. Therefore, in an astrophysical condition, the three quantities  $\rho, T, Y_e$  are solved in a time-dependent manner. In particular, for the case of neutrino-driven wind in a supernova, neutrino flux from the proto-neutron star that is forming as the consequence of the core collapse crucially affects  $Y_e$ .

**1.2.2.2  $\alpha$  process** Even if a complete equilibrium is not achieved, the equilibrium may hold partially (“quasi-statistical equilibrium”, QSE). A prominent example is the  $\alpha$ -rich freeze-out. In this case, the bottleneck reaction is the synthesis of  $^{12}\text{C}$  from three  $\alpha$  particles. In an neutron-rich condition,  $^4\text{He}(\alpha n, \gamma)^9\text{Be}(\alpha, n)^{12}\text{C}$  is the formation channel for  $^{12}\text{C}$ . This is effectively a four-body reaction because  $^9\text{Be}$  is not much stable: the first reaction  $^4\text{He}(\alpha n, \gamma)^9\text{Be}$  is tightly balanced in the statistical equilibrium. Since the capture of  $\alpha$  particles occurs between  $T = 5 \times 10^9 \text{ K}$  to  $2.5 \times 10^9 \text{ K}$ , the ejecta density when it crosses this temperature region determines whether  $\alpha$  particles remain uncaptured. I call the process of synthesizing heavier nuclei from  $\alpha$  particles the  $\alpha$  process here.

The fraction of  $\alpha$  particles that remain uncaptured can be estimated following the formulation of [Hoffman et al. \(1997\)](#). Here I briefly summarize the equations. At the beginning of the  $\alpha$  process ( $T_9 = 5$ , where  $T_9$  is the temperature in GK), the material is composed of free neutrons and  $\alpha$  particles. The electron fraction determines the ratio between neutrons and  $\alpha$  particles: almost all the protons are captured into  $\alpha$  particles. The mass fractions of  $\alpha$  and  $n$  are

$$X_{\alpha,0} = 2Y_{e,i} \quad (14)$$

$$X_{n,0} = 1 - 2Y_{e,i}. \quad (15)$$

The composition of the resulting material should satisfy

$$\frac{1}{2}X_{\alpha,f} + \frac{\bar{Z}}{\bar{A}}X_s \simeq Y_{e,f}, \quad (16)$$

where  $Y_{e,f}$  is the electron fraction at  $T_9 = 2.5$ .

Since  $^9\text{Be}$  is not much stable, we can assume that the fraction of  $^9\text{Be}$  is in statistical equilibrium throughout the  $\alpha$  process. Therefore,

$$Y_9 \simeq 8.66 \times 10^{-11} Y_\alpha^2 Y_n \rho_5^2 T_9^{-3} \exp(18.26/T_9), \quad (17)$$

where  $Y_9$  is the number fraction for  $^9\text{Be}$ . In this case,  $\alpha$  particles and neutrons decrease only through the formation of Carbon. Once it passes the bottleneck, the  $\alpha$  capture proceeds to form seed nuclei. Taking  $F, G$  as the average number of  $\alpha$  particles and neutrons per one seed nucleon, the time evolution of the  $\alpha$  and neutron abundances are:

$$\frac{dY_\alpha}{dt} \simeq -FY_\alpha Y_9 \rho N_A \langle \sigma v \rangle_{\alpha,n}, \quad (18)$$

$$\frac{dY_n}{dt} \simeq -GY_\alpha Y_9 \rho N_A \langle \sigma v \rangle_{\alpha,n}. \quad (19)$$

Substituting the  $Y_9$  and changing the variable from time to temperature by assuming

$$T_9(T) = T_9(0) \exp(-t/\tau_{\text{dyn}}), \quad (20)$$

we obtain

$$\frac{dY_\alpha}{dT_9} \simeq FY_\alpha^3 Y_n g(T_9) \tau_{\text{dyn}}, \quad (21)$$

$$\frac{dY_n}{dT_9} \simeq GY_\alpha^3 Y_n g(T_9) \tau_{\text{dyn}}, \quad (22)$$

where

$$g(T_9) \simeq 8.66 \times 10^{-6} \rho_5^3 T_9^{-4} \exp(18.26/T_9) N_A \langle \sigma v \rangle_{\alpha n}. \quad (23)$$

The function  $g(T_9)$  determines the fraction of  $\alpha$  particles that remain after the Helium burning. In the case of  $Y_{e,i} < \bar{Z}/\bar{A}$ , where  $\bar{Z}/\bar{A}$  is the average proton-to-nucleon ratio for the seed nuclei, the final composition favors the presence of neutrons. Since neutrons work as a catalyst for Carbon synthesis, we can take  $Y_n \simeq Y_{n,0}$  during the  $\alpha$  process. In this case, the fraction of  $\alpha$  particles that remain in the ejecta is

$$Y_{\alpha,f}^{-2} - Y_{\alpha,0}^{-2} \simeq 2FY_{n,0} \tau_{\text{dyn}} \int_{2.5}^5 g(T_9) dT_9. \quad (24)$$

Here we assume constant entropy during the adiabatic expansion:  $S \simeq C(T_9)T_9^3/\rho_5$ . Here we eliminate density term from  $g(T_9)$ :

$$g(T_9) \simeq 8.66 \times 10^{-6} S^{-3} C(T_9)^3 T_9^5 \exp(18.26/T_9) N_A \langle \sigma v \rangle_{\alpha n}. \quad (25)$$

The  $g(T_9)$  monotonically increases with the temperature. The main contribution to the integral comes from  $4 \lesssim T_9 \lesssim 5$ . Therefore, we approximate  $C(T_9) \simeq 3.33$  and obtain

$$\int_{2.5}^5 g(T_9) dT_9 \simeq 6.4 \times 10^8 S^{-3} \text{ s}^{-1}. \quad (26)$$

Therefore, entropy is the factor that determines the fraction of  $\alpha$  particles that remain unburned.

**1.2.2.3 Normal core-collapse supernova** The innermost ejecta of a normal SN after the core collapse had been considered the astrophysical sites for the  $r$ -process (e.g., [Qian and Woosley 1996](#)). However, they are now eliminated from the list of the origin of the heaviest  $r$ -process elements (although weak  $r$ -process might occur: see, e.g., [Wanajo et al. 2011; 2018](#)). This is because of the weak interactions with neutrinos emitted from the newly formed proto-neutron star. The neutrino flux regulates the neutron richness via reactions  $\nu_e + n \rightleftharpoons p + e^-$  and  $\bar{\nu}_e + p \rightleftharpoons n + e^+$ . The ejecta is exposed to a strong flux of neutrinos from the de-leptonizing proto-neutron star. Recent simulations suggest that the equilibrium is tilted rather proton-rich, and it is unlikely for the ejecta to be sufficiently neutron-rich for synthesizing the heaviest  $r$ -process elements.

**1.2.2.4 Neutron-star mergers** A neutron star is composed of neutrons. As the densely packed neutrons are released to lower densities by a merger, neutron captures occur, and  $r$ -process elements are synthesized. A significant amount of very neutron-rich ( $Y_e \lesssim 0.2$ ) material is ejected via the tidal deformation and breaking of the neutron star (“dynamical ejecta”). The neutron richness is sufficient for synthesizing the heaviest  $r$ -process elements. In addition, neutrino wind from the hypermassive neutron star formed as the merger’s remnant significantly enhances the ejecta’s mass (“wind ejecta”). The high ( $\sim 10$  GK) temperature allows the electron-positron pair production. These particles “protonize” the material via



reaction. The equilibrium value of the electron fraction  $Y_e$  could be more than 0.5 (proton-rich). However, it is often the case that the time duration for the interaction is not sufficient for the equilibrium. In that case, the ejecta is moderately neutron-rich ( $Y_e \simeq 0.3$ ), synthesizing the first peaks of the  $r$ -process elements. The contributions of these two components could make the  $r$ -process abundance pattern in the Universe.

**1.2.2.5 Collapsars** Collapsars, a collapse of a rotating massive star that produces long gamma-ray bursts, is proposed as the origin of the  $r$ -process elements (Siegel et al. 2019). An accretion disk is formed around the central black hole during the collapse. The disk becomes neutron-rich if the density of the accretion disk is sufficiently high. Assuming the material is (i) transparent to neutrinos and (ii) holds equilibrium for other reactions, Fermi energy for an electron increases. In that case, a neutron is favored in the reaction  $n + \nu_e \rightleftharpoons p + e^-$ . Therefore, the disk becomes neutron-rich. If the disk is expelled and the density decreases quickly,  $r$ -process elements are synthesized.

High density on the disk plane outside the innermost stable circular orbit is the condition that allows the synthesis of the  $r$ -process elements. The density is translated to the accretion rate by assuming an accretion disk model. Shakura-Sunyaev accretion disk model (Shakura and Sunyaev 1973) is the standard methodology. Briefly, material needs to lose angular momentum in order to accrete to the center. This is achieved by transporting angular momentum outward. The transport is mediated by viscosity. They have assumed a dimensionless viscosity parameter  $\alpha = \nu/(c_s h)$  to close the equations. Here,  $c_s$  and  $h$  are sound speed and the scale height of the disk at the radius we consider, and  $\nu$  is the kinematic viscosity ( $= \mu/\rho$ . Viscosity coefficient  $\mu$  [dyn cm<sup>-2</sup> s] is defined in a Couette flow: it satisfies  $\tau = \mu v/h$ , where  $\tau$  is the shear stress [dyn cm<sup>-2</sup>],  $v$  is the velocity of the plate, and  $h$  is the width of the flow). The parameter  $\alpha$  satisfies  $0 < \alpha < 1$  and the exact value of  $\alpha$  is unknown: it is treated as a model parameter.

The  $r$ -process elements are synthesized if the accretion rate is higher than an ignition accretion rate:

$$\dot{M}_{\text{ign}} = K_{\text{ign}}(a) \left( \frac{\alpha}{0.01} \right)^{5/3}, \quad (28)$$

where  $K_{\text{ign}}(a) \simeq 10^{-3} M_{\odot} s^{-1}$  depends on the blackhole spin  $a$ .

## 2 Introduction to the chemical evolution: what do we learn from spectroscopic observations?

The elemental abundances of the ISM in a galaxy evolves with time. The initial compositions are shaped by the Big Bang nucleosynthesis (BBN): 75% is Hydrogen (H), 25% is Helium (He), and a trace amount of Lithium (Li). The first generation of stars form from the primordial gas and synthesizes heavy elements. When the stars die, they disperse elements to the surrounding ISM. The next generation of stars form from the metal-enriched material. The ISM abundance at each moment is imprinted in a star. Although some stars lose information on initial compositions through complex evolution processes, most retain their initial abundances. Therefore, we can infer the evolution of chemical abundances in the ISM of a galaxy by spectroscopic observations of stars.

The most natural way to describe the chemical enrichment history is to plot stars on the age-abundance plane. There are a few ways to infer the age of a star. One is the isochrone fitting on the color-magnitude diagram. The age estimate for each star is published in recent surveys such as the GALAH survey (Buder et al. 2018; 2021). The typical error in the age is  $\sim 2$  Gyr. This information is helpful for the chemical evolution of the timescale longer than  $\sim$  Gyr. Another way to infer the stellar age is asteroseismology, which is helpful for giant stars. Stellar oscillations tell us about their surface gravity. Together with the size of the star, we can infer the mass. Since we know the relation between the stellar mass and lifetime, we can estimate the age.

Although these methodologies work to some extent, it is generally impossible to infer a star's age. The best proxy is the abundance of iron (Fe). Observers can measure the iron number fraction over Hydrogen,  $[\text{Fe}/\text{H}]$ , via spectroscopy. ISM is metal-free at first, and then Fe accumulates due to stellar lifecycles. Old stars are Fe-poor compared to new stars. Plotting two abundance ratios  $[\text{X}/\text{H}]$  and  $[\text{Fe}/\text{H}]$  reveal the accumulation history of element X. More typical plots take  $[\text{X}/\text{Fe}]$  or  $[\text{X}/\text{Mg}]$  as the y-axis of the plot, as it clearly shows the relative timescale of the synthesis of the element X compared to Fe or Mg.

The spectroscopic observations first target stars in the Milky Way, and now it expands to galaxies within  $\sim 100$  kpc, about halfway to the edge of the Local Group. A few tens of stellar groups moving together (satellite galaxies) are discovered, and elemental abundances are measured. Here I summarize chemical abundance studies on various systems in the literature.

### 2.1 Chemical evolution of $\alpha$ elements in the Milky-Way and dwarf galaxies

$\alpha$  elements are synthesized predominantly in massive stars. Therefore, they are helpful as the standard of comparison because they are synthesized without delay. In contrast, the production of Fe, the most typically observed element, delays the formation of the progenitor star. This is because type-Ia supernova, which produces about half of Fe observed in the Sun, significant delays from the formation of the progenitor stars.

Figure 7 shows the  $[\text{Mg}/\text{Fe}]-[\text{Fe}/\text{H}]$  plot for stars in dwarf galaxies and the Milky Way. There is a clear decreasing trend for the Milky Way stars from  $[\text{Fe}/\text{H}] \sim -1$ : this is a

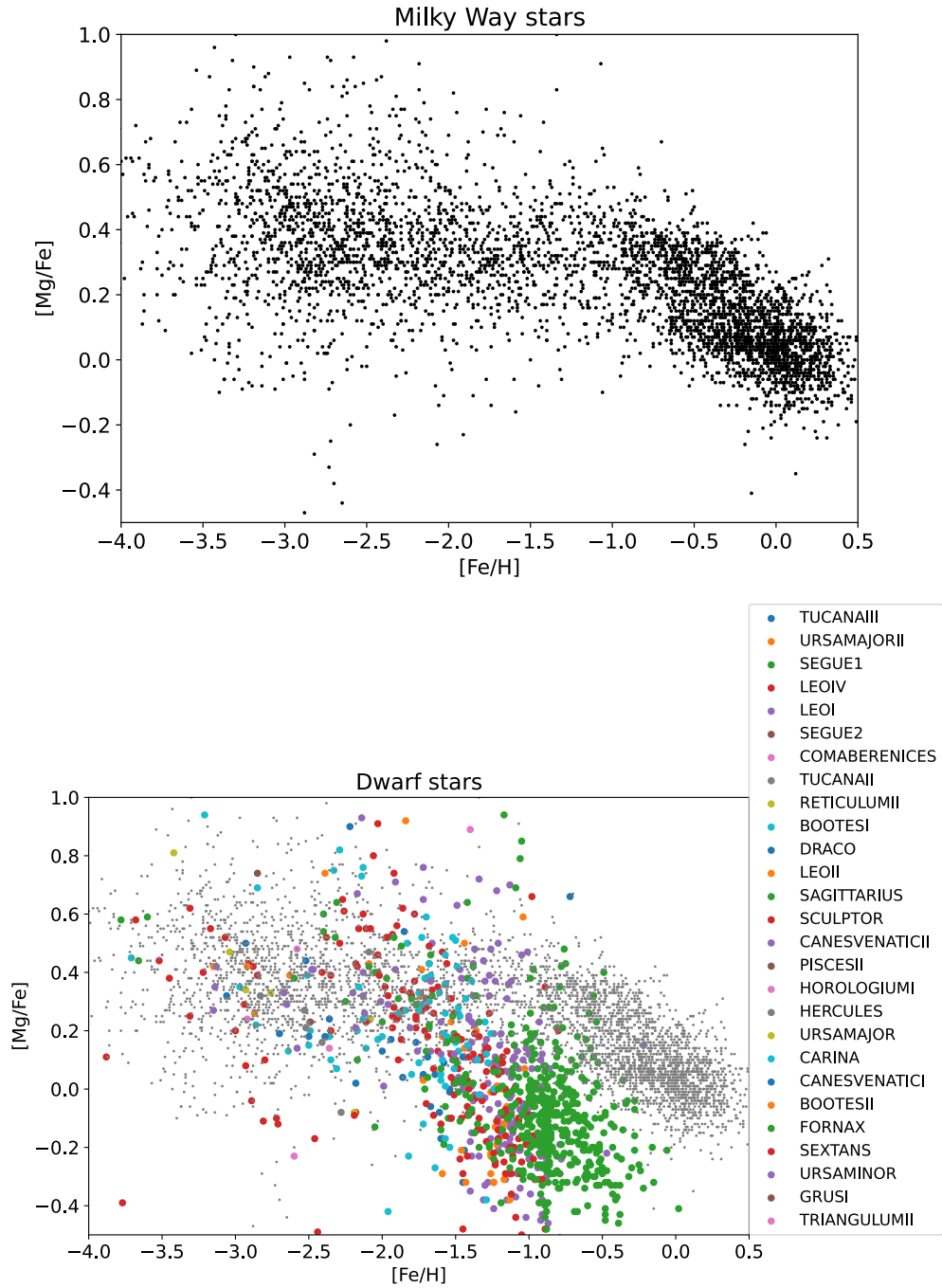


Figure 7:  $[Mg/Fe]$ - $[Fe/H]$  plot for the Milky Way stars (upper panel) and dwarf galaxies (lower panel). Typical error is  $\sim 0.1$  dex. I have ignored data with the  $[Mg/Fe]$  error of more than 0.3 dex. The data is obtained from saga database ([Suda et al. 2017](#)).

consequence of delayed type-Ia contribution. Mg, an  $\alpha$  element, is instantly emitted to the ISM after star formation. On the other hand, half of Fe comes from type-Ia supernova, which significantly delays from the formation of the progenitor star (Maoz et al. 2012). Therefore, old, metal-poor stars ( $[\text{Fe}/\text{H}] \lesssim -1$ ) are enriched predominantly with massive stars, while metal-richer stars get more considerable contribution from type-Ia supernovae.

Their typical delay timescale is  $\sim 1$  Gyr. The decline starts when the timescale of chemical enrichment overcomes that of type-Ia delay. Therefore, the position of the “knee” is a good indicator for the chemical enrichment timescale: Milky-Way has reached  $[\text{Fe}/\text{H}] \sim -1$  after 1 Gyr of star formation. Dwarf galaxies show lower  $[\text{Mg}/\text{Fe}]$  at  $[\text{Fe}/\text{H}] \sim -1$  compared to Milky Way stars. This is a consequence of slow enrichment (Frebel and Bromm 2012): when dwarf galaxies reach  $[\text{Fe}/\text{H}] \sim -1$ , the typical stellar age in the galaxies is far older than 1 Gyr. Therefore, the fraction of type-Ia contribution is larger than the Milky Way, resulting in lower  $[\text{Mg}/\text{Fe}]$ .

## 2.2 Barium

Barium has strong transitions in 3892, 4131, 4166, 3525, and 5854 Å. Ba abundances are available even for very low quantities in most cases. Together with Eu, it is used to estimate the neutron-capture process contribution.

Figure 8 shows the evolution of Ba abundance normalized by Mg. Here, Mg is synthesized in massive stars: the contribution from type-Ia SNe moves points only to the right and not in the vertical direction. Milky-Way stars of  $[\text{Fe}/\text{H}] \gtrsim -1.0$  show an increasing trend: this is a consequence of AGB star contribution. The effect is twofold: (i) since stars with 1.5–3  $M_{\odot}$  contribute to the enrichment most efficiently, we expect delays of  $\sim$  Gyr timescale. (ii) In addition, the  $s$ -process nucleosynthesis requires seed nuclei to synthesize heavy elements. The abundance of seed nuclei is proportional to metallicity  $[\text{Fe}/\text{H}]$ : therefore, an increase of  $[\text{Fe}/\text{H}]$  results in more efficient  $s$ -process production.

Fornax and Sagittarius dwarf galaxies show high  $[\text{Ba}/\text{Mg}]$  compared to stars in the Milky Way. These galaxies have  $[\text{Mg}/\text{Fe}]$  knees at lower metallicities: therefore, timescales relevant for the enrichment are more than 1 Gyr. Considering the long timescale and the increasing trend, it is likely that the origin is the AGB stars. The trend is yet to be explained and would be an interesting starting point for more detailed modeling.

For solar metallicity stars, Ba is an  $s$ -process element. However, the  $r$ -process contribution is known to be more significant in the metal-poor regime. They are often used as the tracer for the  $r$ -process in metal-poor stars. For details, see Section 5.

## 2.3 Europium

Europium (Eu) is primarily synthesized in the  $r$ -process. Eu is most often used as the tracer for  $r$ -process elements as it is  $\sim 94\%$  synthesized in the  $r$ -process (Arlandini et al. 1999), and it has transitions at optical wavelength. Most spectroscopic observations use lines at 4129, 4205 Å (e.g. Ji et al. 2016a), and 6645 Å (e.g. Sneden et al. 1997). These lines are not strong, and it is often impossible to obtain the elemental abundances in low  $[\text{Eu}/\text{H}]$  stars. Therefore, Eu abundance trends seen in the metal-poor regime are not trustworthy.

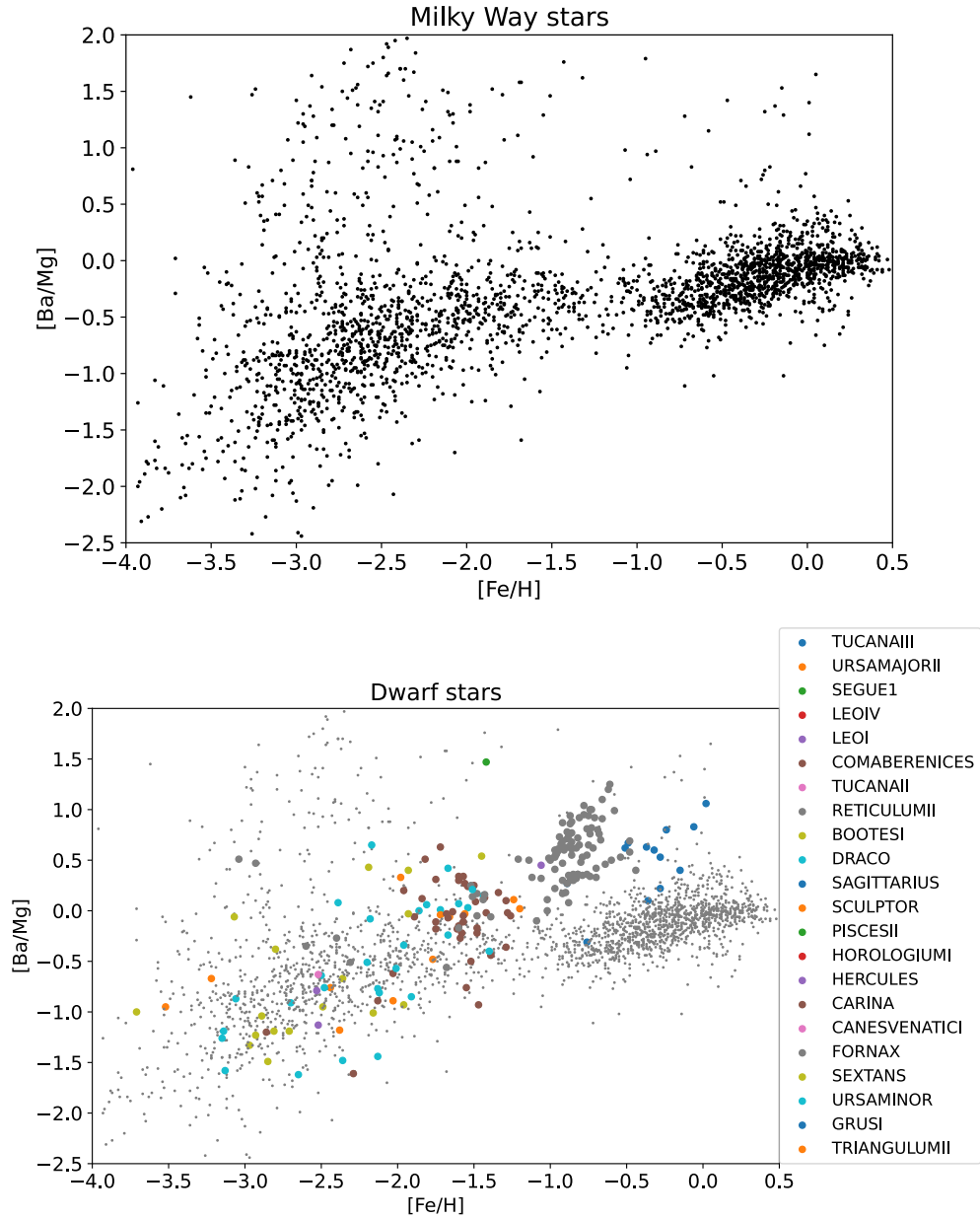


Figure 8:  $[\text{Ba}/\text{Mg}]-[\text{Fe}/\text{H}]$  plot for the Milky Way stars (upper panel) and dwarf galaxies (lower panel). Typical error is  $\sim 0.2$  dex. The data is obtained from saga database (Suda et al. 2017).

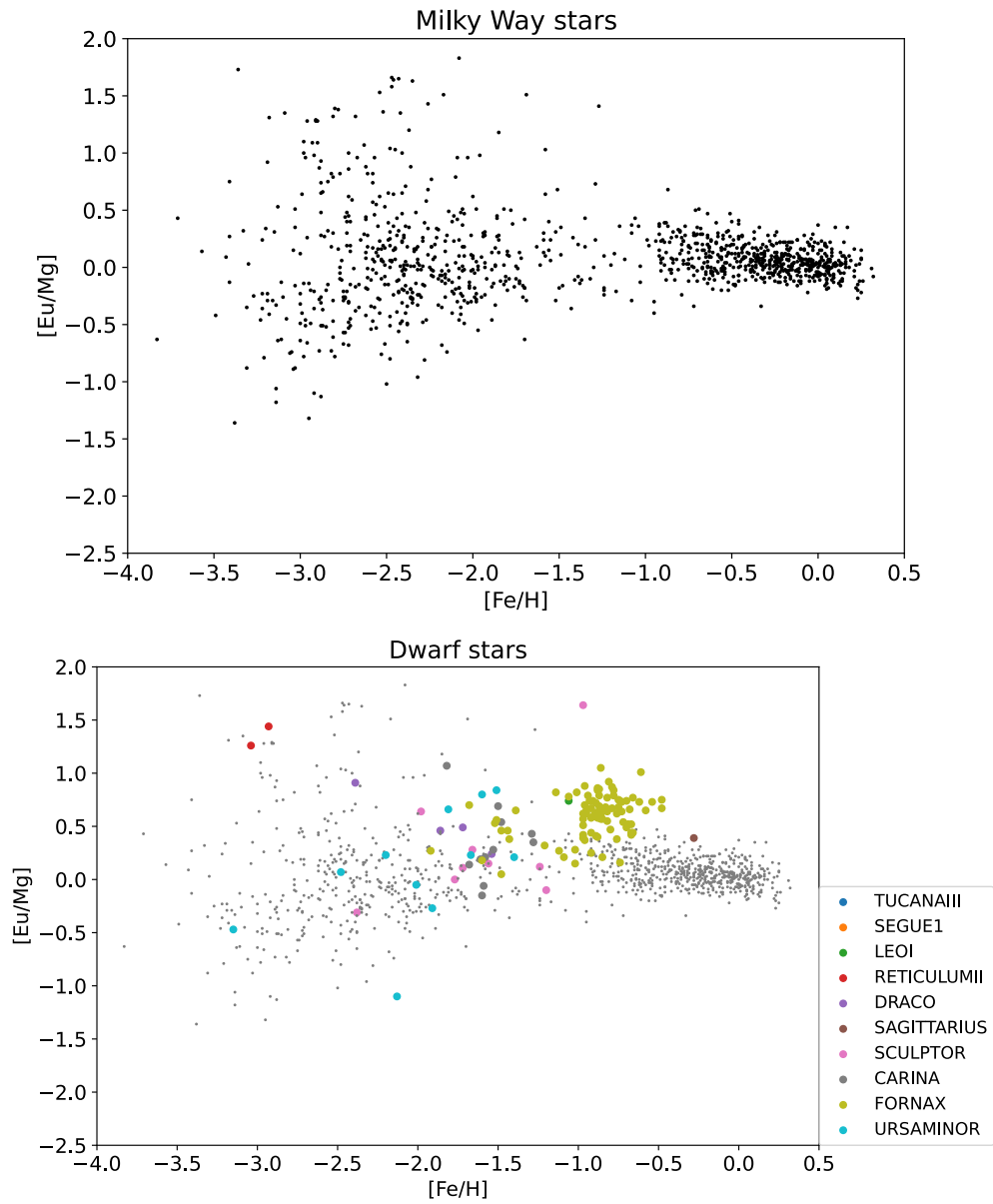


Figure 9:  $[\text{Eu}/\text{Mg}]$ - $[\text{Fe}/\text{H}]$  plot for the Milky Way stars (upper panel) and dwarf galaxies (lower panel). Typical error is  $\sim 0.2$  dex. The data is obtained from saga database ([Suda et al. 2017](#)).

In the metal-rich region, the [Eu/Mg] abundance trend is almost flat. This suggests that the timescale for the  $r$ -process enrichment is short, comparable to massive stars. This evidence is against the neutron star merger model because a long delay is expected from inefficient binary coalescence. Other scenarios, such as the magneto-rotational supernova (Nishimura et al. 2015) and the collapsars (Siegel et al. 2019), are considered as the origin of  $r$ -process elements to overcome this problem. Another direction is to consider complex effects of galactic chemical evolution, such as the natal kick of binary neutron stars (Banerjee et al. 2020a). Also, Schönrich and Weinberg (2019) consider two-phase (hot and cold) interstellar medium. They assume that neutron-star merger enriches cold medium due to low energy, while supernova injects elements into the hot medium. The medium in the hot phase requires an additional delay for cooling before star formation. The abundance trend can be explained if the gas cooling timescale and merger timescale are comparable. However, the question still needs to be solved, and the origin of the  $r$ -process is still under debate.

Argast et al. (2004) argue that delayed sources such as NSM are not favored from Eu abundances of low-metallicity stars. The key argument is the  $r$ -process abundances of metal-poor stars: they claim that the long delay of NSM is incompatible with the relatively high  $r$ -process abundances of metal-poor stars. However, the conclusion depends on star formation history and the minimum delay time. Assuming a lower star formation rate at the earliest evolution would result in a more  $r$ -abundance distribution for metal-poor stars, which is rather consistent with the observations (See Section 5).

## 2.4 Strontium

Sr is a first-peak neutron-capture element. It has many strong lines. Therefore, abundances are available for almost all stars. However, modeling the production of Sr is complicated from the theory side because many astrophysical objects produce this element. In addition to the usual  $r$  and  $s$  processes, the “light-element primary process” are proposed to produce Sr. Since the required neutron-richness is less extreme, the usual supernova is expected to produce Sr. Sr-rich while Eu-poor stars observationally confirm the need for such a process compared to heavier neutron-capture elements (Honda et al. 2004; 2006). An electron-capture supernova is an interesting event relevant for Sr (see, e.g., Wanajo et al. 2011). Electron capture in the core reduces the pressure support catastrophically, resulting in an explosion. Mild neutron richness is expected in the ejecta, which allows the production of Sr in copious amount. For details, see Section 3.

## 2.5 Ultrafaint dwarf galaxies

The existence of satellite galaxies smaller than the classical dwarfs has been expected for a long time. The first detection was in 2005, thanks to the Sloan digital sky survey (SDSS, Willman et al. 2005a;b). After the first discovery, similar small galaxies have been discovered in large numbers. Dark energy survey (DES) and Panoramic Survey Telescope & Rapid Response System (Pan-STARRS), the two surveys conducted after SDSS, have further increased the number of ultrafaint dwarf galaxies (UFDs). Today,  $\sim 50$  UFDs have been identified around the Milky Way.

UFDs represent an old stellar population, which makes them crucial for the chemical study of galaxies. [Brown et al. \(2014\)](#) examined the star formation history of six (Hercules, Leo IV, UMa I, Boo I, CVn II, and ComBer) UFDs using deep Hubble imaging. They have concluded that the five UFDs except for UMa I form more than 75% of stars by  $z \simeq 10$ . For UMa I, approximately half of its stars form by  $z \simeq 3$ . This observation is consistent with the theoretical idea that the heating by cosmic reionization has quenched the star formation ([Bullock et al. 2000](#)): the gravitational potential is too shallow for retaining gas after the heating. The quenching by cosmic reionization was further supported by cosmological simulations ([Jeon et al. 2017](#); [Wheeler et al. 2019](#); [Agertz et al. 2020](#)).

[Ji et al. \(2016b\)](#) have found that Reticulum II, a UFD discovered by DES, is highly enriched with  $r$ -process elements. The abundance ratio  $[r/Fe]$  is as high as 2.0, which indicates that the chemical history is very different from most stars in the Milky Way. The estimated mass of  $r$ -process elements is  $\sim 0.01 M_{\odot}$ . The most natural interpretation is that a rare and prolific  $r$ -process event has enriched the system at once. The  $r$ -process mass is consistent with the neutron star merger ejecta. The scenario is further supported by later galaxy formation simulations ([Safarzadeh and Scannapieco 2017a](#); [Tarumi et al. 2020b](#)).

From the example above, we see that the other reason UFDs are essential is the discretization of rare events. Since the stellar mass is small ( $\lesssim 10^5 M_{\odot}$ ), the expected number of events with the occurrence rate of  $10^{-5} M_{\odot}^{-1}$  is less than one. In that case, some UFDs experience one or more events, while others do not host such events. Therefore, we can see the difference between enriched and unenriched populations.

## 2.6 Galaxies outside Local group

We cannot spatially resolve each star for galaxies outside the Local Group. Instead, integrated light from stellar components or emission lines from the interstellar medium is observed. For these cases, information on the neutron-capture elements is not available. However, helpful information is the Nitrogen abundances (see, e.g., [Spite et al. 2005](#); [Chiappini et al. 2006](#)). Nebular emission of Nitrogen is observed from galaxies. At solar metallicity, Nitrogen is predominantly produced in CNO cycles in stars (converted from Carbon and Oxygen). However, Nitrogen abundances of low-metallicity galaxies suggest that a “primary” production mechanism is needed. The only means for the primary Nitrogen production discussed is rotating massive stars.

## 2.7 Globular clusters

Globular clusters (GCs) have old stellar populations. Their color and luminosity are well-fitted by an isochrone on a color-magnitude diagram, indicating that all stars are formed in a short ( $\lesssim 1$  Gyr) period of time. However, a detailed investigation shows a small spread on the isochrone. Two interpretations are (i) age spread ( $\sim 500$  Myr) and (ii) Helium abundance spread ([Bastian and Lardo 2018](#)). In either case, the “older” or “He-rich” population is referred to as second-generation (SG) stars, whereas those with typical elemental abundances are called the first-generation (FG) stars.

Interestingly, GCs show an anomaly in the light metal abundances. The SG stars are enriched with the ashes of Hydrogen burning: i.e., CNO cycle, NeNa-chain, MgAl-chain,

while its Fe abundance is the same as that of FG stars. To meet these criteria simultaneously is a difficult task, and no existing models can explain the formation mechanism of this trend (see [Bastian and Lardo 2018](#) for details). For the study of GCs, see Section 6.

## 2.8 Aim of this research

This research aims to clarify the origin of neutron-capture elements and use these elements to probe the formation histories of galaxies. Previous works study MW and classical dwarf galaxies. Recent spectroscopic observations of UFDs enhance data. UFDs are particularly important because of their short star formation histories and small stellar masses. The existence of highly  $r$ -process enriched UFDs and the non-detection of Eu in others is fully consistent with the theoretical expectation that the  $r$ -process elements are synthesized in rare and prolific events. Along with this interpretation, we can cleanly study the production of the  $s$ -process elements with Ba (see Section 3). Furthermore, their stellar distribution profile is new information that allows us to probe the formation history (see Section 4).

On the other hand, metal-poor stars in the Milky Way tell us more about shorter timescales (see Section 5). While chemical evolution for the MW is well studied in general, the  $r$ -process in the metal-poor regime is an exception. The reason is the weakness of Eu absorption lines. As we have seen in Section 2.3, the Eu abundance at the metal-poor regime is not reliable. Here, Ba can be used as a tracer for the  $r$ -process abundances. Another caveat is the existence of post-mass transfer systems. We can eliminate their contributions by imposing a Carbon abundance limit.

Neutron-capture elements are useful tracers for the formation processes of galaxies and other stellar systems. In Section 6, I study the  $r$ -process enrichment of a GC, M15. The  $r$ -process abundance spread has been known for ten years. Previous works explain the abundance spread by invoking an  $r$ -process event between FG and SG star formation. However, the scenario would be inconsistent with the independence of the abundances of Na and Eu. Therefore, there has yet to be a satisfactory scenario that explains the abundance spread. Section 6 is the first work that simulates metal mixing around the natal cloud of a GC and explains the abundance spread as an inhomogeneity in the natal cloud. It suggests that the number of star formation epochs is one. This work serves as an example of using  $r$ -process elements to constrain the formation channel of a GC.

While metal mixing studies are crucial to interpret spectroscopic observations of stars appropriately, direct observations of nucleosynthesis sites are also critical. Kilonova AT2017gfo is the unique observation of NSM. An absorption feature at  $\sim 8000 \text{ \AA}$  is observed and interpreted as a Sr feature. However, the feature might originate from He with a non-local thermal equilibrium effect. Section 7 studies the level populations in kilonova ejecta, and argue that spectral feature can be explained by He. He is a good indicator of ejecta entropy, which would be useful for probing the mass ejection mechanism of NSM.

Figure 10 illustrates where each Section is placed in a broader context. Sections 3–6 discuss the enrichment process of the interstellar medium during the stellar lifecycles. The last Section is devoted to the study that directly probes the environment of nucleosynthesis.

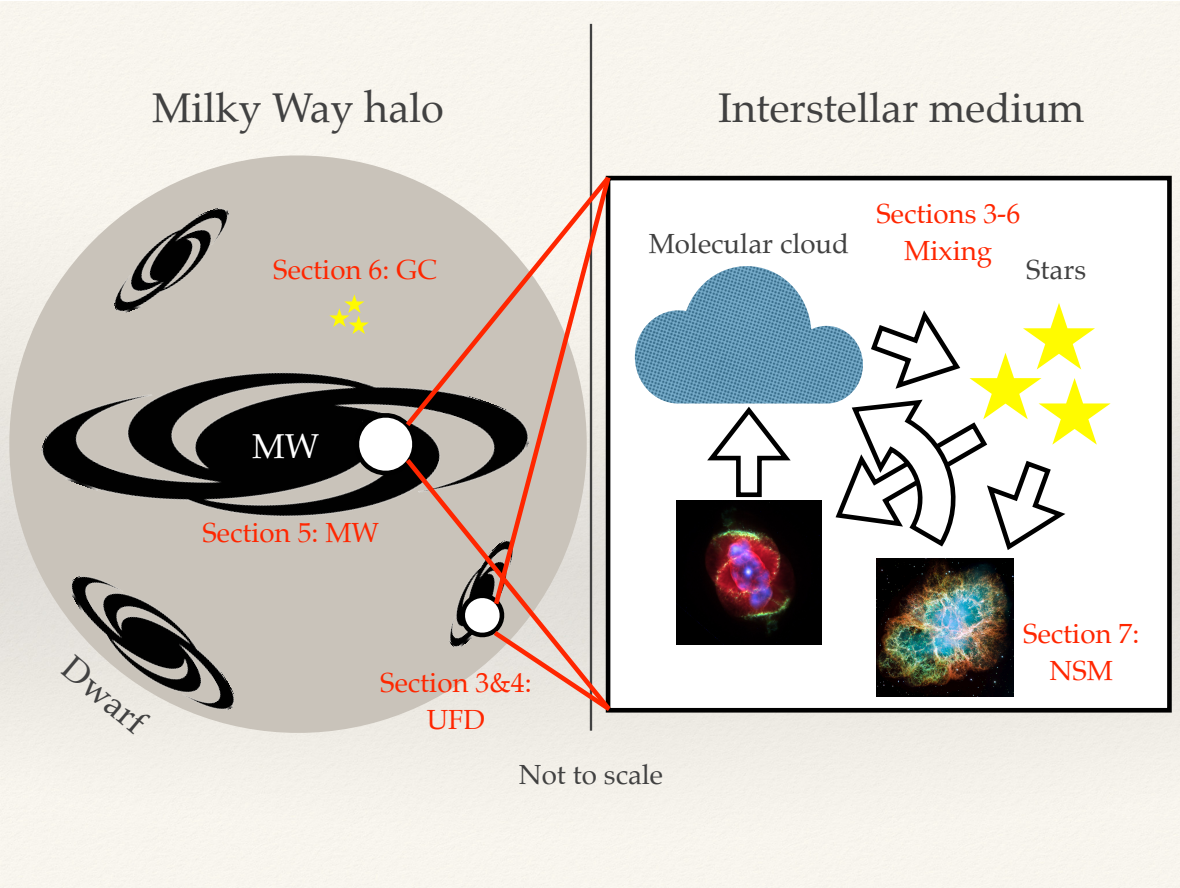


Figure 10: A schematic figure showing the general overview of the works in this thesis.

### 3 *S*-process elements in ultrafaint dwarf galaxies

As we have seen in the first two sections, the heaviest elements in the Universe are synthesized in two neutron capture processes, *r* and *s*. It is generally accepted that the *s*-process occurs mainly in the AGB stage of low-mass stars. However, the existence of additional sources has not been eliminated. UFDs are useful probe for the *s*-process nucleosynthesis because of the small stellar mass: contribution from rare and prolific *r*-process events can be eliminated. Similar works with larger systems such as classical dwarfs and the MW exist in the literature, but they are suffered from the difficulty in *r*-process contamination. Here, using Eu-poor UFDs, we investigate *s*-process nucleosynthesis at metal-poor ( $[\text{Fe}/\text{H}] < -2$ ) environment for the first time.

#### 3.1 Neutron-capture elements in ultrafaint dwarf galaxies

The main interest in *s*-process nucleosynthesis is the neutron-producing site in the AGB star. It is thought that protons in the convective envelope are mixed into the upper layer of the helium core, triggering the  $^{13}\text{C}(\alpha, n)^{16}\text{O}$  reaction. This layer is called ‘ $^{13}\text{C}$  pockets’ (see, e.g. [Busso et al. 1999](#)). The efficiency of the *s*-process with the  $^{13}\text{C}$ -pocket depends on the free parameters but is chosen to reproduce the solar values using the Galactic Chemical Evolution (GCE) model ([Travaglio et al. 2004b](#); [Käppeler et al. 2011](#)). Another place where neutrons are produced is in the convective shell, driven by the flash of a helium shell, where they are produced via  $^{22}\text{Ne}(\alpha, n)^{25}\text{Mg}$  in the intermediate-mass AGB star ([Iben 1975](#)). Possibilities of other sources for the *s*-process elements have also been explored in the metal-poor stars of the galactic halo. [Suda et al. \(2004\)](#) discuss that neutrons are produced in the helium flash convection zone when the convective shell reaches the bottom of the hydrogen-burning shell for low-mass AGB stars with very low metallicity. This mechanism could explain the *s*-process elements in some of carbon-enhanced metal-poor stars. Fast-rotating massive stars have also been investigated to explain the *s*-process abundances in such stars ([Choplin et al. 2017](#)).

Theoretical models for *s*-process nucleosynthesis can be tested with observations of barium (Ba) and strontium (Sr) in stars with low metal content. However, because the main contributors to the *s*-process are low-mass, long-lived stars, they contribute to the chemical evolution of the galaxy with significant delay. This delay is observed in disk stars of Milky Way (MW), where the abundance of Ba ( $[\text{Ba}/\text{Fe}]$ ) increases monotonically as the abundance of iron ( $[\text{Fe}/\text{H}]$ ). For low metallicity environment such as UFDs, it is unclear whether Ba is produced entirely by the AGB stars. Indeed, theoretical studies have shown that both Ba and Sr can also be produced by *r*-process in MW and dwarf galaxies ([Cescutti et al. 2006](#); [Hirai et al. 2019](#)).

[Ishimaru et al. \(2015\)](#) modeled the contribution of neutron star mergers (NSM) to the *r*-process enrichment of dwarf galaxies and concluded that the NSM could explain the low-metallicity behavior. [Hirai et al. \(2015\)](#) simulated the formation and *r*-process enrichment of dwarf spherical (dSph) galaxies and concluded that the NSM could explain the *r*-process abundance of dSph galaxies. In concordance cosmology, large galaxies like MW gain mass mainly by merging. Using simulations, [Brauer et al. \(2019\)](#) find that about half of *r*-II ( $[\text{Eu}/\text{Fe}] > 1.0$ ) stars could be explained by stars formed in UFDs that are now disrupted.

Understanding the chemical enrichment of these small systems therefore provides important insights into the history of galactic chemical enrichment.

UFDs show several distinct chemical abundances (Simon 2019). The old stellar population allows us to probe chemical enrichment of short ( $\sim 100$  Myr) timescales. Also, the small stellar mass discretizes the contribution of rare events. For example, europium (Eu), a typical  $r$ -process element, is detected in only three galaxies out of about 20 UFDs with the attempts of Eu measurement. A natural interpretation on the Eu abundances among UFDs is that the source of  $r$ -process elements are rare and prolific events (Ji et al. 2016a; Hansen et al. 2020). Since a UFD is usually less chemically evolved, it provides important insights into early chemical enrichment in the universe. Recently, observers obtain detailed chemical abundances of metal-poor stars in UFDs (e.g. Frebel et al. 2014; Ishigaki et al. 2014; Chiti et al. 2018; Ji et al. 2019b). These observations consistently suggest that in the absence of a clear  $r$ -process signature, there is a dearth of neutron-capture elements (including Ba and Sr) in UFD compared to the MW.

Here, we model the  $s$ -process enrichment of UFDs. We model their formation and evolution using cosmological simulations, which is outlined in Section 3.2.1. The characteristic star-formation history and the small stellar mass of the UFD provide clues to understanding the history of neutron-capture elements. The simulation results are presented in Section 3.3. We argue in Section 3.4 that additional source of  $s$ -process elements is favored to explain the abundance of Ba observed in UFD stars.

## 3.2 Method

### 3.2.1 Cosmological Simulations

We use AREPO, a moving-mesh hydrodynamic cosmological simulation code (Springel 2010; Pakmor et al. 2016; Weinberger et al. 2019). The cosmological parameters are taken from Planck 2018 results (Planck Collaboration et al. 2020):  $H_0 = 67.4 \text{ km s}^{-1} \text{ Mpc}^{-1}$ ,  $\Omega_m = 0.315$ ,  $\Omega_b = 0.049$ ,  $\sigma_8 = 0.810$ ,  $n_s = 0.965$ . Initial conditions for the simulations are generated by MUSIC (Hahn and Abel 2011). The size of the simulation box is 1 comoving  $h^{-1} \text{ Mpc}$  on each side. The zoom-in technique is utilized: it resolves small scales of the simulated galaxies. In the zoom-in region, each dark matter particle has  $100 M_\odot$  and the target mass for each gas cell is  $20 M_\odot$ .

We use the same galaxy samples as in my previous paper (Tarumi et al. 2020b). The three halos are referred to as ‘L-UFD’, ‘M-UFD’, and ‘S-UFD’ in this work. The smallest sample galaxy (S-UFD) has the stellar mass of  $\sim 100 M_\odot$ , which is insufficient to see the abundance distribution. Therefore, the results for L-UFD and M-UFD are mainly discussed. Figure 11 presents the star formation histories of our model galaxies. Their halo and stellar masses ( $M_h, M_*$ ), and the radius ( $R_{200}$ ) at redshift  $z = 8$  are  $(M_h, M_*, R_{200}) = (1.7 \times 10^8 M_\odot, 12,000 M_\odot, 1.7 \text{ kpc})$ , and  $(1.0 \times 10^8 M_\odot, 4,100 M_\odot, 1.6 \text{ kpc})$ . These mass ranges are appropriate as UFD progenitors (Safarzadeh et al. 2018). In our final snapshot ( $z = 6.4$ ), these galaxies grow to  $(M_h, M_*, R_{200}) = (2.1 \times 10^8 M_\odot, 12,900 M_\odot, 2.5 \text{ kpc})$ , and  $(2.0 \times 10^8 M_\odot, 3,800 M_\odot, 2.2 \text{ kpc})$ .

We use the ISM model that is different from the standard AREPO simulations (Springel and Hernquist 2003). The model computes heating and cooling self-consistently, and apply

that to obtain the gas temperatures (Inoue and Yoshida 2019). The gas density field is represented with cells separated by Voronoi mesh. Each gas cell contains physical quantities such as density, temperature, and chemical abundances. Galaxy formation simulations are susceptible to numerical fragmentation when it is close to the resolution limit (Truelove et al. 1997). For convergence of the results, Jeans length needs to be resolved at least with seven cells (Ceverino et al. 2010). The smallest scale for the pressure support is set at 0.2 comoving pc  $h^{-1}$ . The star-formation rate (SFR) of each gas cell is computed as

$$(SFR) = 0.079m_g/t_{SF}, \quad (29)$$

where  $m_g$  is the mass of the gas cell and  $t_{SF} = (G\rho_g)^{-1/2}$  is a timescale for star formation. To avoid star formation in shocked gas, a temperature condition  $T < 10000$  K is set for star formation.

Feedback from SNe is modeled by “wind particles”. The wind models gas outflow driven by explosions of massive stars. Gas cells that satisfy the star formation conditions form stars stochastically. When a star particle is formed, wind particle is also formed and ejected from the star forming region. The ratio of numbers between star particles and wind particles are determined by the energy deposition by SNe. Massive ( $8 - 100 M_\odot$ ) stars are assumed to explode instantaneously. The energy of  $1.7 \times 10^{51}$  erg is assumed for the computation of wind particles. The wind particles carry 40% of metal contents of the parent gas particle (Vogelsberger et al. 2013). The newly formed wind particles are ejected to random directions, with the initial velocity of  $3.46\sigma_{DM}$ . The  $\sigma_{DM}$  represents the one-dimensional velocity dispersion of the surrounding dark-matter particles (Springel and Hernquist 2003). The trajectory of an ejected wind particles is computed purely gravitationally. A wind particle disappears if it reaches a low-density region (gas cell) of  $\rho_g < 0.05\rho_{th}$ , or the time reaches the maximum lifetime. When a wind particle disappears, it deposits its mass, metals, momentum, and energy into the gas cell. Energy injection from type-Ia SNe and the winds of AGB stars are not considered.

### 3.2.2 Chemical evolution

Each star particle in a galaxy formation simulation represents a star cluster. The Chabrier initial-mass function (IMF) (Chabrier 2001) is assumed. A star particle enriches the surrounding ISM with metals. The amount of elements distributed to nearby cells is computed as follows. First, the mass range of stars that ends its lifetime within the next timestep is computed considering the age and metallicity of the star particle. Then, the mass of ejected metal in the timestep is computed by integrating the elemental yield over the mass range. The yield and lifetime of stars is taken from Portinari et al. (1998). Finally, the elements are distributed to nearby gas cells. The share of elements received by a gas cell is computed following the smoothed-particle-hydrodynamics (SPH) kernel function. The kernel size is determined during simulation so that effectively  $64 \pm 1$  cells are involved in the metal enrichment. This process is performed for each star particle at each timestep. Type-Ia SNe delays from the formation of the parent stars. The delay time distribution is assumed to be power-law with the index of  $-1.12$ , and 0.0013 type-Ia SNe occur from 40 Myr to 10 Gyr after the formation of  $1 M_\odot$  of star particles. The yield is obtained from Travaglio et al. (2004a).

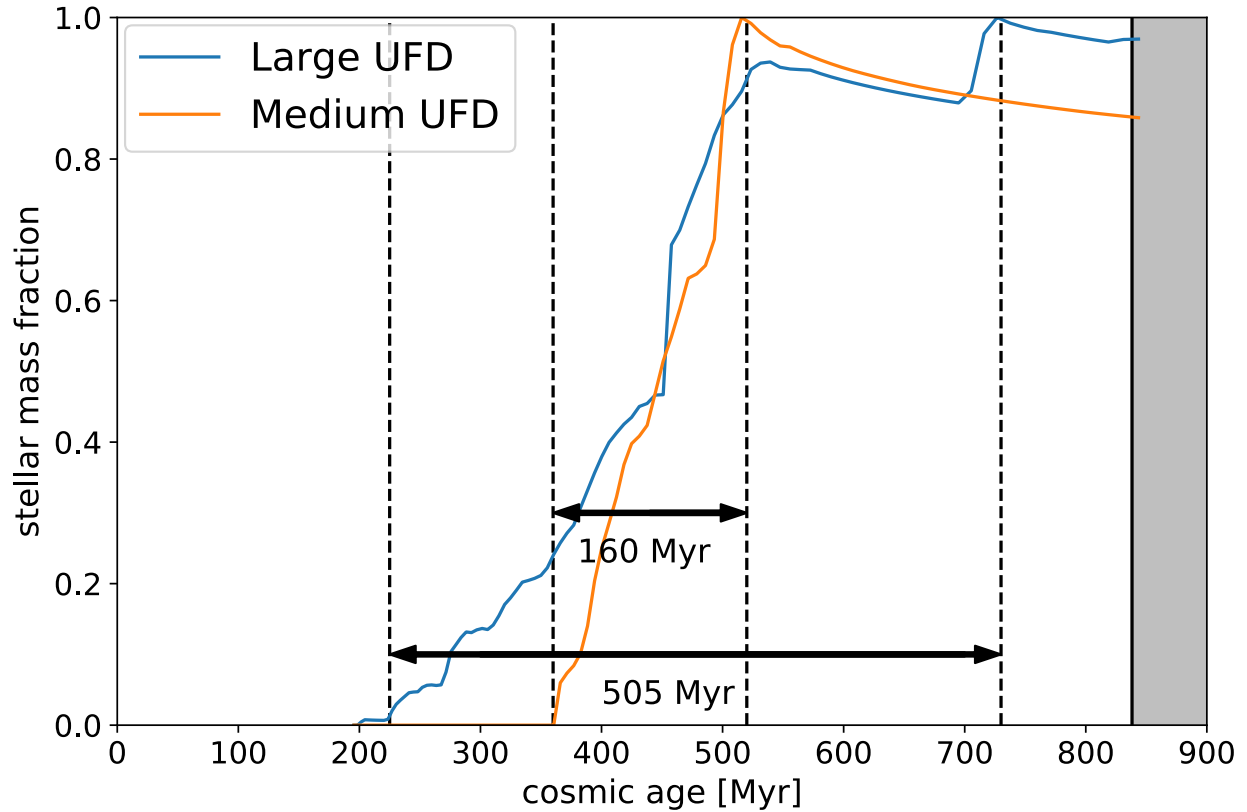


Figure 11: History of star formation for our simulated galaxies. L-UFD is represented by the blue curve, which forms stars for  $\sim 500$  Myr. The stellar mass peaks at  $\sim 12,000 M_{\odot}$  at the cosmic age of  $\sim 700$  Myr. Orange curve is for M-UFD, which forms stars only for  $\sim 160$  Myr. The peak stellar mass is  $\sim 4000 M_{\odot}$ . The L-UFD merges with another galaxy at a cosmic age of  $\sim 500$  Myr at redshift 10. Cosmic reionization is represented by the gray shaded region, and no or little star formation is expected thereafter.

The median of the metallicity  $[\text{Fe}/\text{H}]$  for L- and M- UFDs are  $-2.66$  and  $-2.96$ . The values are consistent with observed UFDs (e.g.  $-2.71$  for Segue 1: see [Simon 2019](#) for other UFDs).

In our high-resolution simulation, the masses of star particles are too small to apply the single stellar population approximation. Since we are interested in the  $s$ -process abundances, we sample the number of AGB stars stochastically. The  $s$ -process yield table is taken from FRUITY database ([Cristallo et al. 2015; 2016](#)). The mass-grid of the table is 1.3, 1.5, 2.0, 2.5, 3.0, 4.0, 5.0, and 6.0  $M_{\odot}$ . In the simulation, we take mass bins at 1.4, 1.75, 2.25, 2.75, 3.5, 4.5, 5.5, and 6.5  $M_{\odot}$ . Then, we compute the expected number of stars that fall within each bin assuming the Chabrier IMF ([Chabrier 2001](#)). The energy input is discretized similarly: the number of SNe from each star particle for each timestep is randomly sampled and constrained to be an integer value.

Note that Sr is produced only in AGB stars in our fiducial model. In reality, Sr could be produced via various channels such as electron-capture supernovae (ECSNe, see, e.g., [Wanajo et al. 2011; 2018](#)). Their contribution is uncertain because of the mass range of progenitor star for ECSNe is not constrained. Therefore, we treat this channel as an additional source, and discuss their contribution individually. The treatment will be described in the next subsection.

### 3.2.3 Rotating massive stars and electron-capture supernovae

Rotating massive stars (RMSs) and ECSNe are considered as additional channels for  $s$ -process production. These sources are included as additional channels, and the effects are discussed individually. These models are called ‘‘RMS model’’ and ‘‘ECSN model’’ hereafter. [Limongi and Chieffi \(2018\)](#) argue that rotationally induced mixing allows chemical diffusion between H shell-burning layer, inert radiative He layer, and the central convective He-burning layer during He core burning. It enhances the production of neutron via  $^{22}\text{Ne}(\alpha, n)^{25}\text{Mg}$  reaction. The rare isotope  $^{22}\text{Ne}$  is produced via the following processes. First,  $^{12}\text{C}$  synthesized in core He burning diffuses to shell H burning layer. The H burning is mediated by the CNO cycle. Therefore,  $^{12}\text{C}$  is converted to  $^{14}\text{N}$ . The produced  $^{14}\text{N}$  goes back to the core, and it captures  $\alpha$  particles to form  $^{18}\text{F}$ .  $^{18}\text{F}$  decays to  $^{18}\text{O}$  and it captures  $\alpha$  again to form  $^{22}\text{Ne}$ . This isotope captures  $\alpha$  again, producing neutrons. Slow rotators produce lighter neutron-capture elements such as Sr, whereas fast rotating stars produce heavier  $s$ -process elements such as Ba. We adopt yield from [Limongi and Chieffi \(2018\)](#). The distribution of the rotation velocities is taken from [Prantzos et al. \(2018\)](#).

Stars with the mass at the lowest end of Fe-core collapse SNe explode as ECSNe ([Nomoto 1987; Janka et al. 2008; Wanajo et al. 2018](#)). Weak  $r$ -process is expected in the ejecta at the center, which produce a large amount of Sr. Although the SN 2018zd and the origin of Crab pulsars are proposed as being ECSNe ([Hiramatsu et al. 2020](#)), no SNe are confirmed to be ECSNe. Therefore, we cannot infer the rate of ECSNe observationally. The precise theoretical prediction of ECSNe mass range is difficult, and  $0 - 1 M_{\odot}$  is typically assumed. The yield is assumed to be  $7.9 \times 10^{-5} M_{\odot}$  following the e8.8 model of [Wanajo et al. \(2018\)](#). [Hirai et al. \(2019\)](#) constrained the mass range to be  $8.2 - 8.4 M_{\odot}$  by modeling the Sr enrichment of classical dwarf galaxies. In this work, we assume that an ECSN occur every 5000  $M_{\odot}$  of stars formed. This is 2% of core-collapse supernovae (CCSNe) rate, which is equivalent to

the mass range of  $8.0 - 8.1 M_{\odot}$ .

### 3.3 Results

#### 3.3.1 Fiducial model

Figure 12 shows the abundances of *s*-process elements  $[\text{Ba}/\text{Fe}]$  and  $[\text{Sr}/\text{Fe}]$  as a function of metallicity  $[\text{Fe}/\text{H}]$  for stars in the MW halo and UFDs. We do not present the results from S-UFD because the number of datapoints is not sufficient to make a meaningful comparison. All the results are taken at redshift 6.4.

The simulated Ba abundances are not sufficient. To discuss quantitatively, we define “Ba-poor” stars here as those with upper limits on  $[\text{Ba}/\text{Fe}]$ , or the abundance  $[\text{Ba}/\text{Fe}]$  is less than  $-1.5$ . In observations, the Ba-poor fraction is 45%. On the other hand, the fractions are 96, 97, and 100% for L-, M-, and S-UFDs. It is also clear from the median lines of each model. The color of each point represents the formation epoch of the star particle in our simulations.

UFDs enriched with the *r*-process behave qualitatively different. The *r*-rich group is Reticulum II (Ret II), Tucana III (Tuc III), and Grus II (Gru II)<sup>1</sup>. Stars in these UFDs (plotted in green) have higher abundances of Ba and Sr than stars in other UFDs (plotted in red). Since *r*-process synthesize Ba and Sr, it is reasonable that their abundances are systematically higher than those without *r*-process contribution. Dashed lines show the median trend along the  $[\text{Fe}/\text{H}]$  of simulated UFDs that have previously experienced a single *r*-process event. Ba and Sr abundances are very high due to the *r*-process contribution, and we cannot infer the information on the *s*-process enrichment.

For Eu-undetected UFDs, the *s*-process abundances show large variations even among simulated UFDs. Note that these are not contaminated by the *r*-process. L-UFD show higher Ba and Sr abundances than M-UFD and S-UFD, even when comparing stars with similar Fe abundances. The differences reflect the history of star formation. L-UFD forms stars for 500 Myr, while M-UFD and S-UFD stop star formation within 150 Myr. Longer star formation duration allows contribution of events with longer delays: the AGB stars. Therefore, the abundance of *s*-process elements is higher in L-UFD.

The spread in Ba and Sr abundances within each galaxy could be an interesting piece of information. Observations of Bootes I (Boo I), Carina II (Car II), and Coma Berenices (ComBer) show significant scatters, whereas other UFDs show almost homogeneous abundances. Note that the number of datapoints is limited: it is still too early to conclude whether a UFD have significant abundance spread. Our simulations (L-UFD and M-UFDs) show large scatters. S-UFD contain too small number of stars and we cannot discuss the scatter.

Spreads in the formation times and spatial positions both play a role for shaping the abundance trends in a UFD. The colors of points in Figure 12 show that the abundance spread in L-UFD originates from time difference, whereas that in M-UFD is from spatial inhomogeneity. This difference represent the duration of star formation for these galaxies. M-

---

<sup>1</sup>Segue 1 contains one star with enhanced Eu and Ba abundances. It is a CH star, and the high neutron-capture element abundance originate from previous mass transfer from the former AGB star in a binary system. Therefore, it does not reflect the ISM abundances at its formation.

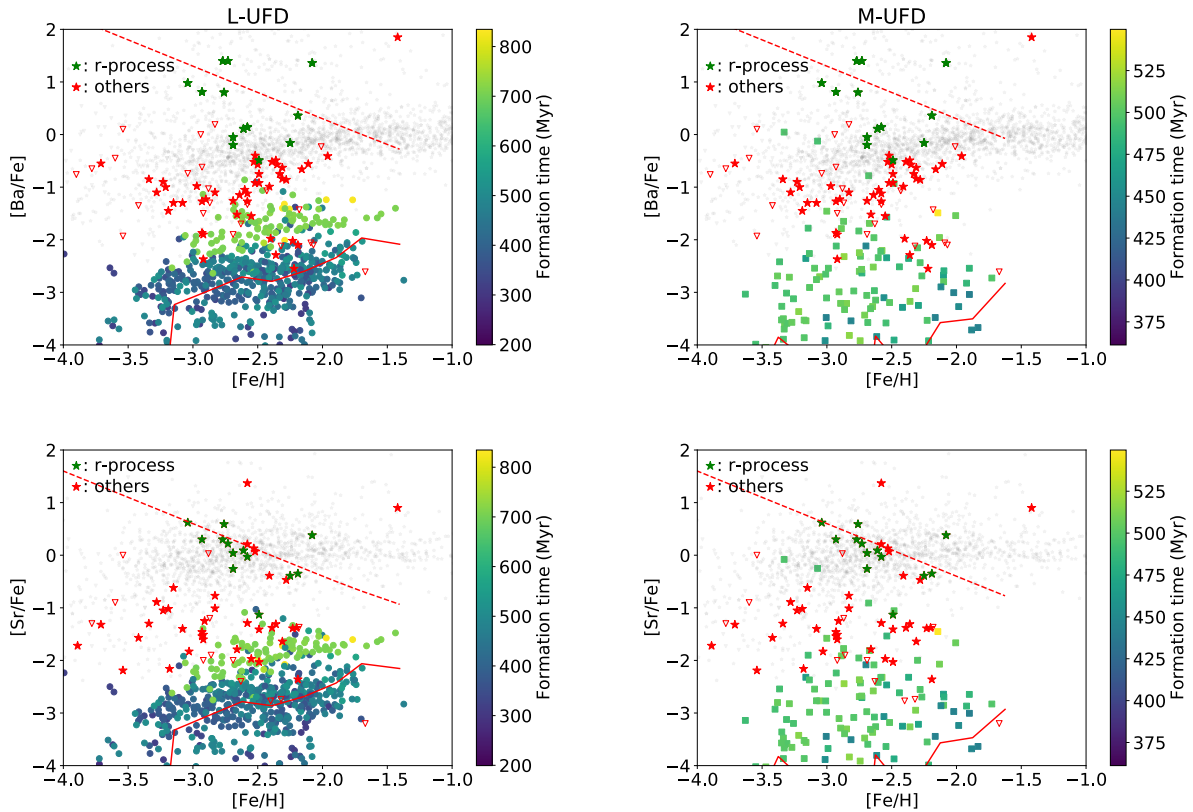


Figure 12: Ba and Sr abundances as a function of metallicity ( $[\text{Fe}/\text{H}]$ ) for stars in our model UFDs at  $z = 6.4$ , compared with the observational data in literatures (stars and triangles). The median of  $[\text{Ba}/\text{Fe}]$  and  $[\text{Sr}/\text{Fe}]$  in each  $[\text{Fe}/\text{H}]$  bin for model UFDs is shown with the red solid lines. The red dashed lines include a “boost” assuming that an  $r$ -process event has enriched the system to  $[\text{Ba}/\text{H}] = -1.7$  ( $[\text{Sr}/\text{H}] = -2.5$ ). The  $[\text{Fe}/\text{H}]$  bin size is 0.25 dex. Panels on the left is for L-UFD and the right is for M-UFD, respectively. The data points of L- and M-UFDs are indicated with filled circles and squares, respectively. Observational data are obtained from the SAGA database (Suda et al. 2008; 2017), together with some latest data added manually. The green symbols represent the stars that show the characteristic abundance patterns for the  $r$ -process (seven stars from Retiuculum II, five stars from Tucana III, and one star from Grus II). Red star symbols are those without Eu detections. The list of plotted UFDs are: Bootes I, Bootes II, Canes Venatici II, Carina II, Carina III, Coma Berenices, Grus I, Hercules, Horologium I, LeoIV, Pisces II, Reticulum II, Segue 1, Segue 2, Triangulum II, Tucana II, Tucana III, Ursa Major, Ursa Major II, and Willman I. Open red triangles show stars with only upper limits available.

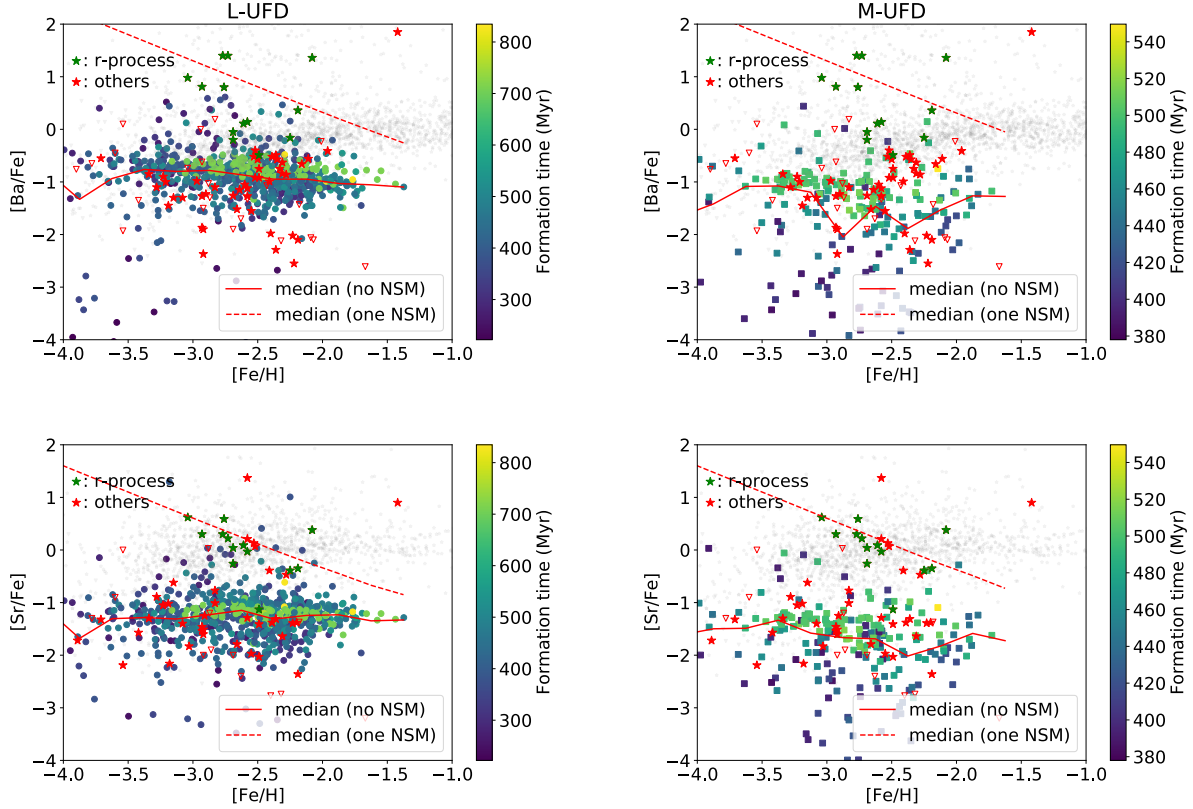


Figure 13: Models with additional contribution to Ba production from RMSs. The yield is obtained by [Limongi and Chieffi \(2018\)](#). Following the rotation velocity distribution by [Prantzos et al. \(2018\)](#), we assume that 23 and 2 % of stars are rotating at  $300 \text{ km s}^{-1}$  at metallicity  $Z = -3$  and  $-2 Z_{\odot}$ , and 72 and 48 % of stars are rotating at  $150 \text{ km/s}$  at metallicity  $Z = -3$  and  $-2 Z_{\odot}$ , respectively. The  $[\text{Ba}/\text{Fe}]$  and  $[\text{Sr}/\text{Fe}]$  values of the observations are reproduced well. On the other hand, some UFDs (e.g. Segue 1) show very low Ba abundances, suggesting that the source of Ba should be relatively rare stars.

UFD forms stars only for 150 Myr. The duration is too short to mix the ISM and homogenize the abundance ([Tarumi et al. 2020b](#)). L-UFD, on the other hand, form stars for  $\sim 500$  Myr. The timescale is sufficient to mix the ISM. However, now the timewise scatter becomes important: 500 Myr is sufficient to change the ISM abundances significantly.

### 3.3.2 Rotating massive star model

Figure 13 presents the  $s$ -process abundances of simulated stars including RMS contribution. The observed distribution of  $s$ -process element abundances are reproduced well. The difference from the fiducial model is the flat  $[\text{Ba}/\text{Fe}]$  trend against  $[\text{Fe}/\text{H}]$ . In our fiducial model, where the origin of Ba is AGB stars,  $[\text{Ba}/\text{Fe}]$  increases as a consequence of time delay and the metallicity dependence of Ba yield. However, in RMS model, Ba is dominantly produced by rapid rotators ( $300 \text{ km s}^{-1}$ ). The fraction of rapid rotators depends very strongly on metallicity. Although the yield of Ba from RMS increases with metallicity, the fraction of

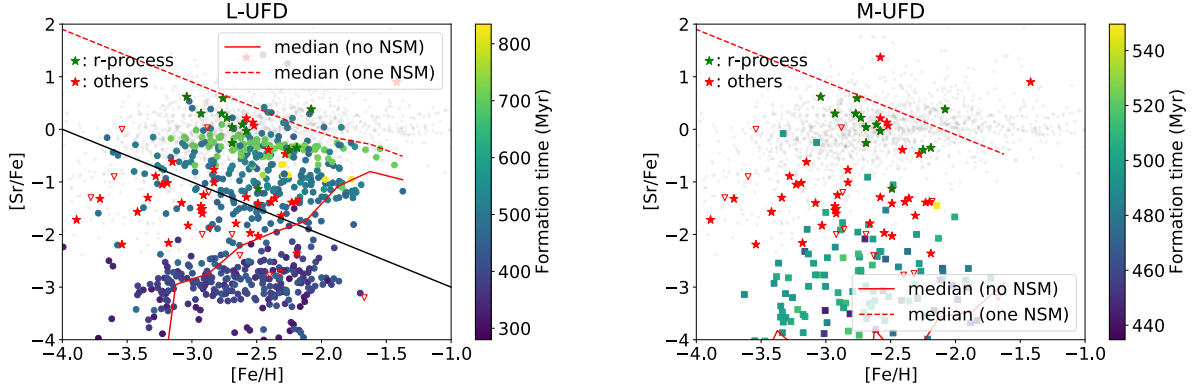


Figure 14: Results of ECSN model. We only show Sr abundances because ECSNe only affect Sr production. The Sr production is quite efficient and the Sr abundances are clearly separated between stars that are enriched or not.

fast-rotating stars decreases. These two effects work in the opposite direction and compensate with each other.

Another difference is the small  $[\text{Ba}/\text{Fe}]$  scatter seen in L-UFD. Since the RMS contributes to  $s$ -process enrichment without much delay, the time-wise inhomogeneity becomes small (see Figure 13). This effect works for both Ba and Sr. On the other hand, the scatter is still large in M-UFD: the spatial inhomogeneity exists even in this model.

### 3.3.3 Electron-capture supernova model

Figure 14 shows the Sr abundances of L- and M-UFDs in ECSN model. The numbers of ECSNe in L- and M- UFDs are five and one, respectively. The stars in M-UFD has very low  $[\text{Sr}/\text{Fe}]$ . This is because the ECSN occurred at the last moment of the star formation. Therefore, almost no stars are formed from the ECSN ejecta. In L-UFD, on the other hand, there is a gap at  $[\text{Sr}/\text{Fe}] \sim -2$  in the distribution. The amount of Sr synthesized in one ECSN is huge. Therefore, even one ECSN is sufficient to strongly enhance Sr abundances. Although the median line gradually increases  $-3 < [\text{Fe}/\text{H}] < -2$ , it does not represent gradual increase of the abundance. The fraction of high  $[\text{Sr}/\text{Fe}]$  group (i.e. formed out of more than one ECSN ejecta) increases gradually as we look higher  $[\text{Fe}/\text{H}]$ .

## 3.4 Discussion

### 3.4.1 $R$ -process contribution

The chemical evolution of  $s$ -process elements has been studied for a long time (e.g. [Cescutti et al. 2006](#)). We have assumed in our fiducial model that  $s$ -process elements are produced in low-mass stars with  $M \lesssim 3 M_{\odot}$ . The long time delay and the metallicity dependence of  $s$ -process yield makes AGB stars less efficient at enriching low-metallicity stars. Chemical evolution simulations (e.g. [Cescutti et al. 2006](#)) suggest that the origin of Ba in MW stars with  $-3 < [\text{Fe}/\text{H}] < -2$  is the  $r$ -process. This is consistent with the observations: see

Section 5. Similarly, [Hirai et al. \(2019\)](#) argue that the Sr production in classical dwarf galaxies mainly occur by the  $r$ -process.

For UFDs, however, the argument is different. Due to their small stellar masses, the  $r$ -process contribution is discretized:  $r$ -rich UFDs have one or more, whereas other UFDs have zero. The stochasticity of  $r$ -process in each UFD is required to explain the very high Eu abundances seen in Ret II. This interpretation also naturally explains the moderate abundances of Tuc III and Gru II, with natal kick of binary neutron stars ([Tarumi et al. 2020b](#)), or a larger mass of gas that dilutes the  $r$ -rich ejecta ([Marshall et al. 2018](#)). The large Eu abundance spread seen in low metallicity halo stars is also naturally explained by rare and prolific  $r$ -process enrichment. The dashed lines in Figure 12 show that, if the  $r$ -process contributes to a UFD, it will dominate the Ba production. Following this picture, we exclude the contribution from the “rare and prolific  $r$ -process events” to Ba production. In Section 3.6, we show the expected abundance of Ba for UFD stars, assuming that Ba is synthesized in the  $r$ -process.

### 3.4.2 Production of $s$ -process elements in the fiducial model

The median  $[\text{Ba}/\text{Fe}]$  are  $\sim -2.5$  (L-UFD) and  $[\text{Ba}/\text{Fe}] \sim -4$  (M-UFD) for stars with the metallicity of  $-3 < [\text{Fe}/\text{H}] < -2$  (see Figure 12). These values correspond to the integrated yield from a single stellar population (SSP) age of 100 Myr and 25 Myr for L and M-UFDs. Similar results are obtained if we use  $[\text{Sr}/\text{Fe}]$  instead. Even if we change the Ba yields of AGB stars, we expect that the typical  $[\text{Ba}/\text{Fe}]$  of stars formed will be that of SSP at 100 (25) Myr in L- (M-) UFDs. These timescales are too short for low-mass AGB stars to contribute. Therefore, we argue that another source of Ba is required to explain the Ba abundances of UFDs. The additional source should contribute to chemical enrichment within  $\sim 100$  Myr.

Since gas heating by reionization in space can effectively quench star formation in these small galaxies by  $z \sim 6$ , the duration of UFD star formation can be limited to a few hundred Myrs. Moreover, considering their low halo masses, the onset of star formation in the UFD is not expected to be early. Indeed, our simulations predict that the star formation begins when the cosmic age is  $\sim 300$  Myr. Therefore, the period of star formation in UFD is shorter than  $\sim 700$  Myr. In the simulation, L-UFD shows comparable lengths of star formation. Therefore, we consider L-UFD as one of the most AGB-enriched UFDs. Even this UFD fails to reproduce the Ba abundance in the observations. This suggests that the Ba production in these systems is more efficient in the Universe.

A simple solution to enhance the production of Ba would be to adopt different AGB yields. A 10–100 times higher yield could resolve the inconsistency. However, due to the secondary nature (i.e. the yield is proportional to metallicity) of the  $s$ -process, such large values is unlikely. If the yield is enhanced at low metallicity, the same set of stellar parameters would produce larger amounts of  $s$ -process elements with the same enhancement factor. This produces an excess of Ba abundance at a higher metal content, approximately at  $[\text{Fe}/\text{H}] \sim -1$ . A possible solution for AGB stars to account for the  $s$ -process abundance in UFDs would be to introduce a metallicity dependence into the stellar evolution model, increasing Ba production by a factor of 10 – 100 at  $[\text{Fe}/\text{H}] \sim -2$  while keeping Ba production at a higher metallicity at the current value.

Super-AGB stars is proposed as an additional source of the  $s$ -process ([Doherty et al.](#)

2017). The typical mass of a progenitor star is  $6 - 8 M_{\odot}$ , therefore they contribute to chemical enrichment within 100 Myr. To test their possibility, we adopt the  $s$ -process yields from Doherty et al. (2017)<sup>2</sup> and recalculated the stellar element abundances. Super-AGB stars can enrich  $s$ -process elements earlier, but the absolute abundance of Ba in the UFD does not increase much. This is because the mass range of the progenitor stars is too narrow, which results in the low production efficiency of  $s$ -process elements. For super-AGB stars to become a major source of Ba in UFDs, their yields need to increase significantly, by a factor of about 10.

Since Sr is lighter than Ba, it is synthesized under less extreme conditions (e.g., "light element primary process", Montes et al. 2007). Such "exclusive" Sr sources is necessary to explain the presence of Sr-enhanced stars relative to heavier elements such as Ba and Eu (Honda et al. 2004). Hirai et al. (2019) consider ECSNe and RMSs as additional Sr sources. They conclude that additional sources of Sr such as these are necessary to reproduce the Sr abundances in dwarf galaxies.

In our fiducial model, only AGB stars produce Sr. Figure 12 shows the same trend as Ba: the Sr production is not sufficient. We estimate the Sr mass needed to explain the observations to be ( $[\text{Sr}/\text{Fe}] \sim -1$ ) is  $10^{-8} M_{\odot}$  per  $1 M_{\odot}$  in the first 100 Myr. Given the large difference in Sr composition between UFDs, there may be a rare and prolific source of Sr production.

### 3.4.3 On additional sources – rotating massive stars

RMSs can synthesize  $s$ -process element (Limongi and Chieffi 2018). Fast (300 km/s) rotators efficiently produce heavy  $s$ -process elements such as Ba while slow (150 km/s) rotators mainly synthesize Sr. The Sr to Ba ratio is  $[\text{Sr}/\text{Ba}] \sim -0.6$  and  $[\text{Sr}/\text{Ba}] \sim 0.9$  for fast and slow rotators. Figure 15 shows the  $[\text{Sr}/\text{Ba}]$  ratios of the RMS model for L- and M-UFDs. The median metallicities are  $-2.66$  and  $-2.96$ . Their  $[\text{Sr}/\text{Ba}]$  ratios are close to the IMF-averaged value at  $\log(Z/Z_{\odot}) = -3$ . L-UFD contains a population of stars that are pulled toward the value for  $\log(Z/Z_{\odot}) = -2$ . The difference from  $[\text{Fe}/\text{H}]$  of  $-3$  to  $-2$  is the rotation velocity distribution. The fraction of fast rotators significantly decrease from  $\log(Z/Z_{\odot}) = -3$  to  $\log(Z/Z_{\odot}) = -2$ , whereas that for slow rotator does not change much. Therefore, at higher metallicity,  $[\text{Sr}/\text{Ba}]$  gets higher.

From the amount of Ba, we can compute the required fraction of fast rotators at  $-3 \lesssim [\text{Fe}/\text{H}] \lesssim -2$  because Ba is mostly synthesized in fast rotators. The fraction needs to be about 10%. This constraint comes from the IMF-averaged Ba production and is therefore degenerate with the RMS yield. Ba abundances of UFD stars supports that  $\sim 1 \times 10^{-9} M_{\odot}$  of Ba should be produced for every  $1 M_{\odot}$  of star formation.

Although  $[\text{Ba}/\text{Fe}]$  and  $[\text{Sr}/\text{Fe}]$  in the UFD can be explained by RMS contribution, there may be a tension between simulations and observations for the distribution of  $[\text{Sr}/\text{Ba}]$ . The  $[\text{Sr}/\text{Ba}]$  values of stars observed with UFD appear to be independent of the metallicity  $[\text{Fe}/\text{H}]$ . However, if RMS is the dominant origin of these elements, we would expect  $[\text{Sr}/\text{Ba}]$  to increase as  $[\text{Fe}/\text{H}]$  as the rotation slows down. The number of stars in each UFD is too small to sufficiently sample the IMF, but the UFD as a whole has enough mass to detect the metallicity trend if it exists.

---

<sup>2</sup>We obtain the yield from the author personally.

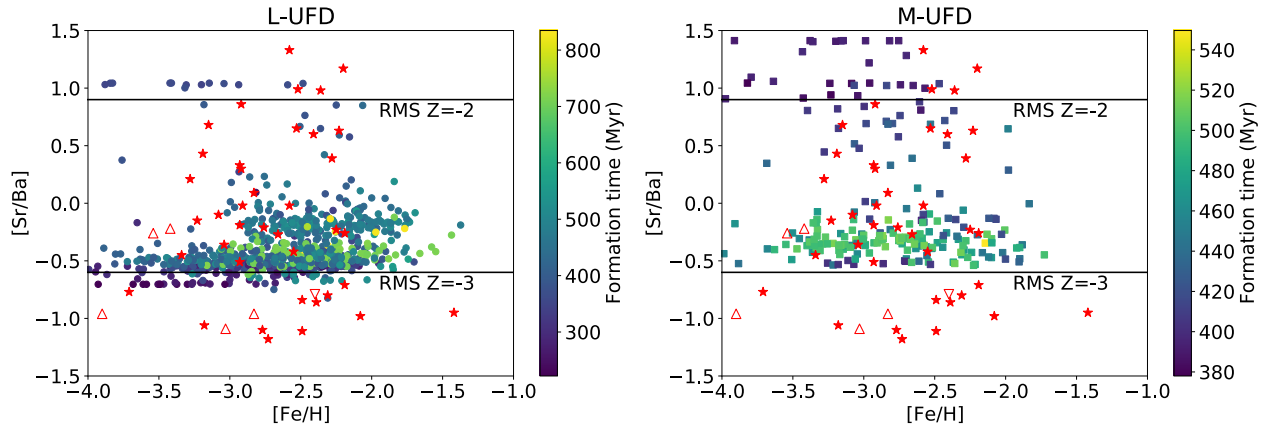


Figure 15: Plots of  $[\text{Sr}/\text{Ba}]-[\text{Fe}/\text{H}]$ . The horizontal lines show IMF-averaged values for metallicity  $-3$  and  $-2$ . Points does not necessarily fit between these lines because the lines are IMF-averaged values.

Another important test is the measurement of N. Recently, [Ji et al. \(2020\)](#) reported the measurement of N through molecular line of CN. They detect CN in three stars in a UFD Carina II (Car II). There seems no correlation between N and Ba or Sr. If RMS is the primary producer of  $s$ -process elements, then these  $s$ -enhanced stars should also have enhanced N. The stellar mass of Car II is about  $\sim 10^4 M_{\odot}$  (the same as our L-UFD), which is sufficient to average the RMS effect to the IMF-average. Currently, it is not possible to discuss in detail due to the large measurement error ( $\gtrsim 0.5$  dex) and the limited number of observations, but it would be very interesting to determine the N abundances of the UFD as a validation of the RMS scenario. The UFD is particularly important because if RMS exists, they will dominate the production of neutron capture elements and N.

### 3.4.4 On additional sources – electron-capture supernovae

ECSNe are very efficient at producing Sr. As Figure 14 shows, the amount from one ECSN is sufficient to imprint a conspicuously high Sr abundance. The mass range of the progenitor stars is unconstrained. Theoretical determination of the mass range is almost impossible because the range is only a small fraction of the stellar mass (e.g.  $\sim 0.1 M_{\odot}$  of a  $\sim 10 M_{\odot}$  star).

Assuming that the synthesized Sr is diluted with a metal-free gas of less than  $10^7 M_{\odot}$ , a single ECSN will enrich the system to  $[\text{Sr}/\text{H}] \gtrsim -4$ . Small UFDs could have very low Sr content ( $[\text{Sr}/\text{H}] \sim -4.0$ ) without any contribution from the ECSN: Segue I, Segue II, Triangulum II, Bootes II, and Grus I are likely such UFDs. If Tuc-033 is a foreground contaminant, then Tuc II would also be such a UFD. Figure 16 illustrates this trend well. The five smallest UFDs have  $[\text{Sr}/\text{H}] < -4$ . We argue that the very low Sr content of these darker UFDs is due to the absence of ECSNe in these systems. This does not mean that the heavier UFDs are enriched with at least one ECSN. Their  $[\text{Sr}/\text{H}]$  is not sufficiently low to rule out a contribution from ECSNe.

From the amount of Sr in the UFD, we can determine an upper limit on the rate of ECSNe. Figure 16 shows that galaxies less bright than  $2400 L_{\odot}$  do not experience ECSNe.

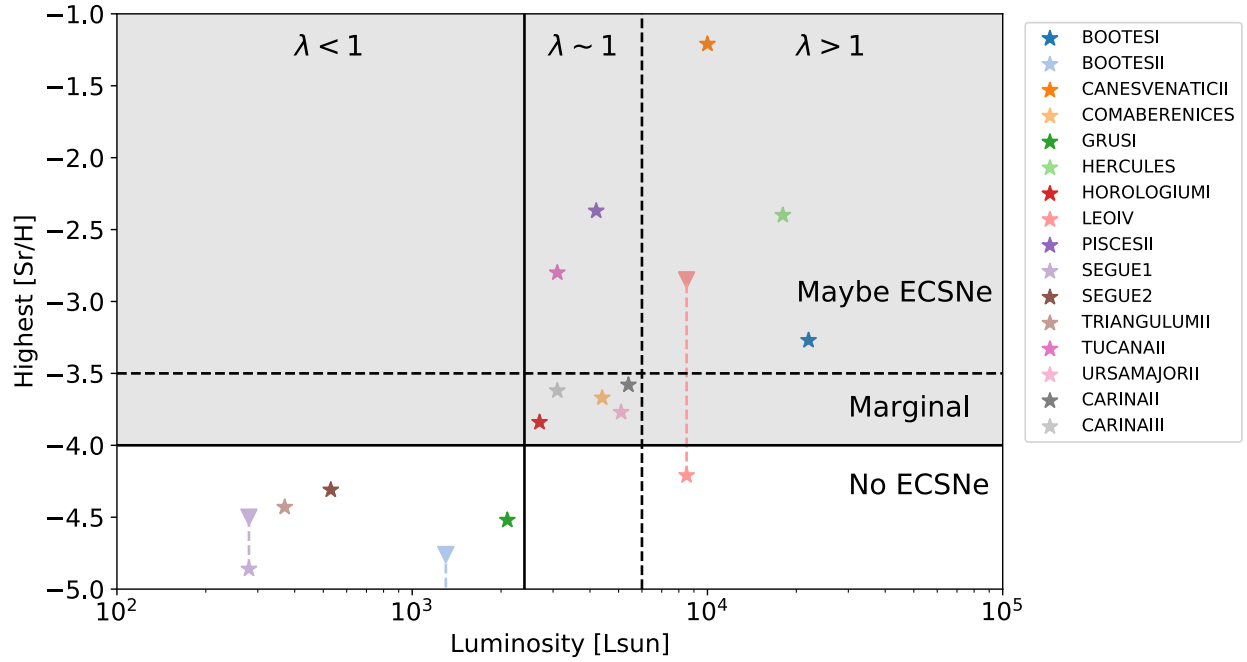


Figure 16:  $[\text{Sr}/\text{H}]$  limits plotted against luminosity of UFDs. Stellar markers represent detections of Sr abundances. We show the highest detection within each UFD. Downward triangle is the highest upper limits if the constraint is weaker than the highest detection in the system. The CH star in Segue 1 is removed from the plot as it likely represents the abundance of the binary companion.

Here we assume that one ECSN occurs for every 2000  $L_{\odot}$  of stars. Assuming that the ratio of stellar mass to luminosity is 1 (but it is not that simple; see [Martin et al. 2008](#), UFDs generally have mass-luminosity ratios greater than 1), the mass of currently surviving stars is  $\sim 2000 M_{\odot}$ . Assuming that 40% of the stars survive to the present (in the case of the Chabrier IMF), the mass of the original stars formed should have been  $5000 M_{\odot}$ . Therefore, the incidence of ECSN is constrained to be less than one in every 5000  $M_{\odot}$  star. This roughly corresponds to a mass range  $\Delta M$  of  $0.1 M_{\odot}$ . For example, assuming that  $8.0 - 8.1 M_{\odot}$  stars explode as ECSNe, the rate is  $1/5000 M_{\odot}$ . If one assumes that one ECSN enriches the system to  $[\text{Sr}/\text{H}] = -3.5$  (assuming that the mixing gas mass is  $10^{6.5} M_{\odot}$ ), the luminosity limit would be  $2000 L_{\odot}$ , which would limit the fraction to be smaller than  $1/12500 M_{\odot}$ .

Pieces II, Hercules, and Canes Venatici II are highly Sr-enhanced UFDs. ECSNe could explain such high abundances of Sr. L-UFD contains some stars with  $[\text{Sr}/\text{Fe}] \sim 0$  due to ECSNe enrichment. Considering the small explosion energy of ECSNe ( $\sim 10^{50}$  erg, we can take the dilution mass to be as small as  $\sim 10^4 M_{\odot}$ . In this case, the star would be enriched to  $[\text{Sr}/\text{H}] \sim -1$  with a single ECSN, explaining the Sr-rich stars in [François et al. \(2016\)](#).

### 3.4.5 Initial mass function variation

The IMF could be different in low-metallicity environments ([Kroupa et al. 2013](#); [Gennaro et al. 2018](#)). [Komiya et al. \(2009\)](#) propose that a log-normal IMF with the center at  $3 - 20 M_{\odot}$  explains well the fraction of *s*-process enhancements in carbon-enhanced metal-poor stars in MW halo. [Geha et al. \(2013\)](#) find that a shallower IMF slope explains the color-magnitude diagram of observed UFDs. Theoretical investigation for the IMF of zero-metal stars (“population III stars”) predict that it is top-heavy ([Hirano et al. 2014](#)). Therefore, the IMF of stars in UFDs might also be top-heavy. On the other hand, [Conroy and van Dokkum \(2012\)](#) point out that a bottom-heavy IMF is favored from the spectral features by  $\text{Na}_{\text{I}}$ ,  $\text{Ca}_{\text{II}}$ , and  $\text{FeH}$ .

As a simple test for the IMF variation, we test three non-traditional IMF: top-heavy (log-flat), Komiya-like (log-normal, with a center of  $4 M_{\odot}$  and 0.15 dex of the standard deviation), and bottom-heavy (Salpeter, [Salpeter 1955](#)) IMF. Figure 17 shows the results. The  $[\text{Ba}/\text{Fe}]$  values are smaller in the model with the top-heavy IMF than in our fiducial model (see Figure 12). The top-heavy IMF enhances the Fe production, while Ba production is not enhanced. Note that the top-heavy form has a similar  $[\text{Fe}/\text{H}]$  distribution compared to our model, even though it produces more Fe from unit stellar mass formed. This is because the total mass of stars in the UFD is reduced due to stronger feedback compared to the fiducial model, and consequently, the total amount of iron is comparable. The middle panel shows the results for the bottom-heavy IMF case. For initial masses  $M \gtrsim 1 M_{\odot}$ , the IMFs are nearly identical because of the expected contribution of chemical enrichment. Therefore, this result is almost identical to our fiducial run. The figure below shows the results with a komiya-like IMF. This IMF has a larger fraction of intermediate to massive stars, which results in more Ba and less Fe production. It better reproduces the observed  $[\text{Ba}/\text{Fe}]$  trend. Note that in addition to the stars in the log-normal part of the IMF, a low-mass companion star in the binary system is assumed to have formed and survived to the present day, but the companion star is not explicitly represented in this simulation.

The Integrated-galaxy IMF theory discuss that the IMF depends on SFR ([Kroupa et al.](#)

2013). In a molecular cloud that forms stars actively, high-mass stars preferentially form, while in slow star-forming clouds, low-mass star formations are more likely. The star formation period of our UFD sample is about 100 Myr, and the total stellar mass is about  $\sim 10^4 M_\odot$ , so the star formation rate is  $10^{-4} M_\odot \text{ yr}^{-1}$ . This low SFR is expected to suppress star formation below  $\gtrsim 10 M_\odot$  (see Fig. 35 of Kroupa et al. 2013). The suppression of Fe production while constant Be production may be a natural consequence of the low SFR in such slowly star-forming system. The important thing is to apply the IMF variation to other systems with different SFRs in the same framework. Further study is needed to investigate this effect.

Interestingly, the elemental abundances of second-generation stars in globular clusters can be explained by the super-AGB stars (e.g. Bastian and Lardo 2018). There are also implications for other problems, such as the mass-budget problem, where the mass fraction of second generation stars is inexplicably high (Renzini 2008). The log-normal IMF with a large mass fraction of super-AGB stars may partially solve the mass budget problem. In addition, this IMF significantly reduces the Fe production. Therefore, there is no significant difference in metallicity between first and second generation stars. Since the IMF proposed by Komiya et al. (2007) is for stars with  $[\text{Fe}/\text{H}] \lesssim -2$  (Suda et al. 2013; Lee et al. 2014), we cannot conclude that this is a viable solution to the GC abundance anomaly considering the metallicity of GCs (many have  $[\text{Fe}/\text{H}] > -2$ ). However, interestingly, the enhancement of super-AGB fraction would solve two problems in completely different contexts.

The Ba abundances inexplicable by AGB stars might be an evidence of another source of  $r$ -process elements. Observations of MW stars clarify that  $[\text{Ba}/\text{Fe}]$  does not increase with metallicity between  $-2.0 < [\text{Fe}/\text{H}] < -1.5$ . It suggests that the  $s$ -process yields from AGB stars is not the dominant contributors (Matsuno et al. 2020). However, their  $[\text{Eu}/\text{Ba}]$  ratio is lower than the  $r$ -process value. Therefore, both  $r$ - and  $s$ -process events should have contributed to the enrichment of stars in this metallicity range. An interesting test is to measure the Eu abundances of UFD stars to clarify which processes have contributed dominantly to the chemical enrichment.

### 3.4.6 On ultra-faint dwarfs with internal Ba spreads

A few UFDs (such as Boo I, Car II, and ComBer) show a clear internal spread in  $[\text{Ba}/\text{Fe}]$ ; the spread in Ba could be due to temporal or spatial inhomogeneity. If it is temporal (see Figure 12), then AGB stars are the origin of the spread and star formation in these systems is long ( $\sim 300$  Myr). The upper left panel of Figure 12 shows that AGB stars can reproduce the abundance spreads within a galaxy. However, there is a tension in the  $[\text{Ba}/\text{Fe}]$  value. In our simulations, the  $[\text{Ba}/\text{Fe}]$  is -1.5 even for later forming stars, but some Car II and Boo I stars have a  $[\text{Ba}/\text{Fe}]$  of -0.5. The difference in  $[\text{Ba}/\text{Fe}]$  values between these observed UFDs and our simulation UFDs may suggest that, in reality, star formation in these systems is longer ( $>1$  Gyr) than in our simulation. In the case of spatial inhomogeneity (see Figure 13), fast-rotating massive stars may be the origin of Ba. These stars produce sufficient amounts of Ba to produce several stars with  $[\text{Ba}/\text{Fe}]$  of -0.5. The star formation period should be as short as 200 Myr. However,  $[\text{Ba}/\text{Fe}]$  does not show an increasing trend in this model and cannot reproduce Boo I. A possible solution would be to change the distribution of rotational velocities. An important validation of this nonstandard scenario is to look at the correlation

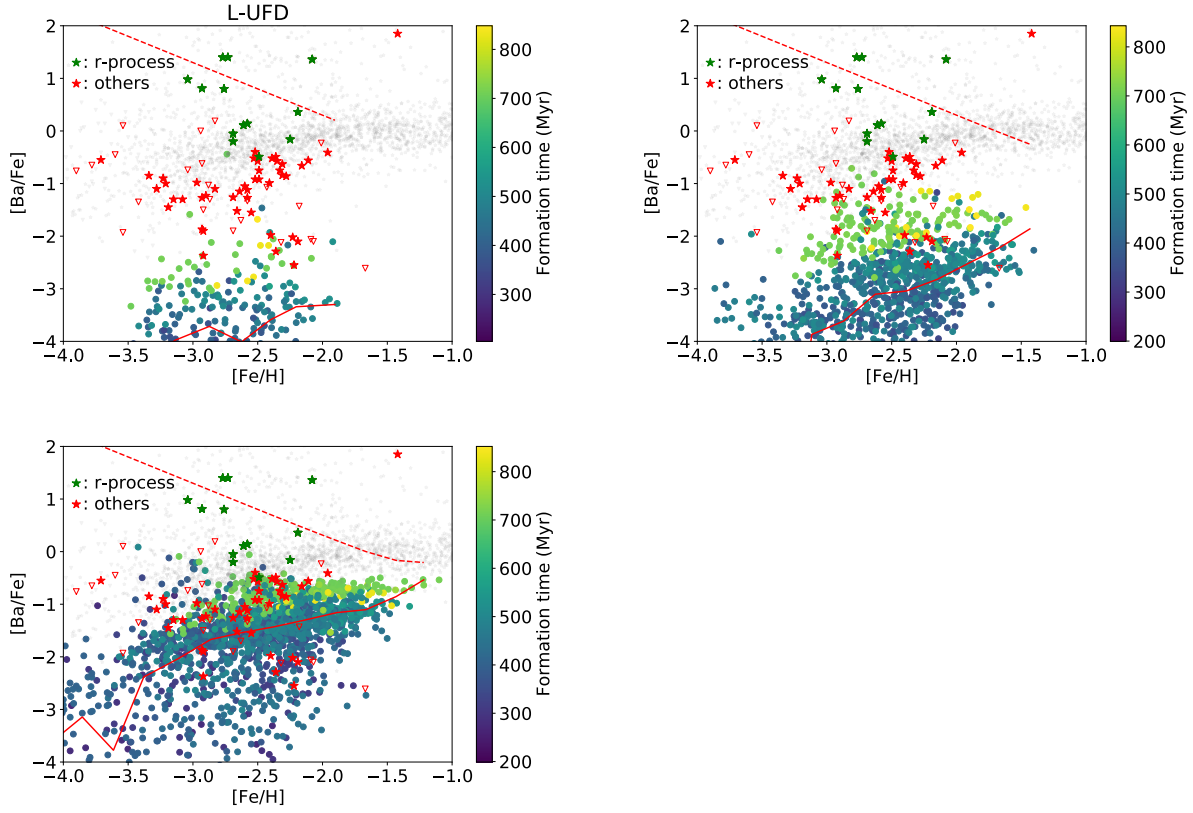


Figure 17: The results for IMF variation tests. The top panel shows the top-heavy (log-flat) model. Ba production per stellar mass increases slightly but the Fe increase is way more significant, lowering the  $[\text{Ba}/\text{Fe}]$ . The middle panel presents bottom-heavy (Salpeter) IMF results. The difference from Chabrier IMF is only the increase of low-mass stars that do not contribute to the chemical enrichment: therefore, the prediction is mostly the same as in our fiducial case. The bottom panel shows the Komiya-like IMF (log-normal, centered at  $4 M_{\odot}$  and the standard deviation of 0.15 dex). Since the AGB fraction increases significantly, the Ba production is enhanced and the Fe production is suppressed at the same time. The  $[\text{Ba}/\text{Fe}]$  roughly matches the one of UFDs. Same symbols as Figure 12 are used for observational data.

between N and Sr or Ba. For RMS to be viable as the origin, the co-production of these elements must be observationally confirmed; accurate measurement of the abundance ratio of N would answer this question.

### 3.4.7 Effects of tidal stripping

Some UFDs show signatures of tidal stripping. The stripping would make a UFD fainter than its original mass, biasing the interpretation. Our assumption on zero  $r$ -process may be invalid if its original stellar mass is more than ( $\sim 10^5 M_\odot$ ). In addition, their potential well could be deeper than the assumption: therefore, it could keep forming stars after the cosmic reionization. Boo I and Ursa Major II could be such partially disrupted UFDs (Belokurov et al. 2006; Zucker et al. 2006). They are relatively metal-rich: some stars show  $[Ba/Fe] > -1$ . Our models fail to reproduce stars with  $[Ba/Fe] \sim -0.5$ . This might indicate that such “Ba-rich” stars are actually the signature of past tidal disruption history. Note, however, that the orbits of most UFDs are sufficiently wide to exclude the possibility of past tidal disruption history (Simon 2018). Also, some UFDs show  $[Ba/Fe] \sim -1$  while they do not show any traces of disruption.

## 3.5 Conclusions

We have studied the production of  $s$ -process elements in UFDs. The basic assumption is that UFDs without Eu enhancements do not experience  $r$ -process events in the past. We have shown that the AGB stars only are not sufficient to reproduce Ba abundances, even though we have used one of the most up-to-date yields. Our findings are summarized as follows.

1. Ba production should be efficient ( $\sim 1 \times 10^{-9} M_\odot$  per  $1 M_\odot$  of stars in the first 100 Myr) even in metal-poor environments such as UFDs. The delay needs to be short. Super-AGB stars are not efficient at producing Ba.
2. RMSs explains the Ba abundances of UFDs if  $\sim 10\%$  of stars are fast ( $\sim 300 \text{ km s}^{-1}$ ) rotators. An interesting test is the measurement of N. If RMSs are the dominant contributors to the  $s$ -process elements in UFDs, we expect a correlation between N and  $s$ -process elements.
3. ECSNe produce copious amount of Sr. Sr abundance would be more than  $[Sr/H] \gtrsim -4$  once a UFD experiences one ECSN. Observations show that low-luminosity UFDs show particularly low Sr abundances. We argue that these UFDs should not experience any ECSNe. From their luminosities, the rate of ECSNe should be less than 2% of CCSNe, narrowing the width of the progenitor mass range to  $\lesssim 0.1 M_\odot$  at  $-3 < [Fe/H] < -2$ .
4. Ba abundances could be explained by introducing an IMF centered around the  $s$ -process producers, i.e., AGB stars. It needs to be top-light in order to suppress the Fe production. The IMF might be a consequence of low SFRs in UFDs.

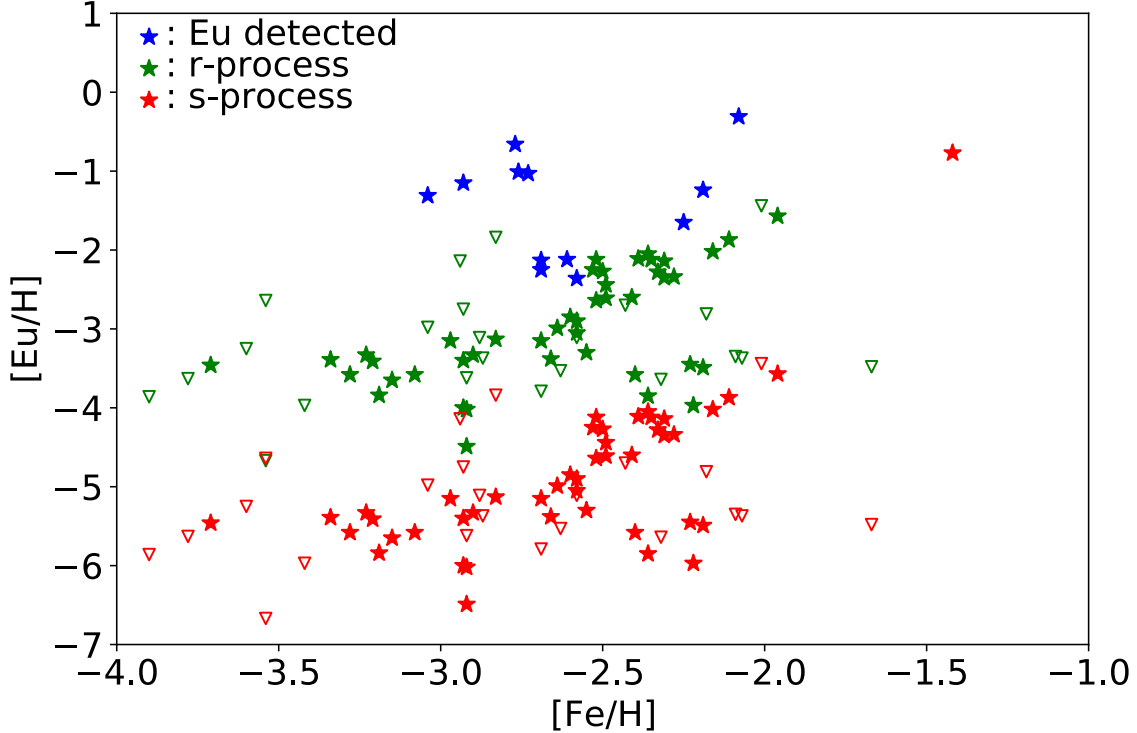


Figure 18:  $[\text{Eu}/\text{H}]$  distribution of UFD stars estimated from their Ba abundances. Blue markers show stars with Eu detection in Ret II, Tuc III, and Gru II. A CH star in Segue 1 is plotted with red because we know it is from the  $s$ -process. For other UFD stars, each Ba data produces two dots colored with green and red. The assumed Eu to Ba ratio are  $[\text{Eu}/\text{Ba}] = 0.8$  ( $r$ -process) and  $-1.2$  ( $s$ -process, respectively).

## 3.6 Additional analyses

### 3.6.1 R-process

Figure 18 shows the expected  $[\text{Eu}/\text{H}]$  abundances of UFD stars estimated from Ba abundances. The blue symbols are stars with Eu detection. The green symbols are the estimates under the assumption of  $r$ -process, and the red symbols are the ones with the  $s$ -process. The values of some green symbols are higher than those of blue symbols, suggesting that if the origin of Ba is the  $r$ -process, it would be detected. For some stars, the possibility of pure  $r$ -process is already eliminated (e.g. Car II, Ji et al. 2020). The upper limits of  $[\text{Eu}/\text{H}] \sim -3.5$  is needed to eliminate the possibility for most of UFD stars.

### 3.6.2 Super-AGB

Figure 19 shows the results of model with super-AGB contributions. Symbols are the same as in Figure 12. It enhances  $[\text{Ba}/\text{Fe}]$  and  $[\text{Sr}/\text{Fe}]$  at  $[\text{Fe}/\text{H}] < -3$  but not significantly at  $[\text{Fe}/\text{H}] \gtrsim -3$ . Note that the black curve is a bit different from the curve in Figure 12 due to

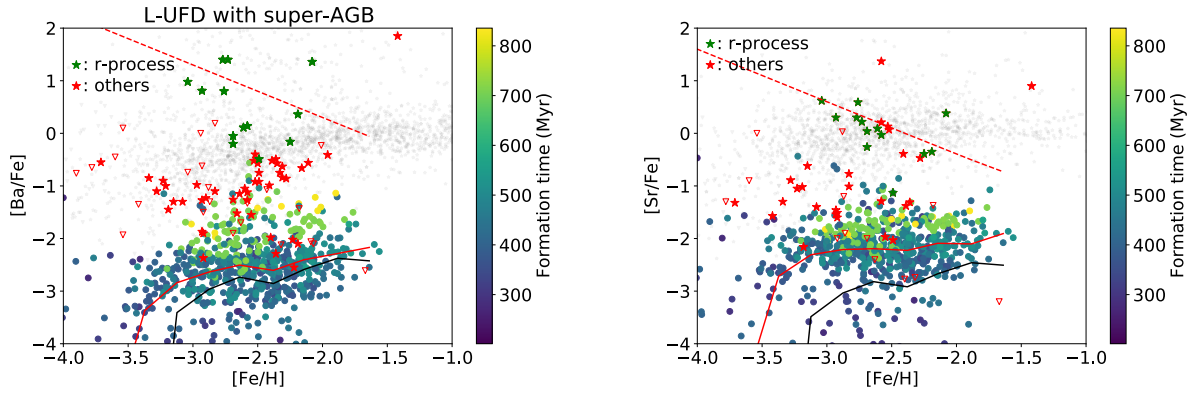


Figure 19: Model with contribution from super-AGB stars. The black curves show the model results without contribution from super-AGB stars. It enhances  $[Ba/Fe]$  and  $[Sr/Fe]$  but it is not sufficient to reproduce the observed UFD abundances.

the stochastic nature of our model.

## 4 Formation of an extended ultrafaint dwarf galaxy via early mergers of building-blocks

As we have seen in the previous section, UFDs are useful systems for galactic archaeology as they discretize contributions from rare events. To fully exploit their potential, we need information on the star formation history and, ideally, the ages of stars. However, precise stellar ages have been out of reach due to their old stellar population. This section investigates the formation process of a UFD with an extended stellar profile. This is the first work for a UFD that investigates the connection between stars' kinematic information and their formation history with numerical simulations.

### 4.1 Stellar distribution profile in ultra-faint dwarf galaxies

There is a recent claim that an extended structure of a UFD, Tucana II (Tuc II), is observed (Chiti et al. 2021). Seven out of 19 giant stars are located at the distances larger than  $2r_h$ , where  $r_h$  is the half-light radius. The farthest star is observed at the distance of more than 1 kpc from the center. The star is unlikely to be a halo interloper because its radial velocity ( $-129.1 \text{ km s}^{-1}$ ) is very different from other background stars, and the metallicity is very low ( $[\text{Fe}/\text{H}] = -2.77$ ) and consistent with other stars in Tuc II.

Considering the fact that other UFDs are all compact, the mechanism for forming such an extended UFD is interesting. One possibility is the tidal disruption by the potential of MW halo. A UFD could be disrupted if it comes close ( $\lesssim 20 \text{ kpc}$ ) to the center of the MW (Peñarrubia et al. 2008). However, the orbital distance of Tuc II from the MW center is too far (58 kpc) to be disrupted. The stellar structure of Tuc II appears to also disfavor the tidal disruption scenario (Chiti et al. 2021). It is interesting to investigate the another mechanism to reproduce such extended stellar distribution.

Here we propose that an early galaxy-galaxy merger could reproduce such UFD with an extended stellar profile. A galaxy merger disrupts the stellar density profile. We justify this scenario using galaxy formation simulations. We follow the formation of UFD that experience a merger.

### 4.2 Simulations of early galaxies

#### 4.2.1 Galaxy formation model

The galaxy formation models settings are mostly the same as in Section 3.2.1. We use the galaxy formation code AREPO (Springel 2010; Weinberger et al. 2020). The initial conditions are generated with MUSIC (Hahn and Abel 2011). The cosmological parameters are the ones in Planck 2018 results (Planck Collaboration et al. 2020):  $H_0 = 67.4 \text{ km s}^{-1} \text{ Mpc}^{-1}$ ,  $\Omega_m = 0.315$ ,  $\Omega_b = 0.049$ ,  $\sigma_8 = 0.810$ ,  $n_s = 0.965$ .

#### 4.2.2 Final galaxy after the merger

Only one galaxy experiences a merger after the formation of the first star in the galaxy, among our five sample galaxies. The mass of the dark matter halo ( $M_{\text{DM}}$ ) and the stellar

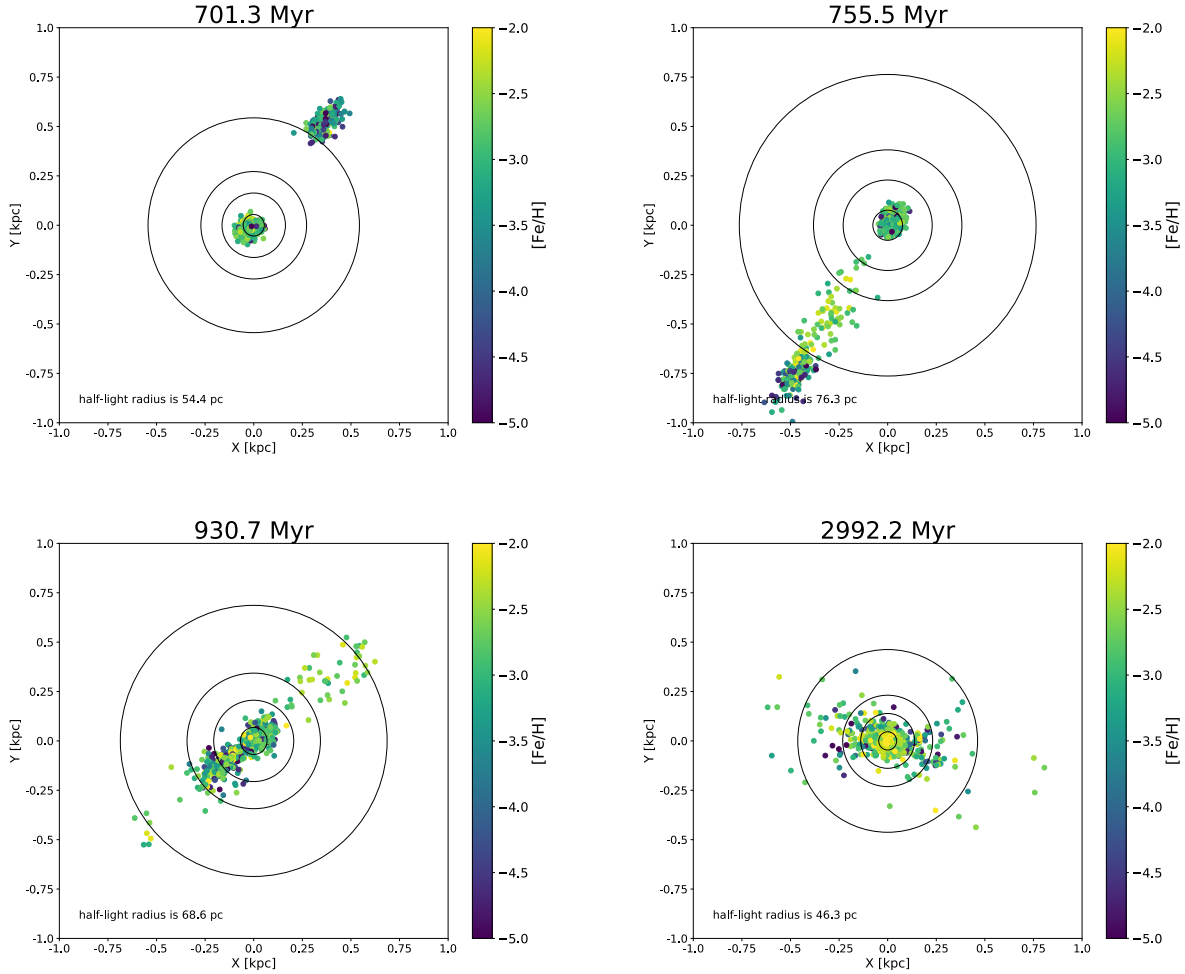


Figure 20: Spatial distribution of stars in our main simulation. A region of 2 kpc box is plotted. The system evolves from top left to bottom right. Four concentric circles show one, three, five, and ten times the half-light radius of the system. The radius is computed on the projected plane. The top left panel shows the galaxy before the encounter of the two systems. The top right panel presents the projection plot of stars after the disruption of the infalling system. The bottom left panel shows the stellar distribution at  $\sim 200$  Myr after the merger. An elongated structure develops in the direction of the infall. The bottom right panel shows that the extended bar-like structure survives even after  $\sim 2,500$  Myr.

mass ( $M_*$ ) of the two building blocks before the merger (at 510 Myr) are  $(M_{\text{DM}}, M_*) = (8.5 \times 10^7 M_\odot, 3,900 M_\odot)$  and  $(5.0 \times 10^7 M_\odot, 7,500 M_\odot)$ , respectively. The merger is a major merger, with the mass ratio of  $\sim 1.4$ . As for metallicity, the median and the quartile deviation of  $[\text{Fe}/\text{H}]$  in the infalling galaxy are  $-3.06$  and  $1.36$ , while these for the central galaxy are  $-2.72$  and  $0.70$ .

The merger of two halos (identified by the halo finder) occur when the age of the Universe is 510 Myr. The close encounter of stellar components are at 700 Myr. During and after the merger, about  $3,000 M_\odot$  of stars are formed. Compared to the stars formed before the merger, they have higher metallicities: the median and the quartile deviation are  $-2.29$  and  $0.56$ . At  $z = 4.5$  (when the cosmic age is 1,370 Myr), the merged galaxy has grown to  $(M_{\text{DM}}, M_*) = (2.5 \times 10^8 M_\odot, 14,000 M_\odot)$ . The median and the quartile deviation for the metallicity of the final merged galaxy are  $[\text{Fe}/\text{H}] = -2.7$  and  $0.82$ . The metallicity distribution agrees well with that of UFDs in general including Tuc II:  $[\text{Fe}/\text{H}] = -2.77$ . A bar-like structure is formed as a consequence of the merger. The length is  $\sim 1$  kpc and it survives for more than 2.5 Gyr after the merger. It is interesting that the two farthest stars in Tuc II are both located in the direction perpendicular to the one expected if it is from tidal disruption. This may indicate that the stellar component of Tuc II is formed as a consequence of a past major merger.

At redshift  $z = 4.5$ , we switch off the hydrodynamical calculation. The stellar dynamics are followed purely gravitationally afterwards. By that time, gas mass in the simulated galaxy is low: thus, further star formation is unlikely. The simulation runs for 1.5 Gyr further, until the cosmic age of 3 Gyr.

## 4.3 Properties of our merged galaxy

### 4.3.1 Stellar distribution

Figure 20 shows the evolution of stellar distribution during and after the merger. The circles show radii with 1, 3, 5, and 10 times the half-light radius  $r_{\text{half}}$ , where  $r_{\text{half}}$  is determined as the median of the orbital radius of stars in the plane of projection. Colors represent the metallicities of the star particle.

The two building blocks are compact before the merger (top left panel). Even the farthest star is within  $3 r_{\text{half}}$  and the distributions are almost spherical. The first close encounter disrupts the infalling galaxy (top right panel). The member stars jump out of the original galaxy. A bar-like structure develops  $\sim 200$  Myr after the merger (bottom left panel). The bar is composed of (i) stars from the disrupted galaxy, and (ii) stars formed during the merger. The length of the bar is  $\sim 1$  kpc with small fluctuation between snapshots. The structure survives for  $\sim 2,500$  Myr after the merger (bottom right panel). Stars upscattered by the merger still orbit at large distance from the center. Although the structure is extended, the orbital distance for the farthest star is still smaller than the virial radius, indicating that these stars are bound to the halo. Dynamical friction and redistribution of orbital energies do not effectively occur over the  $\sim 2$  Gyr after the merger.

Figure 21 shows the stellar distribution in a typical galaxy that do not experience mergers. The distribution appears almost spherical and remains compact. Quantitatively, 95% of stars orbit within  $< 3 r_{\text{half}}$  and only one star (0.3%) is at  $5 r_{\text{half}}$ . These fractions are consistent

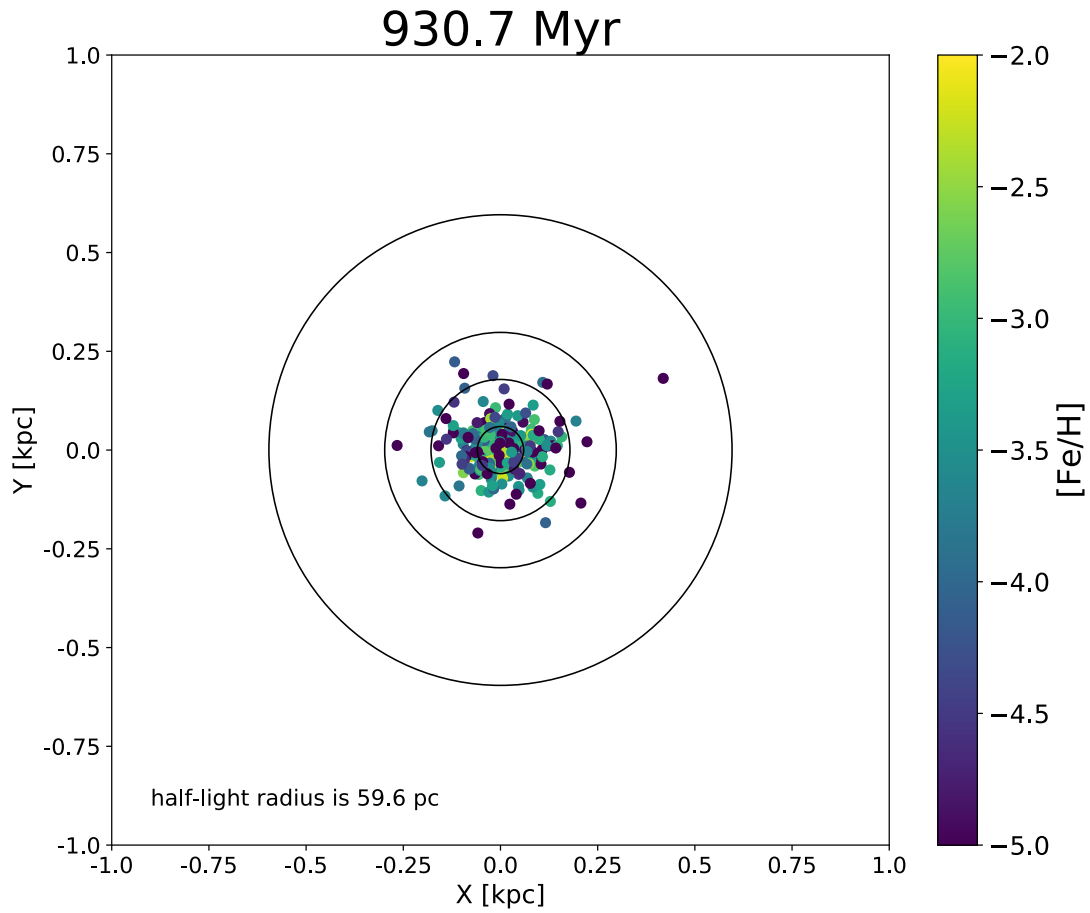


Figure 21: A projection plot of stars in a typical galaxy. Symbols mean the same as in Figure 20. Most stars are located within  $5 r_{\text{half}}$  and there is only one exception. To quantify, the fraction of stars at  $> 5 r_{\text{half}}$  is 0.3% (see Figure 22).

with an exponential profile. Most of our simulated samples that do not experience mergers show such compact structures.

### 4.3.2 Outer halo stars

We analyze the fraction of stars at large radii (“outer halo stars”). Figure 22 shows the time evolution of the fraction of stars at  $> 5 r_{\text{half}}$ . Galaxies without merger show  $f_5 \sim 0$ , which is consistent with the fraction expected with an exponential profile (0.2%). Contrastingly, the fraction for Tuc II is  $f_5 = 2/19 = 10.5\%$ , which is similar to the fraction of the de Vaucouleurs profile (11.5%).

The behavior of merged galaxy is very different from non-merger galaxies. The faraway fraction surges at the moment of merger. The fraction decreases slightly as the system dynamically relaxes, and the fraction  $f_5$  settles at  $\sim 10\% \sim 500 \text{ Myr}$  after the merger. The difference between the merged galaxy and the other galaxies remains significant even after 2.5 Gyr. The fraction of outer halo stars in our merged sample is consistent with that of Tuc II ( $\sim 10\%$ ).

### 4.3.3 Metallicity gradient

Figure 23 compares the iron abundance  $[\text{Fe}/\text{H}]$  between our merged galaxy sample and Tuc II. The top panel plots all the stars in the simulation. The bottom panel shows only the stars formed during and after the merger. We find a weak negative radial metallicity gradient by a linear regression (solid lines). The negative gradient robustly exists in all the snapshots after the merger, although the slope fluctuates from  $-0.2 \text{ dex kpc}^{-1}$  to  $-0.8 \text{ dex kpc}^{-1}$ .

The bottom panel of Figure 23 presents the positions of stars formed during and after the merger. Interestingly, the distribution of stars are even more extended than the top panel. The metallicity gradient seems to exist on both panels. For the mechanism of the gradient formation, see the next section.

## 4.4 Discussion

To show that a major merger can reproduce an extended stellar structure around a UFD, we have run and analyzed a set of galaxy formation simulations. As a result, a bar-like structure forms in the direction of the infall. The elongated structure has the length of  $\sim 1 \text{ kpc}$  and it survives for at least 2.5 Gyr. The surface stellar density profile  $\Sigma(R)$  is crucially changed by the merger. After the relaxation of the structure, about 7% of stars are located at large radii of  $> 5 r_{\text{half}}$ . In contrast, galaxies that do not experience merger are compact. Almost no stars exist at  $> 5 r_{\text{half}}$ . The profile is consistent with an exponential function.

### 4.4.1 Surface density profile

de Vaucouleurs (1948) propose an empirical relation for the surface brightness profile of elliptical galaxies:

$$I(R) \propto \exp\left[-7.669\left(\frac{R}{R_e}\right)^{1/4}\right]. \quad (30)$$

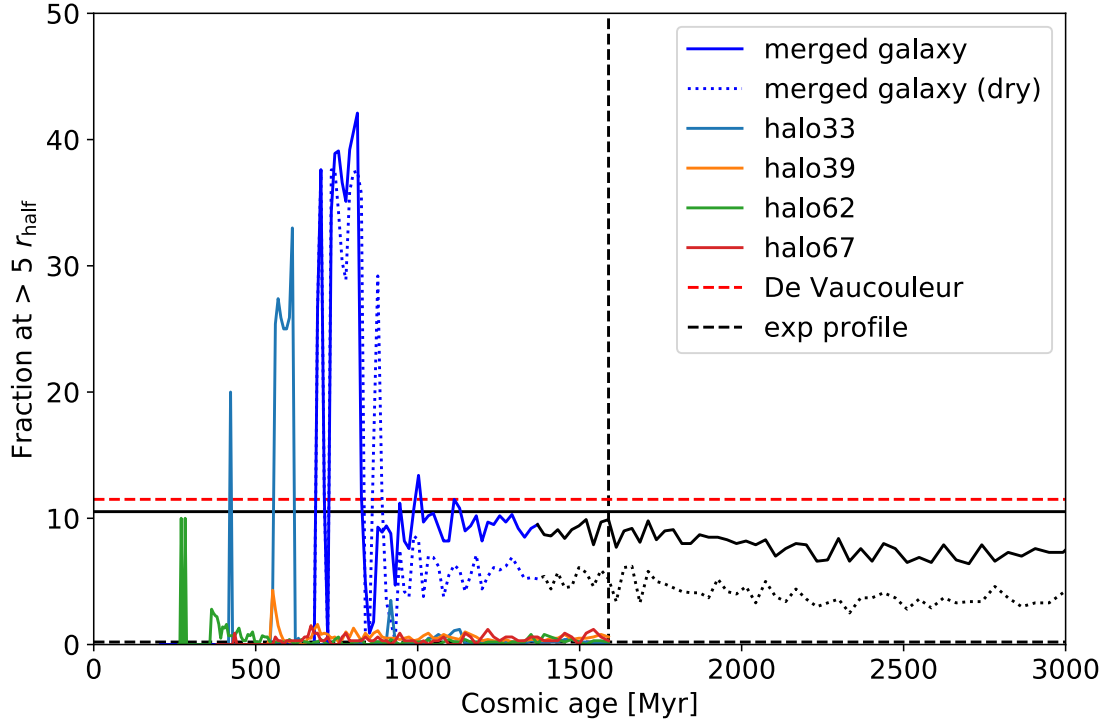


Figure 22: The time evolution of the fraction of outer halo stars at  $> 5 r_{\text{half}}$  for each galaxy ( $f_5$ ). Blue solid line represents the merged galaxy. After  $t = 1.4 \text{ Gyr}$ , we switch off the hydrodynamical calculation and the color is changed to black (see text for discussion). Dotted lines show results obtained when we only include stars formed prior to the merger in the analysis. Other galaxy samples are shown with different colors: they are mostly at 0%. The fraction surges due to the merger. The fraction decreases and settles at 7–10% in a few hundred Myr. The fraction for Tuc II is  $2/19 = 10.5\%$  (black horizontal line) and consistent with the de Vaucouleur profile ( $f_5 = 11.5\%$ ; red dashed line). The fraction for the other, non-merger galaxies are significantly small. It converge to  $f_5 \sim 0$ , which is rather consistent with an exponential profile.

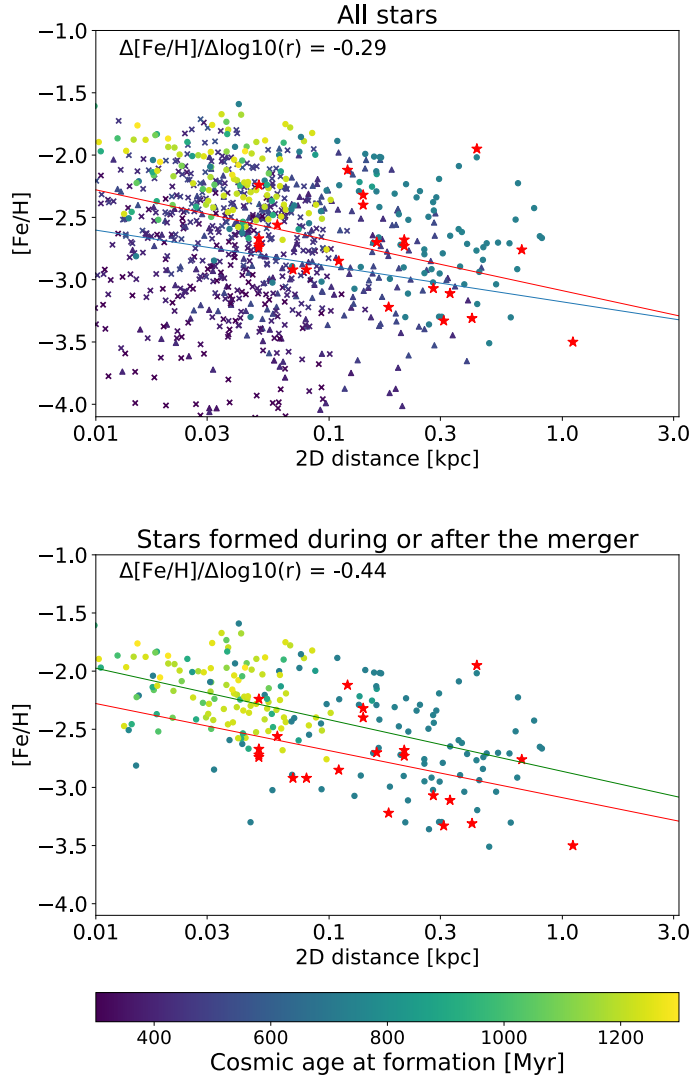


Figure 23: The metallicity gradient in the galaxy samples after the merger. Top panel shows all the stars in the merged galaxy. Red symbols represent stars in Tuc II (observation), and the other symbols (triangles, crosses, and circles) show star particles in the simulation. For simulated stars, colors show their formation epochs. Triangles, crosses, and circles are for stars in the infalling galaxy, in the central galaxy, and those formed during or after the merger. The blue line represents the result of the linear regression for the simulated star particles. We exclude stars with  $[\text{Fe}/\text{H}] < -4.0$  from the regression. The bottom panel only shows stars formed during or after the merger (i.e., green circles in the top panel). Here the color depicts stellar formation time. The green line presents the result of the linear regression only for this sample.

It is often the case that dwarf spheroidal galaxies show more centrally concentrated profiles, with the Sérsic indices of  $\sim 1$  (Muñoz et al. 2018), which is an exponential profile as seen in most of our galaxy samples. Galaxy merger dynamically heats the system and changes the stellar density profile from a compact King profile (King 1966) to an extended de Vaucouleurs profile (Eq. 30) (Aguilar and White 1986). The resulting profile is robust in the sense that another merger produces a galaxy with de Vaucouleur profile. Our numerical experiments show that the earliest galaxies follow the same trend: a merger heats the system and elongate the stellar structure. We expect that galaxies that do not experience mergers will remain compact. The profile of such a galaxy would be similar to an exponential function.

#### 4.4.2 Origin of the metallicity gradient

A presence of the metallicity gradient is reported for Tuc II (Chiti et al. 2021): the gradient is  $-0.87 \pm -0.30$  dex kpc $^{-1}$ . The gradient is similar to what we find in our post-merger galaxy sample (see Figure 23). White (1980) discuss the formation of metallicity gradient for a remnant of a galaxy merger. Population mixing during the merger weakens the gradient as expected, although not completely eliminating. However, we also need to consider star formation after the merger: metal-rich stars formed after the merger could help establish a metallicity gradient.

The metallicity gradient seen in our sample is formed as follows. First, the infalling galaxy is metal-poorer than the central galaxy by 0.3 dex. The metal-richer central galaxy remains undisrupted, and stars in that galaxy tend to orbit close to the center of the remnant galaxy. On the other hand, the infalling galaxy is disrupted by the merger and the stars are upscattered to large radii.

Here comes another contribution from stars formed during and after the merger. We find in our analysis that the most stars orbiting at a large distance are formed during the merger (see the bottom panel in Figure 23). The infalling galaxy contains gas at the time of the infall, and a fast encounter with the central galaxy spurs the formation of stars. Stars formed in this starburst are metal-poor and have large orbital energies. Stars still form after the merger for a few 100 Myr after the merger. These stars are metal-rich, and they remain in the central region because they form there. The consequence of these events is the metallicity gradient shown in Figure 23.

The story for the formation of the gradient in our merged sample is similar to the picture presented in White (1980). A steep gradient is produced in our simulation. The mixing of population between galaxies is incomplete but is efficient within each galaxy.

There may be an interesting relationship between the mechanism for the metallicity gradient formation and the observations of classical dwarf spheroidals (dSphs) in the Local Group with multiple stellar subcomponents (see, e.g., Tolstoy et al. (2004); Walker and Peñarrubia (2011)). Several dSphs show multiple stellar subcomponents with different metallicity within each system. In these galaxies, the metal-rich component is centrally concentrated, while the metal-poor component is more extended. Benítez-Llambay et al. (2016) study the formation of such multiple stellar components in classical dSphs using cosmological simulations. Tentative evidence for the anomalously broad stellar distribution and metallicity gradient in Tuc II may provide clues to the formation mechanism of such multiple stellar populations. Further observations will be important to determine which stars are present.

### 4.4.3 Long-time evolution of an early merged galaxy

We stop the simulation at 2.5 Gyr after the merger. After this, the simulated galaxy is absorbed by a larger galaxy by a merger. To make a comparison to UFDs such as Tuc II, we need to consider many processes that would affect the structures of the galaxies. Let us consider the possibility that a merged galaxy could end up falling into a massive halo like the Milky Way. We discuss (1) dynamical friction, (2) relaxation, and (3) tidal interactions with the host halo and other satellite galaxies.

The timescale for the dynamical friction for a UFD of mass  $M$ , that orbits in a host halo with the velocity dispersion of  $\sigma$  is:

$$t_{\text{fric}} = \frac{19 \text{ Gyr}}{\ln \Lambda} \left( \frac{r_i}{5 \text{ kpc}} \right)^2 \frac{\sigma}{200 \text{ km s}^{-1}} \frac{10^8 M_\odot}{M}, \quad (31)$$

where  $r_i$  and  $\ln \Lambda \simeq 6$  are the initial distance from the center and the Coulomb logarithm (Binney and Tremaine 2008). We obtain the initial radius  $r_i$  of  $\sim 10$  kpc that is affected by the dynamical friction within the cosmic age of 14 billion years. It means that a UFD would sink to the center if it falls within  $\sim 10$  kpc from the center. The low value indicates that the dynamical friction becomes significant only if a UFD comes very close to the center of the host galaxy.

For the two-body relaxation, we estimate the effect of a non-smooth gravitational field generated by member stars of the UFD. Assuming  $N = 10^4$ ,  $m = 1 M_\odot$ ,  $M = 10^8 M_\odot$ ,  $R = 0.1 R_{\text{vir}}$ ,  $\log \Lambda = 10$  is given by  $t_{\text{relax}} = (8N(Gm/R)^2 v^{-4} \log \Lambda)^{-1} t_{\text{cross}}$ , the two-body relaxation timescale is  $3 \times 10^{15}$  yr. This is longer than the age of the Universe, indicating that the relaxation is not efficient at modifying the stellar structure in a UFD.

Lastly, tidal interaction from the host halo may affect the stellar structure. More specifically, it may increase the half-light radius and invalidate our analysis. After the infall, a UFD is affected by the tidal field by the central galaxy. Some UFDs orbit very close to the center show evidence for past tidal disruption history. An example is Tucana III (not II!), with the estimated pericentric orbital radius of 3 kpc (Simon et al. 2017; Li et al. 2018). However, in the same estimate, the pericentric distance for Tuc II is 39 kpc. Another work estimates it to be 29 kpc (Fritz et al. 2018): the estimate depends on the mass estimate of the MW halo. In any case, the orbit for Tuc II is not very close to the center (Simon 2018). Peñarrubia et al. (2008) argue that the stellar component is more resilient to tidal effect compared to the dark matter halo because they are in smaller radii. Considering the fact that the dark matter component is still present in Tuc II, we expect that the tidal effect on stellar component has not been significant.

### 4.4.4 Chemical enrichment

Tuc II has one outlier in terms of chemical abundance, Tuc II-033 (Chiti et al. 2018). The star has very high Sr abundance, moderately high Ba abundance, and low  $\alpha$ -element abundances. The abundance pattern is typical for stars affected by delayed contributions from AGB stars and type-Ia SNe.

Our numerical experiments have shown that a major merger can reproduce a UFD with an extended stellar profile, that is comparable to the one observed in Tuc II. Star formation

in an isolated UFD would be quenched by the cosmic reionization. However, if galaxy merger happens, gas could be supplied by the infalling galaxy, which allow further star formation. Stars formed during the merger have higher metallicity and also higher  $s$ -process elements (Tarumi et al. 2020a). The  $s$ -process enrichment by AGB stars can be traced with Ba abundances. The abundance of Tuc II-033 can be explained by the AGB contribution if the Ba yield in AGB stars was higher by  $\sim 0.5$  dex. We have already shown that a stellar population with an overall higher Ba abundance exist in L-UFD, which are formed after the merger.

The chemical abundances of Tuc II seems to be affected by its early merger. However, other possibilities for the neutron-capture elements exist. In particular, the high Sr abundance of Tuc II-033 cannot be easily explained only by the AGB contribution. Additional Sr sources such as electron-capture supernovae (Wanajo et al. 2018) may be required.

We conclude that, assuming that Tuc II-033 is truly a member star, Tuc II is a remnant galaxy of wet major merger. Additional measurements of neutron-capture element for all other Tuc II stars, especially in large distances, would help further clarify the formation and evolution history of chemical abundances as well as Tuc II itself.

#### 4.4.5 Galactic building blocks

UFDs are considered to be surviving early galaxies that serves as the building-blocks for large galaxies, given their low metallicities and old ages (Frebel and Bromm 2012; Simon 2019). The extended halo of Tuc II, and the fact that the overall structure of Tuc II can be explained by a past merger of primordial low-metallicity galaxies, casts doubt on Tuc II and other UFDs as surviving building blocks. However, the simulations suggest that the detailed structure of the UFD provides information about past merger events and the type of primitive ancestors that formed the UFD. Future exploration of extended structures around other UFDs is warranted.

The mass of our merged galaxy sample is  $2.5 \times 10^8 M_{\odot}$ . Considering the fact that the current mass of Tuc II is  $10^7 M_{\odot}$  at 1 kpc from the center (Chiti et al. (2021)), Tuc II may have been more massive in the past. It seems suggestive that our numerical experiments show that even UFD-sized galaxy could have experienced mergers in the past.

#### 4.4.6 On the fraction of galaxies with extended stellar profiles from early merger

We have seen that the remnant of a major merger of two primordial galaxies could result in a UFD with an extended stellar profile. To estimate the occurrence rate of such galaxy mergers, we have conducted a set of numerical experiments. We simulate the formation of 15 galaxy samples, and we find only one system that undergo a major merger. Thus, we give a rough estimate of the fraction of such an extended stellar halo to be  $\sim 10\%$ , although the fraction should be taken as a lower limit. The fraction might be higher in an over-density regions such as MW halo. Also, the fact that we only simulate up to  $z = 4$  may lower the fraction of mergers. Some of our simulated galaxies might develop an extended stellar structure via the late-time mergers.

Galaxy formation simulations with a larger volume would help answer the question on the merger rate quantitatively. It needs to resolve star formation in each galaxy. The fraction

of such early merger galaxies is an important quantity to compare with observations.

## 4.5 Summary and Conclusion

We have conducted a set of numerical experiments of galaxy formation for primordial galaxies in the history of the Universe. We have investigated a major merger of two first galaxies. The merger dynamically heats the system, induces starburst, and, forms an extended stellar distribution as a consequence. The radial stellar density profile of the remnant galaxy is similar to a de Vaucouleur profile, whereas that for non-merger galaxies have exponential profiles. Our simulations reproduce the observed extended profile and the metallicity gradient of the UFD Tuc II.

We propose that future observations to search for extended profiles around existing UFDs will allow us to probe the formation history of these systems in the early Universe. If an observed UFD has a centrally concentrated profile such as an exponential function, the galaxy did not experience any significant mergers in the past. We can regard such galaxies as candidates for surviving first galaxies (Frebel and Bromm 2012). On the contrary, if a UFD has an extended profile like the de Vaucouleur profile, the galaxy may have experienced a (wet) major merger in the past, as likely the case for Tuc II.

Theoretical studies on the effects of tidal heating and other processes after falling into the host halo would help uncover the evolution processes of extended galaxies. Exploration into the variation among UFDs would also be interesting. The population will help us better understand the formation of early galaxies in a cosmological context. More generally, such studies will be a stepping stone for uncovering the evolution history of our Milky Way.

## 5 *R*-process elements in the Milky-Way

The MW is a large galaxy. Therefore, it represents the statistical properties of the source, such as the delay time distribution. Previous works that focus on the chemical evolution of the MW investigate metal-rich regimes. This work studies the metal-poor regime, where a thorough study is lacking. Timescale for metal-poor systems is short. Therefore, we expect that it is sensitive to shorter delay time.

### 5.1 Enrichment of *r*-process elements in our galaxy

Kilonova observations that associates the the gravitational event GW170817 have provided evidence that a large amount of *r*-process elements are synthesized in NSM (Margutti and Chornock 2020 for a review). The estimated merger rates and masses of *r*-process elements synthesized are in very good agreement with those independently estimated from the *r*-process element abundances of stars in the Milky Way and UFDs (Ji et al. 2016a; Beniamini et al. 2016a; Côté et al. 2018; Hotokezaka et al. 2018), as well as from geological measurements of radioisotopes (see, e.g., Hotokezaka et al. 2015).

A potential problem for the NSM scenario as the origin of *r*-process elements is the time delay between the formation of the progenitor star and coalescence. Chemical evolution models with a delay time distribution of  $\propto \Delta t^{-1}$  cannot explain the distribution of Eu abundances in stars at disk metallicity  $[\text{Fe}/\text{H}] \gtrsim -1$  (Côté et al. 2019). Although several effects have been considered to solve this problem (e.g., including natal kick on a neutron star, steep delay time distributions, and turbulent diffusion (Wehmeyer et al. 2015; Simonetti et al. 2019; Tsujimoto and Baba 2019; Banerjee et al. 2020b; Dvorkin et al. 2020)), no satisfactory solution has been provided. The lack of evidence for the time delay seen in the chemical abundances is the main argument supporting other scenarios including magneto-rotating supernovae (MRSNe, Nishimura et al. 2015; 2017), collapsars (Siegel et al. 2019), peculiar magnetar formation (Metzger et al. 2008; Thompson and ud-Doula 2018), and common envelope jet supernovae (Grichener and Soker 2019). These events have no delay from the formation of the progenitor stars as they are associated with the death of massive stars.

A crucial question regarding the origin of the *r*-process elements is: is there any observational evidence for a delay between star formation and nucleosynthesis? Or, do *r*-process elements synthesized preferentially in the early universe? Elemental abundance ratios and the overall metallicities allow us to probe the history of metal enrichment of a galaxy. A useful plot is the  $[r/\text{Mg}] - [\text{Fe}/\text{H}]$  plot. The aim of this work is to infer the time delay of *r*-process element production in a model-independent manner and to determine the origin of the *r*-process elements.

Previous works include Ishimaru et al. (2004), who used three stars with low Eu abundance in  $[\text{Fe}/\text{H}] \sim -3$  and found that the most massive stars are excluded from the candidates for the origin of the *r*-process elements. However, this measurement would be consistent if *r*-process events were sufficiently rare because the chemical enrichment could be retarded by diffusion processes. Here we use a larger sample of Ba abundances from stars with very low metal abundances ( $[\text{Fe}/\text{H}] < -2$ ). The larger sample size would allow us to distinguish the intrinsic time delay in *r*-process from the delay of diffusion origin. Section 5.2 briefly describes the astrophysical scenarios suggested in the literature. in Section 5.3, we present

the observations and discuss their trends. In Section 5.4, we discuss the implications for the origin of  $r$ -processes in the Universe.

## 5.2 Possible candidates for the $r$ -process elements and their delay times

We classify the origin of  $r$ -process elements into three categories in terms of the time delay between SFR of a galaxy and the  $r$ -process element synthesis. These include (i) a delayed scenario (NSM model), (ii) a no-delay scenario (Rare SN model), and (iii) a “negative” delay scenario (Collapsar model: the meaning of the “negative” delay is discussed below). Any astrophysical scenarios fall into one of these categories.  $\alpha$ -elements (including Mg) are assumed to be predominantly produced in normal CCSNe (without delay). We also assume that the rate of  $r$ -process events are low, about 1/1000 of CCSN rate. We discuss these scenarios in turn.

### 5.2.1 The delayed scenario (neutron star merger model)

A NSM delays from the formation of the progenitor star due to the long coalescence time. Indeed, the only confirmed NSM (GW170817) occurs in a galaxy with little star formation activity, which suggests a long delay of  $\sim 1$ –10 Gyr for the event (Blanchard et al. 2017; Levan et al. 2017). Theoretical predictions for the NSM delay time has a wide distribution from  $\sim 10$  Myr to longer than the age of the Universe. The distribution of the delay time is described by a function  $DTD$  (delay-time distribution):

$$\dot{N}_r(t) \propto \int_0^t dt' DTD(\Delta t) SFR(t'), \quad (32)$$

where  $\dot{N}_r$  is the rate of  $r$ -process events,  $\Delta t = t - t'$  is the time between the merger and the formation of binary neutron stars (BNS), and  $SFR$  is the star formation rate of the galaxy. The functional form of  $DTD$  is  $\propto \Delta t^{-1}$ , with minimum delay  $\Delta t_{\min}$  as another parameter. Beniamini and Piran (2019) find that a steeper power law of  $DTD \propto \Delta t^{-1.3}$  with  $\Delta t_{\min} \sim 35$  Myr is favored from the orbital spacing of the Galactic BNS. Wanderman and Piran (2015) find that  $DTD \propto \Delta t^{-1}$  with  $\Delta t_{\min} \approx 20$  Myr explains the redshift distribution of short gamma-ray bursts (GRBs) well.

### 5.2.2 No-delay scenario (rare supernova model)

Peculiar SNe such as MRSNe have been proposed as the candidate for the origin of heavy  $r$ -process elements (Nishimura et al. 2015). We here assume that the ratio of such SNe to usual CCSNe is constant in time, as it is not constrained by the observations. With this assumption, we obtain a production rate proportional to that of  $\alpha$  elements, i.e.,  $\dot{N}_r(t) \propto SFR(t)$ .

### 5.2.3 A "negative" delay scenario (collapsar model)

Recently, [Siegel et al. \(2019\)](#) propose that the central engine of a long GRB, i.e., the massive outflow from a collapsar, may synthesize a copious amount of  $r$ -process elements.<sup>3</sup> We classify the collapsar model to a negative delay scenario. The "negative" delay is counterintuitive (it occurs after birth, of course, not before). We use this in an averaged sense: the rate for the long-GRBs are higher in galaxies with large specific SFRs and low metallicity ([Svensson et al. 2010](#); [Palmerio et al. 2019](#)). The redshift distribution of long GRBs clearly demonstrates the trend: it peaks at higher redshifts than the SFR of the universe ([Wanderman and Piran 2010](#)). We therefore assume that the ratio of  $r$ -process events to CCSNe decreases with time:

$$\dot{N}_r(t) \propto A(t)SFR(t), \quad (33)$$

where  $A(t)$  is a decreasing function that accounts for the fact that the collapsar event rate is higher at earlier times. We assume  $A(t) \propto t^{-0.5}$  to mimic the redshift distribution of long GRBs and the SFR of the Universe at  $z \lesssim 3$  ([Wanderman and Piran 2010](#)). Note that the rate for long GRB is not constrained in the early universe. We here clarify that the "negative" delay scenario is not limited to collapsars, but can be applied to other objects that peak at higher redshift than the Cosmic star formation rate.

## 5.3 $R$ -process delay inferred from very metal-poor stars

Chemical abundances of metal-poor stars is a crucial tracer for the  $r$ -process history. Europium (Eu) is the most commonly used tracer because the contribution from the  $s$ -process is minor, and it has relatively strong lines. However, if we are to measure very small amounts of Eu, their lines are not sufficiently strong. Barium (Ba) is another element synthesized in  $r$ -process. Although the  $s$ -process contribution is significant for solar metallicity stars, the delay of  $s$ -process is significant. Ba has been used as the tracer for the  $r$ -process ([François et al. 2007](#); [Duggan et al. 2018](#)). Here we study the variation in the abundance of Ba in the low metallicity region ( $-4 \lesssim [\text{Fe}/\text{H}] \lesssim -2$ ). At this metallicity region the  $r$ -process contribution dominates over that of the  $s$ -process. Figure 24 shows the ratio of  $[\text{Eu}/\text{Ba}]$  for Milky-Way metal-poor stars. The  $r$ -process ratio is 0.7, and ratio close to this value suggests that Ba is synthesized dominantly by the  $r$ -process. The contribution of the  $s$ -process becomes significant at  $[\text{Fe}/\text{H}] \gtrsim -2.0$  and gradually gets more important. Stars with the lower metallicity have  $[\text{Eu}/\text{Ba}]$  values consistent with the  $r$ -process.<sup>4</sup>

Figure 25 is a schematic diagram showing the evolution of  $[\text{Ba}/\text{Mg}]$  against  $[\text{Fe}/\text{H}]$ . The ISM in a galaxy is initially metal-poor, and stars formed out of these are plotted on the left. For these stars, the number of  $r$ -process enrichment event is small. [Beniamini and Hotokezaka \(2020\)](#) point out that the chemical inhomogeneity of the ISM crucially affect the  $r$ -process abundances in the ISM at a given location, if it originate from a single enrichment event. The volume fraction of the highly enriched ISM is so small that a typical star (outside the enriched region) will have a very low  $[\text{Ba}/\text{Mg}]$ . This inhomogeneous effect disappears as soon as the

<sup>3</sup>The  $r$ -process synthesis in collapsars is still under debate ([Fujibayashi et al. 2020](#)).

<sup>4</sup>We have excluded the  $s$ -enhanced carbon-enhanced metal-poor (CEMP- $s$ ) stars. These stars are enriched by mass-transfer from companion stars. They do not represent the abundances of the natal cloud and therefore the abundance evolution of the galaxy.

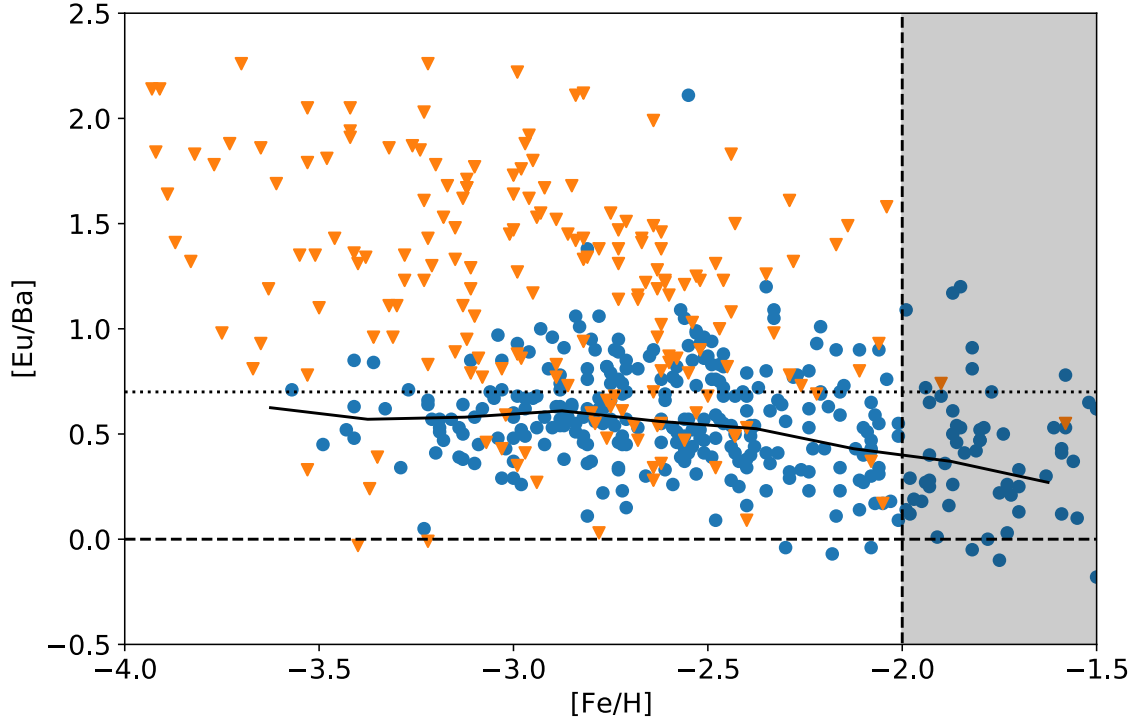


Figure 24: The evolution of  $[\text{Eu}/\text{Ba}]$  for very metal-poor stars. Measurements are plotted with blue and upper limits are in orange triangles. The dotted horizontal line shows the production ratio in the  $r$ -process ( $[\text{Eu}/\text{Ba}] = 0.7$ ; [Snedden et al. 2008](#)). Carbon-rich stars ( $[\text{C}/\text{Fe}] > 0.5$ ) are omitted because they are likely affected by binary mass transfer. For  $[\text{Fe}/\text{H}] < -2$  stars, the deviation of  $[\text{Eu}/\text{Ba}]$  from the  $r$ -process ratio is only  $\sim 0.2$  dex, which suggest that the  $s$ -process contribution for the production of Ba is not dominant.

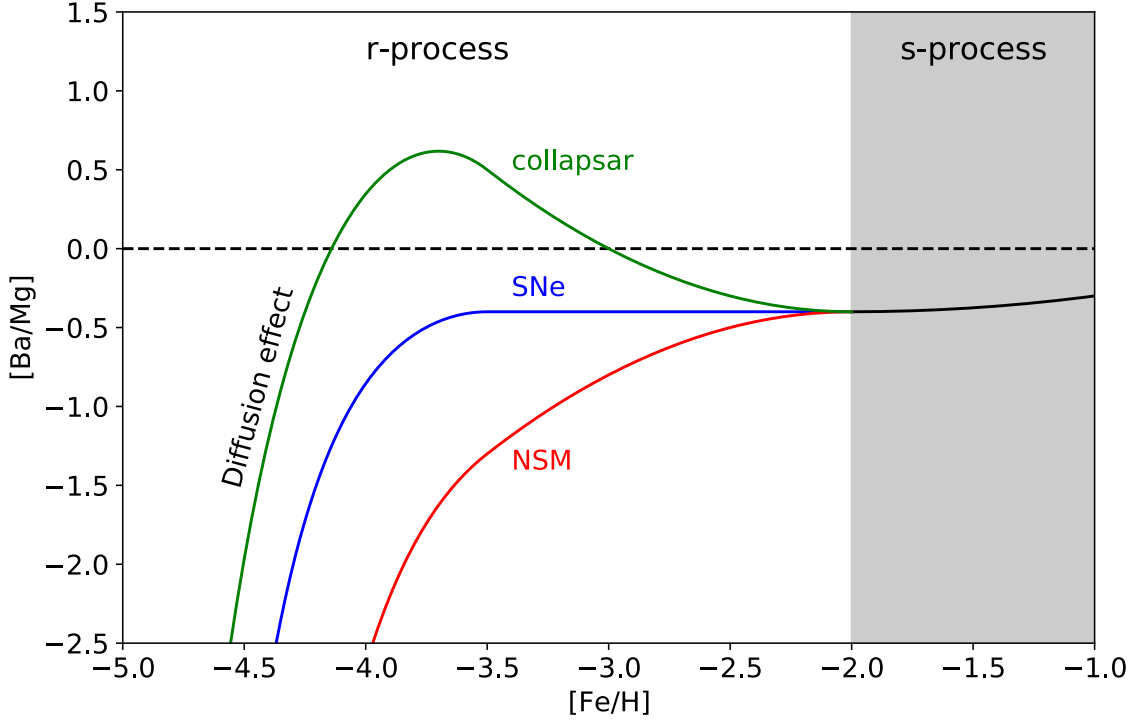


Figure 25: The model evolution of barium abundances  $[\text{Ba}/\text{Mg}]$  against  $[\text{Fe}/\text{H}]$  in the three delay time distribution scenario. For all of these, we expect a sharp increase  $[\text{Ba}/\text{Mg}]$  at the metal-poorest regime as a consequence of the inhomogeneous diffusion. The time duration when the inhomogeneity is significant is shorter than the mixing time: it is significant only when the Ba enrichment is dominated by one event at a given location. At the metallicity of  $-3.5 \lesssim [\text{Fe}/\text{H}] \lesssim -2.0$ , the inhomogeneity effect is already diminished and the  $[\text{Ba}/\text{Mg}]$  trend represents the true time delay of  $r$ -process nucleosynthesis. At higher metallicity ( $-2.0 \lesssim [\text{Fe}/\text{H}]$ ),  $s$ -process contribution becomes significant.

number of events contributing to the enrichment increases, and the [Ba/Mg] track converges to represent the intrinsic delay in  $r$ -process events. In  $[\text{Fe}/\text{H}] \gtrsim -2$ , the contribution of the  $s$ -process becomes significant. We discuss very metal-poor stars in  $[\text{Fe}/\text{H}] \lesssim -2$  because we are interested in studying the enrichment of the  $r$ -process.

Figure 26 compares the results of our numerical experiments with the observed metal-poor stars. Two curves, the “linear mean” and the “median”, are plotted on top of each other, to discuss quantitatively. The linear mean  $\mu(\text{Ba}/\text{Mg})$  is defined as:

$$\mu(\text{Ba}/\text{Mg}) = \frac{1}{N_{\text{star}}} \sum_i^{N_{\text{star}}} 10^{[\text{Ba}/\text{Mg}]_i}, \quad (34)$$

where  $i$  runs from 1 to the total number of stars in each  $[\text{Fe}/\text{H}]$  bin. Stars with only upper limits on Ba abundances are ignored. Ba has a very strong line feature and there are not many stars only with upper limits. Assuming  $[\text{Ba}/\text{Mg}] = -10$  for all upper limit stars changes the curve very little.

We must be careful when we interpret the increasing trend of  $[\text{Ba}/\text{Mg}]$  with  $[\text{Fe}/\text{H}]$ . Time delay certainly induces the increasing trend as in Figure 25. However, another possibility exists: the median of the abundances of a rare event could show a pseudo-increase in the trend because of the inhomogeneity. This is a consequence of a long tail on the high concentration side: if we look at the abundance distribution shortly after the deposition of  $r$ -process elements, very small amount of matter are highly enriched, however unlikely to be included in the stellar abundances. Such distorted abundance distributions occur naturally in the concentration of elements in the ISM. If we measure the abundance distribution of  $r$ -process elements in the ISM before complete mixing, the median value is lower than the “one zone” prediction, which assumes instantaneous mixing.

On the other hand, the linear mean  $\mu([\text{Ba}/\text{Mg}])$  is robust to the inhomogeneity effect. Appropriate weights are given to both  $r$ -rich and  $r$ -poor gases. By comparing median to the observations, deviations occur and the importance of the  $r$ -poor gas, which is dominant in volume, is overestimated. If the Mg and Fe distributions are assumed to be uniform and the entire system is sampled with sufficient resolution, the linear mean exactly matches the one-zone model using the instantaneous mixing approximation. We therefore conclude that the increase in the linear mean  $\mu([\text{Ba}/\text{Mg}])$  is the result of a time delay between the production of Mg and  $r$ -process elements. The remaining question is the validity of the assumptions. That is, (i) the denominator (Mg) and x-axis (Fe) must be homogeneous, and (ii) the volume sampling must be sufficient. If these conditions fail, the linear mean would deviate symmetrically from the one-zone calculation. Therefore, we argue that the inhomogeneous effect alone would give a clear increasing trend seen in observations.

An independent argument is the gradual increase in the median value of  $[\text{Ba}/\text{Mg}]$ . As explained above, the median can tend to increase due to inhomogeneity effects. However, the increase is very rapid in this case, since it occurs exponentially. The range of typical  $[\text{Fe}/\text{H}]$  increases can be estimated by the volume fraction of the  $r$ -rich bubble. Here, assuming a one-zone value  $[\text{Ba}/\text{Mg}]_{1\text{zone}}$  of  $\sim -0.5$ , we estimate the metallicity range ( $\Delta[\text{Fe}/\text{H}]$ ) from  $[\text{Ba}/\text{Mg}] \sim -2.0$  to  $[\text{Ba}/\text{Mg}] \sim -0.5$ .  $r$ -rich bubble ( $1\sigma$  region) volume is  $\sim \sigma^3$ . The median value of  $[\text{Ba}/\text{Mg}]$  converges to the one-zone value when the volume fraction is  $\sim 1$ .

The volume of each bubble increases as  $\propto t^{3/2}$ , and the number of bubbles as  $t^{\alpha+1}$ . Here,

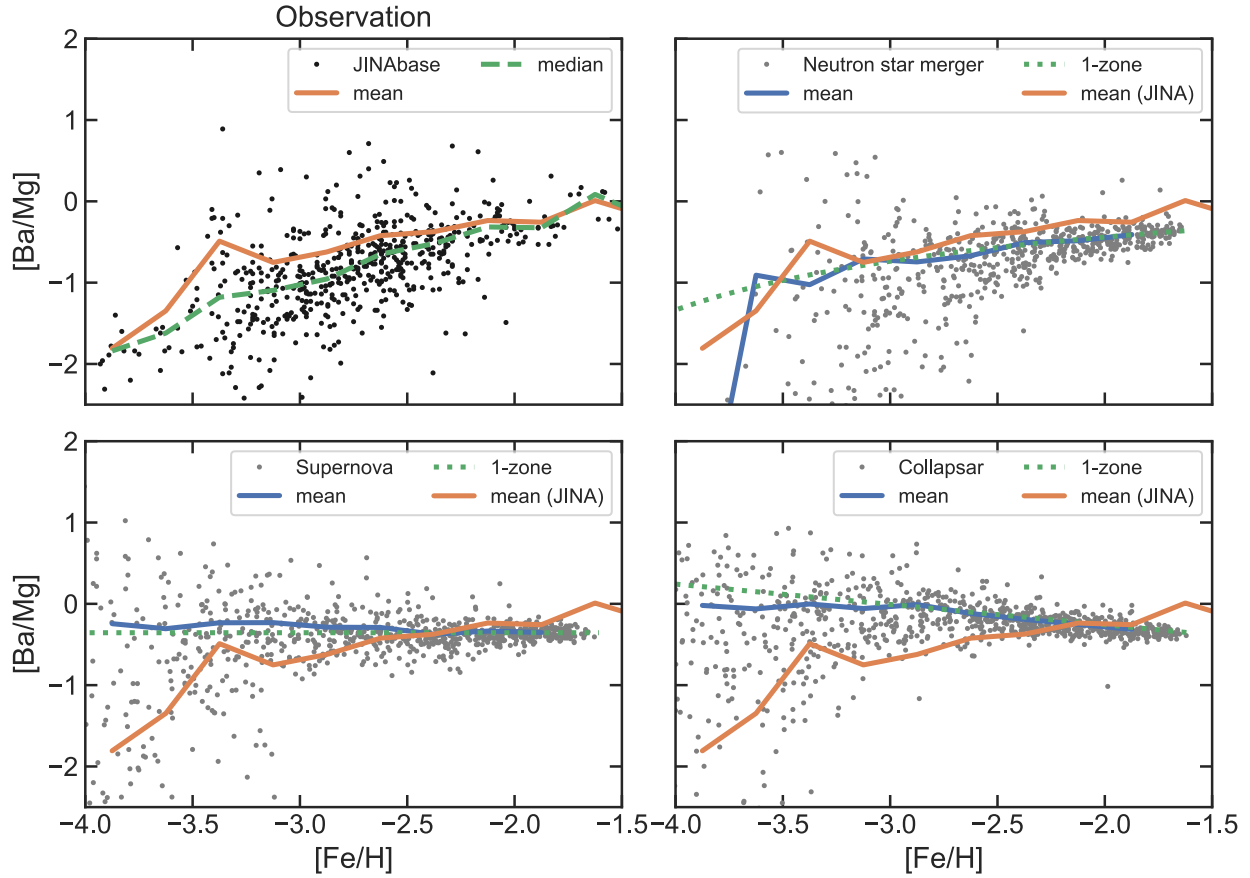


Figure 26:  $[\text{Ba}/\text{Mg}] - [\text{Fe}/\text{H}]$  plots for the observations of Milky Way stars and our model results. Upper left panel shows the observations. The abundance data is taken from JINAbase (Abohalima and Frebel 2018). Carbon-rich stars ( $[\text{C}/\text{Fe}] > 0.5$ ) are eliminated. The other panels show results for our model. We plot the synthetic observations for each model. Upper right panel shows the results from the positive delay model. The no-delay model is shown in the bottom left panel. Bottom right panel shows the negative delay model results. The SFR is assumed to be  $\propto t^\alpha$ , where we take  $\alpha = 1$  for all models. For the positive delay model, we use the power law function  $DTD \propto t^{-1}$  and the minimum delay time is taken at 20 Myr, having NSM in mind. In the no delay model, the  $r$ -process enrichment occurs without delay. In the negative delay model, we assume that the distribution of the  $r$ -process enrichment is proportional to  $SFR(t) \times t^{-0.5}$  so that  $r$ -process enrichment occurs preferentially at the early times. We assume that the diffusion coefficient  $D$  is  $D = 0.2\text{kpc}^2/\text{Gyr}$  in all models. The curve labeled “1-zone” represents the results of 1-zone modeling, i.e., assuming instantaneous mixing,  $D \rightarrow \infty$ .

(*SFR density*)  $\propto t^\alpha$  is assumed. Thus, the total volume fraction  $V_{\text{tot},1\sigma}$  grows as  $\propto t^{\alpha+5/2}$ . Since the Fe abundance is proportional to the number density of stars,  $[\text{Fe}/\text{H}]$  increases logarithmically. Therefore,  $[\text{Fe}/\text{H}] \sim (1 + \alpha) \log_{10}(t) + \text{const}$ . The value of  $[\text{Fe}/\text{H}]$  at the time of  $[\text{Ba}/\text{Mg}]$  one-zone convergence is

$$[\text{Fe}/\text{H}] \approx \log_{10}(V_{\text{tot},1\sigma}) \cdot \frac{(\alpha + 1)}{(\alpha + 5/2)} + \text{const}. \quad (35)$$

$[\text{Fe}/\text{H}]$  when the median value of  $[\text{Ba}/\text{Mg}]$  passes through  $[\text{Ba}/\text{Mg}]_{1\text{zone}} - 1.5$  can be derived by the same procedure, substituting  $V_{\text{tot},3\sigma} = 3^3 \cdot V_{\text{tot},1\sigma}$  for  $V_{\text{tot},1\sigma}$ <sup>5</sup>. Finally,  $\Delta[\text{Fe}/\text{H}]$  can be derived as  $\Delta[\text{Fe}/\text{H}] \approx \log_{10}(3^3) \cdot (\alpha + 1)/(\alpha + 5/2)$ . This gives  $0.56 \lesssim \Delta[\text{Fe}/\text{H}] < 1.4$  for  $\alpha > 0$ . However, the observed data show a slower increase of  $\Delta[\text{Fe}/\text{H}] \sim 2.0$ , which cannot be reproduced by diffusion.

Here we present the results of a Monte Carlo numerical experiment of the chemical enrichment of the Milky Way in the early stages of its evolution ( $\lesssim 1$  Gyr). Note that this model is easily generalizable to model the chemical evolution of other galaxies by modifying the function of the star formation history. Outflow from galaxies (Emerick et al. 2018) is not considered in our model, although we believe this is not a crucial problem. Figure 26 shows results from our model. We prepare a  $\text{kpc}^3$  box initially filled with hydrogen at a density  $\approx 20 \text{ cm}^{-3}$ , where the SFR is  $SFR \propto t^\alpha$  and normalized so that the average CCSN rate is  $10^3 \text{ Myr}^{-1} \text{ kpc}^{-3}$ . Fe and Mg are randomly injected into space at a rate proportional to the SFR.

Fe and Mg production from each CCSN is assumed to be  $m_{\text{Fe}} = 0.04 M_\odot$  (e.g. Nakar et al. 2016) and  $m_{\text{Mg}} = 0.05 M_\odot$ , and each  $r$ -process event produces  $m_{\text{Ba}} = 3 \cdot 10^{-4} M_\odot$ . the overall fraction of  $r$ -process events is fixed at 1/1000 of the CCSNe rate (Beniamini et al. 2016a; Hotokezaka et al. 2018).

The number density of an element  $X$  at position  $\vec{r}$  at time  $t$  can be written as:

$$n_X(\vec{r}, t) = \sum_{t_j < t - t_*} \frac{N_X}{K_j(\Delta t_j)} \exp\left[-\frac{|\vec{r} - \vec{r}_j|^2}{4D\Delta t_j}\right] \quad (36)$$

where  $N_X$  is the total number of element  $X$  produced in each event,  $t_j, \vec{r}_j$  are time and spatial location of the  $j$ -th event,  $\Delta t_j = t - t_j$ ,  $K_j(\Delta t_j) = (4\pi D \Delta t_j)^{3/2}$ , and  $D$  is the diffusion coefficient<sup>6</sup>. Following Beniamini and Hotokezaka (2020), the simulation is performed with  $D$  set to  $0.2 \text{ kpc}^2/\text{Gyr}$ . We track stars formed at random locations within the box. The abundance of the star is given by the abundance of the ISM at its birth location and birth time.

Figure 26 shows the synthetic data obtained with our model. The abundance trends are also shown, with a one-zone model and the linear averages computed with the same procedure (Equation 34) as for the real data. As we have expected, the linear mean converges to the

<sup>5</sup>Assuming the concentration follows a Gaussian distribution,  $10^{-1.5} \times e^{-0.5} \simeq e^{-3.95} = e^{-7.9/2}$ . Therefore, the size of the region with  $[\text{Ba}/\text{Mg}]$  value higher than  $[\text{Ba}/\text{Mg}]_{1\text{zone}} - 1.5$  is the  $3\sigma$  region because  $\sqrt{7.9\sigma} \simeq 3\sigma$ . The volume of a  $3\sigma$  region is 27 times that of the  $1\sigma$  region. The total volume fraction of the  $3\sigma$  regions becomes 1 when that of  $1\sigma$  regions is  $1/3^3$ .

<sup>6</sup>When  $K_j$  gets as large as the boxsize, we fix  $K_j$  in order to avoid an artificial leakage of the elements (Beniamini and Hotokezaka 2020).

one-zone results for all models; the no-delay and negative delay models overproduce Ba-rich stars with  $[\text{Ba}/\text{Mg}] > 0$  compared to the observations.  $S$ -process contribution would not solve the inconsistency. Furthermore, the ratio  $[\text{Ba}/\text{Mg}]$  converges to the one-zone line within about 0.5 dex of  $[\text{Fe}/\text{H}]$ . Thus, the gradual increase in the observations of  $[\text{Ba}/\text{Mg}]$  can be attributed to the gradual production of  $r$ -process elements compared to the formation of Mg, i.e., the delay of  $r$ -process events from CCSNe. We also perform simulations with  $DTD \propto \Delta t^{-1.3}$  as proposed by [Beniamini and Piran \(2019\)](#) and obtained similar results. Finally, we also examined  $[\text{Eu}/\text{Mg}]$  in Figure 29. The plot of stars with Eu detection do not show a clear increasing trend in  $[\text{Eu}/\text{Mg}]$  as opposed to  $[\text{Ba}/\text{Mg}]$ . However, this is natural because the data would be biased toward Eu-rich stars. The result is fully consistent if we also include stars with upper limits on Eu.

Figure 27 shows the distribution of  $[\text{Ba}/\text{Mg}]$  ratio for stars in classical dwarf galaxies. A similar increasing relation between  $[\text{Ba}/\text{Mg}] - [\text{Fe}/\text{H}]$  is established also in dwarf galaxies, despite the possible difference in the star formation timescale, although the number of data points is small. Such similarity is expected to occur when (1)  $\alpha$ , the time dependence of SFH is similar, (2) the DTD of  $\propto \Delta t^{-1}$  is a good approximation, (3)  $t_{\text{min}}$  is shorter than the chemical enrichment timescale of the galaxy to  $[\text{Fe}/\text{H}] \sim -3$ , and (4) contributions of the  $s$ -process and type-Ia SNe are not significant. Thus, the fact that a similar trend is established supports the conclusion of a delay in the  $r$ -process, and also suggests that a scenario with a constant delay time is unlikely. Here we ignored the uncertainty in the outflow, which is expected to be significantly different between galaxies, and can have a large impact on the chemical abundances [Emerick et al. \(2018\)](#). We stress that the trend is robust even without accounting for this effect. Note that we omit UFDs here because of the discretization of the  $r$ -process events ([Beniamini et al. 2016a](#)). The distribution of  $r$ -process abundances do not represent the delay of population, but is dominated by the timing of one event ([Safarzadeh and Scannapieco 2017b](#); [Beniamini et al. 2018](#); [Tarumi et al. 2020c](#)).

## 5.4 Conclusions and discussions

Observations of Ba abundances in metal-poor stars in our Galaxy reveal that  $[\text{Ba}/\text{Mg}]$  increases significantly with increasing  $[\text{Fe}/\text{H}]$  at  $[\text{Fe}/\text{H}] < -2.0$ . This increase likely represents the intrinsic delay of  $r$ -process events. The increase in linear mean and the gradual increase in median values cannot be explained solely by a delay due to diffusion, and they reveal that the formation of  $r$ -process elements requires an intrinsic time delay. Therefore, we conclude that there is a significant delay in the formation of  $r$ -process elements in this metal abundance region, which is naturally expected in the NSM scenario (Figure 26 and see also, e.g., [Côté et al. 2019](#)).  $R$ -process synthesis in the other candidates such as MRSNe and collapsars do not delay from the formation of the progenitor stars. Consequently, even ignoring the contribution of the  $s$ -process, we find that Ba is overproduced at low metallicity. We therefore regard such sources as incompatible with the trend in observations. We stress that this is new evidence in favor of NSM being the source of the  $r$ -process elements, at least in the low metallicity environment  $[\text{Fe}/\text{H}] \lesssim -2$ . A similar analysis for Eu using only the detected samples would show noisy behavior (see Section 5.6)). By including the upper limit as a zero-abundance, traces of the increasing trend can be seen, as with Ba.

The  $[\text{Ba}/\text{Mg}]$  ratio of very low metallicity stars in classical dwarf galaxies also support the

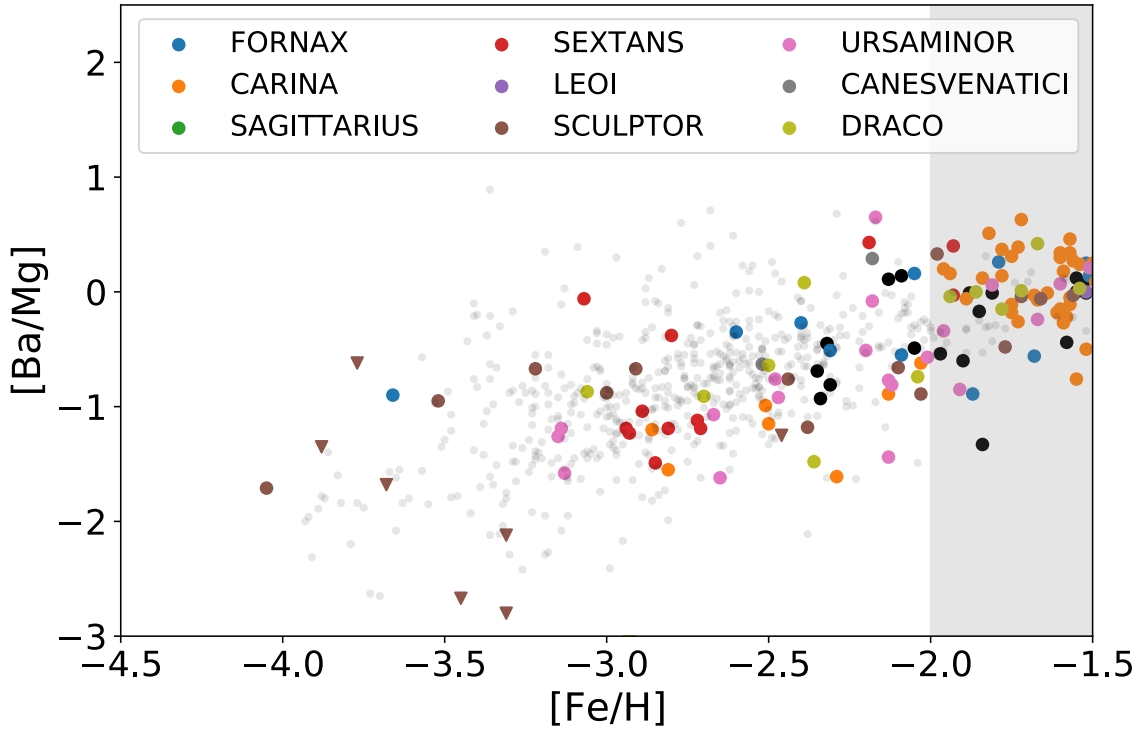


Figure 27: The abundances of Ba and Fe for classical dwarf galaxies. The Ba abundance is normalized by Mg abundance. Detections and upper limits are shown with circles triangles. The data is obtained from the SAGA database (Suda et al. 2017). The gray dots in the background are stars in the MW, and the black dots are mean abundances of globular clusters in MW halo (Pritzl et al. 2005). The dwarf galaxies are on the same track of the Milky Way stars, supporting the interpretation that the gradual rise of  $[Ba/Mg]$  is caused by the intrinsic delay of  $r$ -process events.

presence of significant time delay. Although the sample size is small and the dwarf galaxies might have different star formation histories, most stars follow the same trend as stars in the Milky Way (Figure 27, see also Reichert et al. 2020). Therefore, this “delay” is likely a common feature and can be verified in a larger sample of dwarf galaxies with Ba abundances.

Note that Ba is detected in most metal-poor stars, as noted by Roederer (2013). Such a “floor” of Ba abundances may suggest that we may need additional neutron capture process that is working. The existence of such an event is also supported by the Ba abundance in the UFD (Section 3). In this case, the increasing trend in  $[r/\text{Mg}]$  may actually be steeper than obtained by the Ba observations. However, our argument on the increase of the mean is still valid, and stars with such extremely low Ba content do not affect the resulting linear mean of  $[\text{Ba}/\text{Mg}]$ .

Metal-poor stars may have originally formed in disrupted dwarf galaxies. Our argument remains the same even in that case. As Figure 27 illustrates, each dwarf galaxy shows the secular evolution of abundances. The ubiquitous increasing trend in dwarf galaxies can be explained by a time delay in the enrichment of the  $r$ -process.

Some GCs including M15 exhibit internal abundance spread of  $r$ -process elements. The short star formation duration makes it difficult for delayed sources to enrich the star-forming cloud. However, given the small metallicity spread within each GC, the difficulty is shared by all the candidates. One possible solution is the spreading of Eu in the ISM; the formation process of GCs is not well understood and it would be interesting to investigate the origin of such  $r$ -process spreading. I will investigate this possibility in Section 6.

Surveys of disk stars (e.g. Buder et al. 2021) show  $[\text{Eu}/\text{Mg}] \sim 0$  at high metallicity, supporting short or no time delays for  $r$ -process events. The timescale for  $[\text{Fe}/\text{H}]$  evolution is different from low metallicity: at relatively high metal abundances of  $[\text{Fe}/\text{H}] \gtrsim -1$ , the ratio of  $[\text{Eu}/\text{Mg}] \sim 0$  is confirmed. It suggests that the delay should be shorter than 1–10 Gyr. Similar features were found in Sculptor dwarf galaxy, where Skúladóttir et al. (2019) find  $[\text{Eu}/\text{Mg}] \sim 0$ . They also show an increase of  $[\text{Ba}/\text{Mg}]$ , providing clear evidence of a delayed contribution from AGB stars. Recently, Matsuno et al. (2021) studied  $r$ -process enrichment in Gaia-Enceladus stars. They find that the  $r$ -process abundance normalized by the  $\alpha$  elements is significantly overabundant with  $[\text{Eu}/\text{Mg}] \sim 0.3$  and the  $[\text{Eu}/\text{Mg}]$  ratio does not evolve with metallicity. The  $r$ -process delay is observed at  $[\text{Fe}/\text{H}] \lesssim -2$  but not at  $[\text{Fe}/\text{H}] \gtrsim -1$  may suggest that the time delay of the  $r$ -process events is typically on the order of several hundred Myr. The value is consistent with the estimate from Galactic BNS population (Beniamini and Piran 2019).

The typical delay times of NSMs are comparable to or longer than those of AGB stars. The seemingly larger delay of AGB stars is likely due to the metallicity dependence of the  $s$ -process. At the lowest metallicity of  $[\text{Fe}/\text{H}] \lesssim -2$ , the  $s$ -process yield is suppressed due to the scarcity of seed nuclei for  $s$ -process nucleosynthesis. Therefore, we naturally expect that the AGB star contribution comes later than the  $r$ -process in the NSM, which is also consistent with observations.

As noted in Section 5.1, it has recently been suggested that the BNS natal kick plays an important role in shaping the abundance distribution of the  $r$ -process (Banerjee et al. 2020b). For this to be the case, a typical center-of-mass kick of  $\Delta v_{\text{cm}} \gtrsim 100 \text{ km s}^{-1}$  is required. However, Beniamini and Piran (2016) find that the kicks imparted to the BNS is rather weak. The kinetics of the Galactic BNS favors  $\Delta v_{\text{cm}} < 10 \text{ km s}^{-1}$  and also that the

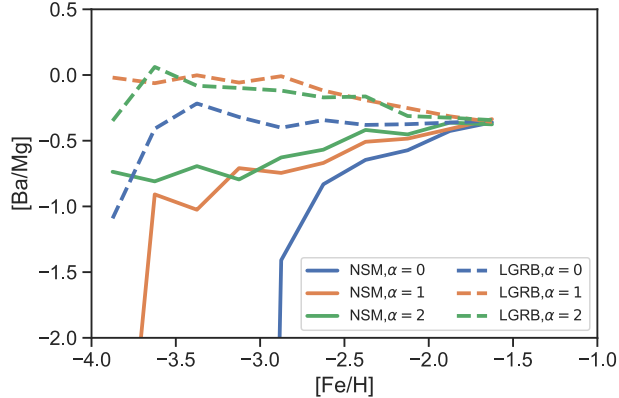


Figure 28: The mean  $[\text{Ba}/\text{Mg}]$  trends in model galaxies with various  $\alpha$ , the star formation history. Lines with different color represent different star formation histories. Dashed and solid lines show results with the collapsar and the NSM model.

inferred kick does not correlate with the observed GW merge time. If the natal kick plays a crucial role on the MW chemical evolution, it would make the explanation difficult for the highly  $r$ -enriched UFD (see [Beniamini et al. 2016b](#)), while the abundances measured in Reticulum II and classical dwarfs are perfectly consistent with the estimates from the BNS ([Beniamini et al. 2016a](#)). On the other hand, there are some constraints from short GRBs. [Perets and Beniamini \(2021\)](#) find that the offset distribution of these GRBs relative to the center is perfectly consistent with the stellar distribution in the host galaxy. These facts suggest that the kick effect is not dominant in determining the location of the BNS merger.

In summary, we find that a delay of  $100 \text{ Myr} \sim 1 \text{ Gyr}$  is required between star formation and the formation of  $r$ -process elements for a significant increase in  $[r/\text{Mg}]$  in the lowest metallicity stars. For objects with no or negative delays, the data are inconsistent with observations, even accounting for inhomogeneous effects; the NSM naturally introduces a similar level of delay, making it a promising origin for the  $r$ -process in the Universe.

## 5.5 Star formation history

Figure 28 shows the mean  $[\text{Ba}/\text{Mg}]$  trends with three different assumptions on the star formation history. The solid and dashed lines represent the results from positive and negative delay models. The NSM model shows an increasing trend while the collapsar model shows the opposite trend. As shown in Figure 27, the similar increasing trends for dwarf and white dwarf galaxies indicate that the NSM is the likely origin of the  $r$ -process in both environments.

## 5.6 Analysis with Eu

Figure 29 shows the analysis with Eu. It does not show the increasing trend seen in Ba because of the large number of upper limits and the large bias of the observed population. Including stars only with upper limits at  $[\text{Fe}/\text{H}] \lesssim -3$  shows a weak increasing trend.

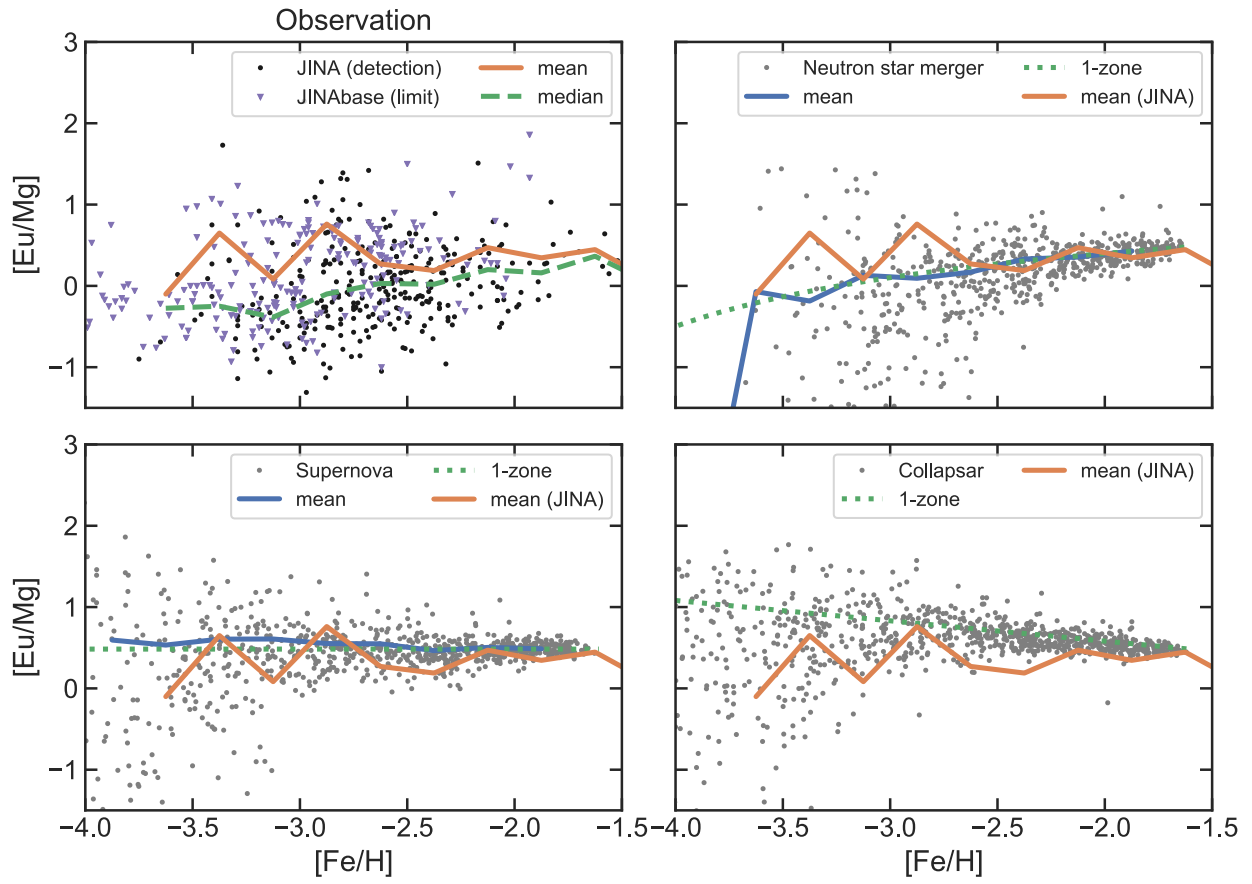


Figure 29: Same as Figure 26 but with Eu. Note that the upper limits are not included for the mean and median curves.

## 6 *R*-process abundance spread in a globular cluster

Neutron-capture elements are useful for probing the formation process of a system. Here, we use *r*-process elements to study the formation process of a globular cluster. A GC with an internal Eu abundance spread has been known for a long time. However, no scenario has explained the independence of Na and Eu abundances. Here, for the first time, we explain the abundance features. The scenario is tested with a numerical simulation, and the event rate is estimated in the context of galactic-scale metal mixing.

### 6.1 Abundance anomalies and *r*-process abundance spread in a globular cluster

GCs are old stellar clusters. They are very compact and the stellar densities are very high: the total stellar mass is  $\sim 10^5 M_{\odot}$  and the stars are packed within  $\sim 10$  pc sphere. GCs are known for a long time. The distribution of stars on the HR diagram is well fitted with one isochrone, suggesting that all the stars are born at the same time, and the chemical abundances are uniform. However, detailed investigation into the color-magnitude diagram (CMD) (see [Renzini 2008](#) and references therein) clarified that there is a spread on CMD. Today, almost all GCs older than 2 Gyr show detectable spread. The existence of multiple populations (MPs) seems to be common ([Bastian and Lardo 2018](#)).

Spectroscopic observations tell us more interesting information. Abundances of light elements show significant ( $\sim 1$  dex) spread among stars in each GC. More importantly, there is an anticorrelation between a few pairs of elements: Na and O, C and N, and sometimes Mg and Al. The sum of C, N, and O are constant among stars. This suggests that hydrogen burning catalysed by CNO element (that is, CNO cycle) had occurred and influenced the progenitor gas of a GC. The same argument holds for Ne-Na chain and Mg-Al chain. In contrast to the variety of light element abundances, Fe abundance is almost constant within each GC <sup>7</sup>. The origin of the peculiar chemical abundances remains a mystery, and will serve as an essential clue to clarify the formation process of GCs.

Abundances of neutron-capture elements are measured in GCs. Some GCs show abundance spread for *s*-process elements. Papers report that the increase in the *s*-process elements are correlated with (i) the sum of CNO elements and (ii) Fe ([Johnson and Pilachowski 2010](#); [Marino et al. 2011](#)). Although low-mass ( $\lesssim 3 M_{\odot}$ ) AGB stars are the origin of *s*-process elements, they cannot deplete Oxygen and reproduce the Na-O anticorrelation. There is no satisfactory model that explains the *s*-process abundance spread within a GC. We need to be cautious because small spread could originate from systematics in the spectral fitting process ([Bastian and Lardo 2018](#)).

For the *r*-process the situation is slightly clearer. M15 is the only GC with a clear spread in the abundance of europium (Eu) ([Snedden et al. 1997](#); [Otsuki et al. 2006](#); [Sobeck et al. 2011](#); [Roederer 2011](#); [Cohen 2011](#); [Worley et al. 2013](#)) while most GCs show uniform abundances. The origin of the spread is not understood. Models try to explain the spread by invoking an *r*-process event between the formation of first and second generations of stars ([Bekki and](#)

---

<sup>7</sup>there are a few exceptions such as  $\omega$  centauri, which shows internal metallicity spread (e.g. [Johnson and Pilachowski 2010](#)).

Tsujiimoto 2017; Zevin et al. 2019). In this case, only the second generation stars, which are formed after the event, could be enriched with  $r$ -process elements.

This work addresses the problem of the  $r$ -process abundance spread. We consider that the abundance spread was present in the progenitor gas cloud as proposed in Roederer (2011). A merger of wandering BNS enriches narrow region in the interstellar medium. The  $r$ -enriched region dissolves to surrounding material slowly. A GC with  $r$ -process abundance spread is formed if it is formed before the local  $r$ -rich region disappears.

## 6.2 Method

### 6.2.1 Formation of globular clusters in cosmological simulation

**6.2.1.1 Cosmological simulations** We investigate to clarify in which conditions a GC can have an Eu abundance spread. First, we perform cosmological galaxy formation simulations to identify compact small clusters (GCs). Next, we inject  $r$ -process elements into gas cells around the GC formation site and re-simulate GC formation. We then investigate the  $r$ -process abundances in the stars.

We use AREPO as the simulation code (Springel 2010; Pakmor et al. 2016; Weinberger et al. 2019). We adopt the Planck 2018 results (Planck Collaboration et al. 2020):  $\Omega_m = 0.315$ ,  $\Omega_b = 0.049$ ,  $\sigma_8 = 0.810$ ,  $n_s = 0.965$ ,  $H_0 = 67.4 \text{ km s}^{-1} \text{ Mpc}^{-1}$  as the cosmological parameters. Initial conditions are generated with MUSIC (Hahn and Abel 2011). We use the zoom-in technique to simulate sufficiently large galaxy with high resolution. We first run a low-resolution box simulation with the side length of  $10 \text{ cMpc } h^{-1}$ . We then identify a dark matter halo of  $2.5 \times 10^{11} M_\odot$  at redshift 4.

We run a zoom-in simulation for the region around the target dark matter halo. The mass of each dark matter particle in the zoom-in region is  $1.0 \times 10^5 M_\odot$  and target gas cell mass (typical mass of a gas cell) is  $1.9 \times 10^4 M_\odot$ . The masses of stars formed are similar to the target gas cell mass. Therefore, a typical GC with the total stellar mass of  $4 \times 10^5 M_\odot$  is resolved by  $\sim 20$  star particles. The number is sufficient to see the distribution and spread of elemental abundances.

**6.2.1.2 Star formation and feedback** A gas cell is converted to or spawns a star particle when the hydrogen number density of a gas cell is higher than  $10^4$  per  $1 \text{ cm}^3$ . Star formation is allowed only in cool ( $T < 10000 \text{ K}$ ) gas cells. The condition on temperature is needed to prohibit star formation in dense gas cells shocked by SNe.

A momentum injection method is adopted for SNe feedback. A well-known problem in the energy feedback scheme is that if the mass resolution is not sufficient, resulting temperature of SNe-heated ISM would be lower than the reality. At temperatures  $\sim 10^5 \text{ K}$ , the cooling rate is a decreasing function of temperature due to bound-bound transitions: therefore, the rate is overestimated and cooled quickly. In this case, energy is lost almost instantly and no net effect appears on the ISM. In reality, high pressure of the heated material pushes surrounding ISM outward, imparting momentum. The momentum cannot be extracted by “cooling” because this is a bulk motion.

Momentum-injection feedback models are investigated by many works (Kimm and Cen 2014; Hopkins et al. 2018; Marinacci et al. 2019). We follow their implementation. If the

mass of a gas particle is more than  $1000 M_{\odot}$ , momentum is imparted to the gas cell. The initial momentum  $P_{\text{SN}} = \sqrt{2E_{\text{SN}}M_{\text{SN}}}$  is enhanced by a factor of  $f_{\text{enhance}} = \sqrt{1 + M_{\text{cell}}/\Delta M}$ . Here,  $E_{\text{SN}}$  and  $M_{\text{SN}}$  are energy and ejecta mass of the SN. These parameters are assumed to be  $10^{51}$  erg and  $15.2 M_{\odot}$ .  $\Delta M$  is the mass imparted to a gas cell. The momentum boost from each SN is capped (Cioffi et al. 1988; Marinacci et al. 2019):

$$p_{\text{terminal}} = 4.8 \times 10^5 E_{\text{SN}} \left( \frac{n_{\text{H}}}{1 \text{ cm}^{-3}} \right)^{-1/7} f(Z)^{3/2} M_{\odot} \text{ km s}^{-1}, \quad (37)$$

where  $f(Z) = \min[(Z/Z_{\odot})^{-0.14}, 2]$  is a metallicity factor that affects cooling rate.

Radiation from young massive stars in a newly formed stars is another important feedback (Stinson et al. 2013). A simple feedback scheme is implemented. To model the strong radiation from young stars, each star particle injects energy of  $2.3 \times 10^{36}$  erg  $\text{s}^{-1}$  per solar mass of stars for the first 4 Myr after formation. The rate corresponds to the number of UV photons of  $8.0 \times 10^{46}$   $\text{s}^{-1}$  assuming that the average photon energy is  $\langle h\nu \rangle = 18$  eV (e.g. Fukushima et al. 2020). During the 4 Myr, we do not allow cooling for the irradiated cells.

The fractions of energy and momentum imparted to a gas cell is determined by a kernel function. The function is proportional to the solid angle subtended by the cell, i.e.,

$$w_i = \frac{\Delta\Omega_i}{4\pi}. \quad (38)$$

The model computes the kernel function for the closest 64 cells around the star particle.

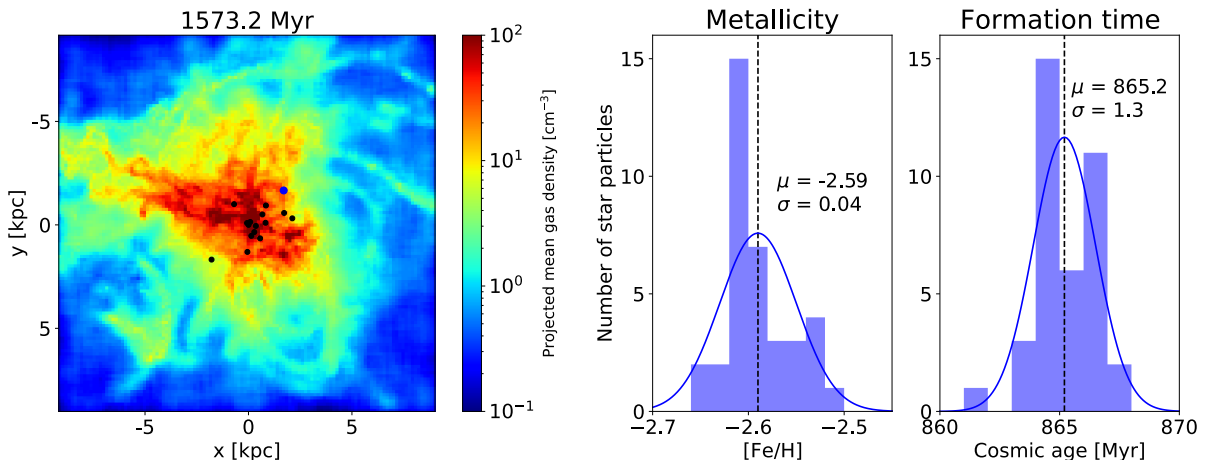


Figure 30: Left panel: average projected gas density of the target galaxy at the cosmic age of  $\sim 1.6$  Gyr (redshift 4.0). The GCs are annotated with black points and the target GC we analyze is with blue. Right panel: Distributions of metallicity and formation times of the target GC.

**6.2.1.3 Identification of GCs** GCs are self-bound objects with nearly constant  $[\text{Fe}/\text{H}]$  which are generally very compact. We identify cluster candidates as follows. First, we find star particles in extremely high stellar density environments with at least  $3 \times 10^5 M_{\odot}$  of

stars within 10 pc. Next, we find compact groups of stars by the k-means clustering. As a result, we find 19 groups of stellar particles that are sufficiently dense and well separated from each other. We exclude two most massive ( $> 10^8 M_\odot$ ) groups because they contain stars of various ages and metallicities. They are most likely nuclear clusters that used to be centers of now-disrupted dwarf galaxies. The other 17 clusters have short star formation periods ( $\lesssim 10$  Myr) and homogeneous abundances of Fe. The masses of these clusters are  $4.0 \times 10^5 M_\odot - 2.8 \times 10^6 M_\odot$ . Finally, we consider stars within 89 pc (300 cpc h<sup>-1</sup>) of the cluster center to be members of the cluster. We confirm in the final snapshot at  $z = 4$  that these clusters remain self-bound. Such clusters are observed as "old" GCs and are likely to be bound until present. If we change the distance criteria to 5 pc and 20 pc, the number of GCs identified would be 10 and 21.

Figure 30 shows the projection plot of gas density. We select the one marked by a large blue circle as the target GC. All of these GCs give similar results, so we use this cluster as a typical example. Other GC locations are indicated by solid black circles. The right panel of Figure 30 shows the distribution of the metallicity and formation time of the target GC stars. At the cosmic age of 861.4 Myr, the first star particle is formed. The star formation continued up to 5.8 Myr. The average of the formation time is 865.2 Myr ( $z = 6.5$ ). The average and the standard deviation of Fe abundance [Fe/H] are  $-2.59$  and  $0.04$ . The target GC has a total stellar mass of  $6.4 \times 10^5 M_\odot$  at the final snapshot. The small spread of Fe abundance is fully consistent with that of GC in the observations ( $\sim 0.06$  dex, see [Carretta and Gratton 1997](#)).

### 6.2.2 Element diffusion

We test the non-uniform mixing of  $r$ -process elements by numerical simulations. In the same approach as in the previous paper, the NSM, an  $r$ -process event, is modeled as a point explosion ([Tarumi et al. 2020b](#)). Eu is deposited in and around the target interstellar medium (ISM) forming the target GC. The diffusion and dilution of Eu into the surrounding ISM is followed in the simulation. Stars in the target GC are formed after the enrichment by the  $r$ -process elements.

We use 20 snapshots dumped at the time before the formation of the target GC, 3–5 Myr away from the adjacent snapshots. The formation site of the target cluster is determined for each snapshot. First, we identify the IDs of the gas cells that constitute the natal cloud of the GC. Then, we then search for the positions of the cells back in time. The "planned site" for the target GC formation is determined as the median coordinates of all flagged gas cells. Eu is then deposited in gas cells around the planned site. We also test the cases where NSMs occur off-centered positions to investigate the relationship between distance and the resulting Eu abundance spread. Four concentric spheres around the planned site are taken. On each surface, 26 points of  $(\theta, \phi) = (0, 0), (\pi/4, i), (\pi/2, i), (3\pi/4, i), (\pi, 0)$  with  $i$  running every  $\pi/4$  from 0 to  $7\pi/4$  in spherical polar coordinates are picked. In total,  $26 \times 4 = 104$  points are considered as explosion points. For the radius of the spheres, let  $t$  be the deposition time before GC formation. For snapshots with ( $t < 30$  Myr,  $30$  Myr  $< t < 60$  Myr,  $60$  Myr  $< t$ ), the radii are (100, 200, 300, 400) pc, (200, 400, 600, 800) pc, and (300, 600, 900, 1200) pc, respectively.

A scalar component mimicking Eu is injected into the gas cells around the explosion

points. Eu is injected into a gas cell within the snowplow radius  $r_{\text{sp}}$  from an explosion. The radius  $r_{\text{sp}}$  is computed as follows (Mo et al. 2010): at the end of the self-similar Sedov-Taylor phase, the blast wave radius is

$$r_{\text{sh}} = 23 \times \left( \frac{n}{1\text{cm}^{-3}} \right)^{-19/45} \times \left( \frac{E}{10^{51}\text{erg}} \right)^{13/45} \text{ pc}, \quad (39)$$

and the velocity is

$$v_{\text{sh}} = 200 \times \left( \frac{n}{1\text{cm}^{-3}} \right)^{2/15} \times \left( \frac{E}{10^{51}\text{erg}} \right)^{1/45} \text{ km s}^{-1}, \quad (40)$$

where  $n$  is the number density of the gas cell in a unit of  $\text{cm}^{-3}$ . It then expands while conserving momentum (snowplow phase). When the expansion velocity of the shell becomes comparable to the ISM turbulence velocity ( $\sim 10\text{km s}^{-1}$ ), this is the end of the snowplow phase and the shell dissolves into the ISM. The shell radius at the dissolution is

$$r_{\text{sp}} = r_{\text{sh}} \times \left( \frac{v_{\text{sh}}}{10\text{km s}^{-1}} \right)^{1/3}. \quad (41)$$

This approach typically distributes Eu to  $\sim 10^5 M_{\odot}$  of gases.

The amount of injected Eu is  $5 \times 10^{-5} M_{\odot}$ . This is in agreement with the estimates from kilonova AT2017gfo (Cowperthwaite et al. 2017) and Reticulum II (Ji et al. 2016a). The amount of Eu injected to each gas cell is set in proportion to the volume of the gas cell. Otsuki et al. (2006) suggests that more than one event, with different ratios of light to heavy elements, has contributed to the  $r$ -process enrichment of M15. We assume that there are two types of  $r$ -process events, lanthanide poor and rich, as the observations require. The birth cloud is rich in both events and has an averaged abundance of  $[\text{Eu}/\text{H}] = -2.1$ . This value is motivated by the abundances of Milky Way halo stars:  $[\text{Fe}/\text{H}] \sim -2.4$  stars in the halo show the Eu abundances of  $[\text{Eu}/\text{Fe}] \sim 0.3$ . This constant "pre-enrichment" allows direct comparisons between our simulation results and M15 observations, although its origin is not clear. Further discussion will be given on the origin of the light  $r$ -process elements and lanthanides in Section 6.4.3.

## 6.3 Results

### 6.3.1 Eu abundance distribution

Figure 31 shows the distributions of Eu abundance for four snapshots. The red line in the figure represents the Eu abundance distribution of stars in M15 (Worley et al. 2013), smoothed with the kernel density estimation. The blue histogram is the results of our numerical simulation. The top left panel shows the best model results: Eu deposition is 19.0 Myr before GC formation. The explosion point is 100 pc away from the formation point. The observed abundance distribution of Eu is well reproduced. In the other implementation where  $\Delta t = 19.0$  Myr and  $R = 100$  pc in the same model parameters, similar abundance distributions of Eu were obtained, although the distributions were slightly different. The figure at the top right shows another model: the parameters are  $\Delta t = 30.7$  Myr and  $R = 100$  pc. The

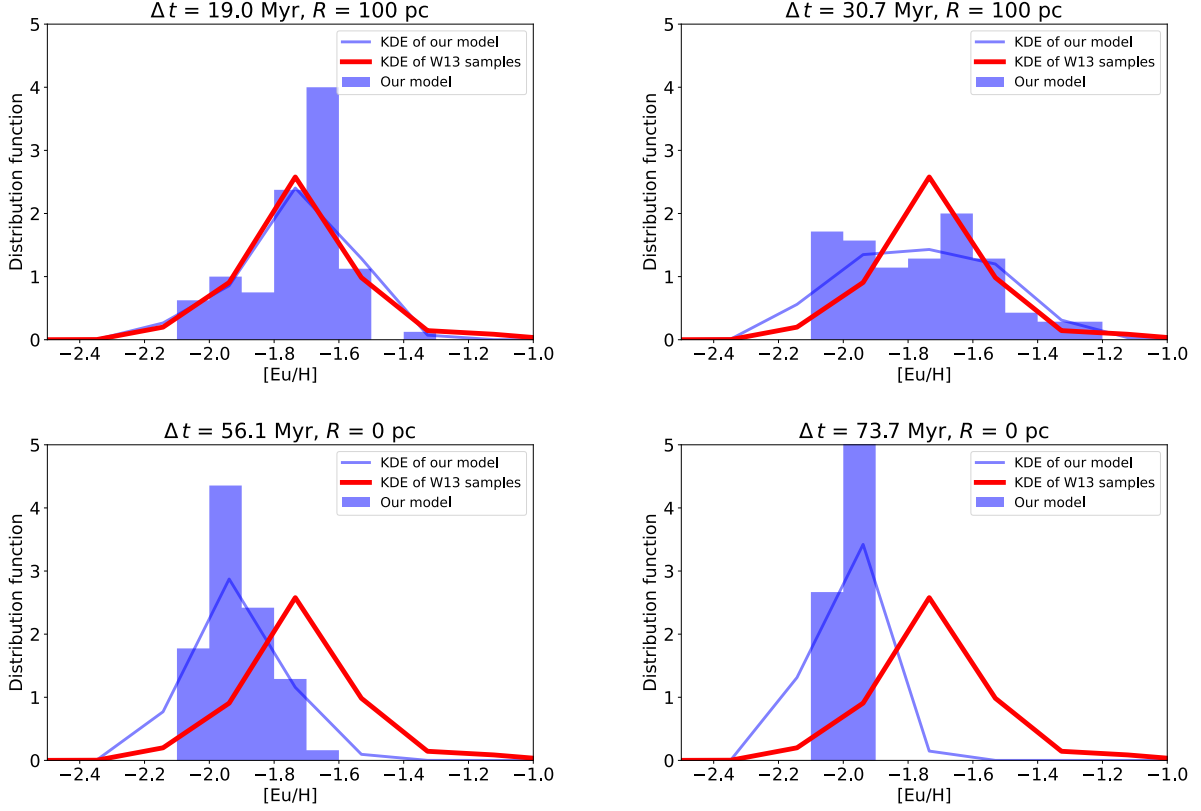


Figure 31: Histograms of Europium abundance ( $[\text{Eu}/\text{H}]$ ) for our simulated GC in models compared to the observed abundances of M15 stars. The red line shows the observed distribution smoothed with the kernel density estimation (KDE) [Worley et al. \(2013\)](#). The blue histograms and lines show the distributions in the numerical experiments. The bandwidth is 0.1 dex. The top two panels show models with (19.0 Myr, 100 pc) and (30.7 Myr, 100 pc) that reproduce the  $[\text{Eu}/\text{H}]$  spread well. These distributions show significant spread, with the standard deviation of  $\sigma > 0.15$  dex. The bottom panels are ones with longer dilution times. They show some inhomogeneities, although their standard deviations are smaller than M15 and could be consistent with the observational errors.

distribution function has a different shape from observations but considerable spread is seen. Interestingly, this model displays a bimodal distribution. The peak at the low abundance is at  $[\text{Eu}/\text{H}] = -2.1$ , indicating that these stars are not enriched by the NSM. It is interesting that such a bimodal distribution can be reproduced by our heterogeneous ISM model without assuming multiple star formation epochs.

The lower two panels of Figure 31 show the results of models that fail to reproduce the observed distribution. In the  $\Delta t = 56.1$  Myr and  $R = 0$  pc model in the lower left, the NSM ejecta is diluted with a large amount of ISM, even though NSM occurs in the center. As a result, the standard deviation of the abundance of Eu was found to be as small as 0.1 dex, which is comparable to the observed uncertainty. The other model is  $\Delta t = 73.7$  Myr and  $R = 0$  pc (bottom right). In this model, Eu from the last NSM is almost entirely mixed in the ISM, and the overall amount of Eu and its spread are too small to be consistent with

observations. From these results, we argue that the Eu abundance spread in M15 can be explained if the  $r$ -process enrichment (NSM) occurs  $\sim 100$  pc away from the birth cloud and there is a short ( $\sim 20$  Myr) time delay for mixing with ISM, the observed Eu content can be explained.

### 6.3.2 Distribution of Eu abundance spread

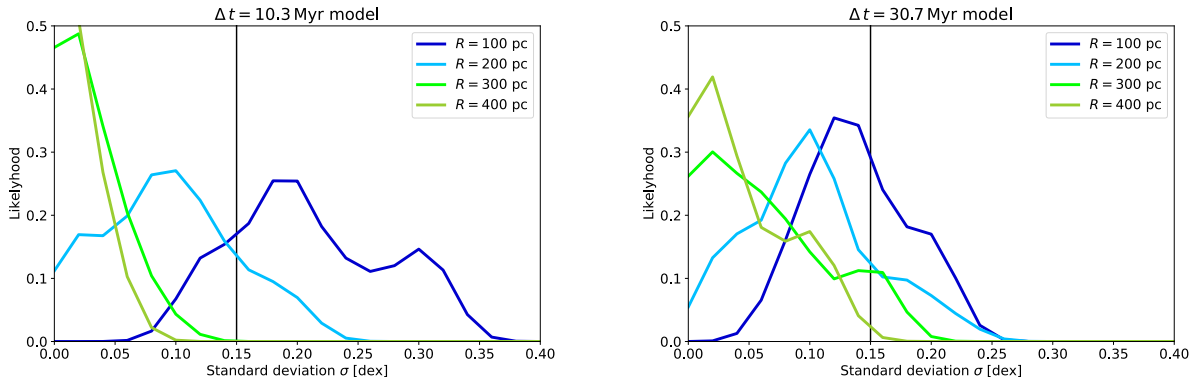


Figure 32: Histograms of  $\sigma_{[\text{Eu}/\text{H}]}$  (standard deviation of Eu abundance  $[\text{Eu}/\text{H}]$  in a model) for each set of model parameters  $(\Delta t, R)$ . Each histogram contain 26 datapoints. The vertical line denotes  $\sigma = 0.15$  dex, the abundance spread seen in observations of M15 stars (Worley et al. 2013). The distribution is smoothed by the kernel density estimation for the illustration purpose (the bandwidth is 0.02 dex).

Figure 32 shows the spread of Eu abundance for the  $\Delta t = 10.3$  and 30.7 Myr models.  $\Delta t = 10.3$  Myr,  $R = 100$  pc models show a spread of abundance equal to or greater than M15 in over 80% of cases. The percentage decreases with increasing distance, and models with  $R \gtrsim 300$  pc show no observable spread. At longer delay times ( $\Delta t = 30.7$  Myr), the non-uniformity of the  $R = 100$  pc model decreases to 35%. This is due to the greater dilution of the NSM ejecta. However, 15% of the models with  $R = 300$  pc show a large Eu spread for this longer time period. With time evolution, the probability decreases for models with smaller  $R$ , but models with relatively large  $R$  may have higher chance of displaying the spread.

The volume of ISM that remains non-uniform can be calculated. We define the region as follows: if a GC is formed within, the spread in Eu composition  $\sigma$  would be greater than  $\sigma > 0.15$  dex. This volume is about  $0.02 \text{ kpc}^3$  and is nearly constant for the first 50 Myr. This reflects the fact that the decrease in probability of the low  $R$  model and the increase in probability of the high  $R$  model compensate for each other; after 50 Myr, the volume rapidly drops to zero due to dilution.

## 6.4 Discussion

We have shown that GC member stars exhibit a large spread in Eu abundances under certain conditions. We discuss the characteristics of the stellar population of M15 and propose a

valid model for its formation and evolution.

### 6.4.1 Sodium abundance

Figure 33 shows the distribution of M15 stars on the  $[\text{Eu}/\text{H}]-[\text{Na}/\text{H}]$  plane and the corresponding histograms, showing a bimodality with two peaks at  $[\text{Eu}/\text{H}] \simeq -2.1$  and  $[\text{Eu}/\text{H}] \simeq -1.7$  (see also section 3.1). No correlation is found between Eu and Na. We discuss several scenarios for the formation of M15 and its enrichment in the  $r$ -process based on these facts.

Multiple star formation epochs are assumed in a popular GC formation model. During the first starburst, several BNSs form. One (or more) of them merge and enrich the cluster before the second star formation. As a result, only the SG stars are enriched with Eu and have higher  $[\text{Eu}/\text{H}]$  than FG stars. The Eu abundance distribution of M15 can be reproduced in this scenario (Bekki and Tsujimoto 2017; Zevin et al. 2019). Here, an important feature is that the event only enriches the SG stars. The lower right panel of Figure 7 shows a schematic figure of the expected distribution. The FG stars have a similar composition to halo stars, and no Eu abundance spread is expected. In addition, FG stars are not affected by the neon sodium (NeNa) chain. On the other hand, SG stars are strongly affected by both the  $r$ -process events and the NeNa chain, which is why they appear in the upper right corner. Among SG stars, as in our model studied in section 3, there may be a spread in the abundance of Eu depending on the time scale of star formation. If this scenario is true, we would see a clear bimodal distribution of  $[\text{Eu}/\text{H}]$ . Another prediction is that the abundances of Eu and Na would correlate. GCs are known to exhibit Na-O anticorrelation (see, e.g. Bastian and Lardo 2018), which is an evidence of past hydrogen burning between the FG and SG star formation epochs. SG stars are likely to be enriched in both Na and Eu. We expect a positive correlation between  $[\text{Eu}/\text{H}]$  and  $[\text{Na}/\text{H}]$ . However, observations of M15 stars do not present such trend.

Another scenario is that the stellar abundance spread in M15 represents that in the natal cloud. In this case, the number of star formation epochs in M15 would significantly affect the Na-Eu relation. If all stars in M15 are formed in a single burst, then Eu and Na would be independent of each other. Therefore, the distribution is simply random, as shown in the lower left panel of Figure 7 (red color map and histogram). On the other hand, if M15 stars form in multiple star-forming bursts, only FG stars will have a spread of Eu. SG stars are formed in a mixture of stellar winds from multiple first generation stars. The Eu abundance spread is averaged out so they would not have a spread of Eu abundance. The middle figure below (green color map and histogram) show the expected distribution in this scenario.

Carretta et al. (2009) study the Na-O anticorrelation of 15 GCs and argues that the criterion for SG stars is  $[\text{Na}/\text{Fe}] > [\text{Na}/\text{Fe}]_{\text{min}} + 0.3$ . This threshold translates to  $[\text{Na}/\text{H}] = -2.09$  in the case of W13 sample as  $[\text{Na}/\text{H}] = -2.39$ :  $[\text{Fe}/\text{H}] = -2.32$  and  $[\text{Na}/\text{Fe}] = -0.07$ . It is evident that the SG stars also have a large  $[\text{Eu}/\text{H}]$  spread, comparable to that of the FG stars. We therefore conclude that a single starburst is strongly supported as the formation scenario for GC stars.

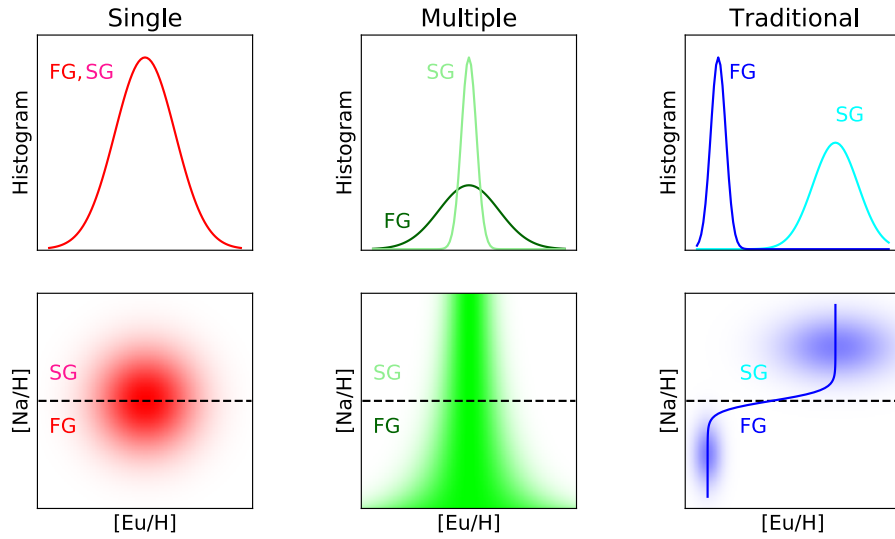
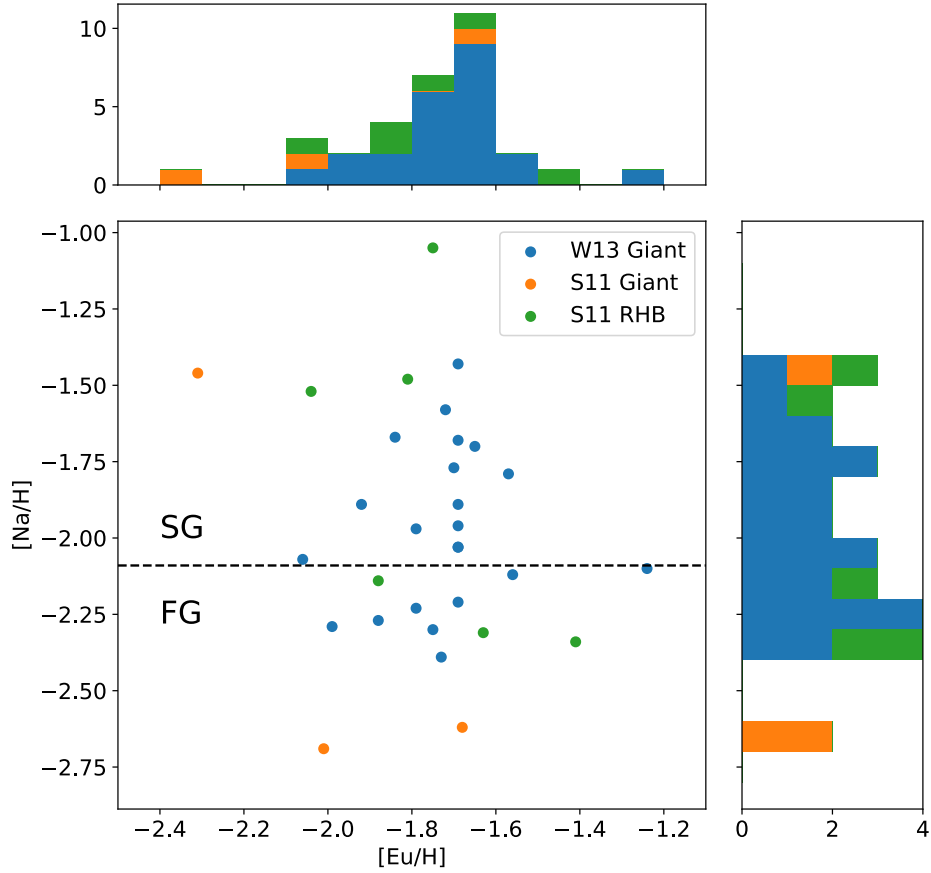


Figure 33: Top panel: distribution of  $[Na/H]$  and  $[Eu/H]$  observations in [Worley et al. \(2013\)](#) and [Sobeck et al. \(2011\)](#). The histograms show  $[Eu/H]$  and  $[Na/H]$  abundances. Bottom panels: expected distributions in three different scenarios. Our models are the two panels on the left. The difference is whether the stars in a GC forms in one or multiple bursts.

### 6.4.2 Fraction of globular clusters with internal Eu spread

We have seen that if the last NSM occurred  $\lesssim 50$  Myr before the GC formation, the GC could have a significant Eu content spread. Each NSM creates an inhomogeneous region of about  $\sim 0.02 \text{ kpc}^3$ : if a GC forms within, it would exhibit Eu abundance spread. Here we estimate the rate of formation for such Eu abundance spread.

One NSM creates a  $0.02 \text{ kpc}^3$  region over 50 Myr. Assuming a stellar mass of  $10^7 M_\odot$  for a galaxy at the cosmic age of 1 Gyr, the average star formation rate is  $10^{-2} M_\odot \text{ yr}^{-1}$ . One core-collapse supernova is produced for every  $100 M_\odot$  of star formation, giving a CCSN rate of about  $\sim 10^2 \text{ Myr}^{-1}$ . Assuming an NSM rate of  $10^{-3}$  of the CCSN, the NSM rate is about  $\sim 10^{-1} \text{ Myr}^{-1}$ . Thus, about  $\sim 5$  NSMs occur during 50 Myr, indicating a large spread of Eu in the  $0.1 \text{ kpc}^3$  region. In our simulations, most clusters form in the central 1 kpc.<sup>8</sup> Therefore, assuming a star-forming region size of about  $\sim 1 \text{ kpc}^3$ , the fraction of star-forming regions with a large Eu spread is 10%. This is consistent with about one in  $\sim 7$  metal-poor GC systems with  $[\text{Eu}/\text{H}] \lesssim -2$  (M68, NGC6287, NGC6293, M92, NGC6397, M15, and M30 to our knowledge. See also Roederer 2011; Cohen 2011). Note that this ratio depends on metallicity (or the baseline Eu content). Assuming a low Eu background, GCs are more likely to have a spread of Eu abundances. Estimating the volume of clouds forming GCs is subject to large uncertainties. Given the low metallicity of GCs, we argue that this assumption about the formation location may only be valid for early immature galaxies with stellar masses as low as  $\lesssim 10^7 M_\odot$ .

### 6.4.3 Origin of $r$ -process elements

For the numerical experiment, we have assumed that an  $r$ -process event synthesizes  $5 \times 10^{-5} M_\odot$  of Eu, having NSM in mind. However, other processes have also been proposed as origins, including collapsars (Siegel et al. 2019) and magneto-rotational supernovae (Nishimura et al. 2015) (see Section 5.2). The origin is still under debate.

Otsuki et al. (2006) noted that the spread of abundance ratios of lighter  $r$ -process elements such as yttrium (Y) and zirconium (Zr) are smaller than those of Eu, as seen in Figure 34. The lines in the figure show the enrichment by NSM of two different yields. The top two show model curves assuming (i) uniform Y and Zr compositions of  $[\text{Y}/\text{H}] = -2.7$ ,  $[\text{Zr}/\text{H}] = -2.3$ , (ii) uniform Eu composition of  $[\text{Eu}/\text{H}] = -2.1$ , and (iii) NSM ejecta abundance ratio of  $[\text{Y}/\text{Eu}] = -1.0$ ,  $[\text{Zr}/\text{Eu}] = -0.9$ . The last condition is motivated by the light-to-heavy  $r$ -process ratio seen among  $r$ -II stars (Montes et al. 2007; Ji et al. 2019a; Tsujimoto et al. 2020). Note that this ratio is enriched in lanthanides by about  $\sim 0.5$  dex relative to the solar  $r$ -process pattern; NSMs (or  $r$ -process events) that dominantly enriched M15 have a lower [light- $r$ /Eu] than the solar  $r$ -process ratio, consistent with those of  $r$ -II stars. Interestingly, recent multi-wavelength observations of kilonova events suggest low ejecta opacity (Waxman et al. 2018). The estimated lanthanide fraction is lower than the solar abundance pattern but with large uncertainties. Future kilonova observations and modeling are expected to further elucidate the detailed abundance ratios of  $r$ -process elements produced in the NSM. The different origin of light and heavy elements is supported by previous studies (e.g., Otsuki

---

<sup>8</sup>Although these clusters form within  $\sim 1$  kpc from the center, galaxy mergers throw these systems away from the center. This mechanism might be important to sprinkle GCs in MW halo region.

et al. 2006; Honda et al. 2006). In addition, given the small physical scale of M15, the number of lanthanide-rich  $r$ -process events that formed the Eu spread in M15 is likely to be one; the similarity of the lanthanide fraction of events to the  $r$ -II stars in the MW halo suggests that the number of events that contributed to the  $r$ -process element abundance in the  $r$ -II stars number is likely to be one. These stars may have formed in a narrow, isolated environment that was less affected by lanthanide-poor  $r$ -process events. For more details, see the next part.

## 6.5 Conclusion

We have shown that a GC can display an internal spread of  $r$ -process abundances if an  $r$ -process event occurred within  $\sim 10$  Myr and  $\sim 100$  pc. The  $r$ -process event should be lanthanide-rich as in the events for Reticulum II. Considering the no correlation between Na and Eu distributions, a single star formation epoch is favored as the formation scenario of a GC. This challenges the standard (AGB) GC formation scenario.

## n-capture element abundances against Eu

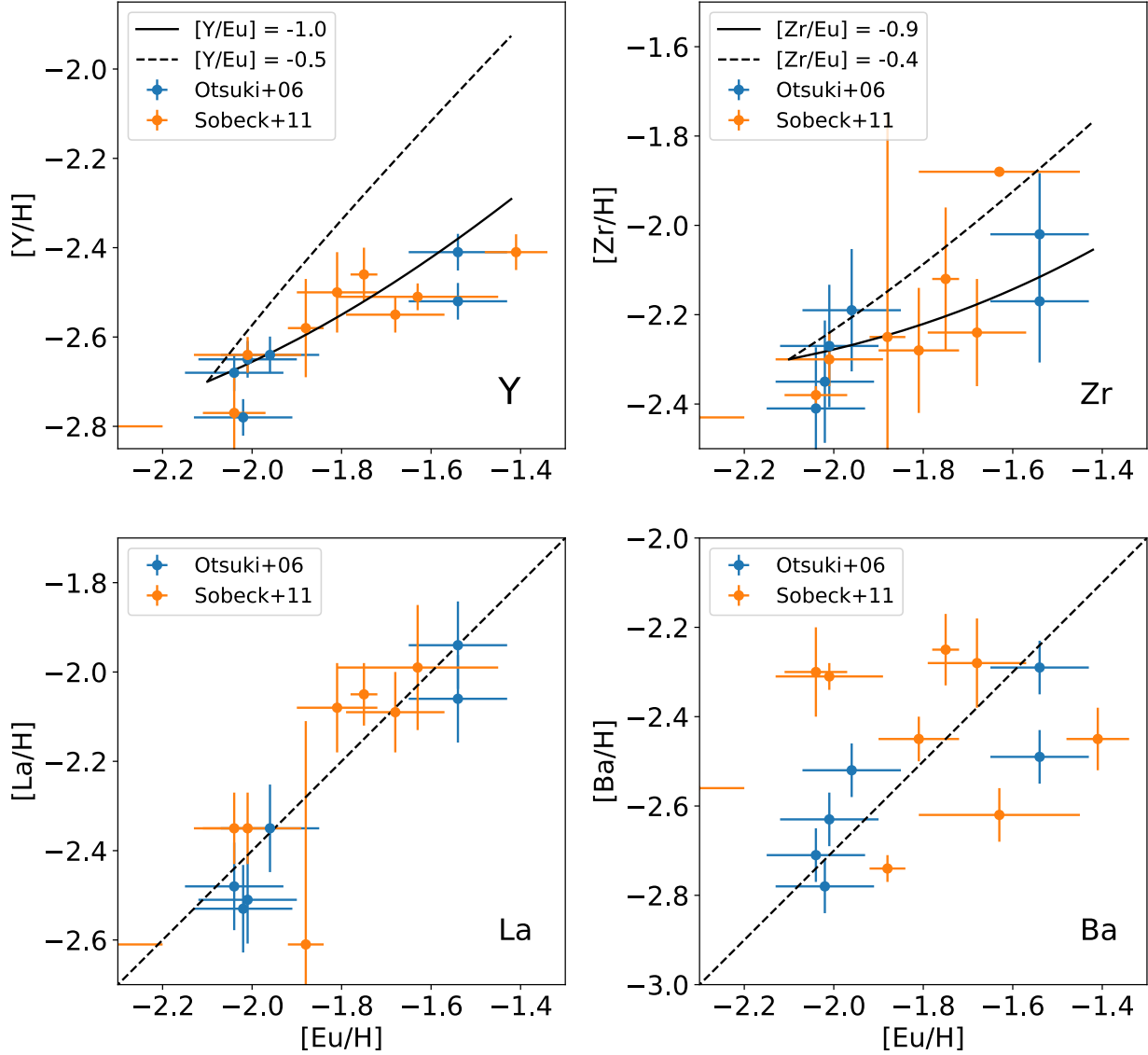


Figure 34: The abundances of heavy and light  $r$ -process elements. The top panels show the ratio of light (Y, Zr) to heavy (Eu) neutron-capture elements and the bottom panels show relations between heavy (La, Ba, Eu) neutron-capture elements. The dashed lines show the expected abundances assuming an event with solar  $r$ -process abundance pattern have contributed (Bisterzo et al. 2014), while the solid curves show that for case of lanthanide-rich event (Tsujimoto et al. 2020). The observational data are taken from Otsuki et al. (2006) and Sobeck et al. (2011).

## 7 Non-local thermal equilibrium analysis for Helium and Strontium line signatures in kilonova

Previous sections address the mixing of elements inside galaxies. We also need to study the nucleosynthesis sites of the  $r$ -process elements to address the problem thoroughly. NSM is a promising candidate for the  $r$ -process elements, as we have seen in Section 5. Here, we study the kN spectrum’s absorption feature to probe the NSM environment.

This work focuses on level populations of atoms in kN ejecta, which is a unique feature compared to previous works in the literature. Hydro-simulations that consistently solve radiative transfer and energy input/output require assuming local thermal equilibrium (LTE). However, to model the line absorption strength, non-LTE modeling is appropriate because level populations determine the result. Here, we model level populations without assuming LTE at the cost of simplifying the hydro-simulation part. The photospheric temperature is determined by fitting, while the ionization rate is computed from a theoretical model. The energy consistency is secured by the fact that the  $r$ -process decay heating rate is consistent with the luminosity.

### 7.1 Theoretical works on kilonova

Kilonova (kN, Metzger et al. 2010) is an electromagnetic counterpart to the merger of binary neutron stars. The emission is powered by the radioactive decays of  $r$ -process elements. Only one kN (AT2017gfo) that associates with a gravitational wave event (GW170817) has been observed (see Metzger 2017; Nakar 2020; Margutti and Chornock 2021; for reviews). The spectrum and the light curve of the kN imprints valuable information on the nucleosynthesis in the event (Barnes and Kasen 2013; Kasen et al. 2013; Tanaka and Hotokezaka 2013).

The spectra in the optical to near-infrared bands were obtained by several groups (Chornock et al. 2017; Kasliwal et al. 2017; Kilpatrick et al. 2017; Pian et al. 2017; Smartt et al. 2017). The most remarkable feature in its photospheric phase is the existence of a strong absorption feature around 8000 Å. The feature persists for  $\sim$  a week after the merger (Kilpatrick et al. 2017; Pian et al. 2017). Since the ejecta is likely composed of heavy  $r$ -process elements, such absorption feature may be composed of many absorption lines. However, the number density of strong lines decrease at longer wavelength of  $\gtrsim$  10000 Å (Domoto et al. 2022). It is worth investigating the possibility of single ion species producing such absorption feature. Watson et al. (2019b) argue that the feature is a P-Cygni profile (line profile characteristic of expanding matter, with an emission feature on the long wavelength side and an absorption feature on the short wavelength side) produced by the three lines of singly ionized Sr (Sr II) at 10039, 10330, 10918 Å. The wavelength is blueshifted by  $0.2c$ . If true, the feature is the first direct evidence of  $r$ -process elements in the neutron star merger spectra.

An alternative explanation is absorption by neutral Helium (He I) 10833 Å absorption line. The presence of He in NSM ejecta is first pointed out by Fernández and Metzger (2013).  $\alpha$  particles in the ejecta is the consequence of  $\alpha$ -rich freeze-out (see Section 1). The exact amount of He in the ejecta depends on the entropy and electron fraction. Perego et al. (2022) show that  $\alpha$  decays of the heaviest nuclei also produces the  $\alpha$  particles. However, they have concluded that the P-Cygni feature in the spectrum is unlikely to be the He signature,

because the luminosity of kN is too high. However, they have used the numerical code for the type-Ib supernova, and the applicability is questionable. In addition, the mass of He in NSM ejecta is highly uncertain (Wanaajo 2018; Fujibayashi et al. 2022).

Previous works on radiative transfer simulations for kN including Watson et al. (2019a) assume LTE, where the ionization levels and excited level populations are computed by the Saha equilibrium and the Boltzmann distribution of the ejecta temperature at the position. The LTE assumption may be valid during the photospheric phase (Pognan et al. 2022). However, in NSM ejecta, high-energy particles originate from the radioactive decays of  $r$ -process elements. These particles contribute to overionization of the ejecta, which significantly deviates the populations from the LTE values (Hotokezaka et al. 2021). In particular, He is an element that is significantly affected by such non-thermal particles. It is crucial to include the effect of non-thermal processes to model the line strength of He in NSM ejecta.

We model the level population of He I and Sr II in kNe under the irradiation of non-thermal electrons produced by  $\beta$ -decay of  $r$ -process elements. We will show that the P-Cygni feature can be reproduced by the 10833 Å He I line. Unlike type Ib supernovae, which have higher photospheric temperatures and higher He density, this is the only absorption line of He observable in the kN photospheric phase. In the case of Sr, the Sr II abundance decreases with time because ionization of Sr II  $\rightarrow$  Sr III proceeds. Consequently, the line strength is expected to get weaker from 1.5 day to 4.5 day after merger, which seems to contradict to the observed feature.

## 7.2 Basic picture

### 7.2.1 He and Sr level structures

Figure 35 shows the energy level structure of neutral He relevant to the line at 10833 Å. The He I 10833 Å line comes from transition between two excited levels  $2^3S$  and  $2^3P$ . Since He have two electrons, their spins form spin-0 (singlet) and spin-1 (triplet) states for each orbital part of the wavefunction. An exception is the ground state, which contain both electrons in the  $1s$  orbit: since two electrons around He nuclei cannot take the same orbital and spin states at the same time, only singlet state is allowed for the ground state. The  $2^3S$  state is a metastable state. Note that the excitation energy from the ground level to He I,  $2^3S$  is 19.8 eV, which is prohibitively high for thermal particles of kilonova photospheric temperatures ( $\lesssim 5000$  K). Therefore, excitations by any thermal processes are negligible. However, the excited state He I,  $2^3S$  can be highly populated through recombination from ionized He.

Kilonova shines because of energy input from radioactive energy. Therefore, many high-energy particles such as high-energy electrons and photons ( $\beta, \gamma$  particles) exist in the ejecta. They can easily ionize neutral He because their energies are more than keV. Then, the ionized He captures an electron and it becomes neutral again. A good fraction of the recombination results in excited states and  $\sim 75\%$  of excited He I will become any of the triplet states (Osterbrock and Ferland 2006). Natural transitions are so efficient that the excited states soon decays to the most stable level connected by allowed transitions. Here, the spin quantum number plays a significant role: the triplet states and the singlet states are decoupled because spin-flipping transitions are prohibited. For instance, the natural transition to the ground

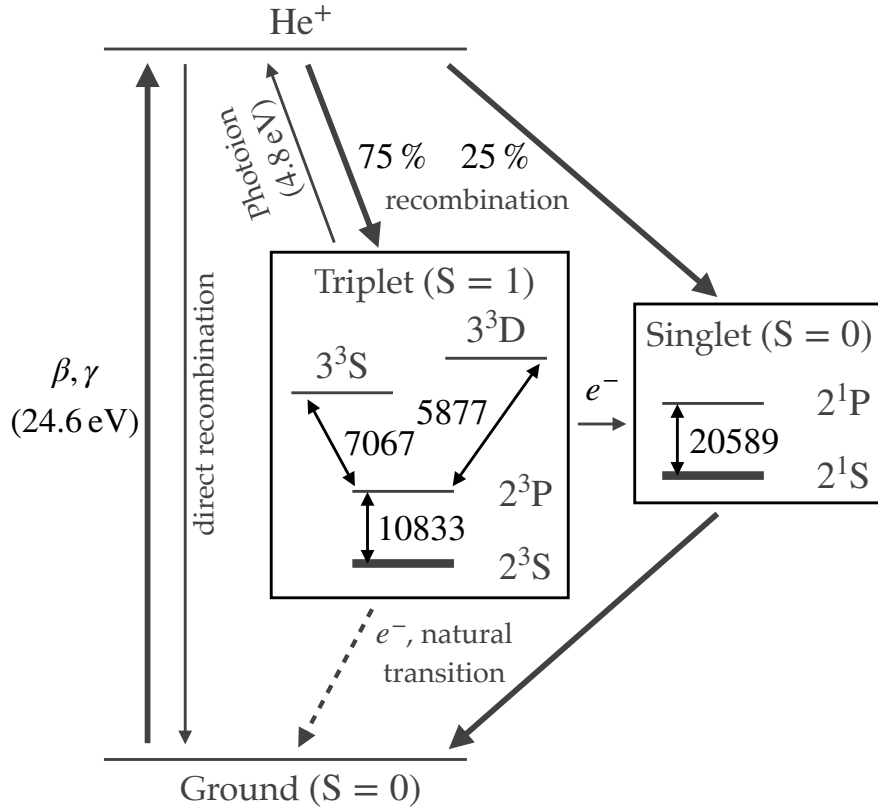


Figure 35: A schematic figure for the level structure of He.

state from the 2<sup>3</sup>S is extremely inefficient: the Einstein's A-coefficient for this transition is  $\sim 10^{-4} \text{ s}^{-1}$ . The dominant depopulation mechanism is by interactions with thermal electrons or photoionization by thermal photons, depending on the photospheric temperature. If the temperature is high, there are sufficiently high fraction of high-energy ( $> 4.8 \text{ eV}$ ) photons that can ionize from the 2<sup>3</sup>S state. Otherwise, electron collisions flips the spin to the ground (1<sup>1</sup>S) state or excited singlet states (2<sup>1</sup>S, 2<sup>1</sup>P) and then it decays to the ground state. Although 2<sup>1</sup>S is a metastable state, it decays to the ground state via two-photon process which is relatively efficient (Drake et al. 1969).

Figure 36 is the same figure for singly ionized Sr. It has one electron in the valence shell because there are 37 electrons in total and 36 makes a closed shell. The three lines with  $\sim 10000 \text{ \AA}$  come from transitions between 4D (the valence electron in the 4d orbit) and 5P (the valence electron in the 5p orbit) states. The 4D states are metastable because the orbital angular momentum is different by two from the ground (5S) states.

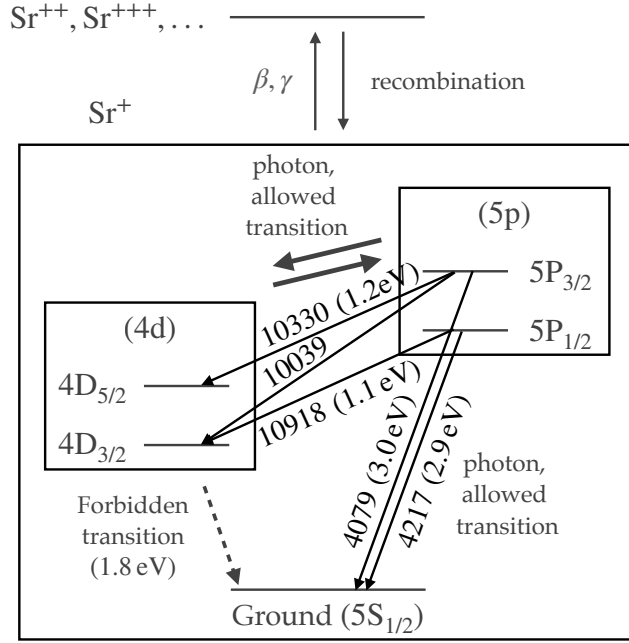


Figure 36: A schematic figure for the level structure of Sr<sup>+</sup>. The energy levels crucial for the line is the 4D states. Since this state is metastable, natural decay to the ground state is slow. This level is connected to the ground state via the 5P states.

### 7.2.2 Line optical depth

Strength of the line spectral feature in an expanding medium can be calculated by the Sobolev optical depth (Sobolev 1960; Jeffery and Branch 1990):

$$\begin{aligned} \tau_s &= \frac{g_u}{8\pi g_l} A_{lu} n_l \lambda_{lu}^3 t \left( 1 - \frac{n_u g_l}{n_l g_u} \right) \\ &\approx 0.23 t_d \lambda_{\mu\text{m}} n_l f_{lu}, \end{aligned} \quad (42)$$

where  $A_{lu}$ ,  $n_l$ ,  $n_u$ ,  $\lambda_{lu}$ ,  $t$ ,  $g_l$ ,  $g_u$  are Einstein's A coefficient, number densities of lower and upper levels, wavelength of the transition, and degrees of freedom for lower and upper levels. Time in unit of day is  $t_d$  and the wavelength in unit of  $\mu\text{m}$  is  $\lambda_{\mu\text{m}}$ . Feature of the line would appear if  $\tau_s \gtrsim 1$ .

What are the optical depths needed to reproduce the spectral feature in AT2017gfo? Figure 37 shows the comparison of model to observed spectra between 1.43 and 4.40 days after the merger. We assume an optical depth profile that decreases as  $\tau_s = \tau_{s0} (v/v_{\text{phot}})^{-5}$  and take  $\tau_{s0}$  as a free parameter. The fact that the emission is predominantly black-body suggests that most material is inside the photosphere for the first few days. The sharp power of  $v^{-5}$  is motivated by the fact that significant material should be within  $v = 0.155c$ , which is the photospheric velocity at 4.40 days in our model. The optical depths required to reproduce the observation is  $\sim 1.0$  for all the epochs. The shape of the line profile depends on the assumption of the profile:  $\tau_{s0}$  could be modified by a factor of a few by taking another power-law index.

Oscillator strengths for neutral Helium ( $2^3\text{S} \rightarrow 2^3\text{P}$ ) and singly ionized Strontium ( $4\text{D} \rightarrow 5\text{P}$ ) are  $f_{lu} \approx 0.54$  and 0.089. Substituting these to Equation 42 and assuming  $(1 -$

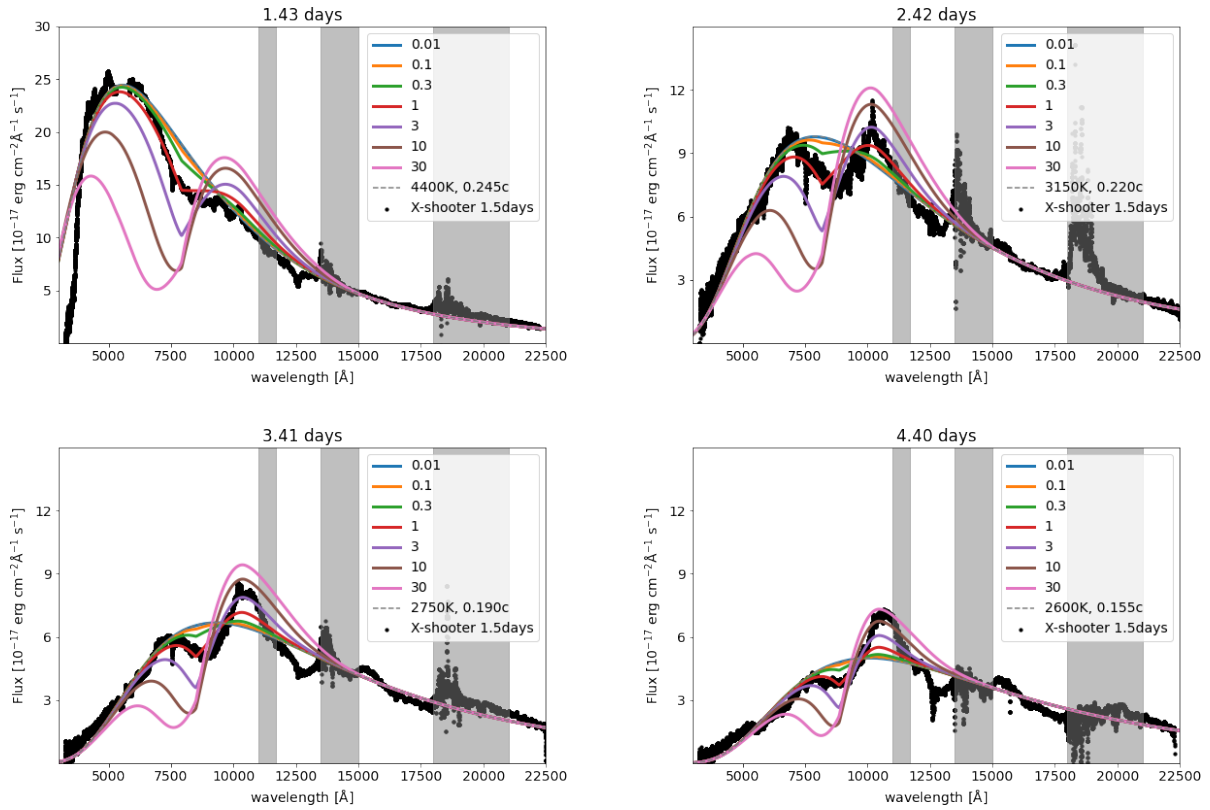


Figure 37: P-Cygni profiles of the observed spectrum and the theoretical model. The shaded regions are the wavelengths where telluric absorption is significant. Black lines show observed spectrum. Colored lines show the absorption line feature in the simplest model of  $\tau_s = \tau_{s0}(v/v_{\text{phot}})^{-5}$ .

$n_u g_l / n_l g_u) \simeq 1$ , densities required to produce the line feature are

$$n(\text{He I}, 2^3\text{S}) \gtrsim 7.4 t_d^{-1} \text{ cm}^{-3}, \quad (43)$$

and

$$n(\text{Sr II}, 4^2\text{D}) \gtrsim 50 t_d^{-1} \text{ cm}^{-3} \quad (44)$$

respectively.

The number densities of He and Sr including any ionization states at a velocity coordinate  $v$  is:

$$n(t, v) \approx 10^6 t_d^{-3} \frac{m_{\text{ej}}(\geq v)}{0.01 M_\odot} \frac{Y}{0.01} \left( \frac{v}{0.2c} \right)^{-3} \text{ cm}^{-3}, \quad (45)$$

where  $Y$  and  $m_{\text{ej}}(\geq v)$  are the number fraction of He and Sr and the total mass of ejecta moving faster than  $v$ . The average mass number is assumed to be 100. Either neutral Helium or singly ionized Strontium can produce P-Cygni profile on the spectrum if there are sufficiently high densities of  $2^3\text{S}$  or  $4\text{D}$  states.

### 7.2.3 Radioactive ionization

NSM ejecta at a few days after the merger is composed of radioactive  $r$ -process nuclei which heat the ejecta. The decay energy is first carried by decay products such as  $\alpha, \beta, \gamma$  particles, and fission fragments (Barnes et al. 2016). These high-energy particles deposit energy into the ejecta by ionizing atoms and ions, or by interacting with free electrons.

We can estimate the ionization states of Helium and Strontium by ionization equilibrium. Here we assume that ionization is mostly done by the nonthermal particles. The ionization rate  $\beta_i$  is

$$\beta_i(t) = \frac{\dot{q}_\beta(t)}{w_i}, \quad (46)$$

where  $\dot{q}_\beta \approx 1 t_d^{-1.3} \text{ eV/s}$  and  $w_i$  are the radioactive heating rate per ion and the energy required to ionize one atom, “work per ion pair”, of a given ion. To obtain  $w_i$ , we need to compute degradation of high-energy particles via various processes that will be explained later. In general, a few percent of energies of high-energy particles are spent by ionization of elements. Therefore,  $w_i$  will be  $\sim 20$  times higher than their ionization potential energies. Recombinations occur between ions and electrons with Maxwell-Boltzmann (thermal) distribution. In this case, a “recombination rate coefficient”  $\alpha$  is available. The recombination rate is  $\alpha n_i n_e$ . We require the ionization and recombination rates to be equal:

$$n_{i+1} \approx \frac{\beta_i}{\alpha_i n_e} n_i. \quad (47)$$

## 7.3 Method

We need  $n_{\text{He}_{2^3\text{S}}}$  and  $n_{\text{Sr}_{4\text{D}}}$  at each radius to model the line signature. For this purpose, we compute rate equations of transitions among various levels. The equations include all the processes relevant for the populations. I describe the assumptions in our model.

Epoch [days]	$T_\gamma$ [K]	$v_{\text{phot}}/c$
1.43	4400	0.245
2.42	3150	0.22
3.41	2750	0.19
4.40	2600	0.155

Table 1: Temperatures and velocities of photosphere obtained by fitting.

### 7.3.1 Geometry

We prepare a spherically symmetric homogeneous shells expanding at constant velocities so that  $r = vt$  holds. A power-law density profile is assumed:

$$\rho(v, t) = \begin{cases} \rho_0(v/v_0)^{-n}(t/t_0)^{-3} & (0.1 < v/c < 0.5) \\ 0 & (\text{otherwise}) \end{cases} \quad (48)$$

where we assume  $M_{\text{ej}} = 0.04 M_\odot$  and determine the constant  $\rho_0$ . The mass fractions of He and Sr are assumed to be  $M_{\text{He}}/M_{\text{ej}} = 0.1\%$  and  $M_{\text{Sr}}/M_{\text{ej}} = 1\%$ . The composition is homogeneous. For our fiducial calculation we assume  $n = 5$  but we also experiment with other values.

We assume that the ejecta has a sharply defined photosphere at a photospheric velocity of  $v_{\text{phot}}$  at each moment. The photosphere emits blackbody radiation with a temperature  $T_\gamma$ . We consider that this approximation is more or less valid because the spectrum from 1.4 to 4.4 days are well fitted by a blackbody emission except for the P-Cygni feature we discuss. We determine the position (on the velocity coordinate)  $v_{\text{phot}}$  and temperature  $T_\gamma$  of the photosphere by fitting the observed spectrum of AT2017gfo as

$$F(\lambda) = \frac{1}{D^2} \int_0^{r_{\text{max}}} 2\pi x B(\lambda, T(x)) dx \quad (49)$$

where  $r_{\text{phot}} = v_{\text{phot}}t$  is the photospheric radius at each epoch,  $B(\lambda, T)$  is the Planck function for the blackbody radiation, and  $D = 40.7 \text{ Mpc}$  is the distance from the earth (Cantiello et al. 2018). We take into account the relativistic Doppler effect in an approximate manner. Taking  $\theta$  as  $\cos \theta = \sqrt{1 - (x/r)^2}$ ,  $T(x)$  is

$$T(x) = \frac{T}{\gamma(1 - \beta \cos \theta)}. \quad (50)$$

Fits are reasonable for spectra at 1.43-4.40 days. The results are shown in Table 1. We assume that the electron temperature outside the photosphere is constant and is the same as the photospheric temperature:  $T_e = T_\gamma$ .

### 7.3.2 Rate equations and Atomic data

We consider 21 levels for the populations of He. Two levels are for He II and He III, and the other 19 levels represent neutral He up to the quantum number  $n = 4$  for both  $S = 0$  and  $S = 1$  states. Natural transition rates (Einstein's A-coefficients) are obtained from the

NIST database <sup>9</sup>. The stimulated transition rates (the “B” coefficients) are computed from the A-coefficients by the statistical equilibrium of the level populations and the photon field. We consider a geometric dilution factor  $W(v)$ :

$$W(v) = 0.5 \left( 1 - \sqrt{1 - \left( \frac{v_{\text{phot}}}{v} \right)^2} \right) \quad (51)$$

(Mihalas 1978) that considers the solid angle irradiated from a photosphere inside.

If the optical depth of an absorption line becomes very high, an emitted photon is soon absorbed by another ion of the same kind. The net de-excitation rate should be decreased in that case. This is treated by the Sobolev escape probability  $P(\tau_s) = [1 - \exp(-\tau_s)]/\tau_s$  (Castor 1970), where  $\tau_s$  is the Sobolev optical depth (equation 42). The photoionization cross sections from each level, and the recombination rate coefficients  $\alpha$  are taken from Nahar (2010). We have considered excitation by collisions of thermal electrons (Berrington and Kingston 1987; Ralchenko et al. 2008). Ionization by thermal electrons are also considered but the rates are negligibly low.

We assume that photoionization and recombination results in the ground level of He II and He III. For the neutral He, we separately treat the direct recombination to the ground from the excited levels. Namely, 75% of the recombinations to excited states results in the  $2^3\text{S}$  level, while the other 25% populates the  $2^1\text{S}$  level. We also try recombination to  $n = 4$  levels, and have checked that the result did not make any observable difference. This is expected because natural transition cascades occur very quickly ( $\sim 10^6 \text{ s}^{-1}$ ) compared to other processes such as photoionization. Therefore, all the triplet He atom anyway decay to the  $2^3\text{S}$  level. Nonthermal excitation to the spin-triplet states is not significant as singly ionized He dominates over neutral He.

For Sr, we consider ten levels. Five for Sr II ( $5\text{S}_{1/2}, 4\text{D}_{3/2}, 4\text{D}_{5/2}, 5\text{P}_{1/2}, 5\text{P}_{3/2}$ ) and the other five for other ionization levels (Sr I, Sr III, Sr IV, Sr V, Sr VI). A and B coefficients are obtained from the NIST database. Recombination rates are scaled from the Hydrogen values. Here we use the formula

$$\alpha(z, T) = z\alpha(1, T/z^2), \quad (52)$$

which is suggested in Bates et al. (1962) and  $z$  is taken as the charge of an ion. There is no sufficient data for the electron collision strengths. We assume that all the strengths are unity. This simplistic treatment does not cause serious errors in the results, because almost all transitions are dominated by photons in the case of Sr. In an unlikely case of the collision strength of more than 100, the level population is affected by the collision strength.

### 7.3.3 Radioactive ionization

Ionization by high-energy particles crucially affect the level populations of ions in the ejecta. We consider  $\beta$  particles as the ionization source. Work per ion pair  $w_i$  is the energy input required to ionize one ion  $i$ . In astrophysical plasma, the work per ion pair  $w_i$  is 10 – 100 times the ionization potential because a few percent of the energy of non-thermal particles is spent to ionize elements. Axelrod (1980) estimates the  $w_i$  for iron in type-Ia supernova

---

<sup>9</sup><https://www.nist.gov/pml/atomic-spectra-database>

as  $\sim 30$  times the ionization potential. [Hotokezaka et al. \(2021\)](#) give similar values for Nd in kilonova ejecta. We have solved the Spencer-Fano equation to obtain  $w_i$  ([Spencer and Fano 1954](#); [Kozma and Fransson 1992](#)). The calculation details will be presented in our companion paper ([Hotokezaka et al. in prep.](#)). The values of  $w_i$  in neutron star merger ejecta are  $\approx 3000$  eV for He II,  $\approx 600$  eV for He I,  $\approx 300$  eV for Sr II, and  $\approx 450$  eV for Sr III, respectively. The specific heating rate  $\dot{Q}$  [erg s $^{-1}$ ] is taken from [Hotokezaka and Nakar \(2020\)](#). The ionization rate by nonthermal particles is calculated as  $\dot{Q} \times Y_{\text{He}}/W_{\text{HeI}}$ .

## 7.4 Spectrum calculation

[Jeffery and Branch \(1990\)](#) propose a simple and powerful analysis methodology for the formation of the P-Cygni profile and we follow that treatment. We use a cylindrical coordinate with the center of the merger ejecta is at the origin and the observer is at  $z = \infty$ . The other two dimensions are described by a polar coordinate  $(p, \theta)$ , although we are not interested in  $\theta$  as the ejecta is assumed to be also axisymmetric. The  $z$  coordinate corresponds to the Doppler velocity since the ejecta is freely expanding from a point-source and a relation  $r = vt$  holds (homologous expansion).

We assume that a photosphere emitting a blackbody radiation of  $T_{\text{phot}}$  is at  $v_{\text{phot}}$ . Outside the photosphere, the ejecta is optically thin except for the line in question. A photon with the wavelength  $\lambda$  may be scattered at the  $z$ -direction velocity coordinate of  $z(\lambda) = v_z(\lambda)t$  that satisfies

$$\lambda_0 = \lambda(1 + v_z(\lambda)/c), \quad (53)$$

where  $\lambda_0$  is the wavelength of the line in question. Note that we consider the Doppler effect to the first order. We discuss the effect of special relativity in Section 7.7.4.6.

The origin of the photons of the wavelength  $\lambda$  are (i) the photosphere, or (ii) an interaction surface at  $z(\lambda) = v_z(\lambda)t$ . In the latter case, photons with the wavelength  $\lambda_0$  (in the ejecta-comoving frame) are scattered by the line transition. We add these contributions to obtain the intensity from a point  $(p, z)$  as:

$$I(p, z) = \begin{cases} S(p, z)(1 - e^{-\tau}) + B_\nu(T_{\text{phot}})e^{-\tau} & (|p| < v_{\text{phot}}t) \\ S(p, z)(1 - e^{-\tau}) & (\text{otherwise}). \end{cases} \quad (54)$$

Here, the source function  $S(p, z)$  is given by

$$S(p, z) = \frac{2h\nu^3}{c^2} n_l \left( \frac{g_u n_l}{g_l n_u} - 1 \right)^{-1}. \quad (55)$$

The total flux from a velocity surface  $z$  is obtained by integrating the  $p$  and  $\theta$  coordinates:

$$F(z) = \int_0^{p_{\text{max}}} 2\pi p I(p, z) dp. \quad (56)$$

Here, we have assumed that the line absorption is represented by a single transition. For Sr, the three lines are separated by  $\Delta\lambda = 882 \text{ \AA}$ , making the difference of  $\Delta\lambda/\lambda \sim 9\%$ . This approximation does not affect the emergent spectral shape significantly, as the observed blueshifts ( $\sim 0.2c$ ) and the width of the line feature are wider.

## 7.5 Result

### 7.5.1 He model

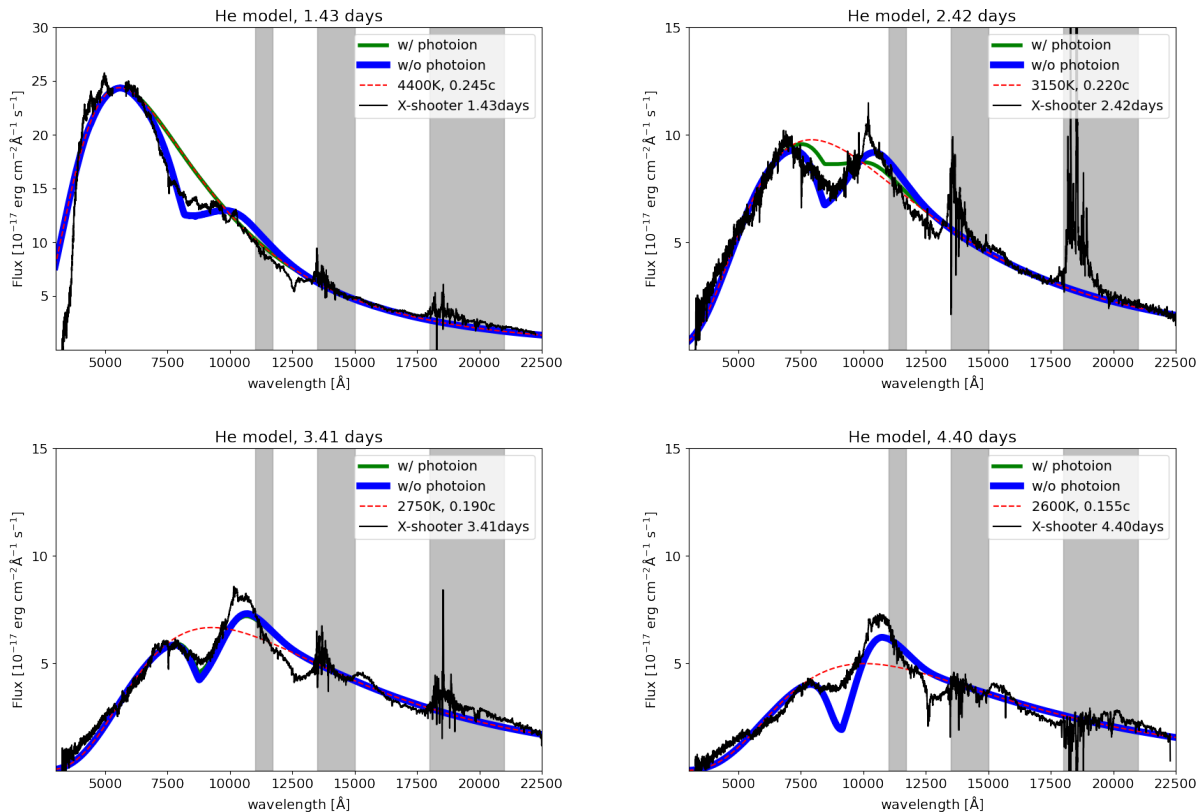


Figure 38: Spectral results for our He model, compared to the observed spectrum at 1.43-4.40 days from merger. The fiducial model assumes that the UV photons do not contribute to the ionization of He  $2^3S$  level. The gray shaded regions show the wavelength where telluric absorption is significant.

In Figure 38, we show our He model results and compare them to the observations. Our main model (blue) reproduces the absorption features well. In this model, photoionization is ignored. Our model (green) reproduces the absorption features at 3.41-4.40 days, while the predictions for the first two epochs are weaker than the observations. The model spectra match well if photoionization from  $n = 2$  levels are ignored for the first two epochs. On the other hand, photoionizations have a minor effect for the later epochs. The level populations and the spectral signatures for these epochs are robust to the uncertainty in the UV blanketing. Therefore, He of 0.2% in mass fraction, which corresponds to  $8 \times 10^{-5} M_{\odot}$ , naturally produces the line feature in AT2017gfo. The spectral feature persists for the first 3.4 days, and it gets stronger at 4.4 days. The estimates of Equation 43 show that the line strength gets weaker quickly. However, photosphere goes inside as time evolution, therefore the photospheric density decrease is slower than  $t^{-3}$  in our calculation.

Photoionization efficiently works to depopulate from the  $2^3S$  level for the first 2.5 days, when the photospheric temperature is relatively high. We have found that the photoionization

rates should be 0–0.3% and 0–30% of blackbody values for 1.43 and 2.42 days to reproduce the observations (see Section 7.6). The ionization threshold is 4.8 eV, which corresponds to  $\sim 2600 \text{ \AA}$  in the ejecta rest frame. The spectrum at 1.43 days clearly shows a cut-off feature at the wavelength of  $4000 \text{ \AA}$  (Figure 38). Therefore, in the model with blackbody UV strength, we overestimate the photoionization depopulation rate. From the theory side, such suppression of UV strength is expected from heavy ions in the ejecta: opacity is higher for UV photons than for optical photons. The suppression of near-UV flux by a factor of a few hundred is typically seen in the results of a Monte-Carlo radiative transfer simulation (e.g., Domoto et al. 2021). To properly assess UV blanketing, knowledge of UV absorption opacity (Mihalas 1978) of  $r$ -process elements is required.

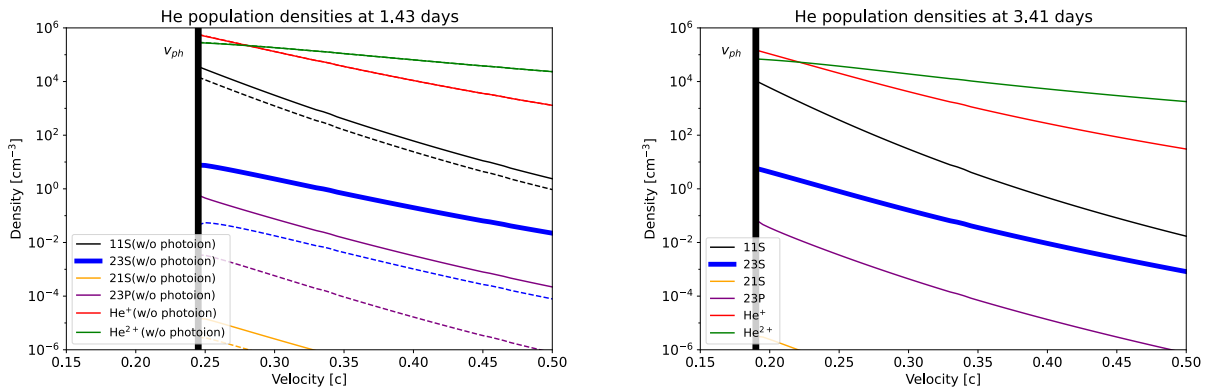


Figure 39: Population of He levels plotted against velocity shell at 1.43 days on the left and 3.41 days on the right. Only outside the photosphere is shown, where the photospheric velocities are  $0.245c$  and  $0.19c$  at 1.43 days and 3.41 days, respectively. The spectral line feature appears when  $n(\text{He I}, 2^3\text{S}) \gtrsim 7.4t_d^{-1} \text{ cm}^{-3}$  around the photosphere is satisfied. The solid lines show the population in the case that the line blanketing of UV photons reduces the photoionization rate. The dotted lines for the 1.43 days model show population without the blanketing. Note that the line blanketing is not important for the level population at 3.41 days.

The population profile of each level at 1.43 and 3.41 days is shown in Figure 39. The photospheric density of the  $2^3\text{S}$  level is higher than the critical value in Equation 43. Line blanketing is crucial for the early epoch: the no-blanketing model predicts the abundance of two dex lower, which is insufficient for the line formation. The wide separation seen in the populations of  $\text{He}^+$  and the  $2^3\text{S}$  level is due to efficient photoionization. The next well-populated level is  $2^3\text{P}$ , which is excited from  $2^3\text{S}$  by blackbody radiation. The population ratio between  $n_{2^3\text{S}}$  and  $n_{2^3\text{P}}$  is well approximated by

$$\frac{n_{2^3\text{P}}}{n_{2^3\text{S}}} = \frac{3}{1} \exp\left[\frac{-(E_{2^3\text{P}} - E_{2^3\text{S}})}{kT_{\text{phot}}}\right] \times W(v). \quad (57)$$

The ratio indicates that the blackbody radiation govern the transition between the two levels. Even the second most populated excited level,  $2^3\text{P}$ , has somewhat lower densities  $\lesssim 1 \text{ cm}^{-3}$ . The absorption lines at  $5877 \text{ \AA}$  and  $7067 \text{ \AA}$  are absent because of the small population. All

the other excited levels have densities less than  $10^{-2} \text{ cm}^{-3}$ , which is too small to produce observable effects on the spectrum. Therefore, we expect that no other He lines appear in a kN.

## 7.5.2 Sr model

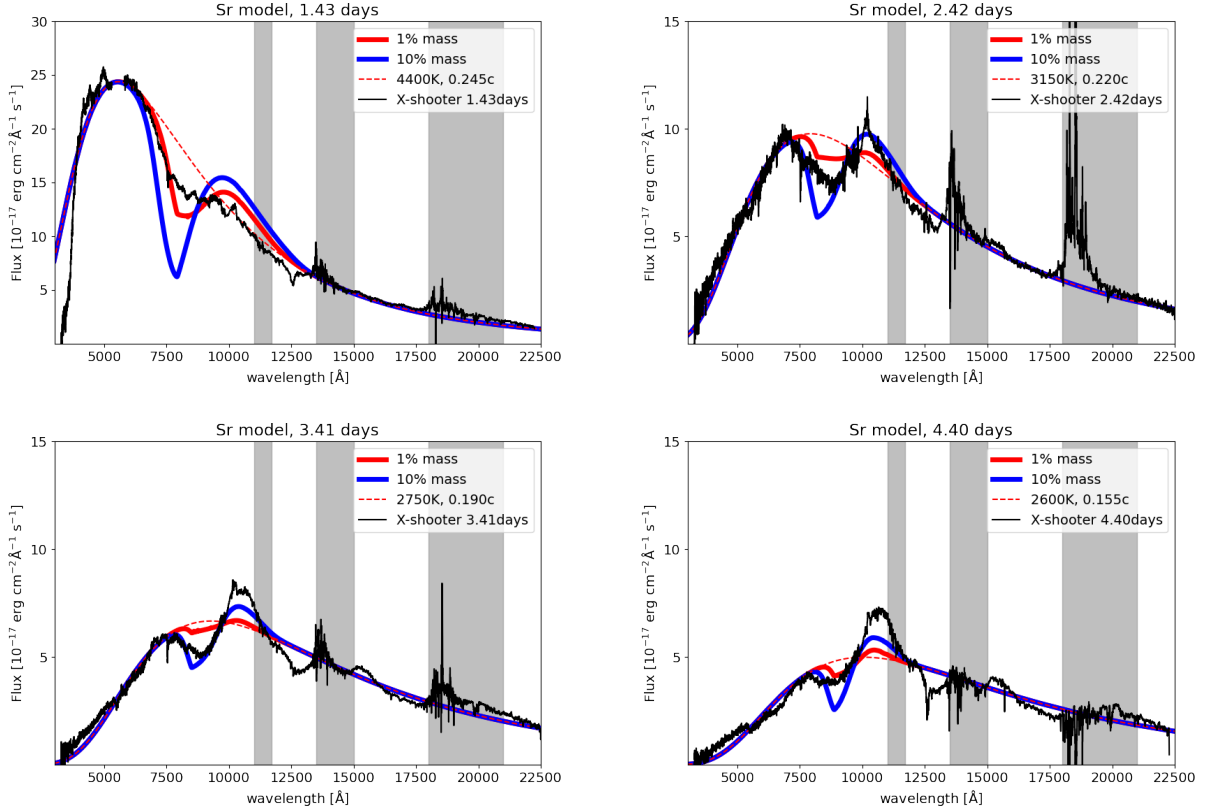


Figure 40: Same as Figure 38 but for the Sr model. The red and blue lines represent model spectra with Sr mass fractions of 1% and 10%. Note that the solar  $r$ -process ratio results in  $\sim 1\%$ .

Figure 40 shows the results for the Sr model. In the fiducial model, the mass fraction of 1%, the P-Cygni feature is stronger than the observation at 1.43 days, while it gets weaker quickly at later epochs. The enhanced model, mass fraction of 10%, produces features consistent with observations at 2.42-4.40 days. However, the feature is too strong at the first epoch.

The weakening of the line feature is a consequence of overionization by non-thermal particles. The decline is quicker than He as in the estimates in Equations 43 and 44. If Sr II is the origin of the line, the photosphere must go inside quickly from 1.43 to 4.40 days. Another intriguing possibility is that the spectral feature at the first two epochs is from Sr II, and He I takes over in the later epochs. Constraints on the time evolution of the photospheric density are crucial for more accurate modeling.

Contrary to the case of He, population ratios between different levels of Sr II are not much affected by the nonthermal particles because 4D levels are in pseudo-equilibrium with the ground level via radiative transitions to 5P levels, which is very efficient. The photospheric temperature determines the population ratio of 4D states against the ground level. The ratio ( $n_{\text{Sr}_{4\text{D}}^+}/n_{\text{Sr}_{5\text{S}}^+}$ ) would be lower if the temperature decreases.

At temperatures around 3000–4000 K, singly ionized Sr is favored at lower temperature in the Saha equilibrium. This effect helps maintain somewhat large population of the 4D level in the later epochs in LTE analyses. However, nonthermal ionization is not affected by the temperature. Although the recombination coefficient introduces a weak dependence, the overall ionization structure does not depend much on temperature. Therefore, in the non-LTE case, the dependence of ionization levels on temperature becomes weak. The population of the 4D level now depends predominantly on the local density, which affects recombination rates.

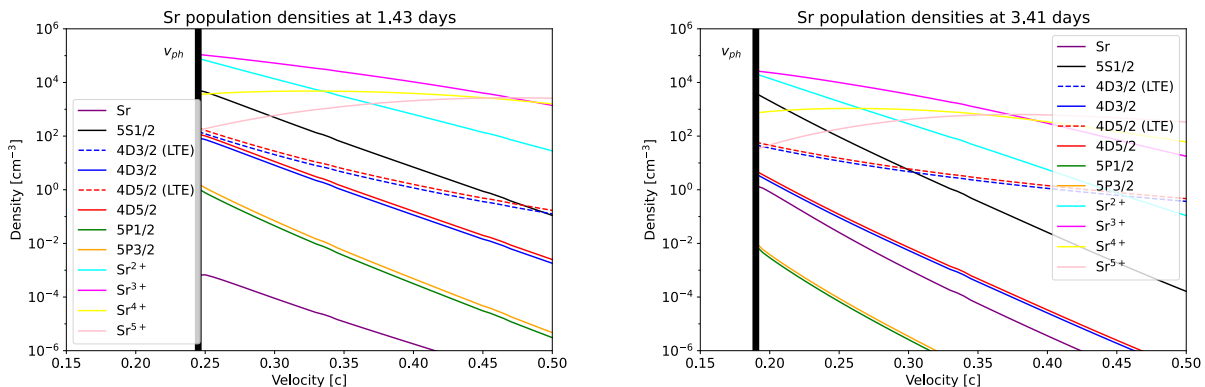


Figure 41: Same as Figure 39 but for the Sr model. The Sr II line feature appears when  $n(\text{Sr II}, 4^2\text{D}) \gtrsim 50t_d^{-1} \text{ cm}^{-3}$  is satisfied. Dashed lines represent populations for  $4^2\text{D}$  levels assuming LTE of the photospheric temperature.

## 7.6 Effect of UV blanketing for He

Figure 42 shows the dependence of photospheric density of He I<sub>235</sub> level. The UV strength needs to be less than  $\sim 0.3\%$  of the blackbody radiation to explain the observation at the first epoch. A similar estimate for the 2.42 days gives the maximum UV strength to be  $\sim 30\%$ .

### 7.6.1 Comparison to SN Ibc on He lines

An interesting comparison can be made between our He model and the He-rich type-Ib supernovae. In our model calculations, we have shown that the single levels are far less populated than the triplet levels. Contrastingly, in type-Ib supernovae, the defining feature is the singlet transition line at 20587 Å line (see, e.g., Lucy 1991).

The population mechanism is the same between  $S = 0$  and  $S = 1$  levels: recombination from singly ionized He. The difference comes from the depopulation mechanism. Figure 43

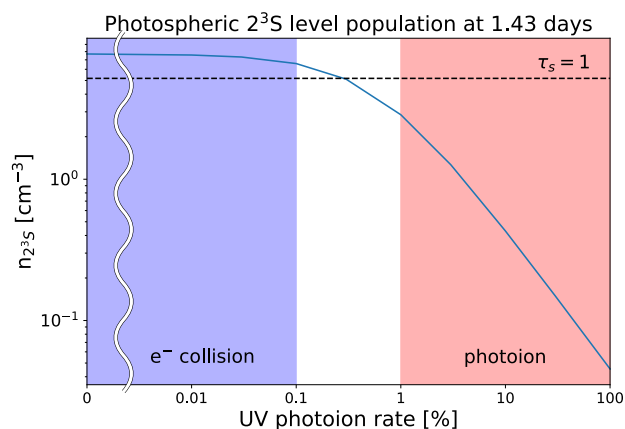


Figure 42: Photospheric density of the line-forming level,  $\text{He}_{2^3S}$ , as a function of UV strength. Photoionization dominates if UV strength is more than 1% of blackbody emission, while electron collision take it over if it is less than 0.1%.

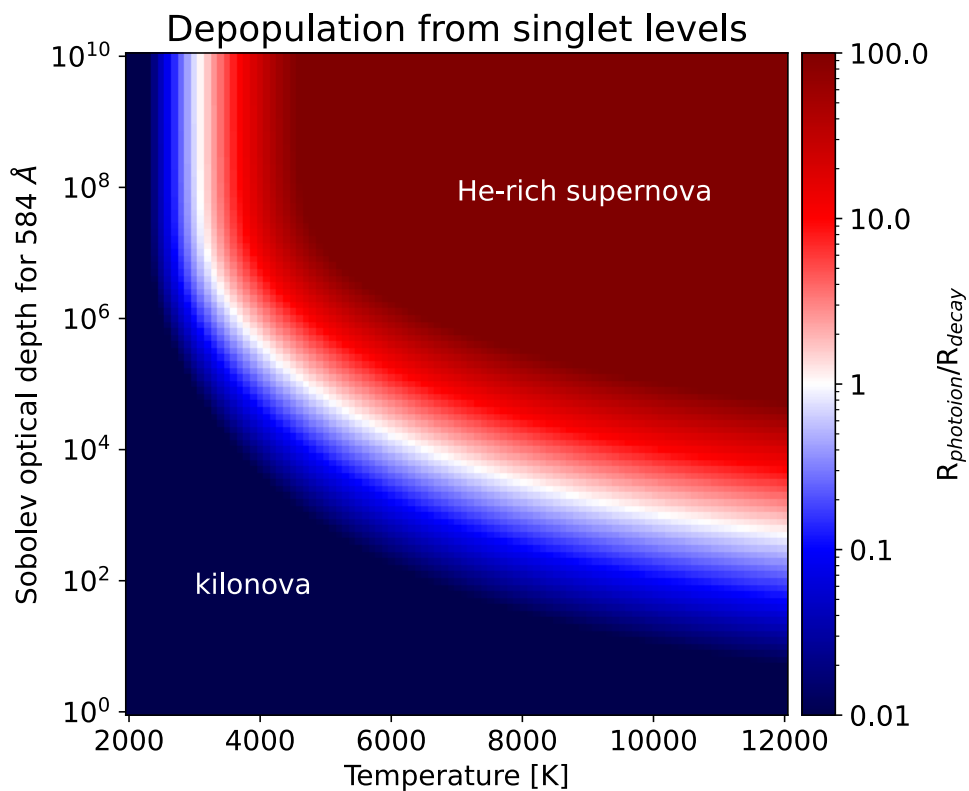


Figure 43: Photoionization rate divided by the natural decay rate from  $n = 2$  singlet levels.

Literature	Type	$X_{\text{He}}$
Goriely et al. (2015)	Dynamical ejecta	$\sim 10^{-1}$
Lippuner et al. (2017)	Massive neutron star wind	$\sim 10^{-1}$
Fernández and Metzger (2013)	Black-hole disk wind	$\sim 10^{-2}$
Kullmann et al. (2022)	Dynamical ejecta	$\sim 10^{-2}$
Perego et al. (2022)	Dynamical ejecta	$\sim 10^{-3}$
Wanajo (2018)	Phenomenological model	$10^{-4}$ – $10^{-3}$
Fujibayashi et al. (2022)	Dynamical & post-merger ejecta	$10^{-4}$ – $10^{-3}$
Perego et al. (2022)	Spiral-shock wind	$\sim 10^{-4}$
Wanajo et al. (2014)	Dynamical ejecta	$\sim 10^{-5}$

Table 2: Mass fraction of Helium in neutron star merger ejecta in simulations in the literature. Note that the values depend on mass ratio and other conditions: the values should be used only as a rough guide to the literature. For the exact mass fractions, readers should refer to original papers.

shows the ratio of the photoionization rate and natural decay rate on the temperature-optical depth plane. We have assumed that the population of  $2^1\text{P}$  is

$$\frac{n_{2^1\text{P}}}{n_{2^1\text{S}}} = \frac{3}{1} \exp\left[\frac{-(E_{2^1\text{P}} - E_{2^1\text{S}})}{kT_{\text{phot}}}\right] \times W, \quad (58)$$

and  $W = 0.5$  assuming the velocity coordinate at the photosphere. Photoionization is the dominant mechanism for type-Ib supernovae, which has high density of neutral He that hinders the natural decay, and the high photospheric temperature. KN ejecta has lower density of He and therefore, the escape probability is high. Once a  $2^1\text{S}$  atom is excited to the  $2^1\text{P}$  level, it quickly decays to the ground level via the very efficient natural decay of  $A_{2^1\text{P} \rightarrow 1^1\text{S}} = 2.0 \times 10^9 \text{ s}^{-1}$ .

## 7.7 Discussion

### 7.7.1 He production in neutron star merger and spectral feature

In the previous section, we have shown that 0.2% of He produces sufficiently strong line feature in the kN spectrum. Non-LTE effect crucially increases the abundances of the  $2^3\text{S}$  level and allows to form the line feature.

Fernández and Metzger (2013) point out that He can be produced in a significant amount in NSM ejecta via the  $\alpha$ -rich freeze-out. They have derived a formula following the formulation by Hoffman et al. (1997) that relates the He mass fraction  $X_{\text{He}}$  and the ejecta entropy. The bottleneck reactions for the He burning before the  $r$ -process is  $^4\text{He}(\alpha n, \gamma)^9\text{Be}(\alpha, n)^{12}\text{C}$ , which is effectively a four-body reaction (three  $\alpha$ s and a neutron). Therefore, the fraction of He at the end of the  $\alpha$ -process can be estimated by the integration of the reaction rate from  $T = 5 \cdot 10^9 \text{ K}$  to  $2.5 \cdot 10^9 \text{ K}$ , when He burning occurs.

Using the He mass fraction, we can estimate the typical entropy of the ejecta. Assuming

that the fraction is  $X_{\text{He}} = 2 \times 10^{-3}$ ,

$$S \simeq 18 \times \left(\frac{\bar{Z}}{36}\right)^{1/3} (1 - 2Y_e)^{1/3} \left(\frac{\tau_{\text{dyn}}}{10[\text{ms}]}\right)^{1/3} [k_B \text{ nuc}^{-1}], \quad (59)$$

where  $\bar{Z}$ ,  $Y_e$ ,  $\tau_{\text{dyn}}$  are the average proton number of the seed nuclei, electron fraction, and the dynamic timescale, which is the timescale for the temperature decrease by a factor of  $e$  (Hoffman et al. 1997). The dynamic timescale  $\tau_{\text{dyn}}$  is uncertain, although Fernández and Metzger (2013) estimate  $\tau_{\text{dyn}} \simeq 100$  [ms] for the black-hole disk wind.

The mass fractions in NSM simulations in the literature are summarized in Table 2. Although the range of  $X_{\text{He}}$  is wide, many simulations predict  $X_{\text{He}} \sim 10^{-2}$ , that is sufficient for the line formation. It is thus plausible that the P-Cygni feature in AT2017gfo is made by the transitions of neutral He. If correct, the He fraction  $X_{\text{He}}$  will be useful to infer the ejecta entropy, which is an independent probe of the physical conditions of the ejecta.

Perego et al. (2022) argues that the He line signature is too weak to be observed. In their models, they estimate that the mass of He in kN ejecta is  $1 - 10 \cdot 10^{-6} M_{\odot}$ , an order of magnitude lower than our assumption ( $8 \times 10^{-5} M_{\odot}$ ). They use an analytical approximation model developed for He-rich ejecta of double-detonation type-Ia SNe in TARDIS. However, it is unclear whether the model applies to the case of a kN. Their results might be consistent with ours if the adopted He masses are similar.

### 7.7.2 Non-local thermal equilibrium effect on Sr

The ionization states of Sr are significantly affected by the non-thermal particles. This is clearly seen in the hindrance of the recombination of Sr III to Sr II from 1.43 days to later epochs. Watson et al. (2019b) model the line signature under the assumption of Sr II lines being the origin. With a one-dimensional Monte-Carlo radiative transfer code TARDIS, they model the strength of Sr line absorption feature. They argue that  $5 \times 10^{-5} M_{\odot}$  of Sr is needed in the line forming region at 1.43 days. The required mass decreases to  $\sim 1 \times 10^{-5} M_{\odot}$  for later epochs.

The decrease in the amount of Sr is the consequence of the recombination from Sr III to Sr II. From 1.43 to 2.42 days, temperature declines from  $\sim 4000$  to  $\sim 3000$  K. During these epochs, the most abundant ionization levels shift from Sr III to Sr II. The picture is significantly different in our model. Since high-energy particles keep the ionization rate relatively high, the ionization states is less sensitive to the temperature decrease. Rather, the decrease in the density strongly affect the ionization states. The line feature gets weaker from 1.43 days to later epochs.

### 7.7.3 Comparison of He and Sr line features

Both He and Sr possibly show the P-Cygni profile. It is crucial to distinguish between these two elements. Observation of other transition lines from these elements is a possible way for such test. For He, however, we have seen that no other lines appear on kN spectrum. Possible candidates for Sr II are strong transitions at 4079 and 4217 Å between the ground and the 5P levels. Sobolev optical depths for these transitions are always higher than the Sr II triplet transitions because (i) the population of the ground states are higher than the

4D states by the Boltzmann factor ( $\sim 10$  including degrees of freedom and assuming the temperature of  $\sim 5000$  K), and (ii) the oscillator strengths of the transitions are higher by a factor of 8. The sharp UV decline in the spectrum at the first epoch may be a consequence of these transitions (Watson et al. 2019b).

Such line signature is not present in the spectra at 2.42-4.40 days. This seems to be contradictory for the Sr model. However, we cannot firmly exclude it because the continuum emission at the wavelength is weak. Although a few spectroscopic observations at early epochs are available (McCully et al. 2017; Andreoni et al. 2017), we could not model the 5S-5P transitions because the shorter wavelength side of the feature was not covered. Also, the single-line assumption is not valid at this wavelength: many lines exist around  $\sim 4000$  Å. Spectra taken at early (0.5 – 1.5 days) epochs, from near-UV to near-IR wavelength range will be crucial for further modeling the level populations.

The forbidden lines from two 4D levels of Sr are also too weak. Blackbody photospheric emission dominates at early epochs. At later ( $\gtrsim 10$  days) epochs, Sr is overionized by beta particles to higher ionization states. We do not expect to see such emission line signature in kilonova.

#### 7.7.4 Model uncertainties and limitations

We compute the populations and spectrum in simplified settings, e.g., we assume that the continuum emission is a blackbody radiation that comes from a sharply defined photosphere. Here we discuss the assumptions and limitations of this work.

**7.7.4.1 UV flux and the photospheric temperature** The flux of ionizing photons ( $> 4.8$  eV) is the crucial parameter for our He photoionization modeling. An increase of the photospheric temperature results in higher UV flux. Another crucial factor is the UV absorption by heavy ions as we have seen in Section 7.6. Observations that accurately determine the UV flux at this wavelength will be crucial for a better modeling of the He level populations. Spectra at early epochs are important also for Sr modeling as we have discussed in 7.7.3.

For Sr, the ratio of the populations between 4D and the ground levels follows the Boltzmann distribution with the photospheric temperature. Therefore, a higher temperature favors the 4D levels. The photon energies of relevant transitions are 3.0 and 1.2 eV: see Figure 36). The wavelengths are close to the optical wavelength, which is not affected by the UV cut-off in the spectrum. The observed flux of the photons that mediate these transitions is not much different from that of blackbody emission. Therefore, we expect that our modeling by blackbody flux approximately captures the physics.

**7.7.4.2 Photospheric density** Ejecta density is crucial because it affects the recombination rate. Higher density gives a stronger spectral feature because of enhanced recombination. The effect is crucial for Sr in particular, because higher density efficiently suppresses over-ionization by non-thermal particles. Sr models produce results consistent with the observation if we enhance the total Sr mass by a few to 10 times from 2.42 to 4.40 days, whereas the amount should be decreased by half for 1.43 days. We regard such an ad-hoc reduction/enhancement by a factor of 20 as unphysical. Still, some higher-order effects such

as ejecta stratification, peculiar density structure, opacity evolution, etc. may affect the photospheric density. Our simple model does not capture such factors, which may be important for the line signature.

**7.7.4.3 Lines of other ions** The NSM ejecta is mostly heavy elements, and their bound-bound transitions dominate the opacity. Our model implicitly assumes that the photosphere is determined by the line expansion opacity. However, the opacity depends on the wavelength. Therefore, the position of photosphere, i.e., the last scattering surface, would also depend on the wavelength. In the wavelength region of  $\gtrsim 8000 \text{ \AA}$ , bound-bound transitions of lanthanides and actinides likely dominate the opacity. We have assumed that these lines are too weak to form an absorption feature, but it may collectively form an absorption-like feature (Kasen et al. 2013; Tanaka and Hotokezaka 2013; Tanaka et al. 2020; Fontes et al. 2020; 2022).

**7.7.4.4 Asphericity** Our model assumes spherical symmetry. In reality, the ejecta shape and the composition distribution are expected to be somewhat aspherical. Some works have pointed out that direction-dependent ejecta composition affect the emission (Kawaguchi et al. 2018; Wollaeger et al. 2018; Bulla 2019; Darbha and Kasen 2020; Korobkin et al. 2021). Because our model focuses on the line signature on continuum emission, it is sensitive to the abundances of the material moving toward the observer. The total amount of elements may be different from the mass estimate under spherical symmetry.

**7.7.4.5 Nonthermal ionization rate** We assume that the radioactive energy contributes to the ionization via  $\beta$  particles and the radioactive heating rate is uniform across the ejecta. However, the nonthermal ionization rates become lower if most of the decay energy comes out as kinetic energies of heavier particles such as  $\alpha$  particles or fission fragments (see, e.g., Wanajo 2018; Wu et al. 2019; Hotokezaka and Nakar 2020). We also note that the radioactive heating rate around Sr, i.e.,  $80 \lesssim A \lesssim 110$  is significantly weaker around 1–10 day than that of  $A \geq 110$ . If the elemental abundances in the ejecta is highly inhomogeneous and it spatially separates Sr from heavier elements, the ionization rate for Sr can be significantly lower. The low ionization rate allows more Sr to remain singly ionized, making absorption features stronger for Sr models at later times.

**7.7.4.6 Relativistic effect** The line formation region can be as fast as  $\sim 0.3c$ . In such a fast ejecta, the Doppler effect needs to be considered. The Doppler effect changes the effective temperature of the blackbody emission (Rybicki and Lightman 1986). The blackbody emission is isotropic on a frame comoving with the photosphere. The expansion velocity of the absorption line forming region is always faster than the photosphere. Therefore, the Doppler effect would lower the temperature of the blackbody emission in the ejecta frame. It could work to decrease the UV flux in the first two epochs to help populate the  $2^3\text{S}$  level of He atoms.

## 7.8 Conclusion

We have shown that He atoms in kN can synthesize the P-Cygni profile, as observed in AT2017gfo, if the mass fraction of He is  $X_{\text{He}} \sim 0.2\%$ . In particular,  $X_{\text{He}} \gtrsim 0.1\%$  is expected from the  $\alpha$ -rich freeze-out of neutron-rich ejecta with an entropy of  $\sim 20 [k_B \text{ nuc}^{-1}]$ . We model the spectra including the non-LTE effects, e.g., radioactive ionization by  $\beta$  particles, which increases the ionization degree in the line forming region. The recombination of electrons and singly ionized He populates the metastable triplet level, which is responsible for the absorption line He I 10833 Å. Our model reproduces the line optical depth at the epochs of 2.4 and 3.4 days. A caveat in our He model for the observed line is that the line strength at the earliest epochs is sensitive to the photoionization rate from the  $2^3\text{S}$  level. In fact, the He I is expected to be absent at 1.43 days if we assume that the continuum radiation has a black body spectrum with 4400 K. However, the sharp cut-off in the observed spectrum around 4000 Å at 1.43 days indicates that the blackbody model overestimates the photoionization rate. Observations of the UV flux at early epochs will be beneficial for correctly modeling the photoionization, which will be a new probe for the mass ejection mechanism from ejecta entropy.

We have also explored the line formation by Sr II triplet around 10000 Å. Although the lines are expected to be among the strongest ones in the LTE condition (Watson et al. 2019a; Domoto et al. 2022), the strength will be significantly reduced by radioactive ionization in the line-forming region. We found that the line signature is likely the strongest at  $\sim 1.5$  days and gets weaker with time because the efficiency of radioactive ionization increases with time. We have shown that Sr of mass fraction  $\sim 1\%$  is sufficient for the line formation at 1.43 days, which is roughly expected from the solar  $r$ -process abundances. However, we found that the model fails to reproduce the spectra at the later epochs unless the mass fraction of Sr around the photosphere increases with time. Alternatively, it is possible that Sr II dominates the line feature at the earlier times while He I dominates at the later times. The two transitions of Sr II at  $\sim 4000$  Å at early epochs will help infer the amount of Sr. Optical properties of light  $r$ -process elements also help constrain the amount of Sr in kN ejecta.

## 8 Summary

Neutron-capture element enrichment of Local group systems is studied in this thesis. Systems of different sizes are useful for constraining nucleosynthesis in different environments. UFDs are particularly useful as it discretizes contribution from rare events such as  $r$ -process in NSM. For  $r$ -poor UFDs, I have pointed out that the AGB stars fail to reproduce the observed Ba and Sr abundances. The typical star formation duration of a UFD is a few hundred Myrs, which is too short for allowing contributions from AGB stars. In addition, the low metallicity further helps to suppress the AGB contribution. RMSs are a possible candidate for the production of  $s$ -process elements. However, further study is needed as the heavy-to-light  $s$ -process element ratio ( $[\text{Ba}/\text{Sr}]$ ) does not follow the expectations from RMS models.

Larger galaxies such as classical dwarfs and the MW are useful for studying the statistical properties such as delay time distribution. Although NSMs are regarded as the most promising candidate for the origin of the  $r$ -process elements, a counterargument still exists in terms of delay time distribution: if NSMs are the origins of the  $r$ -process elements, we expect an increasing trend of  $[r/\text{Mg}]-[\text{Fe}/\text{H}]$ , which is not seen in observations. In Section 5, I have discussed and concluded that the evidence for the time delay is seen in Ba abundances in the metal-poor stars of the MW. Interestingly, classical dwarf galaxies follow the same trend in spite of the variety of star formation histories. This is the first supportive evidence for delayed sources such as NSM.

The inhomogeneous enrichment of  $r$ -process elements in metal-poor systems provides us with a crucial clue for the formation path of a GC. Some works ascribe the  $r$ -process abundance spread in M15 to an  $r$ -process event between formations of FG and SG stars. However, the lack of Na-Eu correlation is a critical counterargument that has been neglected in previous works. The abundance feature is more naturally interpreted as an intrinsic abundance spread in the natal cloud of a GC. This interpretation is justified by the formation rate of such GC, i.e., GC with an internal Eu abundance spread. I have pointed out that the number of star formation epochs in a GC should be one, or otherwise, the SG stars should show smaller Eu abundance spreads than the FG stars.

While galaxy formation simulations and the modeling of chemical enrichment are useful for studying the mixing process, we also need to study the nucleosynthesis sites. Sr line has been claimed to be detected in the kN spectrum. However, non-LTE analysis is required to properly model the level population. I have pointed out that He is a possible candidate for the origin of the line feature. The abundance of He would serve as a potential clue for the mass ejection mechanism.

In summary, for neutron-capture element synthesis, this thesis has clarified that (i) an additional source with a short delay and efficient at low metallicity ( $[\text{Fe}/\text{H}] < -2$ ) should exist and (ii) time delay of the  $r$ -process element synthesis exist, and (iii) spectral feature found in kN AT2017gfo may not be Sr but He. In terms of galaxy formation processes, (iv) a UFD with an extended profile could be formed as a consequence of the wet merger, and (v) the number of star formation epochs for a GC is favored to be one, from the fact that the abundances of Na and Eu are independent with each other.

## 9 Future prospects

Neutron-capture elements are fossils in a galaxy that allows us to probe its formation history. The abundance ratio  $[s/\text{Mg}]$  and  $[r/\text{Mg}]$  are essential information. The diverse abundance trends of  $[s/\text{Mg}]-[\text{Fe}/\text{H}]$  seen among dwarf galaxies is supportive evidence that the information on the galaxy evolution is imprinted in these distributions.

We need to identify the origins of  $r$ - and  $s$ -process elements to exploit their potential. For solar metallicity stars, the origin of the  $s$ -process is the AGB stars. Confirming the  $r$ -process element synthesis in the neutron-star merger event is a recent breakthrough. We find an increasing trend in the  $[r/\text{Mg}]$  abundance in the metal-poor stars in Milky Way. Interestingly, the trends are similarly seen among dwarf galaxy stars, despite the fact that the star formation histories are likely to be diverse. Note that the sample size for abundances in dwarf galaxies is still small. Enhancing the sample size for the  $r$ -process abundances in dwarf galaxies will clarify whether the trend is truly universal. The limiting magnitude of spectroscopic observations with Subaru prime focus spectrograph (PFS) is  $\sim 22$  magnitude<sup>10</sup>. It covers stars at the main-sequence turn-off of the oldest stellar population if the dwarf galaxy is within 30 kpc from the sun. Thirty-meter telescope (TMT) will further progress the limit to  $\sim 26$  magnitude (Moore et al. 2014), which extends the limit to the entire region of the Milky Way halo.

An unsolved problem for neutron star merger as the origin of the  $r$ -process elements is the constant  $[\text{Eu}/\text{Mg}]$  abundances seen among Milky Way disk stars of  $[\text{Fe}/\text{H}] > -0.8$ . Neutron star mergers induce an increasing trend in  $[\text{Eu}/\text{Mg}]$  as metallicity because of the long coalescence time. An interesting follow-up analysis is to look at the stellar age instead of metallicity. The age of a star has been unreachable information because of the difficulty in knowing the precise absolute magnitude of a star. However, the Gaia satellite has greatly improved the distance measurement. With the isochrone fitting, the error in the age estimate is now  $\sim$  Gyr. Asteroseismology with light curves obtained with Kepler and TESS satellites will also help determine stellar age. A successful chemical evolution model after the Gaia satellite needs to explain this age information and the chemical abundances of stars in the Milky Way.

Much theoretical work is still needed to interpret the abundance distribution in dwarf galaxies appropriately. No chemical evolution model successfully explains the diverse trends in neutron-capture element abundances among dwarf galaxies. Two primary sources of uncertainties are the yield from very metal-poor stars and galaxy evolution processes. UFDs have been instrumental in probing the shortest timescales ( $\lesssim 100$  Myr) and very metal-poor environments. The need for another source of the  $s$ -process elements is illuminated. We need to consider the contribution from the source for modeling the chemical evolution of the lowest metallicity stars in dwarf galaxies.

On the other hand, relatively metal-rich ( $[\text{Fe}/\text{H}] > -1$ ) stars are less affected by the additional  $s$ -process source. Therefore, we can assume that the origin of the  $s$ -process elements is the AGB stars, and they are ideal samples for studying galaxy-dependent evolution processes. Fornax dwarf galaxy is the primary sample that displays a peculiar abundance pattern.

---

<sup>10</sup><https://pfs.ipmu.jp/research/performance.html>

Although rotating massive stars are proposed as a possible origin of the *s*-process, there remains significant uncertainty in the structure of a rotating star. A key physical process is angular momentum transport. Chemical diffusion in an evolved rotating star's radiative core region is necessary for the *s*-process nucleosynthesis. However, a single rotating star may lose angular momentum via stellar evolution. Recent observations of red giant stars suggest that the core of a red giant star rotates slower than predictions of stellar models (Fuller et al. 2019), implying that the angular momentum transport is efficient. Applying the same model to a rotating massive star, we expect the core rotation to be too slow to allow the *s*-process synthesis. The calibration of the stellar model for rotating stars is crucial for further investigation of this *s*-process channel.

Another interesting process to consider is the binary stellar evolution. Binary mass transfer spins up the accretor star. If it occurs during the core Helium burning phase, the *s*-process nucleosynthesis is activated. Tidal force from the companion also affects the spin of a star. Such effects of binarity have yet to be addressed in chemical evolution studies because of the poor constraints we obtain from observations. However, the population of observed binary systems is growing: Gaia astrometry is useful for finding binaries with compact objects. The population of peculiar binaries, such as Be star-bloated subdwarf star binary, would help us elucidate the evolution of binary systems.

The understanding of the *r*-process nucleosynthesis in kilonova will progress with the JWST and LIGO O4. The most promising methodology for studying nucleosynthesis is nebular spectroscopy. Thanks to the great sensitivity in the infrared, JWST will see the nebular emission from the heaviest elements synthesized by a neutron star merger. Although the ejecta opacity can estimate the lanthanide fraction, an independent estimate from the nebular spectrum will be crucial for the test of neutron star mergers as the origin of the *r*-process elements.

In summary, neutron-capture elements help decipher the formation history of Local group galaxies. For the *r*-process elements, we first need to test neutron star mergers as the origin of the *r*-process elements. Assuming that the *r*-process elements are synthesized by neutron star mergers, reproducing the flat [Eu/Mg] trend against metallicity will be a crucial exercise that may elucidate the complexity of the chemical evolution processes we do not acknowledge. Another interesting galaxy evolution problem is the diversity of dwarf galaxies. A chemical evolution model that explains the abundances of the variety of galaxies in a unified manner should contain rich physics in galaxy formation. Information on the age of stars will revolutionize the chemical modeling of galaxies.

## Acknowledgements

First and foremost, I would like to express my gratitude to my adviser, Naoki Yoshida, for his support from every aspect during five years of research, from my master's to my Ph.D. His insightful comments have been indispensable for the completion of papers. Next, I would like to thank Kenta Hotokezaka for his guidance on research in general. Studies on neutron star mergers have been only possible with his extensive experience. I have learned a lot from his attitude toward scientific research. Their supervision has been essential for me throughout my study in graduate school.

I want to thank my colleagues who have supported my research. Most research uses numerical simulation code AREPO. Shigeki Inoue has patiently taught me the basics of code during my master's. I have learned the basics of the  $s$ -process nucleosynthesis from Takuma Suda. Discussion with Anna Frebel has been instrumental in studies of UFDs. I have learned a lot about supernova theory and observations from Masaomi Tanaka. All these people have helped me cultivate my interest in a wide range of topics in astrophysics.

Lastly, I would like to sincerely thank my partner, Rei. I always gain energy from spending the happiest time with her. It would have been impossible to complete all the work without her.

## A Acronyms

Table 3: Acronyms

Acronym	Full form	First appearance
AGB	Asymptotic giant branch	Section 1
BBN	Big-bang nucleosynthesis	Section 2
BNS	Binary neutron stars	Section 5
CCSN	Core-collapse supernova	Section 3
CEMP- <i>s</i> star	<i>S</i> -process enhanced carbon-enhanced metal-poor star	Section 5
CMD	Color-magnitude diagram	Section 6
DD	Double-degenerate	Section 1
DES	Dark-energy survey	Section 2
DTD	Delay-time distribution	Section 5
E-AGB	Early-AGB	Section 1
ECSN	Electron-capture supernova	Section 3
FDU	first dredge-up	Section 1
FG	First generation	Section 2
GALAH	GALactic Archaeology with HERMES survey	Section 2
GC	Globular cluster	Section 2
GCE	Galactic chemical evolution	Section 3
GRB	Gamma-ray burst	Section 5
IDROV	Initial distribution of rotational velocities	Section 1
IMF	Initial-mass function	Section 3
ISM	Interstellar medium	Section 1
LTE	Local thermal equilibrium	Section 7
MP	Multiple population	Section 6
MRSN	Magneto-rotational supernova	Section 5
MW	Milky-Way	Section 3
NSE	Nuclear statistical equilibrium	Section 1
NSM	Neutron-star merger	Section 3
Pan-STARRS	Panoramic Survey Telescope & Rapid Response System	Section 2
QSE	Quasi-statistical equilibrium	Section 1
RMS	Rotating massive star	Section 3
SD	Single degenerate	Section 1
SDSS	Sloan digital sky survey	Section 1
SDU	Second dredge-up	Section 1
SFR	Star formation rate	Section 3
SG	Second generation	Section 2
SN	Supernova	Section 1
SPH	Smoothed-particle hydrodynamics	Section 3
SSP	Single stellar population	Section 3
TDU	Third dredge-up	Section 1
TP-AGB	Thermally-pulsing AGB	Section 1
UFD	Ultrafaint dwarf	Section 2
WD	White dwarf	Section 1
dSph	Dwarf spheroidal	Section 3
kN	Kilonova	Section 7

## References

- Abdu Abohalima and Anna Frebel. JINAbase—A Database for Chemical Abundances of Metal-poor Stars. *Astrophysical Journal Supplement*, 238(2):36, October 2018. doi: 10.3847/1538-4365/aadfe9.
- Oscar Agertz, Andrew Pontzen, Justin I. Read, Martin P. Rey, Matthew Orkney, Joakim Rosdahl, Romain Teyssier, Robbert Verbeke, Michael Kretschmer, and Sarah Nickerson. EDGE: the mass-metallicity relation as a critical test of galaxy formation physics. *Monthly Notices of the Royal Astronomical Society*, 491(2):1656–1672, January 2020. doi: 10.1093/mnras/stz3053.
- L. A. Aguilar and S. D. M. White. The Density Profiles of Tidally Stripped Galaxies. *Astrophysical Journal*, 307:97, August 1986. doi: 10.1086/164396.
- R. A. Alpher, H. Bethe, and G. Gamow. The Origin of Chemical Elements. *Physical Review*, 73(7):803–804, April 1948. doi: 10.1103/PhysRev.73.803.
- I. Andreoni, K. Ackley, J. Cooke, A. Acharyya, J. R. Allison, G. E. Anderson, M. C. B. Ashley, D. Baade, M. Bailes, K. Bannister, A. Beardsley, M. S. Bessell, F. Bian, P. A. Bland, M. Boer, T. Boller, A. Brandeker, I. S. Brown, D. A. H. Buckley, S. W. Chang, D. M. Coward, S. Crawford, H. Crisp, B. Crosse, A. Cucchiara, M. Cupák, J. S. de Gois, A. Deller, H. A. R. Devillepoix, D. Dobie, E. Elmer, D. Emrich, W. Farah, T. J. Farrell, T. Franzen, B. M. Gaensler, D. K. Galloway, B. Gendre, T. Giblin, A. Goobar, J. Green, P. J. Hancock, B. A. D. Hartig, E. J. Howell, L. Horsley, A. Hotan, R. M. Howie, L. Hu, Y. Hu, C. W. James, S. Johnston, M. Johnston-Hollitt, D. L. Kaplan, M. Kasliwal, E. F. Keane, D. Kenney, A. Klotz, R. Lau, R. Laugier, E. Lenc, X. Li, E. Liang, C. Lidman, L. C. Luvaul, C. Lynch, B. Ma, D. Macpherson, J. Mao, D. E. McClelland, C. McCully, A. Möller, M. F. Morales, D. Morris, T. Murphy, K. Noysena, C. A. Onken, N. B. Orange, S. Osłowski, D. Pallot, J. Paxman, S. B. Potter, T. Pritchard, W. Raja, R. Ridden-Harper, E. Romero-Colmenero, E. M. Sadler, E. K. Sansom, R. A. Scalzo, B. P. Schmidt, S. M. Scott, N. Seghouani, Z. Shang, R. M. Shannon, L. Shao, M. M. Shara, R. Sharp, M. Sokolowski, J. Sollerman, J. Staff, K. Steele, T. Sun, N. B. Suntzeff, C. Tao, S. Tingay, M. C. Towner, P. Thierry, C. Trott, B. E. Tucker, P. Väisänen, V. Venkatraman Krishnan, M. Walker, L. Wang, X. Wang, R. Wayth, M. Whiting, A. Williams, T. Williams, C. Wolf, C. Wu, X. Wu, J. Yang, X. Yuan, H. Zhang, J. Zhou, and H. Zovaro. Follow Up of GW170817 and Its Electromagnetic Counterpart by Australian-Led Observing Programmes. *Publications of the Astronomical Society of Australia*, 34:e069, December 2017. doi: 10.1017/pasa.2017.65.
- D. Argast, M. Samland, F. K. Thielemann, and Y. Z. Qian. Neutron star mergers versus core-collapse supernovae as dominant r-process sites in the early Galaxy. *Astronomy & Astrophysics*, 416:997–1011, March 2004. doi: 10.1051/0004-6361:20034265.
- Claudio Arlandini, Franz Käppeler, Klaus Wisshak, Roberto Gallino, Maria Lugaro, Maurizio Busso, and Oscar Straniero. Neutron Capture in Low-Mass Asymptotic Giant Branch

- Stars: Cross Sections and Abundance Signatures. *Astrophysical Journal*, 525(2):886–900, November 1999. doi: 10.1086/307938.
- Martin Asplund, Nicolas Grevesse, A. Jacques Sauval, and Pat Scott. The Chemical Composition of the Sun. *Annual Review of Astronomy and Astrophysics*, 47(1):481–522, September 2009. doi: 10.1146/annurev.astro.46.060407.145222.
- T. S. Axelrod. *Late Time Optical Spectra from the NICKEL(56) Model for Type i Supernovae*. PhD thesis, University of California, Santa Cruz, January 1980.
- Projjwal Banerjee, Meng-Ru Wu, and Zhen Yuan. Neutron Star Mergers as the Main Source of R-process: Natal Kicks And Inside-Out Evolution to The Rescue. *arXiv e-prints*, art. arXiv:2007.04442, July 2020a.
- Projjwal Banerjee, Meng-Ru Wu, and Zhen Yuan. Neutron Star Mergers as the Main Source of r-process: Natal Kicks and Inside-out Evolution to the Rescue. *Astrophysical Journal Letters*, 902(2):L34, October 2020b. doi: 10.3847/2041-8213/abbc0d.
- Z. Y. Bao, H. Beer, F. Käppeler, F. Voss, K. Wisshak, and T. Rauscher. Neutron Cross Sections for Nucleosynthesis Studies. *Atomic Data and Nuclear Data Tables*, 76(1):70–154, September 2000. doi: 10.1006/adnd.2000.0838.
- Jennifer Barnes and Daniel Kasen. Effect of a High Opacity on the Light Curves of Radioactively Powered Transients from Compact Object Mergers. *Astrophysical Journal*, 775(1):18, Sep 2013. doi: 10.1088/0004-637X/775/1/18.
- Jennifer Barnes, Daniel Kasen, Meng-Ru Wu, and Gabriel Martínez-Pinedo. Radioactivity and Thermalization in the Ejecta of Compact Object Mergers and Their Impact on Kilonova Light Curves. *Astrophysical Journal*, 829(2):110, October 2016. doi: 10.3847/0004-637X/829/2/110.
- Nate Bastian and Carmela Lardo. Multiple Stellar Populations in Globular Clusters. *Annual Review of Astronomy and Astrophysics*, 56:83–136, September 2018. doi: 10.1146/annurev-astro-081817-051839.
- D. R. Bates, A. E. Kingston, and R. W. P. McWhirter. Recombination Between Electrons and Atomic Ions. I. Optically Thin Plasmas. *Proceedings of the Royal Society of London Series A*, 267(1330):297–312, May 1962. doi: 10.1098/rspa.1962.0101.
- Kenji Bekki and Takuji Tsujimoto. Formation of Globular Clusters with Internal Abundance Spreads in r-Process Elements: Strong Evidence for Prolonged Star Formation. *Astrophysical Journal*, 844(1):34, July 2017. doi: 10.3847/1538-4357/aa77ae.
- V. Belokurov, D. B. Zucker, N. W. Evans, M. I. Wilkinson, M. J. Irwin, S. Hodgkin, D. M. Bramich, J. M. Irwin, G. Gilmore, B. Willman, S. Vidrih, H. J. Newberg, R. F. G. Wyse, M. Fellhauer, P. C. Hewett, N. Cole, E. F. Bell, T. C. Beers, C. M. Rockosi, B. Yanny, E. K. Grebel, D. P. Schneider, R. Lupton, J. C. Barentine, H. Brewington, J. Brinkmann, M. Harvanek, S. J. Kleinman, J. Krzesinski, D. Long, A. Nitta, J. A. Smith, and S. A.

- Snedden. A Faint New Milky Way Satellite in Bootes. *Astrophysical Journal Letters*, 647(2):L111–L114, August 2006. doi: 10.1086/507324.
- Paz Beniamini and Kenta Hotokezaka. Turbulent mixing of r-process elements in the Milky Way. *Monthly Notices of the Royal Astronomical Society*, 496(2):1891–1901, June 2020. doi: 10.1093/mnras/staa1690.
- Paz Beniamini and Tsvi Piran. Formation of double neutron star systems as implied by observations. *Monthly Notices of the Royal Astronomical Society*, 456(4):4089–4099, March 2016. doi: 10.1093/mnras/stv2903.
- Paz Beniamini and Tsvi Piran. The Gravitational waves merger time distribution of binary neutron star systems. *Monthly Notices of the Royal Astronomical Society*, 487(4):4847–4854, August 2019. doi: 10.1093/mnras/stz1589.
- Paz Beniamini, Kenta Hotokezaka, and Tsvi Piran. r-process Production Sites as Inferred from Eu Abundances in Dwarf Galaxies. *Astrophysical Journal*, 832(2):149, December 2016a. doi: 10.3847/0004-637X/832/2/149.
- Paz Beniamini, Kenta Hotokezaka, and Tsvi Piran. Natal Kicks and Time Delays in Merging Neutron Star Binaries: Implications for r-process Nucleosynthesis in Ultra-faint Dwarfs and in the Milky Way. *Astrophysical Journal*, 829(1):L13, Sep 2016b. doi: 10.3847/2041-8205/829/1/L13.
- Paz Beniamini, Irina Dvorkin, and Joe Silk. Retainment of r-process material in dwarf galaxies. *Monthly Notices of the Royal Astronomical Society*, 478(2):1994–2005, August 2018. doi: 10.1093/mnras/sty1035.
- A. Benítez-Llambay, J. F. Navarro, M. G. Abadi, S. Gottlöber, G. Yepes, Y. Hoffman, and M. Steinmetz. Mergers and the outside-in formation of dwarf spheroidals. *Monthly Notices of the Royal Astronomical Society*, 456(2):1185–1194, February 2016. doi: 10.1093/mnras/stv2722.
- K. A. Berrington and A. E. Kingston. Electron excitation in helium: including the n=4 levels in an R-matrix calculation. *Journal of Physics B Atomic Molecular Physics*, 20(24):6631–6640, December 1987. doi: 10.1088/0022-3700/20/24/014.
- James Binney and Scott Tremaine. *Galactic Dynamics: Second Edition*. 2008.
- S. Bisterzo, C. Travaglio, R. Gallino, M. Wiescher, and F. Käppeler. Galactic Chemical Evolution and Solar s-process Abundances: Dependence on the  $^{13}\text{C}$ -pocket Structure. *Astrophysical Journal*, 787(1):10, May 2014. doi: 10.1088/0004-637X/787/1/10.
- P. K. Blanchard, E. Berger, W. Fong, M. Nicholl, J. Leja, C. Conroy, K. D. Alexander, R. Margutti, P. K. G. Williams, Z. Doctor, R. Chornock, V. A. Villar, P. S. Cowperthwaite, J. Annis, D. Brout, D. A. Brown, H. Y. Chen, T. Eftekhari, J. A. Frieman, D. E. Holz, B. D. Metzger, A. Rest, M. Sako, and M. Soares-Santos. The Electromagnetic Counterpart of the Binary Neutron Star Merger LIGO/Virgo GW170817. VII. Properties of the Host

Galaxy and Constraints on the Merger Timescale. *Astrophysical Journal Letters*, 848(2): L22, October 2017. doi: 10.3847/2041-8213/aa9055.

Kaley Brauer, Alexander P. Ji, Anna Frebel, Gregory A. Dooley, Facundo A. Gómez, and Brian W. O’Shea. The Origin of r-process Enhanced Metal-poor Halo Stars In Now-destroyed Ultra-faint Dwarf Galaxies. *Astrophysical Journal*, 871(2):247, February 2019. doi: 10.3847/1538-4357/aafafb.

Thomas M. Brown, Jason Tumlinson, Marla Geha, Joshua D. Simon, Luis C. Vargas, Don A. Vandenberg, Evan N. Kirby, Jason S. Kalirai, Roberto J. Avila, Mario Gennaro, Henry C. Ferguson, Ricardo R. Muñoz, Puragra Guhathakurta, and Alvio Renzini. The Quenching of the Ultra-faint Dwarf Galaxies in the Reionization Era. *Astrophysical Journal*, 796(2): 91, December 2014. doi: 10.1088/0004-637X/796/2/91.

Sven Buder, Martin Asplund, Ly Duong, Janez Kos, Karin Lind, Melissa K. Ness, Sanjib Sharma, Joss Bland-Hawthorn, Andrew R. Casey, Gayandhi M. de Silva, Valentina D’Orazi, Ken C. Freeman, Geraint F. Lewis, Jane Lin, Sarah L. Martell, Katharine J. Schlesinger, Jeffrey D. Simpson, Daniel B. Zucker, Tomaž Zwitter, Anish M. Amarsi, Borja Anguiano, Daniela Carollo, Luca Casagrande, Klemen Čotar, Peter L. Cottrell, Gary da Costa, Xudong D. Gao, Michael R. Hayden, Jonathan Horner, Michael J. Ireland, Prajwal R. Kafle, Ulisse Munari, David M. Nataf, Thomas Nordlander, Dennis Stello, Yuan-Sen Ting, Gregor Traven, Fred Watson, Robert A. Wittenmyer, Rosemary F. G. Wyse, David Yong, Joel C. Zinn, Maruša Žerjal, and Galah Collaboration. The GALAH Survey: second data release. *Monthly Notices of the Royal Astronomical Society*, 478(4): 4513–4552, August 2018. doi: 10.1093/mnras/sty1281.

Sven Buder, Sanjib Sharma, Janez Kos, Anish M. Amarsi, Thomas Nordlander, Karin Lind, Sarah L. Martell, Martin Asplund, Joss Bland-Hawthorn, Andrew R. Casey, Gayandhi M. de Silva, Valentina D’Orazi, Ken C. Freeman, Michael R. Hayden, Geraint F. Lewis, Jane Lin, Katharine J. Schlesinger, Jeffrey D. Simpson, Dennis Stello, Daniel B. Zucker, Tomaž Zwitter, Kevin L. Beeson, Tobias Buck, Luca Casagrande, Jake T. Clark, Klemen Čotar, Gary S. da Costa, Richard de Grijs, Diane Feuillet, Jonathan Horner, Prajwal R. Kafle, Shourya Khanna, Chiaki Kobayashi, Fan Liu, Benjamin T. Montet, Govind Nandakumar, David M. Nataf, Melissa K. Ness, Lorenzo Spina, Thor Tepper-García, Yuan-Sen Ting, Gregor Traven, Rok Vogrinčič, Robert A. Wittenmyer, Rosemary F. G. Wyse, Maruša Žerjal, and Galah Collaboration. The GALAH+ survey: Third data release. *Monthly Notices of the Royal Astronomical Society*, 506(1):150–201, September 2021. doi: 10.1093/mnras/stab1242.

M. Bulla. POSSIS: predicting spectra, light curves, and polarization for multidimensional models of supernovae and kilonovae. *Monthly Notices of the Royal Astronomical Society*, 489(4):5037–5045, November 2019. doi: 10.1093/mnras/stz2495.

James S. Bullock, Andrey V. Kravtsov, and David H. Weinberg. Reionization and the Abundance of Galactic Satellites. *Astrophysical Journal*, 539(2):517–521, August 2000. doi: 10.1086/309279.

- E. Margaret Burbidge, G. R. Burbidge, William A. Fowler, and F. Hoyle. Synthesis of the Elements in Stars. *Reviews of Modern Physics*, 29(4):547–650, January 1957. doi: 10.1103/RevModPhys.29.547.
- M. Busso, R. Gallino, and G. J. Wasserburg. Nucleosynthesis in Asymptotic Giant Branch Stars: Relevance for Galactic Enrichment and Solar System Formation. *Annual Review of Astronomy and Astrophysics*, 37:239–309, January 1999. doi: 10.1146/annurev.astro.37.1.239.
- Michele Cantiello, J. B. Jensen, J. P. Blakeslee, E. Berger, A. J. Levan, N. R. Tanvir, G. Raimondo, E. Brocato, K. D. Alexander, P. K. Blanchard, M. Branchesi, Z. Cano, R. Chornock, S. Covino, P. S. Cowperthwaite, P. D’Avanzo, T. Eftekhari, W. Fong, A. S. Fruchter, A. Grado, J. Hjorth, D. E. Holz, J. D. Lyman, I. Mandel, R. Margutti, M. Nicholl, V. A. Villar, and P. K. G. Williams. A Precise Distance to the Host Galaxy of the Binary Neutron Star Merger GW170817 Using Surface Brightness Fluctuations. *Astrophysical Journal Letters*, 854(2):L31, February 2018. doi: 10.3847/2041-8213/aaad64.
- E. Carretta and R. G. Gratton. Abundances for globular cluster giants. I. Homogeneous metallicities for 24 clusters. *Astronomy & Astrophysics*, 121:95–112, January 1997. doi: 10.1051/aas:1997116.
- E. Carretta, A. Bragaglia, R. G. Gratton, S. Lucatello, G. Catanzaro, F. Leone, M. Bellazzini, R. Claudi, V. D’Orazi, Y. Momany, S. Ortolani, E. Pancino, G. Piotto, A. Recio-Blanco, and E. Sabbi. Na-O anticorrelation and HB. VII. The chemical composition of first and second-generation stars in 15 globular clusters from GIRAFFE spectra. *Astronomy & Astrophysics*, 505(1):117–138, October 2009. doi: 10.1051/0004-6361/200912096.
- J. I. Castor. Spectral line formation in Wolf-Rayet envelopes. *Monthly Notices of the Royal Astronomical Society*, 149:111, January 1970. doi: 10.1093/mnras/149.2.111.
- G. Cescutti, P. François, F. Matteucci, R. Cayrel, and M. Spite. The chemical evolution of barium and europium in the Milky Way. *Astronomy & Astrophysics*, 448(2):557–569, March 2006. doi: 10.1051/0004-6361:20053622.
- Daniel Ceverino, Avishai Dekel, and Frederic Bournaud. High-redshift clumpy discs and bulges in cosmological simulations. *Monthly Notices of the Royal Astronomical Society*, 404(4):2151–2169, June 2010. doi: 10.1111/j.1365-2966.2010.16433.x.
- Gilles Chabrier. The Galactic Disk Mass Budget. I. Stellar Mass Function and Density. *Astrophysical Journal*, 554(2):1274–1281, Jun 2001. doi: 10.1086/321401.
- C. Chiappini, R. Hirschi, G. Meynet, S. Ekström, A. Maeder, and F. Matteucci. A strong case for fast stellar rotation at very low metallicities. *Astronomy & Astrophysics*, 449(2): L27–L30, April 2006. doi: 10.1051/0004-6361:20064866.
- Anirudh Chiti, Anna Frebel, Alexander P. Ji, Helmut Jerjen, Dongwon Kim, and John E. Norris. Chemical Abundances of New Member Stars in the Tucana II Dwarf Galaxy. *Astrophysical Journal*, 857(1):74, April 2018. doi: 10.3847/1538-4357/aab4fc.

- Anirudh Chiti, Anna Frebel, Joshua D. Simon, Denis Erkal, Laura J. Chang, Lina Necib, Alexander P. Ji, Helmut Jerjen, Dongwon Kim, and John E. Norris. An extended halo around an ancient dwarf galaxy. *Nature Astronomy*, February 2021. doi: 10.1038/s41550-020-01285-w.
- Arthur Choplin, Raphael Hirschi, Georges Meynet, and Sylvia Ekström. Are some CEMP-s stars the daughters of spinstars? *Astronomy & Astrophysics*, 607:L3, November 2017. doi: 10.1051/0004-6361/201731948.
- R. Chornock, E. Berger, D. Kasen, P. S. Cowperthwaite, M. Nicholl, V. A. Villar, K. D. Alexander, P. K. Blanchard, T. Eftekhari, W. Fong, R. Margutti, P. K. G. Williams, J. Annis, D. Brout, D. A. Brown, H. Y. Chen, M. R. Drout, B. Farr, R. J. Foley, J. A. Frieman, C. L. Fryer, K. Herner, D. E. Holz, R. Kessler, T. Matheson, B. D. Metzger, E. Quataert, A. Rest, M. Sako, D. M. Scolnic, N. Smith, and M. Soares-Santos. The Electromagnetic Counterpart of the Binary Neutron Star Merger LIGO/Virgo GW170817. IV. Detection of Near-infrared Signatures of r-process Nucleosynthesis with Gemini-South. *Astrophysical Journal Letters*, 848(2):L19, October 2017. doi: 10.3847/2041-8213/aa905c.
- Denis F. Cioffi, Christopher F. McKee, and Edmund Bertschinger. Dynamics of Radiative Supernova Remnants. *Astrophysical Journal*, 334:252, November 1988. doi: 10.1086/166834.
- Judith G. Cohen. No Heavy-element Dispersion in the Globular Cluster M92. *Astrophysical Journal Letters*, 740(2):L38, October 2011. doi: 10.1088/2041-8205/740/2/L38.
- Charlie Conroy and Pieter G. van Dokkum. The Stellar Initial Mass Function in Early-type Galaxies From Absorption Line Spectroscopy. II. Results. *Astrophysical Journal*, 760(1): 71, November 2012. doi: 10.1088/0004-637X/760/1/71.
- Benoit Côté, Chris L. Fryer, Krzysztof Belczynski, Oleg Korobkin, Martyna Chruślińska, Nicole Vassh, Matthew R. Mumpower, Jonas Lippuner, Trevor M. Sprouse, Rebecca Surman, and Ryan Wollaeger. The Origin of r-process Elements in the Milky Way. *Astrophysical Journal*, 855(2):99, March 2018. doi: 10.3847/1538-4357/aaad67.
- Benoit Côté, Marius Eichler, Almudena Arcones, Camilla J. Hansen, Paolo Simonetti, Anna Frebel, Chris L. Fryer, Marco Pignatari, Moritz Reichert, Krzysztof Belczynski, and Francesca Matteucci. Neutron Star Mergers Might Not Be the Only Source of r-process Elements in the Milky Way. *Astrophysical Journal*, 875(2):106, April 2019. doi: 10.3847/1538-4357/ab10db.
- P. S. Cowperthwaite, E. Berger, V. A. Villar, B. D. Metzger, M. Nicholl, R. Chornock, P. K. Blanchard, W. Fong, R. Margutti, M. Soares-Santos, K. D. Alexander, S. Allam, J. Annis, D. Brout, D. A. Brown, R. E. Butler, H. Y. Chen, H. T. Diehl, Z. Doctor, M. R. Drout, T. Eftekhari, B. Farr, D. A. Finley, R. J. Foley, J. A. Frieman, C. L. Fryer, J. García-Bellido, M. S. S. Gill, J. Guillochon, K. Herner, D. E. Holz, D. Kasen, R. Kessler, J. Marriner, T. Matheson, Jr. Neilsen, E. H., E. Quataert, A. Palmese, A. Rest, M. Sako, D. M. Scolnic, N. Smith, D. L. Tucker, P. K. G. Williams, E. Balbinot, J. L. Carlin, E. R.

- Cook, F. Durret, T. S. Li, P. A. A. Lopes, A. C. C. Lourenço, J. L. Marshall, G. E. Medina, J. Muir, R. R. Muñoz, M. Sauseda, D. J. Schlegel, L. F. Secco, A. K. Vivas, W. Wester, A. Zenteno, Y. Zhang, T. M. C. Abbott, M. Banerji, K. Bechtol, A. Benoit-Lévy, E. Bertin, E. Buckley-Geer, D. L. Burke, D. Capozzi, A. Carnero Rosell, M. Carrasco Kind, F. J. Castander, M. Crocce, C. E. Cunha, C. B. D’Andrea, L. N. da Costa, C. Davis, D. L. DePoy, S. Desai, J. P. Dietrich, A. Drlica-Wagner, T. F. Eifler, A. E. Evrard, E. Fernandez, B. Flaugher, P. Fosalba, E. Gaztanaga, D. W. Gerdes, T. Giannantonio, D. A. Goldstein, D. Gruen, R. A. Gruendl, G. Gutierrez, K. Honscheid, B. Jain, D. J. James, T. Jeltema, M. W. G. Johnson, M. D. Johnson, S. Kent, E. Krause, R. Kron, K. Kuehn, N. Nuropatkin, O. Lahav, M. Lima, H. Lin, M. A. G. Maia, M. March, P. Martini, R. G. McMahon, F. Menanteau, C. J. Miller, R. Miquel, J. J. Mohr, E. Neilsen, R. C. Nichol, R. L. C. Ogando, A. A. Plazas, N. Roe, A. K. Romer, A. Roodman, E. S. Rykoff, E. Sanchez, V. Scarpine, R. Schindler, M. Schubnell, I. Sevilla-Noarbe, M. Smith, R. C. Smith, F. Sobreira, E. Suchyta, M. E. C. Swanson, G. Tarle, D. Thomas, R. C. Thomas, M. A. Troxel, V. Vikram, A. R. Walker, R. H. Wechsler, J. Weller, B. Yanny, and J. Zuntz. The Electromagnetic Counterpart of the Binary Neutron Star Merger LIGO/Virgo GW170817. II. UV, Optical, and Near-infrared Light Curves and Comparison to Kilonova Models. *Astrophysical Journal Letters*, 848(2):L17, Oct 2017. doi: 10.3847/2041-8213/aa8fc7.
- S. Cristallo, O. Straniero, L. Piersanti, and D. Gobrecht. Evolution, Nucleosynthesis, and Yields of AGB Stars at Different Metallicities. III. Intermediate-mass Models, Revised Low-mass Models, and the ph-FRUITY Interface. *Astrophysical Journal Supplement*, 219(2):40, August 2015. doi: 10.1088/0067-0049/219/2/40.
- S. Cristallo, D. Karinkuzhi, A. Goswami, L. Piersanti, and D. Gobrecht. Constraints of the Physics of Low-mass AGB Stars from CH and CEMP Stars. *Astrophysical Journal*, 833(2):181, December 2016. doi: 10.3847/1538-4357/833/2/181.
- Siva Darbha and Daniel Kasen. Inclination Dependence of Kilonova Light Curves from Globally Aspherical Geometries. *Astrophysical Journal*, 897(2):150, July 2020. doi: 10.3847/1538-4357/ab9a34.
- Gerard de Vaucouleurs. Recherches sur les Nebuleuses Extragalactiques. *Annales d’Astrophysique*, 11:247, January 1948.
- Carolyn L. Doherty, Pilar Gil-Pons, Lionel Siess, and John C. Lattanzio. Super-AGB Stars and their Role as Electron Capture Supernova Progenitors. *Publications of the Astronomical Society of Australia*, 34:e056, November 2017. doi: 10.1017/pasa.2017.52.
- Nanae Domoto, Masaomi Tanaka, Shinya Wanajo, and Kyohei Kawaguchi. Signatures of r-process Elements in Kilonova Spectra. *Astrophysical Journal*, 913(1):26, May 2021. doi: 10.3847/1538-4357/abf358.
- Nanae Domoto, Masaomi Tanaka, Daiji Kato, Kyohei Kawaguchi, Kenta Hotokezaka, and Shinya Wanajo. Lanthanide Features in Near-infrared Spectra of Kilonovae. *arXiv e-prints*, art. arXiv:2206.04232, June 2022.

- G. W. Drake, G. A. Victor, and A. Dalgarno. Two-Photon Decay of the Singlet and Triplet Metastable States of Helium-like Ions. *Physical Review*, 180(1):25–32, April 1969. doi: 10.1103/PhysRev.180.25.
- Gina E. Duggan, Evan N. Kirby, Serge M. Andrievsky, and Sergey A. Korotin. Neutron Star Mergers are the Dominant Source of the r-process in the Early Evolution of Dwarf Galaxies. *Astrophysical Journal*, 869(1):50, December 2018. doi: 10.3847/1538-4357/aaeb8e.
- Irina Dvorkin, Frédéric Daigne, Stéphane Goriely, Elisabeth Vangioni, and Joseph Silk. The impact of turbulent mixing on the galactic r-process enrichment by binary neutron star mergers across the entire metallicity range. *arXiv e-prints*, art. arXiv:2010.00625, October 2020.
- A. Emerick et al. Metal Mixing and Ejection in Dwarf Galaxies Are Dependent on Nucleosynthetic Source. *Astrophysical Journal*, 869:94, December 2018. doi: 10.3847/1538-4357/aaec7d.
- Rodrigo Fernández and Brian D. Metzger. Delayed outflows from black hole accretion tori following neutron star binary coalescence. *Monthly Notices of the Royal Astronomical Society*, 435(1):502–517, October 2013. doi: 10.1093/mnras/stt1312.
- C. J. Fontes, C. L. Fryer, A. L. Hungerford, R. T. Wollaeger, and O. Korobkin. A line-binned treatment of opacities for the spectra and light curves from neutron star mergers. *Monthly Notices of the Royal Astronomical Society*, 493(3):4143–4171, April 2020. doi: 10.1093/mnras/staa485.
- C. J. Fontes, C. L. Fryer, R. T. Wollaeger, M. R. Mumpower, and T. M. Sprouse. Actinide opacities for modeling the spectra and light curves of kilonovae. *Monthly Notices of the Royal Astronomical Society*, September 2022. doi: 10.1093/mnras/stac2792.
- P. François, E. Depagne, V. Hill, M. Spite, F. Spite, B. Plez, T. C. Beers, J. Andersen, G. James, B. Barbuy, R. Cayrel, P. Bonifacio, P. Molaro, B. Nordström, and F. Primas. First stars. VIII. Enrichment of the neutron-capture elements in the early Galaxy. *Astronomy & Astrophysics*, 476(2):935–950, December 2007. doi: 10.1051/0004-6361:20077706.
- P. François, L. Monaco, P. Bonifacio, C. Moni Bidin, D. Geisler, and L. Sbordone. Abundance ratios of red giants in low-mass ultra-faint dwarf spheroidal galaxies. *Astronomy & Astrophysics*, 588:A7, April 2016. doi: 10.1051/0004-6361/201527181.
- Anna Frebel and Volker Bromm. Chemical Signatures of the First Galaxies: Criteria for One-shot Enrichment. *Astrophysical Journal*, 759(2):115, November 2012. doi: 10.1088/0004-637X/759/2/115.
- Anna Frebel, Joshua D. Simon, and Evan N. Kirby. Segue 1: An Unevolved Fossil Galaxy from the Early Universe. *Astrophysical Journal*, 786(1):74, May 2014. doi: 10.1088/0004-637X/786/1/74.

- T. K. Fritz, G. Battaglia, M. S. Pawlowski, N. Kallivayalil, R. van der Marel, S. T. Sohn, C. Brook, and G. Besla. Gaia DR2 proper motions of dwarf galaxies within 420 kpc. Orbits, Milky Way mass, tidal influences, planar alignments, and group infall. *Astronomy & Astrophysics*, 619:A103, November 2018. doi: 10.1051/0004-6361/201833343.
- Sho Fujibayashi, Masaru Shibata, Shinya Wanajo, Kenta Kiuchi, Koutarou Kyutoku, and Yuichiro Sekiguchi. Viscous evolution of a massive disk surrounding stellar-mass black holes in full general relativity. *Physical Review D*, 102(12):123014, December 2020. doi: 10.1103/PhysRevD.102.123014.
- Sho Fujibayashi, Kenta Kiuchi, Shinya Wanajo, Koutarou Kyutoku, Yuichiro Sekiguchi, and Masaru Shibata. Comprehensive study on the mass ejection and nucleosynthesis in the binary neutron star mergers leaving short-lived massive neutron stars. *arXiv e-prints*, art. arXiv:2205.05557, May 2022.
- Hajime Fukushima, Hidenobu Yajima, Kazuyuki Sugimura, Takashi Hosokawa, Kazuyuki Omukai, and Tomoaki Matsumoto. Star cluster formation and cloud dispersal by radiative feedback: dependence on metallicity and compactness. *Monthly Notices of the Royal Astronomical Society*, 497(3):3830–3845, August 2020. doi: 10.1093/mnras/staa2062.
- Jim Fuller, Anthony L. Piro, and Adam S. Jermyn. Slowing the spins of stellar cores. *Monthly Notices of the Royal Astronomical Society*, 485(3):3661–3680, May 2019. doi: 10.1093/mnras/stz514.
- Marla Geha, Thomas M. Brown, Jason Tumlinson, Jason S. Kalirai, Joshua D. Simon, Evan N. Kirby, Don A. VandenBerg, Ricardo R. Muñoz, Roberto J. Avila, Puragra Guhathakurta, and Henry C. Ferguson. The Stellar Initial Mass Function of Ultra-faint Dwarf Galaxies: Evidence for IMF Variations with Galactic Environment. *Astrophysical Journal*, 771(1):29, July 2013. doi: 10.1088/0004-637X/771/1/29.
- Mario Gennaro, Kirill Tchernyshyov, Thomas M. Brown, Marla Geha, Roberto J. Avila, Puragra Guhathakurta, Jason S. Kalirai, Evan N. Kirby, Alvio Renzini, Joshua D. Simon, Jason Tumlinson, and Luis C. Vargas. Evidence of a Non-universal Stellar Initial Mass Function. Insights from HST Optical Imaging of Six Ultra-faint Dwarf Milky Way Satellites. *Astrophysical Journal*, 855(1):20, March 2018. doi: 10.3847/1538-4357/aaa973.
- S. Goriely, A. Bauswein, O. Just, E. Pllumbi, and H. Th. Janka. Impact of weak interactions of free nucleons on the r-process in dynamical ejecta from neutron star mergers. *Monthly Notices of the Royal Astronomical Society*, 452(4):3894–3904, October 2015. doi: 10.1093/mnras/stv1526.
- Aldana Grichener and Noam Soker. The Common Envelope Jet Supernova (CEJSN) r-process Scenario. *Astrophysical Journal*, 878(1):24, June 2019. doi: 10.3847/1538-4357/ab1d5d.
- Oliver Hahn and Tom Abel. Multi-scale initial conditions for cosmological simulations. *Monthly Notices of the Royal Astronomical Society*, 415(3):2101–2121, Aug 2011. doi: 10.1111/j.1365-2966.2011.18820.x.

- T. T. Hansen, J. L. Marshall, J. D. Simon, T. S. Li, R. A. Bernstein, A. B. Pace, P. Ferguson, D. Q. Nagasawa, K. Kuehn, D. Carollo, M. Geha, D. James, A. Walker, H. T. Diehl, M. Aguena, S. Allam, S. Avila, E. Bertin, D. Brooks, E. Buckley-Geer, D. L. Burke, A. Carnero Rosell, M. Carrasco Kind, J. Carretero, M. Costanzi, L. N. Da Costa, S. Desai, J. De Vicente, P. Doel, K. Eckert, T. F. Eifler, S. Everett, I. Ferrero, J. Frieman, J. García-Bellido, E. Gaztanaga, D. W. Gerdes, D. Gruen, R. A. Gruendl, J. Gschwend, G. Gutierrez, S. R. Hinton, D. L. Hollowood, K. Honscheid, N. Kuropatkin, M. A. G. Maia, M. March, R. Miquel, A. Palmese, F. Paz-Chinchón, A. A. Plazas, E. Sanchez, B. Santiago, V. Scarpine, S. Serrano, M. Smith, M. Soares-Santos, E. Suchyta, M. E. C. Swanson, G. Tarle, T. N. Varga, R. Wilkinson, and DES Collaboration. Chemical Analysis of the Ultrafaint Dwarf Galaxy Grus II. Signature of High-mass Stellar Nucleosynthesis. *Astrophysical Journal*, 897(2):183, July 2020. doi: 10.3847/1538-4357/ab9643.
- Yutaka Hirai, Yuhri Ishimaru, Takayuki R. Saitoh, Michiko S. Fujii, Jun Hidaka, and Toshitaka Kajino. Enrichment of r-process Elements in Dwarf Spheroidal Galaxies in Chemo-dynamical Evolution Model. *Astrophysical Journal*, 814(1):41, November 2015. doi: 10.1088/0004-637X/814/1/41.
- Yutaka Hirai, Shinya Wanajo, and Takayuki R. Saitoh. Enrichment of Strontium in Dwarf Galaxies. *Astrophysical Journal*, 885(1):33, November 2019. doi: 10.3847/1538-4357/ab4654.
- Daichi Hiramatsu, D. Andrew Howell, Schuyler D. Van Dyk, Jared A. Goldberg, Keiichi Maeda, Takashi J. Moriya, Nozomu Tominaga, Ken'ichi Nomoto, Griffin Hosseinzadeh, Iair Arcavi, Curtis McCully, Jamison Burke, K. Azalee Bostroem, Stefano Valenti, Yize Dong, Peter J. Brown, Jennifer E. Andrews, Christopher Bilinski, G. Grant Williams, Paul S. Smith, Nathan Smith, David J. Sand, Gagandeep S. Anand, Chengyuan Xu, Alexei V. Filippenko, Melina C. Bersten, Gastón Folatelli, Patrick L. Kelly, Toshihide Noguchi, and Koichi Itagaki. The electron-capture origin of supernova 2018zd. *arXiv e-prints*, art. arXiv:2011.02176, November 2020.
- Shingo Hirano, Takashi Hosokawa, Naoki Yoshida, Hideyuki Umeda, Kazuyuki Omukai, Gen Chiaki, and Harold W. Yorke. One Hundred First Stars: Protostellar Evolution and the Final Masses. *Astrophysical Journal*, 781(2):60, February 2014. doi: 10.1088/0004-637X/781/2/60.
- R. D. Hoffman, S. E. Woosley, and Y. Z. Qian. Nucleosynthesis in Neutrino-driven Winds. II. Implications for Heavy Element Synthesis. *Astrophysical Journal*, 482(2):951–962, June 1997. doi: 10.1086/304181.
- S. Honda, W. Aoki, Y. Ishimaru, S. Wanajo, and S. G. Ryan. Neutron-Capture Elements in the Very Metal Poor Star HD 122563. *Astrophysical Journal*, 643(2):1180–1189, June 2006. doi: 10.1086/503195.
- Satoshi Honda, Wako Aoki, Toshitaka Kajino, Hiroyasu Ando, Timothy C. Beers, Hideyuki Izumiura, Kozo Sadakane, and Masahide Takada-Hidai. Spectroscopic Studies of Extremely Metal-Poor Stars with the Subaru High Dispersion Spectrograph. II. The r-Process

- Elements, Including Thorium. *Astrophysical Journal*, 607(1):474–498, May 2004. doi: 10.1086/383406.
- Philip F. Hopkins, Andrew Wetzel, Dušan Kereš, Claude-André Faucher-Giguère, Eliot Quataert, Michael Boylan-Kolchin, Norman Murray, Christopher C. Hayward, Shea Garrison-Kimmel, Cameron Hummels, Robert Feldmann, Paul Torrey, Xiangcheng Ma, Daniel Anglés-Alcázar, Kung-Yi Su, Matthew Orr, Denise Schmitz, Ivanna Escala, Robyn Sanderson, Michael Y. Grudić, Zachary Hafen, Ji-Hoon Kim, Alex Fitts, James S. Bullock, Coral Wheeler, T. K. Chan, Oliver D. Elbert, and Desika Narayanan. FIRE-2 simulations: physics versus numerics in galaxy formation. *Monthly Notices of the Royal Astronomical Society*, 480(1):800–863, October 2018. doi: 10.1093/mnras/sty1690.
- Kenta Hotokezaka and Ehud Nakar. Radioactive Heating Rate of r-process Elements and Macronova Light Curve. *Astrophysical Journal*, 891(2):152, March 2020. doi: 10.3847/1538-4357/ab6a98.
- Kenta Hotokezaka, Tsvi Piran, and Michael Paul. Short-lived  $^{244}\text{Pu}$  points to compact binary mergers as sites for heavy r-process nucleosynthesis. *Nature Physics*, 11(12):1042, December 2015. doi: 10.1038/nphys3574.
- Kenta Hotokezaka, Paz Beniamini, and Tsvi Piran. Neutron star mergers as sites of r-process nucleosynthesis and short gamma-ray bursts. *International Journal of Modern Physics D*, 27(13):1842005, January 2018. doi: 10.1142/S0218271818420051.
- Kenta Hotokezaka, Masaomi Tanaka, Daiji Kato, and Gediminas Gaigalas. Nebular emission from lanthanide-rich ejecta of neutron star merger. *Monthly Notices of the Royal Astronomical Society*, 506(4):5863–5877, October 2021. doi: 10.1093/mnras/stab1975.
- Jr. Iben, I. Thermal pulses: p-capture, alpha -capture, s-process nucleosynthesis; and convective mixing in a star of intermediate mass. *Astrophysical Journal*, 196:525–547, March 1975. doi: 10.1086/153433.
- Shigeki Inoue and Naoki Yoshida. Clumpy galaxies in cosmological simulations: the effect of ISM model. *Monthly Notices of the Royal Astronomical Society*, 488(3):4400–4412, September 2019. doi: 10.1093/mnras/stz2076.
- M. N. Ishigaki, W. Aoki, N. Arimoto, and S. Okamoto. Chemical compositions of six metal-poor stars in the ultra-faint dwarf spheroidal galaxy Boötes I. *Astronomy & Astrophysics*, 562:A146, February 2014. doi: 10.1051/0004-6361/201322796.
- Yuhri Ishimaru, Shinya Wanajo, Wako Aoki, and Sean G. Ryan. The Detection of Low Eu Abundances in Extremely Metal-poor Stars and the Origin of r-Process Elements. *Astrophysical Journal Letters*, 600(1):L47–L50, January 2004. doi: 10.1086/381496.
- Yuhri Ishimaru, Shinya Wanajo, and Nikos Prantzos. Neutron Star Mergers as the Origin of r-process Elements in the Galactic Halo Based on the Sub-halo Clustering Scenario. *Astrophysical Journal Letters*, 804(2):L35, May 2015. doi: 10.1088/2041-8205/804/2/L35.

- H. Th. Janka, B. Müller, F. S. Kitaura, and R. Buras. Dynamics of shock propagation and nucleosynthesis conditions in O-Ne-Mg core supernovae. *Astronomy & Astrophysics*, 485(1):199–208, July 2008. doi: 10.1051/0004-6361:20079334.
- D. J. Jeffery and D. Branch. Analysis of Supernova Spectra. In J. C. Wheeler, T. Piran, and S. Weinberg, editors, *Supernovae, Jerusalem Winter School for Theoretical Physics*, volume 6, page 149, January 1990.
- Myoungwon Jeon, Gurtina Besla, and Volker Bromm. Connecting the First Galaxies with Ultrafaint Dwarfs in the Local Group: Chemical Signatures of Population III Stars. *Astrophysical Journal*, 848(2):85, October 2017. doi: 10.3847/1538-4357/aa8c80.
- A. P. Ji, T. S. Li, J. D. Simon, J. Marshall, A. K. Vivas, A. B. Pace, K. Bechtol, A. Drlica-Wagner, S. E. Koposov, T. T. Hansen, S. Allam, R. A. Gruendl, M. D. Johnson, M. McNanna, N. E. D. Noël, D. L. Tucker, and A. R. Walker. Detailed Abundances in the Ultra-faint Magellanic Satellites Carina II and III. *Astrophysical Journal*, 889(1):27, January 2020. doi: 10.3847/1538-4357/ab6213.
- Alexander P. Ji, Anna Frebel, Anirudh Chiti, and Joshua D. Simon. R-process enrichment from a single event in an ancient dwarf galaxy. *Nature*, 531(7596):610–613, March 2016a. doi: 10.1038/nature17425.
- Alexander P. Ji, Anna Frebel, Anirudh Chiti, and Joshua D. Simon. R-process enrichment from a single event in an ancient dwarf galaxy. *Nature*, 531(7596):610–613, Mar 2016b. doi: 10.1038/nature17425.
- Alexander P. Ji, Maria R. Drout, and Terese T. Hansen. The Lanthanide Fraction Distribution in Metal-poor Stars: A Test of Neutron Star Mergers as the Dominant r-process Site. *Astrophysical Journal*, 882(1):40, September 2019a. doi: 10.3847/1538-4357/ab3291.
- Alexander P. Ji, Joshua D. Simon, Anna Frebel, Kim A. Venn, and Terese T. Hansen. Chemical Abundances in the Ultra-faint Dwarf Galaxies Grus I and Triangulum II: Neutron-capture Elements as a Defining Feature of the Faintest Dwarfs. *Astrophysical Journal*, 870(2):83, January 2019b. doi: 10.3847/1538-4357/aaf3bb.
- Christian I. Johnson and Catherine A. Pilachowski. Chemical Abundances for 855 Giants in the Globular Cluster Omega Centauri (NGC 5139). *Astrophysical Journal*, 722(2):1373–1410, October 2010. doi: 10.1088/0004-637X/722/2/1373.
- F. Käppeler, R. Gallino, S. Bisterzo, and Wako Aoki. The s process: Nuclear physics, stellar models, and observations. *Reviews of Modern Physics*, 83(1):157–194, January 2011. doi: 10.1103/RevModPhys.83.157.
- Daniel Kasen, N. R. Badnell, and Jennifer Barnes. Opacities and Spectra of the r-process Ejecta from Neutron Star Mergers. *Astrophysical Journal*, 774(1):25, September 2013. doi: 10.1088/0004-637X/774/1/25.

- M. M. Kasliwal, E. Nakar, L. P. Singer, D. L. Kaplan, D. O. Cook, A. Van Sistine, R. M. Lau, C. Fremling, O. Gottlieb, J. E. Jencson, S. M. Adams, U. Feindt, K. Hotokezaka, S. Ghosh, D. A. Perley, P. C. Yu, T. Piran, J. R. Allison, G. C. Anupama, A. Balasubramanian, K. W. Bannister, J. Bally, J. Barnes, S. Barway, E. Bellm, V. Bhalerao, D. Bhattacharya, N. Blagorodnova, J. S. Bloom, P. R. Brady, C. Cannella, D. Chatterjee, S. B. Cenko, B. E. Cobb, C. Copperwheat, A. Corsi, K. De, D. Dobie, S. W. K. Emery, P. A. Evans, O. D. Fox, D. A. Frail, C. Frohmaier, A. Goobar, G. Hallinan, F. Harrison, G. Helou, T. Hinderer, A. Y. Q. Ho, A. Horesh, W. H. Ip, R. Itoh, D. Kasen, H. Kim, N. P. M. Kuin, T. Kupfer, C. Lynch, K. Madsen, P. A. Mazzali, A. A. Miller, K. Mooley, T. Murphy, C. C. Ngeow, D. Nichols, S. Nissanke, P. Nugent, E. O. Ofek, H. Qi, R. M. Quimby, S. Rosswog, F. Rusu, E. M. Sadler, P. Schmidt, J. Sollerman, I. Steele, A. R. Williamson, Y. Xu, L. Yan, Y. Yatsu, C. Zhang, and W. Zhao. Illuminating gravitational waves: A concordant picture of photons from a neutron star merger. *Science*, 358(6370):1559–1565, December 2017. doi: 10.1126/science.aap9455.
- Kyohei Kawaguchi, Masaru Shibata, and Masaomi Tanaka. Radiative Transfer Simulation for the Optical and Near-infrared Electromagnetic Counterparts to GW170817. *Astrophysical Journal Letters*, 865(2):L21, October 2018. doi: 10.3847/2041-8213/aade02.
- C. D. Kilpatrick, R. J. Foley, D. Kasen, A. Murguia-Berthier, E. Ramirez-Ruiz, D. A. Coulter, M. R. Drout, A. L. Piro, B. J. Shappee, K. Boutsia, C. Contreras, F. Di Mille, B. F. Madore, N. Morrell, Y. C. Pan, J. X. Prochaska, A. Rest, C. Rojas-Bravo, M. R. Siebert, J. D. Simon, and N. Ulloa. Electromagnetic evidence that SSS17a is the result of a binary neutron star merger. *Science*, 358(6370):1583–1587, December 2017. doi: 10.1126/science.aaq0073.
- Taysun Kimm and Renyue Cen. Escape Fraction of Ionizing Photons during Reionization: Effects due to Supernova Feedback and Runaway OB Stars. *Astrophysical Journal*, 788(2): 121, Jun 2014. doi: 10.1088/0004-637X/788/2/121.
- Ivan R. King. The structure of star clusters. III. Some simple dynamical models. *Astronomical Journal*, 71:64, February 1966. doi: 10.1086/109857.
- Yutaka Komiya, Takuma Suda, Hiroki Minaguchi, Toshikazu Shigeyama, Wako Aoki, and Masayuki Y. Fujimoto. The Origin of Carbon Enhancement and the Initial Mass Function of Extremely Metal-poor Stars in the Galactic Halo. *Astrophysical Journal*, 658(1):367–390, March 2007. doi: 10.1086/510826.
- Yutaka Komiya, Takuma Suda, and Masayuki Y. Fujimoto. Early-Age Evolution of the Milky Way Related by Extremely Metal-Poor Stars. *Astrophysical Journal*, 694(2):1577–1594, April 2009. doi: 10.1088/0004-637X/694/2/1577.
- Oleg Korobkin, Ryan T. Wollaeger, Christopher L. Fryer, Aimee L. Hungerford, Stephan Rosswog, Christopher J. Fontes, Matthew R. Mumpower, Eve A. Chase, Wesley P. Even, Jonah Miller, G. Wendell Misch, and Jonas Lippuner. Axisymmetric Radiative Transfer Models of Kilonovae. *Astrophysical Journal*, 910(2):116, April 2021. doi: 10.3847/1538-4357/abe1b5.

- Cecilia Kozma and Claes Fransson. Gamma-Ray Deposition and Nonthermal Excitation in Supernovae. *Astrophysical Journal*, 390:602, May 1992. doi: 10.1086/171311.
- Pavel Kroupa, Carsten Weidner, Jan Pflamm-Altenburg, Ingo Thies, Jörg Dabringhausen, Michael Marks, and Thomas Maschberger. *The Stellar and Sub-Stellar Initial Mass Function of Simple and Composite Populations*, volume 5, page 115. 2013. doi: 10.1007/978-94-007-5612-0\\_4.
- I. Kullmann, S. Goriely, O. Just, R. Ardevol-Pulpillo, A. Bauswein, and H. T. Janka. Dynamical ejecta of neutron star mergers with nucleonic weak processes I: nucleosynthesis. *Monthly Notices of the Royal Astronomical Society*, 510(2):2804–2819, February 2022. doi: 10.1093/mnras/stab3393.
- Young Sun Lee, Takuma Suda, Timothy C. Beers, and Richard J. Stancliffe. Carbon-enhanced Metal-poor Stars in SDSS/SEGUE. II. Comparison of CEMP-star Frequencies with Binary Population-synthesis Models. *Astrophysical Journal*, 788(2):131, June 2014. doi: 10.1088/0004-637X/788/2/131.
- A. J. Levan, J. D. Lyman, N. R. Tanvir, J. Hjorth, I. Mandel, E. R. Stanway, D. Steeghs, A. S. Fruchter, E. Troja, S. L. Schröder, K. Wiersema, S. H. Bruun, Z. Cano, S. B. Cenko, A. de Ugarte Postigo, P. Evans, S. Fairhurst, O. D. Fox, J. P. U. Fynbo, B. Gompertz, J. Greiner, M. Im, L. Izzo, P. Jakobsson, T. Kangas, H. G. Khandrika, A. Y. Lien, D. Malesani, P. O’Brien, J. P. Osborne, E. Palazzi, E. Pian, D. A. Perley, S. Rosswog, R. E. Ryan, S. Schulze, P. Sutton, C. C. Thöne, D. J. Watson, and R. A. M. J. Wijers. The Environment of the Binary Neutron Star Merger GW170817. *Astrophysical Journal Letters*, 848(2):L28, October 2017. doi: 10.3847/2041-8213/aa905f.
- T. S. Li, J. D. Simon, K. Kuehn, A. B. Pace, D. Erkal, K. Bechtol, B. Yanny, A. Drlica-Wagner, J. L. Marshall, C. Lidman, E. Balbinot, D. Carollo, S. Jenkins, C. E. Martínez-Vázquez, N. Shipp, K. M. Stringer, A. K. Vivas, A. R. Walker, R. H. Wechsler, F. B. Abdalla, S. Allam, J. Annis, S. Avila, E. Bertin, D. Brooks, E. Buckley-Geer, D. L. Burke, A. Carnero Rosell, M. Carrasco Kind, J. Carretero, C. E. Cunha, C. B. D’Andrea, L. N. da Costa, C. Davis, J. De Vicente, P. Doel, T. F. Eifler, A. E. Evrard, B. Flaugher, J. Frieman, J. García-Bellido, E. Gaztanaga, D. W. Gerdes, D. Gruen, R. A. Gruendl, J. Gschwend, G. Gutierrez, W. G. Hartley, D. L. Hollowood, K. Honscheid, D. J. James, E. Krause, M. A. G. Maia, M. March, F. Menanteau, R. Miquel, A. A. Plazas, E. Sanchez, B. Santiago, V. Scarpine, R. Schindler, M. Schubnell, I. Sevilla-Noarbe, M. Smith, R. C. Smith, M. Soares-Santos, F. Sobreira, E. Suchyta, M. E. C. Swanson, G. Tarle, D. L. Tucker, and DES Collaboration. The First Tidally Disrupted Ultra-faint Dwarf Galaxy?: A Spectroscopic Analysis of the Tucana III Stream. *Astrophysical Journal*, 866(1):22, October 2018. doi: 10.3847/1538-4357/aadf91.
- Marco Limongi and Alessandro Chieffi. Presupernova Evolution and Explosive Nucleosynthesis of Rotating Massive Stars in the Metallicity Range  $-3 \leq [\text{Fe}/\text{H}] \leq 0$ . *Astrophysical Journal Supplement*, 237(1):13, July 2018. doi: 10.3847/1538-4365/aacb24.
- Jonas Lippuner, Rodrigo Fernández, Luke F. Roberts, Francois Foucart, Daniel Kasen, Brian D. Metzger, and Christian D. Ott. Signatures of hypermassive neutron star

- lifetimes on r-process nucleosynthesis in the disc ejecta from neutron star mergers. *Monthly Notices of the Royal Astronomical Society*, 472(1):904–918, November 2017. doi: 10.1093/mnras/stx1987.
- L. B. Lucy. Nonthermal Excitation of Helium in Type Ib Supernovae. *Astrophysical Journal*, 383:308, December 1991. doi: 10.1086/170787.
- Dan Maoz, Filippo Mannucci, and Timothy D. Brandt. The delay-time distribution of Type Ia supernovae from Sloan II. *Monthly Notices of the Royal Astronomical Society*, 426(4): 3282–3294, November 2012. doi: 10.1111/j.1365-2966.2012.21871.x.
- Raffaella Margutti and Ryan Chornock. First Multimessenger Observations of a Neutron Star Merger. *arXiv e-prints*, art. arXiv:2012.04810, December 2020.
- Raffaella Margutti and Ryan Chornock. First Multimessenger Observations of a Neutron Star Merger. *Annual Review of Astronomy and Astrophysics*, 59:155–202, September 2021. doi: 10.1146/annurev-astro-112420-030742.
- Federico Marinacci, Laura V. Sales, Mark Vogelsberger, Paul Torrey, and Volker Springel. Simulating the interstellar medium and stellar feedback on a moving mesh: implementation and isolated galaxies. *Monthly Notices of the Royal Astronomical Society*, 489(3):4233–4260, November 2019. doi: 10.1093/mnras/stz2391.
- A. F. Marino, C. Sneden, R. P. Kraft, G. Wallerstein, J. E. Norris, G. Da Costa, A. P. Milone, I. I. Ivans, G. Gonzalez, J. P. Fulbright, M. Hilker, G. Piotto, M. Zoccali, and P. B. Stetson. The two metallicity groups of the globular cluster M 22: a chemical perspective. *Astronomy & Astrophysics*, 532:A8, August 2011. doi: 10.1051/0004-6361/201116546.
- J. Marshall, T. Hansen, J. Simon, T. Li, R. Bernstein, K. Kuehn, A. Pace, D. DePoy, A. Palmese, A. Pieres, L. Strigari, A. Drlica-Wagner, C. Lidman, D. Nagasawa, E. Bertin, D. Brooks, E. Buckley-Geer, D. L. Burke, A. Carnero Rosell, M. Carrasco Kind, J. Carretero, C. E. Cunha, C. B. D’Andrea, L. N. da Costa, J. De Vicente, S. Desai, P. Doel, T. F. Eifler, B. Flaugher, P. Fosalba, J. Frieman, J. García-Bellido, E. Gaztanaga, D. W. Gerdes, R. A. Gruendl, J. Gschwend, G. Gutierrez, W. G. Hartley, D. L. Hollowood, K. Honscheid, B. Hoyle, D. J. James, N. Kuropatkin, M. A. G. Maia, F. Menanteau, C. J. Miller, R. Miquel, A. A. Plazas, E. Sanchez, B. Santiago, V. Scarpine, M. Schubnell, S. Serrano, I. Sevilla-Noarbe, M. Smith, E. Suchyta, M. E. C. Swanson, G. Tarle, and W. Wester. Chemical Abundance Analysis of Tucana III, the Second *r*-process Enhanced Ultra-Faint Dwarf Galaxy. *arXiv e-prints*, art. arXiv:1812.01022, Dec 2018.
- Nicolas F. Martin, Jelte T. A. de Jong, and Hans-Walter Rix. A Comprehensive Maximum Likelihood Analysis of the Structural Properties of Faint Milky Way Satellites. *Astrophysical Journal*, 684(2):1075–1092, September 2008. doi: 10.1086/590336.
- Tadafumi Matsuno, Wako Aoki, Luca Casagrande, Miho Ishigaki, Jianrong Shi, Masao Takata, Maosheng Xiang, David Yong, Haining Li, Takuma Suda, Qianfan Xing, and Jingkun Zhao. Star Formation Timescales of the Halo Populations from Asteroseismology and Chemical Abundances. *arXiv e-prints*, art. arXiv:2006.03619, June 2020.

- Tadafumi Matsuno, Yutaka Hirai, Yuta Tarumi, Kenta Hotokezaka, Masaomi Tanaka, and Amina Helmi. *R*-process enhancements of Gaia-Enceladus in GALAH DR3. *arXiv e-prints*, art. arXiv:2101.07791, January 2021.
- Curtis McCully, Daichi Hiramatsu, D. Andrew Howell, Griffin Hosseinzadeh, Iair Arcavi, Daniel Kasen, Jennifer Barnes, Michael M. Shara, Ted B. Williams, Petri Väisänen, Stephen B. Potter, Encarni Romero-Colmenero, Steven M. Crawford, David A. H. Buckley, Jeffery Cooke, Igor Andreoni, Tyler A. Pritchard, Jirong Mao, Mariusz Gromadzki, and Jamison Burke. The Rapid Reddening and Featureless Optical Spectra of the Optical Counterpart of GW170817, AT 2017gfo, during the First Four Days. *Astrophysical Journal Letters*, 848(2):L32, October 2017. doi: 10.3847/2041-8213/aa9111.
- Paul W. Merrill. Spectroscopic Observations of Stars of Class. *Astrophysical Journal*, 116: 21, July 1952. doi: 10.1086/145589.
- B. D. Metzger, G. Martínez-Pinedo, S. Darbha, E. Quataert, A. Arcones, D. Kasen, R. Thomas, P. Nugent, I. V. Panov, and N. T. Zinner. Electromagnetic counterparts of compact object mergers powered by the radioactive decay of r-process nuclei. *Monthly Notices of the Royal Astronomical Society*, 406(4):2650–2662, August 2010. doi: 10.1111/j.1365-2966.2010.16864.x.
- Brian D. Metzger. Kilonovae. *Living Reviews in Relativity*, 20(1):3, May 2017. doi: 10.1007/s41114-017-0006-z.
- Brian D. Metzger, Todd A. Thompson, and Eliot Quataert. On the Conditions for Neutron-rich Gamma-Ray Burst Outflows. *Astrophysical Journal*, 676(2):1130–1150, April 2008. doi: 10.1086/526418.
- Dimitri Mihalas. *Stellar atmospheres*. 1978.
- H. Mo, F. C. van den Bosch, and S. White. *Galaxy Formation and Evolution*. May 2010.
- F. Montes, T. C. Beers, J. Cowan, T. Elliot, K. Farouqi, R. Gallino, M. Heil, K. L. Kratz, B. Pfeiffer, M. Pignatari, and H. Schatz. Nucleosynthesis in the Early Galaxy. *Astrophysical Journal*, 671(2):1685–1695, December 2007. doi: 10.1086/523084.
- Anna M. Moore, James E. Larkin, Shelley A. Wright, Brian Bauman, Jennifer Dunn, Brent Ellerbroek, Andrew C. Phillips, Luc Simard, Ryuji Suzuki, Kai Zhang, Ted Aliado, George Brims, John Canfield, Shaojie Chen, Richard Dekany, Alex Delacroix, Tuan Do, Glen Herriot, Bungo Ikenoue, Chris Johnson, Elliot Meyer, Yoshiyuki Obuchi, John Pazder, Vladimir Reshetov, Reed Riddle, Sakae Saito, Roger Smith, Ji Man Sohn, Fumihiro Uraguchi, Tomonori Usuda, Eric Wang, Lianqi Wang, Jason Weiss, and Robert Wooff. The Infrared Imaging Spectrograph (IRIS) for TMT: instrument overview. In Suzanne K. Ramsay, Ian S. McLean, and Hideki Takami, editors, *Ground-based and Airborne Instrumentation for Astronomy V*, volume 9147 of *Society of Photo-Optical Instrumentation Engineers (SPIE) Conference Series*, page 914724, August 2014. doi: 10.1117/12.2055216.

- Ricardo R. Muñoz, Patrick Côté, Felipe A. Santana, Marla Geha, Joshua D. Simon, Grecco A. Oyarzún, Peter B. Stetson, and S. G. Djorgovski. A MegaCam Survey of Outer Halo Satellites. III. Photometric and Structural Parameters. *Astrophysical Journal*, 860(1):66, June 2018. doi: 10.3847/1538-4357/aac16b.
- Sultana N. Nahar. Photoionization and electron-ion recombination of He I. *New Astronomy*, 15(5):417–426, July 2010. doi: 10.1016/j.newast.2009.11.010.
- Ehud Nakar. The electromagnetic counterparts of compact binary mergers. *Physics Reports*, 886:1–84, November 2020. doi: 10.1016/j.physrep.2020.08.008.
- Ehud Nakar, Dovi Poznanski, and Boaz Katz. The Importance of  $^{56}\text{Ni}$  in Shaping the Light Curves of Type II Supernovae. *Astrophysical Journal*, 823(2):127, June 2016. doi: 10.3847/0004-637X/823/2/127.
- N. Nishimura, H. Sawai, T. Takiwaki, S. Yamada, and F. K. Thielemann. The Intermediate r-process in Core-collapse Supernovae Driven by the Magneto-rotational Instability. *Astrophysical Journal Letters*, 836(2):L21, Feb 2017. doi: 10.3847/2041-8213/aa5dee.
- Nobuya Nishimura, Tomoya Takiwaki, and Friedrich-Karl Thielemann. The r-process Nucleosynthesis in the Various Jet-like Explosions of Magnetorotational Core-collapse Supernovae. *Astrophysical Journal*, 810(2):109, Sep 2015. doi: 10.1088/0004-637X/810/2/109.
- Ken’ichi Nomoto. Evolution of 8–10  $M_{\text{sun}}$  Stars toward Electron Capture Supernovae. II. Collapse of an O + NE + MG Core. *Astrophysical Journal*, 322:206, November 1987. doi: 10.1086/165716.
- Donald E. Osterbrock and Gary J. Ferland. *Astrophysics of gaseous nebulae and active galactic nuclei*. 2006.
- Kaori Otsuki, Satoshi Honda, Wako Aoki, Toshitaka Kajino, and Grant J. Mathews. Neutron-Capture Elements in the Metal-poor Globular Cluster M15. *Astrophysical Journal Letters*, 641(2):L117–L120, April 2006. doi: 10.1086/504106.
- Rüdiger Pakmor, Volker Springel, Andreas Bauer, Philip Mocz, Diego J. Munoz, Sebastian T. Ohlmann, Kevin Schaal, and Chenchong Zhu. Improving the convergence properties of the moving-mesh code AREPO. *Monthly Notices of the Royal Astronomical Society*, 455(1): 1134–1143, Jan 2016. doi: 10.1093/mnras/stv2380.
- J. T. Palmerio, S. D. Vergani, R. Salvaterra, R. L. Sanders, J. Japelj, A. Vidal-García, P. D’Avanzo, D. Corre, D. A. Perley, A. E. Shapley, S. Boissier, J. Greiner, E. Le Floch, and P. Wiseman. Are long gamma-ray bursts biased tracers of star formation? Clues from the host galaxies of the Swift/BAT6 complete sample of bright LGRBs. III. Stellar masses, star formation rates, and metallicities at  $z > 1$ . *Astronomy & Astrophysics*, 623: A26, March 2019. doi: 10.1051/0004-6361/201834179.
- Jorge Peñarrubia, Julio F. Navarro, and Alan W. McConnachie. The Tidal Evolution of Local Group Dwarf Spheroidals. *Astrophysical Journal*, 673(1):226–240, January 2008. doi: 10.1086/523686.

Albino Perego, Diego Vescovi, Achille Fiore, Leonardo Chiesa, Christian Vogl, Stefano Benetti, Sebastiano Bernuzzi, Marica Branchesi, Enrico Cappellaro, Sergio Cristallo, Andreas Flörs, Wolfgang E. Kerzendorf, and David Radice. Production of Very Light Elements and Strontium in the Early Ejecta of Neutron Star Mergers. *Astrophysical Journal*, 925(1):22, January 2022. doi: 10.3847/1538-4357/ac3751.

Hagai B. Perets and Paz Beniamini. No velocity-kicks are required to explain large-distance offsets of Ca-rich supernovae and short-GRBs. *arXiv e-prints*, art. arXiv:2101.11622, January 2021.

E. Pian, P. D’Avanzo, S. Benetti, M. Branchesi, E. Brocato, S. Campana, E. Cappellaro, S. Covino, V. D’Elia, J. P. U. Fynbo, F. Getman, G. Ghirlanda, G. Ghisellini, A. Grado, G. Greco, J. Hjorth, C. Kouveliotou, A. Levan, L. Limatola, D. Malesani, P. A. Mazzali, A. Melandri, P. Møller, L. Nicastro, E. Palazzi, S. Piranomonte, A. Rossi, O. S. Salafia, J. Selsing, G. Stratta, M. Tanaka, N. R. Tanvir, L. Tomasella, D. Watson, S. Yang, L. Amati, L. A. Antonelli, S. Ascenzi, M. G. Bernardini, M. Boër, F. Bufano, A. Bulgarelli, M. Capaccioli, P. Casella, A. J. Castro-Tirado, E. Chassande-Mottin, R. Ciolfi, C. M. Copperwheat, M. Dadina, G. De Cesare, A. di Paola, Y. Z. Fan, B. Gendre, G. Giuffrida, A. Giunta, L. K. Hunt, G. L. Israel, Z. P. Jin, M. M. Kasliwal, S. Klose, M. Lisi, F. Longo, E. Maiorano, M. Mapelli, N. Masetti, L. Nava, B. Patricelli, D. Perley, A. Pescalli, T. Piran, A. Possenti, L. Pulone, M. Razzano, R. Salvaterra, P. Schipani, M. Spera, A. Stameria, L. Stella, G. Tagliaferri, V. Testa, E. Troja, M. Turatto, S. D. Vergani, and D. Vergani. Spectroscopic identification of r-process nucleosynthesis in a double neutron-star merger. *Nature*, 551(7678):67–70, November 2017. doi: 10.1038/nature24298.

Planck Collaboration, N. Aghanim, Y. Akrami, M. Ashdown, J. Aumont, C. Baccigalupi, M. Ballardini, A. J. Banday, R. B. Barreiro, N. Bartolo, S. Basak, R. Battye, K. Benabed, J. P. Bernard, M. Bersanelli, P. Bielewicz, J. J. Bock, J. R. Bond, J. Borrill, F. R. Bouchet, F. Boulanger, M. Bucher, C. Burigana, R. C. Butler, E. Calabrese, J. F. Cardoso, J. Carron, A. Challinor, H. C. Chiang, J. Chluba, L. P. L. Colombo, C. Combet, D. Contreras, B. P. Crill, F. Cuttaia, P. de Bernardis, G. de Zotti, J. Delabrouille, J. M. Delouis, E. Di Valentino, J. M. Diego, O. Doré, M. Douspis, A. Ducout, X. Dupac, S. Dusini, G. Efstathiou, F. Elsner, T. A. Enßlin, H. K. Eriksen, Y. Fantaye, M. Farhang, J. Fergusson, R. Fernandez-Cobos, F. Finelli, F. Forastieri, M. Frailis, A. A. Fraisse, E. Franceschi, A. Frolov, S. Galeotta, S. Galli, K. Ganga, R. T. Génova-Santos, M. Gerbino, T. Ghosh, J. González-Nuevo, K. M. Górski, S. Gratton, A. Gruppuso, J. E. Gudmundsson, J. Hamann, W. Handley, F. K. Hansen, D. Herranz, S. R. Hildebrandt, E. Hivon, Z. Huang, A. H. Jaffe, W. C. Jones, A. Karakci, E. Keihänen, R. Keskitalo, K. Kiiveri, J. Kim, T. S. Kisner, L. Knox, N. Krachmalnicoff, M. Kunz, H. Kurki-Suonio, G. Lagache, J. M. Lamarre, A. Lasenby, M. Lattanzi, C. R. Lawrence, M. Le Jeune, P. Lemos, J. Lesgourgues, F. Levrier, A. Lewis, M. Liguori, P. B. Lilje, M. Lilley, V. Lindholm, M. López-Caniego, P. M. Lubin, Y. Z. Ma, J. F. Macías-Pérez, G. Maggio, D. Maino, N. Mandolesi, A. Mangilli, A. Marcos-Caballero, M. Maris, P. G. Martin, M. Martinelli, E. Martínez-González, S. Matarrese, N. Mauri, J. D. McEwen, P. R. Meinhold, A. Melchiorri, A. Mennella, M. Migliaccio, M. Millea, S. Mitra, M. A. Miville-Deschênes, D. Molinari, L. Montier, G. Morgante, A. Moss, P. Natoli, H. U. Nørgaard-Nielsen, L. Pagano,

- D. Paoletti, B. Partridge, G. Patanchon, H. V. Peiris, F. Perrotta, V. Pettorino, F. Piacentini, L. Polastri, G. Polenta, J. L. Puget, J. P. Rachen, M. Reinecke, M. Remazeilles, A. Renzi, G. Rocha, C. Rosset, G. Roudier, J. A. Rubiño-Martín, B. Ruiz-Granados, L. Salvati, M. Sandri, M. Savelainen, D. Scott, E. P. S. Shellard, C. Sirignano, G. Sirri, L. D. Spencer, R. Sunyaev, A. S. Suur-Uski, J. A. Tauber, D. Tavagnacco, M. Tenti, L. Toffolatti, M. Tomasi, T. Trombetti, L. Valenziano, J. Valiviita, B. Van Tent, L. Vibert, P. Vielva, F. Villa, N. Vittorio, B. D. Wandelt, I. K. Wehus, M. White, S. D. M. White, A. Zacchei, and A. Zonca. Planck 2018 results. VI. Cosmological parameters. *Astronomy & Astrophysics*, 641:A6, September 2020. doi: 10.1051/0004-6361/201833910.
- Quentin Pognan, Anders Jerkstrand, and Jon Grumer. NLTE effects on kilonova expansion opacities. *Monthly Notices of the Royal Astronomical Society*, 513(4):5174–5197, July 2022. doi: 10.1093/mnras/stac1253.
- L. Portinari, C. Chiosi, and A. Bressan. Galactic chemical enrichment with new metallicity dependent stellar yields. *Astronomy & Astrophysics*, 334:505–539, June 1998.
- N. Prantzos, C. Abia, M. Limongi, A. Chieffi, and S. Cristallo. Chemical evolution with rotating massive star yields - I. The solar neighbourhood and the s-process elements. *Monthly Notices of the Royal Astronomical Society*, 476(3):3432–3459, May 2018. doi: 10.1093/mnras/sty316.
- Barton J. Pritzl, Kim A. Venn, and Mike Irwin. A Comparison of Elemental Abundance Ratios in Globular Clusters, Field Stars, and Dwarf Spheroidal Galaxies. *Astronomical Journal*, 130(5):2140–2165, November 2005. doi: 10.1086/432911.
- Y. Z. Qian and S. E. Woosley. Nucleosynthesis in Neutrino-driven Winds. I. The Physical Conditions. *Astrophysical Journal*, 471:331, November 1996. doi: 10.1086/177973.
- Yu. Ralchenko, R. K. Janev, T. Kato, D. V. Fursa, I. Bray, and F. J. de Heer. Electron-impact excitation and ionization cross sections for ground state and excited helium atoms. *Atomic Data and Nuclear Data Tables*, 94(4):603–622, July 2008. doi: 10.1016/j.adt.2007.11.003.
- M. Reichert, C. J. Hansen, M. Hanke, Á. Skúladóttir, A. Arcones, and E. K. Grebel. Neutron-capture elements in dwarf galaxies. III. A homogenized analysis of 13 dwarf spheroidal and ultra-faint galaxies. *Astronomy & Astrophysics*, 641:A127, September 2020. doi: 10.1051/0004-6361/201936930.
- Alvio Renzini. Origin of multiple stellar populations in globular clusters and their helium enrichment. *Monthly Notices of the Royal Astronomical Society*, 391(1):354–362, November 2008. doi: 10.1111/j.1365-2966.2008.13892.x.
- Ian U. Roederer. Primordial r-process Dispersion in Metal-poor Globular Clusters. *Astrophysical Journal Letters*, 732(1):L17, May 2011. doi: 10.1088/2041-8205/732/1/L17.
- Ian U. Roederer. Are There Any Stars Lacking Neutron-capture Elements? Evidence from Strontium and Barium. *Astronomical Journal*, 145(1):26, January 2013. doi: 10.1088/0004-6256/145/1/26.

- George B. Rybicki and Alan P. Lightman. *Radiative Processes in Astrophysics*. 1986.
- Mohammadtaher Safarzadeh and Evan Scannapieco. Simulating neutron star mergers as r-process sources in ultrafaint dwarf galaxies. *Monthly Notices of the Royal Astronomical Society*, 471(2):2088–2096, October 2017a. doi: 10.1093/mnras/stx1706.
- Mohammadtaher Safarzadeh and Evan Scannapieco. Simulating neutron star mergers as r-process sources in ultrafaint dwarf galaxies. *Monthly Notices of the Royal Astronomical Society*, 471(2):2088–2096, October 2017b. doi: 10.1093/mnras/stx1706.
- Mohammadtaher Safarzadeh, Alexander P. Ji, Gregory A. Dooley, Anna Frebel, Evan Scannapieco, Facundo A. Gómez, and Brian W. O’Shea. Selecting ultra-faint dwarf candidate progenitors in cosmological N-body simulations at high redshifts. *Monthly Notices of the Royal Astronomical Society*, 476(4):5006–5015, Jun 2018. doi: 10.1093/mnras/sty595.
- Edwin E. Salpeter. The Luminosity Function and Stellar Evolution. *Astrophysical Journal*, 121:161, January 1955. doi: 10.1086/145971.
- Ralph A. Schönrich and David H. Weinberg. The chemical evolution of r-process elements from neutron star mergers: the role of a 2-phase interstellar medium. *Monthly Notices of the Royal Astronomical Society*, 487(1):580–594, July 2019. doi: 10.1093/mnras/stz1126.
- N. I. Shakura and R. A. Sunyaev. Black holes in binary systems. Observational appearance. *Astronomy & Astrophysics*, 24:337–355, January 1973.
- Daniel M. Siegel, Jennifer Barnes, and Brian D. Metzger. Collapsars as a major source of r-process elements. *Nature*, 569(7755):241–244, May 2019. doi: 10.1038/s41586-019-1136-0.
- J. D. Simon, T. S. Li, A. Drlica-Wagner, K. Bechtol, J. L. Marshall, D. J. James, M. Y. Wang, L. Strigari, E. Balbinot, K. Kuehn, A. R. Walker, T. M. C. Abbott, S. Allam, J. Annis, A. Benoit-Lévy, D. Brooks, E. Buckley-Geer, D. L. Burke, A. Carnero Rosell, M. Carrasco Kind, J. Carretero, C. E. Cunha, C. B. D’Andrea, L. N. da Costa, D. L. DePoy, S. Desai, P. Doel, E. Fernandez, B. Flaugher, J. Frieman, J. García-Bellido, E. Gaztanaga, D. A. Goldstein, D. Gruen, G. Gutierrez, N. Kuropatkin, M. A. G. Maia, P. Martini, F. Menanteau, C. J. Miller, R. Miquel, E. Neilsen, B. Nord, R. Ogando, A. A. Plazas, A. K. Romer, E. S. Rykoff, E. Sanchez, B. Santiago, V. Scarpine, M. Schubnell, I. Sevilla-Noarbe, R. C. Smith, F. Sobreira, E. Suchyta, M. E. C. Swanson, G. Tarle, L. Whiteway, B. Yanny, and DES Collaboration. Nearest Neighbor: The Low-mass Milky Way Satellite Tucana III. *Astrophysical Journal*, 838(1):11, Mar 2017. doi: 10.3847/1538-4357/aa5be7.
- Joshua D. Simon. Gaia Proper Motions and Orbits of the Ultra-faint Milky Way Satellites. *Astrophysical Journal*, 863(1):89, August 2018. doi: 10.3847/1538-4357/aacdfb.
- Joshua D. Simon. The Faintest Dwarf Galaxies. *arXiv e-prints*, art. arXiv:1901.05465, Jan 2019.
- Paolo Simonetti, Francesca Matteucci, Laura Greggio, and Gabriele Cescutti. A new delay time distribution for merging neutron stars tested against Galactic and cosmic data.

*Monthly Notices of the Royal Astronomical Society*, 486(2):2896–2909, June 2019. doi: 10.1093/mnras/stz991.

- Á. Skúladóttir, C. J. Hansen, S. Salvadori, and A. Choplin. Neutron-capture elements in dwarf galaxies. I. Chemical clocks and the short timescale of the r-process. *Astronomy & Astrophysics*, 631:A171, November 2019. doi: 10.1051/0004-6361/201936125.
- S. J. Smartt, T. W. Chen, A. Jerkstrand, M. Coughlin, E. Kankare, S. A. Sim, M. Fraser, C. Inserra, K. Maguire, K. C. Chambers, M. E. Huber, T. Krühler, G. Leloudas, M. Magee, L. J. Shingles, K. W. Smith, D. R. Young, J. Tonry, R. Kotak, A. Gal-Yam, J. D. Lyman, D. S. Homan, C. Agliozzo, J. P. Anderson, C. R. Angus, C. Ashall, C. Barbarino, F. E. Bauer, M. Berton, M. T. Botticella, M. Bulla, J. Bulger, G. Cannizzaro, Z. Cano, R. Cartier, A. Cikota, P. Clark, A. De Cia, M. Della Valle, L. Denneau, M. Dennefeld, L. Dessart, G. Dimitriadis, N. Elias-Rosa, R. E. Firth, H. Flewelling, A. Flörs, A. Franckowiak, C. Frohmaier, L. Galbany, S. González-Gaitán, J. Greiner, M. Gromadzki, A. Nicuesa Guelbenzu, C. P. Gutiérrez, A. Hamanowicz, L. Hanlon, J. Harmanen, K. E. Heintz, A. Heinze, M. S. Hernandez, S. T. Hodgkin, I. M. Hook, L. Izzo, P. A. James, P. G. Jonker, W. E. Kerzendorf, S. Klose, Z. Kostrzewa-Rutkowska, M. Kowalski, M. Kromer, H. Kuncarayakti, A. Lawrence, T. B. Lowe, E. A. Magnier, I. Manulis, A. Martin-Carrillo, S. Mattila, O. McBrien, A. Müller, J. Nordin, D. O’Neill, F. Onori, J. T. Palmerio, A. Pastorello, F. Patat, G. Pignata, Ph. Podsiadlowski, M. L. Pumo, S. J. Prentice, A. Rau, A. Razza, A. Rest, T. Reynolds, R. Roy, A. J. Ruiter, K. A. Rybicki, L. Salmon, P. Schady, A. S. B. Schultz, T. Schweyer, I. R. Seitenzahl, M. Smith, J. Sollerman, B. Stalder, C. W. Stubbs, M. Sullivan, H. Szegedi, F. Taddia, S. Taubenberger, G. Terreran, B. van Soelen, J. Vos, R. J. Wainscoat, N. A. Walton, C. Waters, H. Weiland, M. Willman, P. Wiseman, D. E. Wright, Ł. Wyrzykowski, and O. Yaron. A kilonova as the electromagnetic counterpart to a gravitational-wave source. *Nature*, 551(7678):75–79, November 2017. doi: 10.1038/nature24303.
- C. Sneden, J. J. Cowan, and R. Gallino. Neutron-capture elements in the early galaxy. *Annual Review of Astronomy and Astrophysics*, 46:241–288, September 2008. doi: 10.1146/annurev.astro.46.060407.145207.
- Christopher Sneden, Robert P. Kraft, Matthew D. Shetrone, Graeme H. Smith, G. E. Langer, and Charles F. Prosser. Star-To-Star Abundance Variations Among Bright Giants in the Metal-Poor Globular Cluster M15. *Astronomical Journal*, 114:1964, November 1997. doi: 10.1086/118618.
- Jennifer S. Sobeck, Robert P. Kraft, Christopher Sneden, George W. Preston, John J. Cowan, Graeme H. Smith, Ian B. Thompson, Stephen A. Shtetman, and Gregory S. Burley. The Abundances of Neutron-capture Species in the Very Metal-poor Globular Cluster M15: A Uniform Analysis of Red Giant Branch and Red Horizontal Branch Stars. *Astronomical Journal*, 141(6):175, June 2011. doi: 10.1088/0004-6256/141/6/175.
- V. V. Sobolev. *Moving envelopes of stars*. 1960.
- L. V. Spencer and U. Fano. Energy Spectrum Resulting from Electron Slowing Down. *Physical Review*, 93(6):1172–1181, March 1954. doi: 10.1103/PhysRev.93.1172.

- M. Spite, R. Cayrel, B. Plez, V. Hill, F. Spite, E. Depagne, P. François, P. Bonifacio, B. Barbuy, T. Beers, J. Andersen, P. Molaro, B. Nordström, and F. Primas. First stars VI - Abundances of C, N, O, Li, and mixing in extremely metal-poor giants. Galactic evolution of the light elements. *Astronomy & Astrophysics*, 430:655–668, February 2005. doi: 10.1051/0004-6361:20041274.
- Volker Springel. E pur si muove: Galilean-invariant cosmological hydrodynamical simulations on a moving mesh. *Monthly Notices of the Royal Astronomical Society*, 401(2):791–851, Jan 2010. doi: 10.1111/j.1365-2966.2009.15715.x.
- Volker Springel and Lars Hernquist. Cosmological smoothed particle hydrodynamics simulations: a hybrid multiphase model for star formation. *MNRAS*, 339(2):289–311, Feb 2003. doi: 10.1046/j.1365-8711.2003.06206.x.
- G. S. Stinson, C. Brook, A. V. Macciò, J. Wadsley, T. R. Quinn, and H. M. P. Couchman. Making Galaxies In a Cosmological Context: the need for early stellar feedback. *Monthly Notices of the Royal Astronomical Society*, 428(1):129–140, January 2013. doi: 10.1093/mnras/sts028.
- T. Suda, Y. Komiya, S. Yamada, Y. Katsuta, W. Aoki, P. Gil-Pons, C. L. Doherty, S. W. Campbell, P. R. Wood, and M. Y. Fujimoto. Transition of the stellar initial mass function explored using binary population synthesis. *Monthly Notices of the Royal Astronomical Society*, 432:L46–L50, May 2013. doi: 10.1093/mnrasl/slt033.
- Takuma Suda, Masayuki Aikawa, Masahiro N. Machida, Masayuki Y. Fujimoto, and Jr. Iben, Icko. Is HE 0107-5240 A Primordial Star? The Characteristics of Extremely Metal-Poor Carbon-Rich Stars. *Astrophysical Journal*, 611(1):476–493, August 2004. doi: 10.1086/422135.
- Takuma Suda, Yutaka Katsuta, Shimako Yamada, Tamon Suwa, Chikako Ishizuka, Yutaka Komiya, Kazuo Sorai, Masayuki Aikawa, and Masayuki Y. Fujimoto. Stellar Abundances for the Galactic Archeology (SAGA) Database — Compilation of the Characteristics of Known Extremely Metal-Poor Stars. *Publications of the Astronomical Society of Japan*, 60:1159, October 2008. doi: 10.1093/pasj/60.5.1159.
- Takuma Suda, Jun Hidaka, Wako Aoki, Yutaka Katsuta, Shimako Yamada, Masayuki Y. Fujimoto, Yukari Ohtani, Miyu Masuyama, Kazuhiro Noda, and Kentaro Wada. Stellar Abundances for Galactic Archaeology Database. IV. Compilation of stars in dwarf galaxies. *Publications of the Astronomical Society of Japan*, 69(5):76, October 2017. doi: 10.1093/pasj/psx059.
- K. M. Svensson, A. J. Levan, N. R. Tanvir, A. S. Fruchter, and L. G. Strolger. The host galaxies of core-collapse supernovae and gamma-ray bursts. *Monthly Notices of the Royal Astronomical Society*, 405(1):57–76, June 2010. doi: 10.1111/j.1365-2966.2010.16442.x.
- Masaomi Tanaka and Kenta Hotokezaka. Radiative Transfer Simulations of Neutron Star Merger Ejecta. *Astrophysical Journal*, 775(2):113, October 2013. doi: 10.1088/0004-637X/775/2/113.

- Masaomi Tanaka, Daiji Kato, Gediminas Gaigalas, and Kyohei Kawaguchi. Systematic opacity calculations for kilonovae. *Monthly Notices of the Royal Astronomical Society*, 496(2):1369–1392, August 2020. doi: 10.1093/mnras/staa1576.
- Yuta Tarumi, Takuma Suda, Robert J. J. Grand, Freeke van de Voort, Shigeki Inoue, and Naoki Yoshida. s-process enrichment and the origin of barium in ultrafaint dwarf galaxies. *arXiv e-prints*, art. arXiv:2009.10096, September 2020a.
- Yuta Tarumi, Naoki Yoshida, and Shigeki Inoue. R-process enrichment in ultrafaint dwarf galaxies. *Monthly Notices of the Royal Astronomical Society*, 494(1):120–128, March 2020b. doi: 10.1093/mnras/staa720.
- Yuta Tarumi, Naoki Yoshida, and Shigeki Inoue. R-process enrichment in ultrafaint dwarf galaxies. *Monthly Notices of the Royal Astronomical Society*, 494(1):120–128, March 2020c. doi: 10.1093/mnras/staa720.
- Todd A. Thompson and Asif ud-Doula. High-entropy ejections from magnetized proto-neutron star winds: implications for heavy element nucleosynthesis. *Monthly Notices of the Royal Astronomical Society*, 476(4):5502–5515, June 2018. doi: 10.1093/mnras/sty480.
- Eline Tolstoy, M. J. Irwin, A. Helmi, G. Battaglia, P. Jablonka, V. Hill, K. A. Venn, M. D. Shetrone, B. Letarte, A. A. Cole, F. Primas, P. Francois, N. Arimoto, K. Sadakane, A. Kaufer, T. Szeifert, and T. Abel. Two Distinct Ancient Components in the Sculptor Dwarf Spheroidal Galaxy: First Results from the Dwarf Abundances and Radial Velocities Team. *Astrophysical Journal Letters*, 617(2):L119–L122, December 2004. doi: 10.1086/427388.
- C. Travaglio, W. Hillebrandt, M. Reinecke, and F. K. Thielemann. Nucleosynthesis in multi-dimensional SN Ia explosions. *Astronomy & Astrophysics*, 425:1029–1040, October 2004a. doi: 10.1051/0004-6361:20041108.
- Claudia Travaglio, Roberto Gallino, Enrico Arnone, John Cowan, Faith Jordan, and Christopher Sneden. Galactic Evolution of Sr, Y, And Zr: A Multiplicity of Nucleosynthetic Processes. *Astrophysical Journal*, 601(2):864–884, February 2004b. doi: 10.1086/380507.
- J. Kelly Truelove, Richard I. Klein, Christopher F. McKee, II Holliman, John H., Louis H. Howell, and Jeffrey A. Greenough. The Jeans Condition: A New Constraint on Spatial Resolution in Simulations of Isothermal Self-gravitational Hydrodynamics. *Astrophysical Journal Letters*, 489(2):L179–L183, November 1997. doi: 10.1086/310975.
- Takuji Tsujimoto and Junichi Baba. Galactic r-process Abundance Feature Shaped by Radial Migration. *Astrophysical Journal*, 878(2):125, June 2019. doi: 10.3847/1538-4357/ab22b3.
- Takuji Tsujimoto, Nobuya Nishimura, and Koutarou Kyutoku. r-process Enrichment in the Galactic Halo Characterized by Nucleosynthesis Variation in the Ejecta of Coalescing Neutron Star Binaries. *Astrophysical Journal*, 889(2):119, February 2020. doi: 10.3847/1538-4357/ab655c.

- Mark Vogelsberger, Shy Genel, Debora Sijacki, Paul Torrey, Volker Springel, and Lars Hernquist. A model for cosmological simulations of galaxy formation physics. *Monthly Notices of the Royal Astronomical Society*, 436(4):3031–3067, Dec 2013. doi: 10.1093/mnras/stt1789.
- Matthew G. Walker and Jorge Peñarrubia. A Method for Measuring (Slopes of) the Mass Profiles of Dwarf Spheroidal Galaxies. *Astrophysical Journal*, 742(1):20, November 2011. doi: 10.1088/0004-637X/742/1/20.
- Shinya Wanajo. Physical Conditions for the r-process. I. Radioactive Energy Sources of Kilonovae. *Astrophysical Journal*, 868(1):65, November 2018. doi: 10.3847/1538-4357/aae0f2.
- Shinya Wanajo, Hans-Thomas Janka, and Bernhard Müller. Electron-capture Supernovae as The Origin of Elements Beyond Iron. *Astrophysical Journal Letters*, 726(2):L15, January 2011. doi: 10.1088/2041-8205/726/2/L15.
- Shinya Wanajo, Yuichiro Sekiguchi, Nobuya Nishimura, Kenta Kiuchi, Koutarou Kyutoku, and Masaru Shibata. Production of All the r-process Nuclides in the Dynamical Ejecta of Neutron Star Mergers. *Astrophysical Journal Letters*, 789(2):L39, July 2014. doi: 10.1088/2041-8205/789/2/L39.
- Shinya Wanajo, Bernhard Müller, Hans-Thomas Janka, and Alexander Heger. Nucleosynthesis in the Innermost Ejecta of Neutrino-driven Supernova Explosions in Two Dimensions. *Astrophysical Journal*, 852(1):40, January 2018. doi: 10.3847/1538-4357/aa9d97.
- David Wanderman and Tsvi Piran. The luminosity function and the rate of Swift’s gamma-ray bursts. *Monthly Notices of the Royal Astronomical Society*, 406(3):1944–1958, August 2010. doi: 10.1111/j.1365-2966.2010.16787.x.
- David Wanderman and Tsvi Piran. The rate, luminosity function and time delay of non-Collapsar short GRBs. *Monthly Notices of the Royal Astronomical Society*, 448(4):3026–3037, April 2015. doi: 10.1093/mnras/stv123.
- Darach Watson, Camilla J. Hansen, Jonatan Selsing, Andreas Koch, Daniele B. Malesani, Anja C. Andersen, Johan P. U. Fynbo, Almudena Arcones, Andreas Bauswein, Stefano Covino, Aniello Grado, Kasper E. Heintz, Leslie Hunt, Chryssa Kouveliotou, Giorgos Leloudas, Andrew J. Levan, Paolo Mazzali, and Elena Pian. Identification of strontium in the merger of two neutron stars. *Nature*, 574(7779):497–500, Oct 2019a. doi: 10.1038/s41586-019-1676-3.
- Darach Watson, Camilla J. Hansen, Jonatan Selsing, Andreas Koch, Daniele B. Malesani, Anja C. Andersen, Johan P. U. Fynbo, Almudena Arcones, Andreas Bauswein, Stefano Covino, Aniello Grado, Kasper E. Heintz, Leslie Hunt, Chryssa Kouveliotou, Giorgos Leloudas, Andrew J. Levan, Paolo Mazzali, and Elena Pian. Identification of strontium in the merger of two neutron stars. *Nature*, 574(7779):497–500, Oct 2019b. doi: 10.1038/s41586-019-1676-3.

- Eli Waxman, Eran O. Ofek, Doron Kushnir, and Avishay Gal-Yam. Constraints on the ejecta of the GW170817 neutron star merger from its electromagnetic emission. *Monthly Notices of the Royal Astronomical Society*, 481(3):3423–3441, December 2018. doi: 10.1093/mnras/sty2441.
- B. Wehmeyer, M. Pignatari, and F. K. Thielemann. Galactic evolution of rapid neutron capture process abundances: the inhomogeneous approach. *Monthly Notices of the Royal Astronomical Society*, 452(2):1970–1981, September 2015. doi: 10.1093/mnras/stv1352.
- Rainer Weinberger, Volker Springel, and Rüdiger Pakmor. The Arepo public code release. *arXiv e-prints*, art. arXiv:1909.04667, Sep 2019.
- Rainer Weinberger, Volker Springel, and Rüdiger Pakmor. The AREPO Public Code Release. *Astrophysical Journal Supplement*, 248(2):32, June 2020. doi: 10.3847/1538-4365/ab908c.
- Coral Wheeler, Philip F. Hopkins, Andrew B. Pace, Shea Garrison-Kimmel, Michael Boylan-Kolchin, Andrew Wetzel, James S. Bullock, Dušan Kereš, Claude-André Faucher-Giguère, and Eliot Quataert. Be it therefore resolved: cosmological simulations of dwarf galaxies with 30 solar mass resolution. *Monthly Notices of the Royal Astronomical Society*, 490(3):4447–4463, December 2019. doi: 10.1093/mnras/stz2887.
- S. D. M. White. Mixing processes in galaxy mergers. *Monthly Notices of the Royal Astronomical Society*, 191:1P–4P, April 1980. doi: 10.1093/mnras/191.1.1P.
- Beth Willman, Michael R. Blanton, Andrew A. West, Julianne J. Dalcanton, David W. Hogg, Donald P. Schneider, Nicholas Wherry, Brian Yanny, and Jon Brinkmann. A New Milky Way Companion: Unusual Globular Cluster or Extreme Dwarf Satellite? *Astronomical Journal*, 129(6):2692–2700, June 2005a. doi: 10.1086/430214.
- Beth Willman, Julianne J. Dalcanton, David Martinez-Delgado, Andrew A. West, Michael R. Blanton, David W. Hogg, J. C. Barentine, Howard J. Brewington, Michael Harvanek, S. J. Kleinman, Jurek Krzesinski, Dan Long, Jr. Neilsen, Eric H., Atsuko Nitta, and Stephanie A. Snedden. A New Milky Way Dwarf Galaxy in Ursa Major. *Astrophysical Journal Letters*, 626(2):L85–L88, June 2005b. doi: 10.1086/431760.
- Ryan T. Wollaeger, Oleg Korobkin, Christopher J. Fontes, Stephan K. Rosswog, Wesley P. Even, Christopher L. Fryer, Jesper Sollerman, Aimee L. Hungerford, Daniel R. van Rossum, and Allan B. Wollaber. Impact of ejecta morphology and composition on the electromagnetic signatures of neutron star mergers. *Monthly Notices of the Royal Astronomical Society*, 478(3):3298–3334, August 2018. doi: 10.1093/mnras/sty1018.
- C. C. Worley, V. Hill, J. Sobeck, and E. Carretta. Ba and Eu abundances in M 15 giant stars. *Astronomy & Astrophysics*, 553:A47, May 2013. doi: 10.1051/0004-6361/201321097.
- Meng-Ru Wu, J. Barnes, G. Martínez-Pinedo, and B. D. Metzger. Fingerprints of Heavy-Element Nucleosynthesis in the Late-Time Lightcurves of Kilonovae. *Physical Review Letters*, 122(6):062701, February 2019. doi: 10.1103/PhysRevLett.122.062701.

Michael Zevin, Kyle Kremer, Daniel M. Siegel, Scott Coughlin, Benny T. H. Tsang, Christopher P. L. Berry, and Vicky Kalogera. Can Neutron-star Mergers Explain the r-process Enrichment in Globular Clusters? *Astrophysical Journal*, 886(1):4, Nov 2019. doi: 10.3847/1538-4357/ab498b.

D. B. Zucker, V. Belokurov, N. W. Evans, J. T. Kleyna, M. J. Irwin, M. I. Wilkinson, M. Fellhauer, D. M. Bramich, G. Gilmore, H. J. Newberg, B. Yanny, J. A. Smith, P. C. Hewett, E. F. Bell, H. W. Rix, O. Y. Gnedin, S. Vidrih, R. F. G. Wyse, B. Willman, E. K. Grebel, D. P. Schneider, T. C. Beers, A. Y. Kniazev, J. C. Barentine, H. Brewington, J. Brinkmann, M. Harvanek, S. J. Kleinman, J. Krzesinski, D. Long, A. Nitta, and S. A. Snedden. A Curious Milky Way Satellite in Ursa Major. *Astrophysical Journal Letters*, 650(1):L41–L44, October 2006. doi: 10.1086/508628.